

**PRODUCTION, CHARACTERIZATION AND APPLICATION OF ENGINEERED  
BIOCHARS MADE FROM AGRICULTURAL WASTES FOR EFFECTIVE  
REMEDICATION OF EMERGING CONTAMINANTS IN WATER**

A Dissertation

by

SHENGQUAN ZENG

Submitted to the Office of Graduate and Professional Studies of  
Texas A&M University  
in partial fulfillment of the requirements for the degree of

DOCTOR OF PHILOSOPHY

Chair of Committee,	Eunsung Kan
Committee Members,	Yongheng Huang
	Zong Liu
	Itza Mendoza-Sanchez
Head of Department,	John Tracy

December 2020

Major Subject: Biological and Agricultural Engineering

Copyright 2020 Shengquan Zeng

## ABSTRACT

Biochar (BC) was produced from oxygen-limited pyrolysis of biomass. Bermudagrass (BG), as one of the most productive forage grasses, is widely planted in U.S. with annual dry matter yield of 6-10 tons per acre. The main objectives of this dissertation are to valorize BG to activated BCs by pyrolysis and activation for solving problems of water pollution by emerging contaminants (ECs), which are harmful for ecosystem and human health.

After NaOH and FeCl<sub>3</sub> activations, activated BCs showed high surface areas of 1992 and 1035 m<sup>2</sup>/g and high adsorption capacity of 425 and 265 mg/g BC for antibiotic sulfamethoxazole (SMX), respectively, which were higher than various BCs and activated carbons. Activated BCs were confirmed to adsorb SMX through  $\pi$ - $\pi$  EDA, hydrophobic, and hydrogen bond interactions with intraparticle diffusion limitation. NaOH desorption and thermal oxidation could effectively regenerate SMX-spent activated BCs. In addition, FeCl<sub>3</sub> activated BC without acid washing could remove SMX via simultaneous adsorption and heterogeneous Fenton oxidation.

FeCl<sub>3</sub> activated BC was also applied for adsorption of microcystin-LR (MC-LR) and showed high adsorption capacity compared to other adsorbents. The thermal regeneration showed excellent regeneration efficiency (above 99%) of MC-LR spent FA-BC. In addition, persulfate oxidation showed better performance than Fenton oxidation to regenerate the MC-LR spent FA-BC. Both diffusion and desorption of MC-LR from FeCl<sub>3</sub> activated BC controlled the MC-LR oxidation during the regeneration of MC-LR spent FeCl<sub>3</sub> activated BC by persulfate oxidation.

Besides the removal of SMX and MC-LR via the biochar, additional works were conducted to investigate effects of mechanical refining (MR) and BC addition on the performance of anaerobic digestion (AD) of dairy manure. Biogas and methane yields from AD of dairy manure were

significantly increased after MR pretreatment, due to the increase of manure solubilization, reduction of particle size, and achievement of external fibrillation and internal delamination of fibers in manure. The addition of alfalfa-derived BC lowered the lag phase and CO<sub>2</sub> content of biogas while increasing the COD removal efficiency in the AD of dairy manure. Moreover, the alfalfa-derived BC also resulted in the decrease of total VFAs and acetic acid concentrations.

## **DEDICATION**

Dedicated to my family, for their selfless encouragement and support.

## **ACKNOWLEDGEMENTS**

I would like to express my gratitude to my advisor, Dr. Eunsung Kan, for his support during my doctoral study. I benefited a lot from his useful suggestions and comments. I would also like to thank my committee members, Dr. Yongheng Huang, Dr. Zong Liu, and Dr. Itza Mendoza-Sanchez for their valuable advice.

I am also grateful to my colleagues, Dr. HyunMin Jang, Dr. Yong-Keun Choi, and Dr. Lu Ki Ong for their help. I would also like to thank other colleagues and friends in the Department of Biological and Agricultural Engineering and Texas A&M Agrilife Research Center for making my life a memorable experience.

Lastly, I am very appreciative to my family for their selfless encouragement and support.

## **CONTRIBUTORS AND FUNDING SOURCES**

### **Contributors**

This work was supported by a dissertation committee consisting of Dr. Eunsung Kan (Chair), Dr. Yongheng Huang, and Dr. Zong Liu of the Department of Biological and Agricultural Engineering, and Dr. Itza Mendoza-Sanchez of the School of Public Health.

The data in Chapter 7 were obtained with the undergraduate student (Riley Harris)'s assistance. The results in Chapter 2 and Chapter 3 were already published as two peer-reviewed journal articles. All other works shown in this dissertation were carried out by the students independently.

### **Funding Sources**

This dissertation was supported by Texas A&M University Chancellor Research Initiative Fund (PI: Dr. Eunsung Kan).

# TABLE OF CONTENTS

	Page
ABSTRACT.....	ii
DEDICATION.....	iv
ACKNOWLEDGEMENTS.....	v
CONTRIBUTORS AND FUNDING SOURCES.....	vi
TABLE OF CONTENTS.....	vii
LIST OF FIGURES.....	x
LIST OF TABLES.....	xiv
CHAPTER I INTRODUCTION.....	1
1.1 Emerging contaminants.....	1
1.2 Treatment techniques for ECs.....	2
1.3 Application of biochars for the treatment of ECs.....	3
1.4 Anaerobic digestion.....	5
1.5 Objectives.....	7
CHAPTER II CHEMICAL (NaOH) ACTIVATION OF FORAGE GRASS-DERIVED BIOCHAR FOR TREATMENT OF AQUEOUS ANTIBIOTIC SULFAMETHOXAZOLE.....	8
2.1 Introduction.....	8
2.2 Materials and methods.....	11
2.3 Results and discussion.....	15
2.4 Conclusions.....	31
CHAPTER III IRON-ACTIVATED BERMUDAGRASS-DERIVED BIOCHAR FOR ADSORPTION OF AQUEOUS SULFAMETHOXAZOLE: EFFECTS OF IRON IMPREGNATION RATIO ON BIOCHAR PROPERTIES, ADSORPTION, AND REGENERATION.....	32
3.1 Introduction.....	32
3.2 Materials and methods.....	34
3.3 Results and discussion.....	38
3.4 Conclusions.....	55

	Page
CHAPTER IV SIMULTANEOUS ADSORPTION AND HETEROGENEOUS FENTON OXIDATION FOR REMOVAL OF ANTIBIOTIC SULFAMETHOXAZOLE BY IRON-ACTIVATED BERMUDAGRASS-DERIVED BIOCHAR .....	57
4.1 Introduction .....	57
4.2 Materials and methods .....	60
4.3 Results and discussion.....	63
4.4 Conclusions .....	79
CHAPTER V CHARACTERIZATION, MECHANISM, AND REGENERATION OF IRON ACTIVATED BERMUDAGRASS-DERIVED BIOCHAR FOR MICROCYSTIN-LR ADSORPTION .....	81
5.1 Introduction .....	81
5.2 Materials and methods .....	84
5.3 Results and discussion.....	87
5.4 Conclusions .....	100
CHAPTER VI PERSULFATE OXIDATION-DRIVEN REGENERATION OF MICROCYSTIN-LR SPENT FECL <sub>3</sub> -ACTIVATED BIOCHAR .....	102
6.1 Introduction .....	102
6.2 Materials and methods .....	105
6.3 Results and discussion.....	108
6.4 Conclusions .....	123
CHAPTER VII EFFECT OF ALFALFA-DERIVED BIOCHAR ON ANAEROBIC DIGESTION OF DAIRY MANURE .....	124
7.1 Introduction .....	124
7.2 Materials and methods .....	126
7.3 Results and discussion.....	129
7.4 Conclusions .....	142
CHAPTER VIII EFFECTS OF MECHANICAL REFINING ON ANAEROBIC DIGESTION OF DAIRY MANURE .....	143
8.1 Introduction .....	143
8.2 Materials and methods .....	146
8.3 Results and discussion.....	148
8.4 Conclusions .....	158
CHAPTER IX SUMMARY AND CONCLUSIONS.....	159
REFERENCES .....	162



	Page
APPENDIX A SUPPORTING INFORMATION FOR CHAPTER II.....	182
APPENDIX B SUPPORTING INFORMATION FOR CHAPTER III.....	193
APPENDIX C SUPPORTING INFORMATION FOR CHAPTER IV .....	207
APPENDIX D SUPPORTING INFORMATION FOR CHAPTER V .....	217
APPENDIX E SUPPORTING INFORMATION FOR CHAPTER VI .....	229
APPENDIX F SUPPORTING INFORMATION FOR CHAPTER VII .....	235
APPENDIX G SUPPORTING INFORMATION FOR CHAPTER VIII .....	237

## LIST OF FIGURES

	Page
<b>Figure 2.1</b> Adsorption of SMX onto all BCs. ....	19
<b>Figure 2.2</b> Adsorption kinetics of SMX onto A-BC by fitting the pseudo-first order, pseudo-second order, and Elovich ((a) and (b)) and intra-particle diffusion model ((c) and (d)) and film diffusion model ((e) and (f)) under two different initial concentrations of 2. ....	23
<b>Figure 2.3</b> Reusability test of A-BC using 0.2 M NaOH. ....	31
<b>Figure 3.1</b> Effects of initial pH on adsorption of SMX onto BC800 and IA-BCs and pH-dependent SMX species. Experimental conditions: 100 mL of 100 mg/L SMX, 0.01 g of BC, initial pH of 1-11, and 48 h. ....	44
<b>Figure 3.2</b> Adsorption kinetics of SMX on IA-BC <sub>2.0</sub> . by fitting the pseudo-first order, pseudo-second order, two compartment first order and Elovich ((a) and (b)), film diffusion model ((c) and (d)), and intra-particle diffusion model ((e) and (f)) under two different initial concentrations of 50 mg/L((a), (c) and (e)) and 100 mg/L((b), (d) and (f)). Experimental conditions: 100 mL of 50 and 100 mg/L SMX, 0.01 g of BC, and initial pH of 3. ....	48
<b>Figure 3.3</b> Regeneration experiments for the SMX-spent IA-BC <sub>2.0</sub> using 0.1 M NaOH (a) and thermal oxidation at 573 K and 3 h (b). ....	52
<b>Figure 3.4</b> Comparison of the fraction of SMX in effluent of fixed bed experiment using BC800 and IA-BC <sub>2.0</sub> . The influent concentration of SMX and flow rate were 100 mg/L and 1.28 mL/min ( $C_0$ = SMX concentration in influent and $C_t$ = SMX in effluent at time t (min)). ....	55
<b>Figure 4.1</b> Effect of FeCl <sub>3</sub> /BG impregnation ratio on the performance of iron activated BCs for the adsorption and Fenton oxidation of SMX. Adsorption conditions: 0.01 g of BC, 100 mL of 100 mg/L SMX, initial pH of 3, temperature of 20 °C, and 24 h. Fenton oxidation conditions: 0.01 g of BC, 200 mg/L H <sub>2</sub> O <sub>2</sub> , 100 mL of 100 mg/L SMX, initial pH of 3, temperature of 20 °C, and 24 h. ....	64
<b>Figure 4.2</b> XPS spectra of FA-BC: full survey (a), C 1s (b), Fe 2p (c), and O 1s (d). ....	66
<b>Figure 4.3</b> (a) Adsorption kinetics for SMX on FA-BC. Conditions: 0.01 g of FA-BC, 100 mL of 100 mg/L SMX, temperature of 20 °C, and initial pH of 3. (b) Adsorption isotherm for SMX on FA-BC. Conditions: 0.01 g of FA-BC, 100 mL of 5-100 mg/L SMX, initial pH of 3, temperature of 20 °C, and 2 d. ....	69

<b>Figure 4.4</b> Effect of H <sub>2</sub> O <sub>2</sub> concentration on the removal efficiency of SMX and COD. Conditions: 0.01 g of FA-BC, 100 mL of 100 mg/L SMX, initial pH of 3, temperature of 20 °C, and reaction time of 12 h.....	70
<b>Figure 4.5</b> Effect of reaction temperature on the removal efficiency of SMX and COD. Conditions: 0.01 g of FA-BC, 100 mL of 100 mg/L SMX, initial pH of 3, 200 mg/L H <sub>2</sub> O <sub>2</sub> , and reaction time of 12 h. ....	73
<b>Figure 4.6</b> Reusability of FA-BC for Fenton oxidation of SMX. Conditions: 0.01 g of FA-BC, 100 mL of 100 mg/L SMX, initial pH of 3, 200 mg/L H <sub>2</sub> O <sub>2</sub> , and reaction temperature of 20 °C. ....	76
<b>Figure 4.7</b> SMX removal mechanisms of FA-BC via adsorption and Fenton oxidation.....	78
<b>Figure 4.8</b> Fenton oxidation of SMX by FA-BC in DI water and real wastewater. Conditions: 0.01 g of FA-BC, 100 mL of 100 mg/L SMX, initial pH of 3, 200 mg/L H <sub>2</sub> O <sub>2</sub> , and reaction temperature of 20 °C. ....	79
<b>Figure 5.1</b> Effect of FeCl <sub>3</sub> /BG impregnation ratio on MC-LR adsorption capacity.....	88
<b>Figure 5.2</b> Effect of initial pH on adsorption of MC-LR onto FA-BC.....	91
<b>Figure 5.3</b> Proposed mechanisms of MC-LR adsorption onto FA-BC.....	93
<b>Figure 5.4</b> Thermal regeneration (300 °C) of MC-LR spent FA-BC for successive cycles.....	99
<b>Figure 6.1</b> Adsorption kinetic constants (Pseudo-second order) of MC-LR onto FA-BC at various temperatures. Experimental conditions: 100 mL of 0.5 mg/L MC-LR, 0.004 g of FA-BC, and initial pH of 6. ....	109
<b>Figure 6.2</b> (a) Effect of initial pH on the regeneration efficiency of MC-LR spent FA-BC by PS oxidation. Regeneration conditions: 0.004 g of MC-LR spent FA-BC, 40 mL of 200 mg/L PS, and 20 °C. (b) Effect of PS concentration on the regeneration efficiency of MC-LR spent FA-BC by PS oxidation. Regeneration conditions: 0.004 g of MC-LR spent FA-BC, 40 mL of PS solution, pH 6, and 20 °C. ....	113
<b>Figure 6.3</b> (a) Effect of temperature on the regeneration efficiency of MC-LR spent FA-BC by PS oxidation. (b) Effect of temperature on the MC-LR oxidation rate and PS reaction rate during the regeneration of MC-LR spent FA-BC by PS oxidation. Conditions: 0.004 g of MC-LR spent FA-BC, 40 mL of 200 mg/L PS, and pH 6.....	115
<b>Figure 6.4</b> The temperature-dependent relative increase in the diffusion, diffusion + desorption, and oxidation rate of MC-LR during the regeneration of MC-LR spent FA-BC by PS oxidation.....	116

<b>Figure 6.5</b> The proposed mechanisms for the PS oxidation of MC-LR on FA-BC.....	118
<b>Figure 6.6</b> Reusability of FA-BC for MC-LR adsorption using PS oxidation regeneration. Adsorption conditions: 100 mL of 0.5 mg/L MC-LR, 0.004 g of FA-BC, pH 6, 20 °C and 2 d. Regeneration conditions: 0.004 g of MC-LR spent FA-BC, 40 mL of 200 mg/L PS, pH 6, and 50 °C.....	119
<b>Figure 6.7</b> (a) PS-driven regeneration of tetracycline spent FA-BC at various pH. Regeneration conditions: 0.02 g tetracycline spent FA-BC, 100 mL of 300 mg/L PS, and 2 d. (b) PS-driven regeneration of tetracycline spent FA-BC at various PS concentrations. Regeneration conditions: 0.02 g tetracycline spent FA-BC, 100 mL of PS solution, pH 6, and 2 d. ....	120
<b>Figure 6.8</b> (a) PS-driven regeneration of sulfamethoxazole spent FA-BC at various PS concentrations. Regeneration conditions: 0.01 g sulfamethoxazole spent FA-BC, 100 mL of PS solution, pH 6, and 2 d. (2) PS-driven regeneration of sulfamethoxazole spent FA-BC at various pH and temperatures. Regeneration conditions: 0.01 g sulfamethoxazole spent FA-BC, 100 mL of PS solution, and 2 d.....	122
<b>Figure 7.1</b> Cumulative biogas and methane volume (a,b) and yield (c,d) from AD of dairy manure with addition of different concentrations of AF-BC.....	130
<b>Figure 7.2</b> Daily methane yield from AD of dairy manure with addition of different concentrations of AF-BC. ....	132
<b>Figure 7.3</b> COD (a), ammonia (b), and phosphate (c) concentrations before and after AD of dairy manure with addition of different concentrations of AF-BC. ....	135
<b>Figure 7.4</b> Change of CO <sub>2</sub> concentration during the AD of dairy manure with addition of different concentrations of AF-BC. ....	137
<b>Figure 7.5</b> Changes of VFAs during the AD of dairy manure with addition of 0 g/L (a), 1 g/L (b), 5 g/L (c), and 10 g/L (d) of AF-BC. ....	139
<b>Figure 7.6</b> Changes of TA and pH during the AD of dairy manure with addition of different concentrations of AF-BC. ....	141
<b>Figure 8.1</b> Photograph (a, b, c), optical microscope (d, e, f) and SEM (g, h, i) images of unrefined (a, d, g) and refined manure with 6K revolutions (b, e, h) and 60K revolutions (c, f, i).....	149
<b>Figure 8.2</b> Water retention value (WRV) of unrefined and refined manure at 6K and 60K revolutions.....	151

**Figure 8.3** Cumulative methane and biogas volume (a,b) and yield (c,d) from AD of dairy manure..... 154

## LIST OF TABLES

	Page
<b>Table 2.1</b> The physicochemical characteristics of all BCs.....	16
<b>Table 2.2</b> Summary of kinetic parameters of SMX adsorption on A-BC.....	24
<b>Table 2.3</b> Summary of isotherm model parameters for SMX adsorption on A-BC.....	27
<b>Table 2.4</b> Thermodynamic parameters for the adsorption of SMX on A-BC.....	28
<b>Table 3.1</b> Physicochemical properties of bermudagrass and IA-BCs at various iron impregnation ratios. ....	39
<b>Table 3.2</b> Summary of isotherm parameters of SMX adsorption on IA-BC <sub>2.0</sub> . Experimental conditions: 100 mL of 10-100 mg/L SMX, 0.01 g of BC, initial pH of 3, and 48 h. ....	50
<b>Table 3.3</b> Thermodynamic parameters for the adsorption of SMX on IA-BC <sub>2.0</sub> . Experimental conditions: 100 mL of 100 mg/L SMX, 0.01 g of BC, initial pH of 3, temperature of 303-323 K, and 48 h. ....	51
<b>Table 4.1</b> SMX oxidation rate and H <sub>2</sub> O <sub>2</sub> decomposition rate under various temperatures. Conditions: 0.01 g of FA-BC, 100 mL of 100 mg/L SMX, initial pH of 3, 200 mg/L H <sub>2</sub> O <sub>2</sub> , and reaction time of 12 h. ....	74
<b>Table 5.1</b> The physicochemical properties of feedstock and BCs. ....	88
<b>Table 5.2</b> Summary of kinetic parameters of MC-LR adsorption onto FA-BC.....	95
<b>Table 5.3</b> Summary of isotherm parameters of MC-LR adsorption on FA-BC.....	97
<b>Table 5.4</b> Thermodynamic parameters for the adsorption of MC-LR on FA-BC.....	98
<b>Table 6.1</b> Adsorption kinetic parameters of MC-LR adsorption onto FA-BC under various temperatures (20-50 °C). Experimental conditions: 100 mL of 0.5 mg/L MC-LR, 0.004 g of FA-BC, and initial pH of 6. ....	109
<b>Table 6.2</b> MC-LR and S <sub>2</sub> O <sub>8</sub> <sup>2-</sup> diffusivity at various temperatures. ....	111
<b>Table 7.1</b> Parameters values of modified Gompertz model fitted with the experimental data. ....	133
<b>Table 8.1</b> Mean particle size of unrefined and mechanically refined dairy manure. ....	149
<b>Table 8.2</b> Solubility of dairy manure before and after mechanical refining. ....	152

**Table 8.3** Parameters values of modified Gompertz model fitted with the experimental data ..... 155

**Table 8.4** Operation parameters for AD process with different dairy manure..... 157

# CHAPTER I

## INTRODUCTION

### 1.1 Emerging contaminants

Emerging contaminants (ECs), widely existing in various water resources, are mainly natural and organic compounds, which are recently considered as important water contaminants and can potentially endanger aquatic environments and human health (Rodriguez-Narvaez et al., 2017). ECs mainly include pharmaceuticals, pesticides, endocrine disrupting compounds, disinfectants, surfactants, algal toxins, and so on (Rodriguez-Narvaez et al., 2017; Sophia & Lima, 2018). ECs in aquatic environments are mainly from wastewater treatment plants, landfills, hospitals, manufacturing sites, and agricultural systems (Pal et al., 2010). In addition, ECs can easily accumulate in soil, plants, and animals even under low concentrations ranging from ng/L to µg/L (Ahmed et al., 2017d). Due to low biodegradability and high chemical stability, conventional wastewater treatment processes cannot efficiently remove ECs from aqueous phase (Ahmed et al., 2017d). Therefore, it is of great importance to develop efficient and feasible techniques for the treatment of ECs from wastewater.

Antibiotics, one of the most common ECs, are confirmed to be persistent and with biological activity in the environment, which draws the attention of many researchers (Liu et al., 2009). In the past decades, antibiotics are extensively used as medicines and growth stimulants for animals with average amount of about 16,600 ton/year in the USA (Avisar et al., 2009; Kim et al., 2007). Even low concentrations of antibiotics in various water resources can result in the generation of bacterial resistance and resistance genes, which has become the important global public health issues in the past few years (Sharma et al., 2016).



Microcystins (MCs), released from cyanobacteria during the algal blooms in eutrophic waters, are the most abundant and common cyanotoxins in nature waters (Pavagadhi et al., 2013). MCs can make the aquatic organisms subjected to acute liver failure, cancer, and internal hemorrhage (Liu et al., 2018a). The previous reports from USA and Canada indicate that 80% of source-water samples are contaminated with MCs (Liu et al., 2019). Microcystin-LR (MC-LR), one of the most toxic and abundant MCs, makes up 56%-70% of MCs in USA (Liu et al., 2019; Park et al., 2020). Due to the significant environmental impacts, the World Health Organization (WHO) has stipulated that the safe concentration of MC-LR in drinking water is below 1 µg/L (Park et al., 2018a).

## **1.2 Treatment techniques for ECs**

Various physical, chemical and biological techniques have been applied for the treatment of ECs in the last few decades. Physical methods, including sedimentation and flocculation, exhibit low efficiency for polar or semi-polar ECs owing to their great water solubility (Stackelberg et al., 2007). Most of ECs such as antibiotics are non-biodegradable, which are not easily removed by biological processes such as activated sludge, biological reactor, enzyme degradation, biosorption, and so on (Ahmed et al., 2017d).

Among all treatment techniques, adsorption has been considered as an easily operated, nontoxic, and highly efficient method to eliminate ECs from water (Sophia & Lima, 2018). The previous review mentioned that a variety of adsorbents have been used for the removal of ECs (Sophia & Lima, 2018). For example, Vona et al. (2015) indicated that activated carbon showed high adsorption capacity for antibiotics. In addition, carbon nanotube and graphene are also proved to be efficient adsorbents for the treatment of antibiotics (Yu et al., 2016). However, for these

carbonaceous materials, high production, disposal, and regeneration costs limit their practical applications.

Advanced oxidation processes (AOPs), including Fenton oxidation, ozonation, photocatalysis, persulfate oxidation, and so on, can achieve high removal efficiency and deep mineralization of ECs via the generation of free radicals with powerfully destructive ability (Tu et al., 2020b). Among AOPs, Fenton and persulfate oxidation have been extensively applied for the degradation of organic contaminants. Fenton oxidation process can produce  $\cdot\text{OH}$  radicals with high redox potential (2.8 V), which can non-selectively attack various organic compounds (Ozbey Unal et al., 2019). Persulfate (PS) oxidation has been also used for the degradation of organic compounds by  $\text{SO}_4^{\cdot-}$  radicals, which are produced from the activation of PS by heat, UV, transition metals, and so on (Song et al., 2019). In addition, due to higher redox potential and lifetime,  $\text{SO}_4^{\cdot-}$  exhibits higher stability and wider reactivity compared to  $\cdot\text{OH}$  (Wang et al., 2017c).

### **1.3 Application of biochars for the treatment of ECs**

Biochar (BC), produced from the oxygen-limiting pyrolysis of carbon-rich biomass, have been considered as a feasible adsorbent for the treatment of contaminants from water due to the inexpensive and abundant feedstocks and high environmental friendliness (Mohan et al., 2014). A variety of BCs, produced from agricultural or industrial wastes, have been applied for the removal of ECs from water (Ahmad et al., 2014; Mohan et al., 2014). However, the adsorption of ECs onto raw BCs were often limited by their limited surface areas and poor porous structures (Choi & Kan, 2019; Yao et al., 2018). Therefore, for the improvement of adsorption ability for contaminants, it is significant to increase surface areas and optimize pore structures of raw BCs.

For improving the surface area, pore structures, and surface functional groups, many studies have focused on the BCs activation to enhance the adsorption capacity and functionality of BCs

(Braghiroli et al., 2018; Jang et al., 2018b). Activated BCs have been proved to have excellent adsorption performance for various contaminants (Braghiroli et al., 2018).  $\text{FeCl}_3$  and NaOH have been considered as effective activators to prepare activated BCs. After  $\text{FeCl}_3$  and NaOH activation, the surface area and porosity of BCs were significantly increased, which favored the improvement of adsorption ability for contaminants (Cho et al., 2017; Jang et al., 2018b; Zhu et al., 2016). Moreover,  $\text{FeCl}_3$  activation also resulted in the attachment of various iron species onto BCs (Zhu et al., 2016). In addition, magnetic iron compounds (e.g.  $\text{Fe}_3\text{O}_4$ ) appeared on the surface of  $\text{FeCl}_3$  activated BCs, which enable them to have magnetism and can be separated from the reaction solution by the magnet (Cho et al., 2017).

So far, studies about MC-LR adsorption onto BCs were quite limited (Li et al., 2018; Li et al., 2014a; Liu et al., 2018a). For example, Li et al. (2014a) reported that wood chips-derived BCs could effectively adsorb the MC-LR with the adsorption capacity of 0.926-4.197 mg/g via the electrostatic attraction and hydrogen bonding, and surface functional groups were significant for MC-LR adsorption. Li et al. (2018) found that chicken manure-derived BCs showed better performance for MC-LR adsorption than sawdust-derived BCs and maize straw-derived BCs due to the higher ash content, mesopore volume, and surface functionality. However, to our knowledge, there are still no reports about large molecule MC-LR adsorption onto activated BCs. Therefore, it is of great importance to figure out adsorption behaviors of MC-LR onto activated BCs.

Studies about regeneration of contaminants spent BCs are rarely reported. Contaminants spent BCs can be regenerated by the desorption and decomposition of contaminants on BCs (Dai et al., 2019). Thermal regeneration has been considered as an effective technique for the reuse of adsorbents through the decomposition of contaminants at high temperature (Dai et al., 2019; Wei et al., 2012). In addition, solvent regeneration is also a good method to reuse the adsorbents by the desorption

using inorganic reagents (such as acidic and alkali solution) and organic solvents (such as methanol and ethanol) (Dai et al., 2019). However, thermal treatment requires the high-energy input and causes the damage of structure and reduction of adsorption ability (Wei et al., 2012). In addition, for solvent regeneration, the treatment of large amounts of solvents containing high concentrations of contaminants is time-consuming and expensive (Du et al., 2016). Chemical regeneration can be a feasible option to in situ regenerate the contaminants spent adsorbents by advanced oxidation processes (AOPs). The previous studies indicated that Fenton or PS oxidation processes could be applied for regeneration of contaminants spent commercial activated carbon (An et al., 2015; Kim et al., 2015). However, to our knowledge, no studies have focused on the regeneration of contaminants spent BCs by PS or Fenton oxidation.

Considering production costs and environmental sustainability, the source and availability of feedstock are of great importance for production of BCs. Bermudagrass (BG), as one of the most productive forage grasses, is widely planted in the USA with annual dry matter yield of 6-10 tons per acre (Wang et al., 2010). In addition, about 20% of these forage grasses are often discarded due to formation of pathogenic fungi on the forage grasses (Jang & Kan, 2019c). Considering high quantities of BG production including discarded ones, BG could be potentially a viable biomass feedstock for BC production. However, studies about application of BG-derived BCs for treatment of contaminants are rarely reported.

#### **1.4 Anaerobic digestion**

A large amount of dairy manure (e.g., 0.92 billion tons per year in the U.S.) is generated annually worldwide (Zhang & Schroder, 2014). However, the widespread application of dairy manure to agriculture can cause the contamination of soil, water and air with excessive nutrients, antibiotics, and microbial pathogens (Atandi & Rahman, 2012; Gomez-Brandon et al., 2008; Nasir et al., 2012).

Anaerobic digestion (AD) is one of the most reliable techniques to dispose of dairy manure by converting it to biogas and digestate. AD can also lower emissions of greenhouse gas and mitigate the odor nuisance of manure (Atandi & Rahman, 2012; Jang et al., 2018a). However, current AD of dairy manure has several shortcomings, such as low digestion and biogas production, fluctuating performance, and generation of significant amounts of undigested sludge (Jang et al., 2018a; Li et al., 2015a).

In order to improve the AD performance, a variety of additives have been applied for the AD process, such as activated carbon (AC), carbon nanotube, graphene, iron oxides, BCs, and carbon cloth (Zhang et al., 2018a). BC could offer the benign environment for microbial attachment and growth, resulting in the improvement of the activity of AD microorganism (Wang et al., 2018a). In addition, BC could relieve the pH drop from VFAs accumulation and also reduce the ammonia inhibition in the AD process (Pan et al., 2019b). So far, considerable research about the effects of BCs derived from various solid wastes on AD has been reported. However, no studies have applied inexpensive forage grass-derived BCs in the AD process.

Approximately 40-50% of dairy manure is composed of biofibers, mainly consisting of lignin tightly associated with cellulose and hemicellulose, which is difficult to effectively degrade and hampers AD performance (Angelidaki & Ahring, 2000; Tsapekos et al., 2016). Mechanical refining (MR) is extensively utilized in the pulp and paper industry. MR can open up the biomass structure via external fibrillation and internal delamination (Park et al., 2016), while most mechanical pretreatment methods require strong mechanical force to lower the particle size of substrates. Therefore, compared to other mechanical pretreatment methods, MR is cost-effective and requires reasonable energy consumption (Park et al., 2016). Nevertheless, to the best of our knowledge, the application of mechanical refining to any AD process has not been reported to date.

## 1.5 Objectives

For overcoming current limitations for removal of ECs by BCs and AD of dairy manure, seven research objectives are proposed:

- (1) To prepare and use NaOH-activated bermudagrass-derived BCs for adsorption of antibiotic sulfamethoxazole (SMX) in water.
- (2) To prepare and use iron ( $\text{FeCl}_3$ )-activated bermudagrass-derived BCs for adsorption of antibiotic SMX in water and investigate the iron impregnation ratio on BC properties, adsorption mechanisms, and regeneration.
- (3) To prepare and use iron ( $\text{FeCl}_3$ )-activated bermudagrass-derived BCs for removal of antibiotic SMX by simultaneous adsorption and heterogeneous Fenton oxidation.
- (4) To prepare and use iron ( $\text{FeCl}_3$ )-activated bermudagrass-derived BCs for adsorption of microcystin-LR in water and investigate adsorption mechanisms and regeneration.
- (5) To regenerate microcystin-LR spent iron ( $\text{FeCl}_3$ ) activated bermudagrass-derived BCs by persulfate oxidation.
- (6) To study the effect of mechanical refining on the AD performance of dairy manure.
- (7) To study the effect of forage grass-derived BC on the AD performance of dairy manure.

## CHAPTER II

### CHEMICAL (NaOH) ACTIVATION OF FORAGE GRASS-DERIVED BIOCHAR FOR TREATMENT OF AQUEOUS ANTIBIOTIC SULFAMETHOXAZOLE\*

#### 2.1 Introduction

Sulfamethoxazole (SMX), one of extensively used sulfonamide antibiotics, can treat various diseases and infections for human and animals (Jang et al., 2018c). However, SMX has been detected in various water bodies and soil causing toxic effects in aquatic organisms and prevalence of antibiotic resistance genes due to its widespread utilization, low metabolic efficiency and slow biodegradation (Jang et al., 2018c; Yao et al., 2012; Yao et al., 2018). Given its environmental impacts, it is significant to effectively eliminate the antibiotic SMX from water and wastewater.

Various treatment methods including ozonation, photolysis, electrochemical oxidation and adsorption have been applied for eliminating SMX from water (Jang et al., 2018c). Among these techniques, adsorption has been recognized as a low-cost and practically-feasible process owing to its simple and effective removal of SMX, and no generation of toxic intermediates and byproducts (Jang et al., 2018b; Yao et al., 2018). Up to now, carbon nanotube (Zhao et al., 2016), graphene oxide (Chen et al., 2015a), activated carbon (AC) (Calisto et al., 2015) and clay mineral (Gao & Pedersen, 2005) have been investigated to remove SMX in water. However, compared to low-cost waste-derived biochars, these adsorbents are less economically feasible and environmentally sustainable due to relatively higher costs for manufacturing, regeneration and disposal which hinder their practical applications.

---

\*Reprinted with permission from “Chemical activation of forage grass-derived biochar for treatment of aqueous antibiotic sulfamethoxazole” by Shengquan Zeng, and Eunsung Kan, 2020, ACS Omega, 5 (23), 13793-13801, Copyright 2020 by American Chemical Society.

Biochars (BCs), produced from pyrolysis of biomass under limited oxygen conditions, have been actively studied for their applications for removal of contaminants in water, soil and air (Braghiroli et al., 2018; Reguyal et al., 2017a). It has been reported that BCs can interact with sulfonamides antibiotics through Van der Waals,  $\pi$ - $\pi$ , hydrogen bonding, and electrostatic interactions (Peiris et al., 2017). A variety of BCs derived from alfalfa grass (Choi & Kan, 2019), wood sawdust (Reguyal et al., 2017a), bagasse (Yao et al., 2018), wheat straw and rice straw (Gao & Pedersen, 2005) have been utilized for treatment of SMX in water. However, these raw BCs exhibited low adsorption capacities (less than 100 mg/g BC) with their less developed pore structures and low surface areas (Table S2.1) (Jang et al., 2018b; Jang et al., 2018c).

Activation has been recognized as an effective method to improve surface area and enhance pore volume of BCs (Braghiroli et al., 2018). Activation of BCs has been studied via physical (e.g., steam, CO<sub>2</sub>), chemical (e.g. NaOH, KOH, H<sub>3</sub>PO<sub>4</sub>) and catalytic methods (Ahmed et al., 2017b; Braghiroli et al., 2018; Jang et al., 2018b; Rajapaksha et al., 2015; Taheran et al., 2016; Yang et al., 2016b). However, studies for SMX adsorption onto the activated BCs have been rarely reported. The H<sub>3</sub>PO<sub>4</sub> activation of bamboo resulted in improvement of surface area and pore volume of BC from 0.5 m<sup>2</sup>/g and 0.00053 cm<sup>3</sup>/g to 1.12 m<sup>2</sup>/g and 0.0023 cm<sup>3</sup>/g, while enhancing the adsorption capacity of this activated BC for SMX up to 88.10 mg SMX/g BC (Ahmed et al., 2017b). Moreover, the effective adsorption of SMX (397.29 mg/g BC) using the NaOH-activated *Pinus taeda* BC was achieved by high surface area (959.9 m<sup>2</sup>/g) and hydrophobicity (Jang et al., 2018c).

In addition, the source and availability of feedstock are very important for production of BC in terms of production cost and environmental sustainability. Bermudagrass (BG), as one of the most abundant forage grasses in USA, is widely grown in the southeast part of USA with annual dry matter yield of 6-10 tons per acre (Wang et al., 2010). Moreover, about 20% of these forage grasses



are often discarded because of generation of pathogenic fungi in the forage grasses under excessive moisture conditions during their storage at farms while the fungi-infected forages can cause severe diseases for animals (Jang & Kan, 2019c). Considering high quantities of BG production including discarded ones, BG could be potentially a viable biomass feedstock for BC production. However, the preparation and application of BG-derived BCs has been rarely studied, except that the previous works mentioned that BG derived-BC could be applied for the treatment of tetracycline and chromium in water (Jang & Kan, 2019c; Tu et al., 2020a).

Although  $ZnCl_2$ , NaOH, KOH,  $H_3PO_4$ , and  $FeCl_3$  are commonly used as chemical and catalytic activating agents, zinc cations are toxic in aqueous solution while phosphoric acid is very hazardous and can cause damage to the skin, eyes, mouth, and respiratory tract. In addition, compared to KOH, NaOH is more environmental-friendly and less corrosive (Jang et al., 2018b). In our preliminary study, NaOH and  $FeCl_3$  as the activating agents were used to make activated bermudagrass (BG)-derived BCs under the same pyrolysis conditions. The results showed that the NaOH-activated BG biochar had larger surface area ( $1992 \text{ m}^2/\text{g}$ ) and higher SMX adsorption capacity ( $425 \text{ mg SMX/g BC}$ ) than those of  $FeCl_3$ -activated BG biochar ( $1013 \text{ m}^2/\text{g}$  and  $253 \text{ mg/g BC}$ ) under the same adsorption conditions (100 mL of 100 mg/L SMX, initial pH of 3, 0.01 g BC, and 3 d). Hence, in this study, the NaOH-activated BG biochar was used for the detailed characterization and adsorption experiments.

For the first time, this work studied the detailed characteristic and mechanism about SMX adsorption on the NaOH-activated forage BG BC (A-BC) through isotherm, kinetic, and thermodynamic studies. Therefore, the major objective of this research was the production and characterization of A-BC, and its application for SMX adsorption from water. The batch experiments for the isotherm, kinetic, isotherm and thermodynamic studies were conducted while

highly efficient NaOH-driven regeneration of SMX-saturated A-BC was developed. Based on the detailed investigation of physicochemical properties and adsorption characteristics, possible mechanisms associated with adsorption of SMX onto A-BC were also elucidated.

## **2.2 Materials and methods**

### **2.2.1 Materials**

All chemicals used for this study were bought from Sigma-Aldrich (St. Louis, Missouri, U.S.). Bermudagrass (BG) was obtained from a local hay shop (Stephenville, TX, U.S.). Three commercial activated carbons (Darco<sup>®</sup> G-60, Norit<sup>®</sup> GAC, and Calgon F400) were acquired from Sigma-Aldrich and Calgon Carbon.

### **2.2.2 Production of biochars**

BG, dried and sieved (<500  $\mu\text{m}$ ), was utilized as the feedstock for biochar. 10 g of BG was introduced into the quartz-tube furnace (MTI Corporation, Richmond, U.S.) and converted to biochar under 300 °C for 15 min with 2 L/min of N<sub>2</sub> flow. The first resulting raw BC was named as “R-BC”. The pyrolysis and activation conditions in the current study were same as those in the previous studies, which showed the great performance for preparing the activated biochars (Jang & Kan, 2019a). 40 mL of 4 M NaOH solution and 3 g of R-BC were mixed together at 20 °C for 2 h, and then dried at 105 °C overnight. Afterward, the dry mixture was pyrolyzed under the activation conditions (800 °C, 8 °C/min, 2 L/min of N<sub>2</sub>, and 2 h reaction). The activated BC was named as “A-BC”. As a control, the BG was directly carbonized at 800 °C for 2 h with 8 °C/min which was named as “BC800”. The R-BC, A-BC and BC800 were washed with 3 M HCl (50 mL 3M HCl/g BC) for 1 d, and then repeated to be flushed with a deionized water until the pH of filtered water became neutral. All BCs were dried at 105 °C and sieved (<106  $\mu\text{m}$ ) for following tests. The yields of biochars were evaluated by the Eq. (2.1):

$$\text{Yield (\%)} = A/B \times 100 \quad (2.1)$$

where B represents the weight of BG, and A represents the weight of BCs after washing and drying.

### **2.2.3 Physicochemical properties of biochars**

Chemical compositions of all BCs were determined by an elemental analyzer (Robert Microlit Lab, NJ, USA), and a proximate analysis was carried out based on ASTM standard D7582-10 (ASTM, 2010). Brunauer-Emmett-Teller (BET) surface area was analyzed through the measurements of N<sub>2</sub> sorption at 77 K (Particle Technology Lab, Downers Grove, USA). Functional groups in all BCs were evaluated by a FT-IR spectrometer (Bruker Optik GmbH, Ettlingen, Germany). An X-ray diffractometer (MiniFlex II, DE, USA), operated at 30 kV and 15 mA, was used to evaluate the crystalline structures at the surface of BCs. The surface morphologies of BCs were examined by a scanning electron microscope (SEM) (S-4800, Hitachi Co., Japan). The pH of zero point charges (pH<sub>PZC</sub>) of BCs were evaluated through the procedures described in the previous work (Jang et al., 2018b).

### **2.2.4 Batch adsorption experiment**

The adsorption of SMX on all BCs (R-BC, BC800 and A-BC) was performed at pH 1-10 under the selected conditions. The batch adsorption tests were initiated by mixing 0.01 g of BC with 100 mL of 100 mg/L SMX solution in 250 mL Erlenmeyer flasks for 3 d at 20 °C. The kinetic, isotherm, thermodynamic and regeneration studies were conducted at the selected optimal pH obtained from the above experiments.

The adsorption kinetics were studied by mixing 0.01 g of BC with 100 mL of SMX solution (20 and 100 mg/L). The adsorption isotherm experiments were carried out with 100 mL of SMX solution (10 mg/L to 100 mg/L) and 0.01 g of BC for 3 d. For the thermodynamic analysis, SMX

adsorption onto A-BC was conducted by mixing 100 mL of SMX solution (50 mg/L and 100 mg/L) and 0.01 g of BC at 20-40 °C for 3 d.

To see possible practical application of A-BC for treatment of real wastewater, the adsorption experiment was conducted by stirring 0.01 g of A-BC and 100 mL of wastewater sampled from the 2<sup>nd</sup> lagoon at the dairy farm at Southwest Dairy Center, Tarleton State University (Stephenville, TX) for 3 d. The dairy wastewater from the 2<sup>nd</sup> lagoon at the dairy farm contained various organic and inorganic compounds spiked with 100 mg/L SMX at pH 6.

### **2.2.5 Regeneration study**

To regenerate and reuse the SMX-saturated A-BC, NaOH was selected as the desorption agent in this study. After 3 d adsorption, the SMX saturated A-BC was separated from SMX solution and added into the same volume of NaOH solution (0.1-2.0 M NaOH) for the NaOH-driven desorption for 1 d. After the NaOH desorption, the A-BC was separated from NaOH solution and dried at 65 °C. The conditions for readsorption experiments were the same as those described in Sec. 2.2.4. Four cycles of adsorption-desorption were performed using 0.2 M NaOH solution. The regeneration efficiency of A-BC was calculated by the Eq. (2.2):

$$\text{Regeneration efficiency (\%)} = \frac{Q_n}{Q_0} \times 100 \quad (2.2)$$

where  $Q_0$  is the initial  $Q_e$ , and  $Q_n$  is the  $Q_e$  at  $n$  generation cycles.

### **2.2.6 Modeling of adsorption kinetics, isotherms and thermodynamics**

In this study, the results obtained from the batch adsorption experiments were fitted to five kinetic models for adsorption kinetics, and four isotherm models for adsorption isotherm while used for determining thermodynamic parameters including standard enthalpy change ( $\Delta H^\circ$ ), standard entropy change ( $\Delta S^\circ$ ) and standard Gibbs free energy change ( $\Delta G^\circ$ ) (Shin & Kim, 2016). The detailed descriptions for the models and the thermodynamic properties are listed in Table S2.2.

In this study, the determination coefficients ( $R^2$ ) and the sum of squared error (SSE) were used to determine which model best fit the experimental data:

$$R^2 = 1 - \frac{\sum(Q_{exp} - Q_{cal})^2}{\sum(Q_{exp} - Q_{mean})^2} \quad (2.3)$$

$$SSE = \sqrt{\frac{\sum(Q_{exp} - Q_{cal})^2}{N}} \quad (2.4)$$

where  $Q_{exp}$ ,  $Q_{cal}$  and  $Q_{mean}$  are the experimental value, calculated value and mean of experimental value, respectively, and  $N$  is the number of measurements.

### 2.2.7 Chemical and data analysis

The aqueous SMX concentration was evaluated through the HPLC (LC-2030C model, SHIMADZU, Torrance, CA, U.S.) with a C18 column (3.6  $\mu$ m XB-C18). The operation conditions included the mobile phase (methanol: water (33:67, volume ratio) with 0.1% formic acid), a flow rate of 0.6 mL/min and a UV detector at 265 nm.

Adsorption capacities at equilibrium and time  $t$ ,  $Q_e$  (mg/g) and  $Q_t$  (mg/g), were determined using Eq. (2.5 and 2.6):

$$Q_e = \frac{(C_i - C_e) \times V}{M} \quad (2.5)$$

$$Q_t = \frac{(C_i - C_t) \times V}{M} \quad (2.6)$$

where  $C_i$ ,  $C_e$  and  $C_t$  represent the SMX concentration of initial, equilibrium time and time  $t$  (mg/L),  $V$  represents the solution volume (L) and  $M$  represents the mass of BC used in adsorption tests (g).

The following empirical equation was utilized to calculate the quantitative contribution of single SMX species to overall sorption in a given pH value:

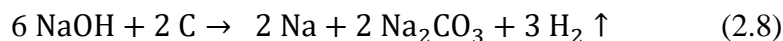
$$K_d = K_d^- \alpha^- + K_d^0 \alpha^0 + K_d^+ \alpha^+ \quad (2.7)$$

where  $\alpha^-$ ,  $\alpha^0$ , and  $\alpha^+$  represent the mass fraction of  $\text{SMX}^-$ ,  $\text{SMX}^0$ , and  $\text{SMX}^+$ , respectively,  $K_d$ ,  $K_d^-$ ,  $K_d^0$ , and  $K_d^+$  (L/kg) represent the adsorption coefficient of total,  $\alpha^-$ ,  $\alpha^0$ , and  $\alpha^+$ , respectively. The contribution percentage of various SMX species was determined by  $K_d^- \alpha^- / K_d$  for  $\text{SMX}^-$ ,  $K_d^0 \alpha^0 / K_d$  for  $\text{SMX}^0$  and  $K_d^+ \alpha^+ / K_d$  for  $\text{SMX}^+$ .

## 2.3 Results and discussion

### 2.3.1 Characterization of biochars

The physicochemical properties of all BCs produced in this study are listed in Table 2.1. The A-BC showed significantly increased BET surface area of 1991.59 m<sup>2</sup>/g compared with R-BC (raw biochar produced at 300 °C, 1.67 m<sup>2</sup>/g) and BC800 (biochar produced at 800 °C, 85.82 m<sup>2</sup>/g). During the NaOH activation at high temperature, the stoichiometric reaction between NaOH and carbon can be described as the following equation (Jang et al., 2018b):



Thus, the high surface area of A-BC can result from the pore enlargement, which is associated with two pathways: (1) evolution of carbon monoxide, carbon dioxide, and hydrogen produced from the breakdown of  $\text{Na}_2\text{CO}_3$  under high temperature and hydroxyl reduction, (2) expanding of spaces between layers of carbon atoms owing to produced sodium interposition into carbon structures, (3) reaction between active alkali intermediates and carbon surface (Foo & Hameed, 2012; Martins et al., 2015). This also explains the yield of A-BC (8.91%) was much lower than those of R-BC (62.05%) and BC800 (29.27%). The BET surface area analysis revealed that the NaOH activation of R-BC led to high enhancement of surface area by factor of 1193. The high surface area of A-BC (1991.59 m<sup>2</sup>/g) was higher than those of various commercial activated carbons (Table S2.3) while offering large active sites for adsorption of contaminants. Moreover, the SEM images of A-BC (Figure S2.1) indicated A-BC possessed the well-developed pore

structure and various sizes of pores including micropores which could support the high surface area of A-BC (Yan et al., 2020b).

**Table 2.1** The physicochemical characteristics of all BCs.

	Elemental analysis (wt.%)							
	C	H	O	N	S	H/C	O/C	(N+O)/C
BG	47.43	6.30	35.66	2.5	0.42	1.60	0.56	0.61
R-BC	59.53	5.07	27.56	4.20	0.09	1.02	0.35	0.41
BC800	68.02	1.58	12.94	3.37	0.05	0.28	0.14	0.19
A-BC	81.22	0.84	7.42	0.83	0.23	0.12	0.07	0.08
	Proximate analysis			BET				
	(% , dry basis)			Surface	Yield	pH <sub>PZC</sub>		
	FC	VC	Ash	area (m <sup>2</sup> /g)	(% )			
BG	6.60	85.71	7.69	0.63	-	-		
R-BC	23.22	73.14	3.64	1.67	62.05	5.07		
BC800	67.92	18.04	14.04	85.82	29.27	4.19		
A-BC	70.96	19.58	9.46	1991.59	8.91	5.63		

BG: Bermudagrass

R-BC: Raw biochar produced at 300°C

BC800: Biochar produced at 800°C

A-BC: Activated biochar

FC: Fixed carbon

VC: Volatile carbon

The proximate analysis results for all BCs listed in Table 2.1 showed significant changes in volatile and fixed carbons. Compared to R-BC, the contents of volatile carbon of BC800 and A-BC decreased from 73.14% to 18.04% and 19.58%, while the contents of fixed carbon increased from 23.22% to 67.92% and 70.96%. This was due to the thermal breakdown and release of volatile matter in carbohydrate fractions of BG feedstock during the heat treatment at high temperature resulting in the development of highly porous structures (Park et al., 2013). The ultimate analysis indicated the C content in A-BC increased to 81.22% after the activation, while the O and H

contents in A-BC markedly decreased to 7.42% and 0.84% compared to R-BC and BC800, respectively. The results were consistent with the previous studies which indicated the decomposition of O and H and the decrease of surface functional groups under high temperature and activated conditions (Jang et al., 2018b; Wang et al., 2017b). The ratios of H/C, O/C and (N+O)/C significantly decreased after the activation, indicating the NaOH activation decreased the O-containing functional groups and polarity of BC while increasing the aromaticity and hydrophobicity of A-BC. This would come from decarboxylation and demethylation reactions and loss of volatile organic matters during the activation (Jang et al., 2018c; Luo et al., 2018). Additionally, A-BC showed higher hydrophobicity (low ratio of O/C) and aromaticity (low ratio of H/C) than various commercial activated carbons (Table S2.3), which could be beneficial for adsorption of hydrophobic contaminants onto the surface of A-BC due to hydrophobic interaction. The XRD patterns listed in Figure S2.2 showed the wide peaks and the lack of sharp peaks, indicating the amorphous structures and low degree of crystallinity in the BCs (Mondal et al., 2016; Zhu et al., 2014b). Moreover, the broad peaks at 23° and 43° in BC800 and A-BC revealed the formation of turbostratic crystallites which are mostly amorphous materials with partly short-range order (Luo et al., 2018; Mondal et al., 2016; Taheran et al., 2016; Zhu et al., 2014b).

The functional groups of all BCs were illustrated by FTIR spectra (Figure S2.3). In comparison with R-BC, the peaks of BC800 and A-BC at 2852 cm<sup>-1</sup> and 2922 cm<sup>-1</sup> (aliphatic C-H stretching vibrations) completely disappeared, indicating the complete carbonization of raw material via the heat treatment at high temperature and NaOH activation (Yakout, 2015). On the contrary, the peak at 2122 cm<sup>-1</sup> for C≡C stretching vibration showed strong intensity in BC800 and A-BC compared to R-BC (Ahmed et al., 2017a). Moreover, the peak intensity at 2122 cm<sup>-1</sup> increased significantly after the activation, indicating that A-BC can provide more electron-donor sites, which are closely



related to  $\pi$ - $\pi$  interactions between biochars and organic contaminants. The peak at  $1575\text{ cm}^{-1}$ , corresponding to C=C stretching vibration, significantly increased in A-BC, revealing the high aromatization during the activation (Ahmed et al., 2017c). Compared to R-BC, the peak at about  $1050\text{-}1060\text{ cm}^{-1}$  for C-O stretching vibration drastically decreased in BC800 and A-BC due to the loss of O-containing functional groups (Zhu et al., 2014b). For A-BC, the peak at  $1059\text{ cm}^{-1}$  (C-O) experienced a negative shift after the SMX adsorption, implying the O-containing functional groups in A-BC interacted with the SMX. Both peaks at  $1575\text{ cm}^{-1}$  (C=C) and  $2120\text{ cm}^{-1}$  (C $\equiv$ C) moved to  $1591\text{ cm}^{-1}$  and  $2122\text{ cm}^{-1}$ , which would result from the interactions of these functional groups with SMX molecules during the adsorption.

### 2.3.2 Effect of initial pH and adsorption mechanism

The initial pH can influence on the SMX adsorption onto BCs through altering properties of SMX and BCs. Owing to  $\text{pK}_1 = 1.6$  and  $\text{pK}_2 = 5.7$  (Table S2.4), the predominant species of SMX were  $\text{SMX}^+$  at  $\text{pH} < 1.6$ ,  $\text{SMX}^0$  at  $1.6 < \text{pH} < 5.7$ , and  $\text{SMX}^-$  at  $\text{pH} > 5.7$  (Jang et al., 2018c). The  $\text{pH}_{\text{PZC}}$  of R-BC, BC800 and A-BC were found to be 5.07, 4.19 and 5.63, respectively (Table 2.1 and Figure S2.4). The surface charges of BCs are positive with the solution pH less than their  $\text{pH}_{\text{PZC}}$ , otherwise they are negative.

As shown in Figure 2.1, compared with A-BC, R-BC and BC800 exhibited the low adsorption capacities for SMX at various pH values (less than  $30\text{ mg/g}$ ), which is possibly attributed to low surface areas of RBC and BC800. For A-BC, the highest SMX adsorption was achieved at pH 3 ( $456\text{ mg/g}$ ), but the increase of pH up to 10 resulted in a decrease of SMX adsorption as the similar trends were found from the previous works (Ahmed et al., 2017b). Although the SMX adsorption capacity of A-BC varied with different pH, the adsorption capacity ( $Q_e$ ) did not change significantly between pH 1 to 9 (85.65% of maximal  $Q_e$  at pH 1; 78.60% of maximal  $Q_e$  at pH 9).

Therefore, the SMX adsorption on A-BC was found to be applicable in a broad range of pH, which was favorable to practical applications of A-BC for wastewater and water treatment.

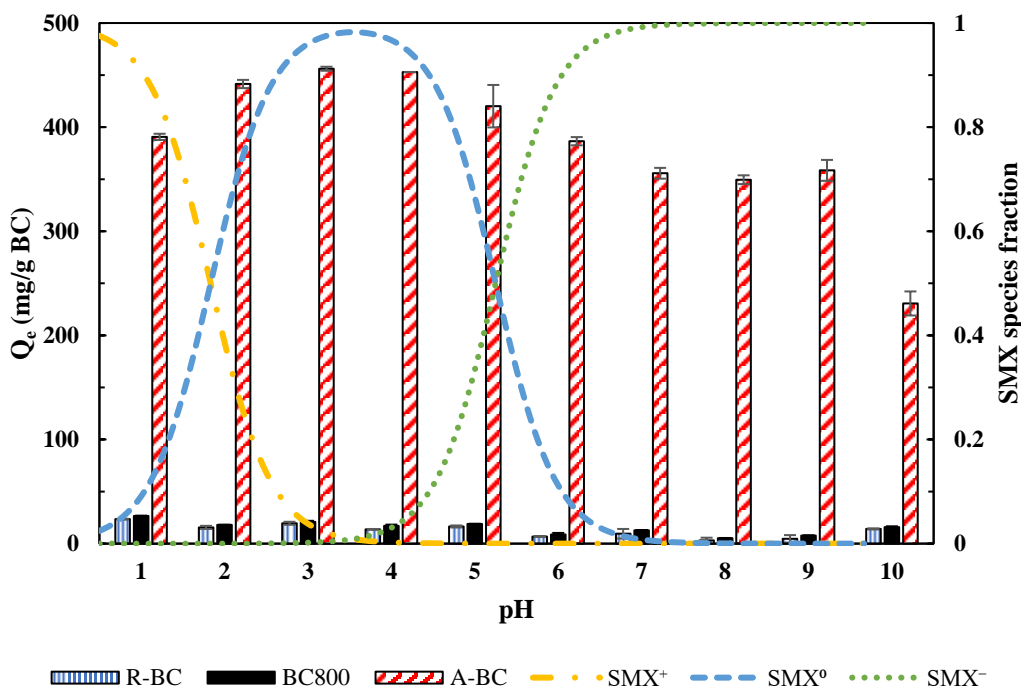


**Figure 2.1.** Adsorption of SMX onto all BCs.

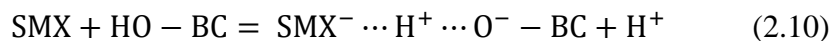
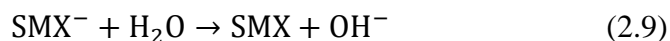
The electrostatic interactions between adsorbate and adsorbent surface significantly affected the adsorption of ionic compounds (Zheng et al., 2013). SMX<sup>+</sup> was predominant (79.92%) at pH 1 (Figure 2.1) and the surface charge of A-BC was near zero at acidic conditions (Figure S2.4). Therefore, the electrostatic interactions were not significant at pH 1. As seen in Figure 2.1, 85.65% of maximal  $Q_e$  was still observed at pH 1. In addition,  $\pi$ - $\pi$  electron donor acceptor (EDA) interaction has been recognized as the major mechanism for sulfonamides adsorption on BCs

(Peiris et al., 2017). SMX can serve as an electron acceptor because the sulfonamide group has the powerful electron-withdrawing capacity, and also the heteroaromatic group becomes electron-deficient because the high electro negativity of the O atom can reduce the electron density of the heteroaromatic group, while the graphitic surface of BC is electron-rich and can serve as an electron donor (Peiris et al., 2017; Tan et al., 2015). Therefore, the non-covalent interaction ( $\pi$ - $\pi$  EDA) can form between the electron-rich  $\pi$  system (BC) and electron-deficient  $\pi$  system (SMX) via attractive interaction. Moreover, as shown in Table S2.5 and S2.6, the contribution of SMX<sup>+</sup> to total adsorption was 91.86% at pH 1. The surface of A-BC includes C=C and C≡C groups (Figure S2.3), which can provide the electrons for  $\pi$ - $\pi$  EDA interaction. Thus, the adsorption at pH 1 may be governed by  $\pi^+$ - $\pi$  EDA interaction between the protonated aniline ring and the  $\pi$ -electron rich surface of A-BC (Peiris et al., 2017; Zheng et al., 2013).

The maximum adsorption capacity of A-BC for SMX was achieved at pH 2-5. Since neutral SMX<sup>0</sup> molecules were predominant species and the surface of A-BC was positively charged at pH 2-5, the electrostatic interaction between A-BC and SMX was not responsible for the SMX adsorption onto A-BC. Therefore, other adsorption mechanisms such as  $\pi$ - $\pi$  EDA interaction, hydrophobic interaction and hydrogen bond would involve in the adsorption of SMX onto A-BC. While SMX has lowest solubility in water at pH 3.22, its solubility increases and decreases at higher and lower than pH 3.22 (Dahlan et al., 1987). As shown in Fig. 1, the adsorption capacities of A-BC for SMX decreased at higher and lower than pH 3, therefore, the SMX adsorption on A-BC was negatively influenced by increasing solubility of SMX. Thus, these findings also confirmed that hydrophobic interaction occurred between SMX and A-BC at pH 2-5, which was consistent with the previous studies (Jang et al., 2018c; Reguyal et al., 2017a). Furthermore, strong hydrogen bonds could be generated between neutral sulfonamides and functional biochars as reported by the previous

studies (Ahmed et al., 2017a). From the analysis of FT-IR spectrum of A-BC before and after the SMX adsorption, the O-containing functional groups of A-BC were found to involve in the SMX adsorption process. Hence, due to the high electro negativity of N and O atoms, hydrogen bond formation could occur between the O-containing functional groups of A-BC and the -NH- and -NH<sub>2</sub> groups in SMX molecule.

In pH 6-10, SMX<sup>-</sup> was predominant and the A-BC surface was negatively charged. Therefore, the K<sub>d</sub> values gradually began to decline due to the existence of electrostatic repulsion (Table S2.5). Additionally, due to the deprotonation of SMX<sup>-</sup> and the decrease of π electron acceptor capacity, π-π EDA interaction significantly decrease at high pH (Yao et al., 2018). However, at pH 6-10, some portion of SMX was still adsorbed onto the negatively charged A-BC. The previous study has reported that charge assisted hydrogen bond (CAHB) interactions can occur between the negative BC surface and sulfonamides (Peiris et al., 2017). Moreover, as shown in Table S2.5 and S2.6, the contribution of SMX<sup>-</sup> to total adsorption was between 77.89% and 99.99% at pH 6-10. Therefore, the adsorption at this pH range may be attributed to negative CAHB between SMX<sup>-</sup> and negatively charged A-BC. More specifically, SMX<sup>-</sup> can firstly make H<sup>+</sup> exchange with H<sub>2</sub>O molecule and release the OH<sup>-</sup> into aqueous solution and OH<sup>-</sup> can be neutralized by H<sup>+</sup> released from O-containing functional groups in A-BC surface to form negative CAHB (Eq.(2.9 and 2.10) (Ahmed et al., 2017a; Ahmed et al., 2017b).



In conclusion, as shown in Figure S2.5, π<sup>+</sup>-π and π-π EDA, hydrophobic, hydrogen bond and CAHB interactions could be considered as possible adsorption mechanisms for adsorption of SMX onto A-BC.

### 2.3.3 Adsorption kinetics

Kinetic studies are essential to comprehend the adsorption mechanisms and rate-limiting steps. In this study, the adsorption kinetics of SMX on A-BC was investigated under two initial concentrations of SMX (20 mg/L and 100 mg/L at pH 3). It is noteworthy that the data from two different concentrations exhibited the same trend. A fast adsorption occurred in a few minutes and reached the equilibrium after 60 min, which indicated a favorable interaction between SMX and A-BC (Figure 2.2).

The kinetic parameters determined from the adsorption results are listed in Table 2.2. With high determination coefficient ( $R^2$ : 0.9933-0.9983), PSO model ( $R^2$ : 0.9933-0.9983) was better fitted with experimental data than PFO model ( $R^2$ : 0.9805-0.9886). In addition, the  $Q_e$  value calculated from PSO model was closer to the experimental  $Q_e$  value, implying that the chemisorption between SMX and A-BC was more important than physisorption (Jang et al., 2018c). The Elovich model was also well-fitted to experimental data with high  $R^2$  value (0.9933-0.9982) and low SSE (4.46-4.75) (Jang et al., 2018c). The parameters (a and b) in Elovich model for A-BC indicated high value of initial adsorption rate and low desorption (Table 2.2). Upon the assumptions for Elovich model, strong chemical interactions would occur on the energetically heterogeneous surface of A-BC (Jang et al., 2018b).

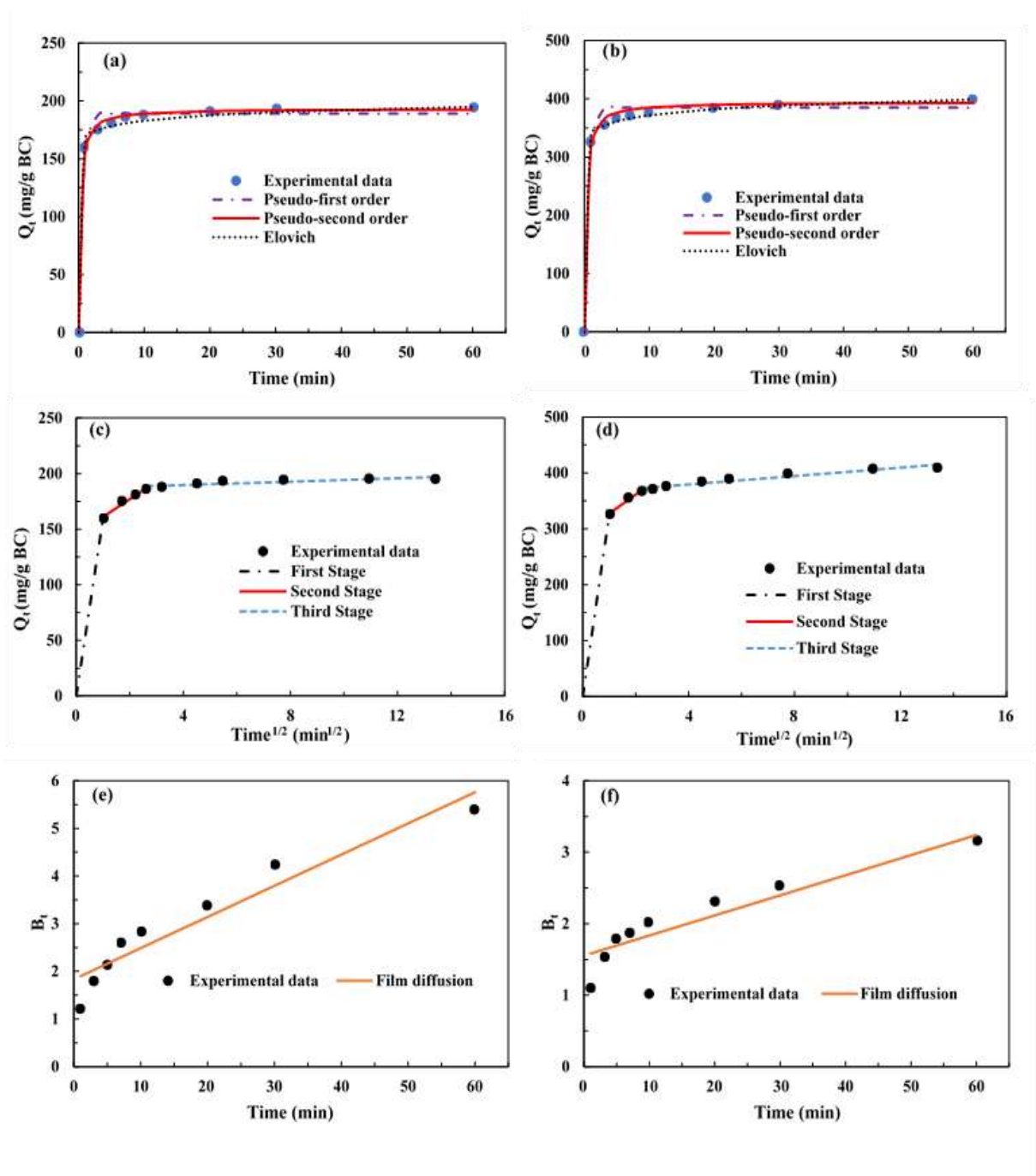


**Figure 2.2.** Adsorption kinetics of SMX onto A-BC by fitting the pseudo-first order, pseudo-second order, and Elovich ((a) and (b)) and intra-particle diffusion model ((c) and (d)) and film diffusion model ((e) and (f)) under two different initial concentrations of 2.

**Table 2.2** Summary of kinetic parameters of SMX adsorption on A-BC.

	20 <sup>a</sup>	100 <sup>a</sup>
Q <sub>e</sub> <sup>b</sup>	194.99	409.03
Pseudo-first order		
Q <sub>e</sub> <sup>c</sup>	189.02	384.57
K <sub>1</sub>	1.83	1.85
SSE	5.81	15.54
R <sup>2</sup>	0.9886	0.9805
Pseudo-second order		
Q <sub>e</sub> <sup>c</sup>	193.46	394.44
K <sub>2</sub>	0.02	0.01
SSE	2.26	9.09
R <sup>2</sup>	0.9983	0.9933
Elovich		
Q <sub>e</sub> <sup>c</sup>	202.41	415.13
a	4.43*10 <sup>11</sup>	7.92*10 <sup>10</sup>
b	0.15	0.07
SSE	4.46	4.75
R <sup>2</sup>	0.9933	0.9982
Intra-particle diffusion		
K <sub>i1</sub>	159.63	326.04
R <sup>2</sup>	1	1
K <sub>i2</sub>	16.00	33.93
R <sup>2</sup>	0.9755	0.9834
K <sub>i3</sub>	0.76	3.76
R <sup>2</sup>	0.7282	0.9273
Film diffusion (Boyd equation)		
R <sup>2</sup>	0.9129	0.9633

<sup>a</sup> Initial concentration of SMX (mg/L).

<sup>b</sup> Observed value Q<sub>e</sub> (mg/g).

<sup>c</sup> Calculated value Q<sub>e</sub> (mg/g).

Adsorption process in porous materials is often controlled by intraparticle or film diffusion or both combined (Jang & Kan, 2019c). In this study, the intra-particle diffusion model was applied to the kinetic results for understanding possible rate-limiting steps. The key parameter (K<sub>i</sub>) in the model indicated intraparticle diffusion limitation. The plots of Q<sub>t</sub> against t<sup>1/2</sup> were distributed into three linear sections representing three various stages (Figure 2.2c and 2.2d). The first stage was ascribed to the rapid diffusion of SMX into the external surface of A-BC. The second stage exhibited gradual adsorption and was attributed to the intraparticle diffusion. In addition, adsorption process

reached the final equilibrium in the third stage, where the intraparticle diffusion rate decreased owing to the decrease of SMX concentration in the solution (Martins et al., 2015; Yang et al., 2016b). However, both second and third stages did not go through the origin, revealing that the intraparticle diffusion was not the sole rate-limiting step (He et al., 2016).

To figure out the adsorption mechanism controlled by the film diffusion, the kinetic data were further evaluated through the film diffusion model Boyd equation (Martins et al., 2015). The calculated  $B_t$  values were plotted with time  $t$  as displayed in Figure 2.2e and 2.2f. When the data points were linear and across the origin, intraparticle diffusion controlled the transfer of adsorbate molecules (Zhang et al., 2011b). As shown in Figure 2.2e and 2.2f, the linear lines from two different initial concentration of SMX did not go through the origin, revealing that film diffusion also participated in the entire adsorption process (Zhang et al., 2011b). Therefore, both film diffusion and intraparticle diffusion may play a significant part during the process of SMX adsorption onto A-BC.



#### 2.3.4. Adsorption isotherm

For comprehensively understanding the nature of interactions between SMX and A-BC, the isotherm models (Langmuir, Freundlich, Temkin and Dubinin-Redushkevich) were fitted to the experimental results (Table 2.3 and Figure S2.6). As summarized in Table 2.3, compared to Freundlich model ( $R^2 = 0.9145$ ), the isotherm results were better matched with Langmuir model ( $R^2 = 0.9418$ ), indicating that monolayer adsorption of SMX molecules would occur on the homogeneous surface of A-BC (Pezoti et al., 2016). Moreover, the low value of  $R_L$  (Langmuir constant, the adsorption/desorption equilibrium for each reactant in contact with a surface) in the Langmuir model suggested that the SMX adsorption onto A-BC was favorable in the SMX concentration used for this study (Table 2.3) (Pezoti et al., 2016). The value of the heterogeneity factor  $1/n$  (0.13) from Freundlich model, close to zero, indicated that A-BC presented high heterogeneity degree (Martins et al., 2015). Moreover, Temkin model exhibited the highest  $R^2$  (0.9736) and lowest SSE (19.27) among all of models. Based on the assumption of Temkin model that adsorption heat is reduced linearly with the surface coverage of adsorbent, the chemisorptive interaction was dominant in the adsorption process (Tang et al., 2018). Furthermore, the obtained mean free energy value ( $E$ ) from Dubinin-Radushkevich model (91.29 kJ/mol) was bigger than 8 kJ/mol, indicating strong chemisorption happened on the surface of A-BC, which supported the result of kinetics analysis (Tang et al., 2018).

**Table 2.3** Summary of isotherm model parameters for SMX adsorption on A-BC.

Langmuir model	
$Q_m$	424.66
$K_L$	6.12
$R_L$	0.016
SSE	28.63
$R^2$	0.9418
Freundlich model	
$K_f$	286.05
$n$	7.55
SSE	34.71
$R^2$	0.9145
Dubinin-Radushkevich model	
$K_{DR}$	429.72
$B_D$	0.00006
$E$	91.29
SSE	37.37
$R^2$	0.9009
Temkin model	
$K_T$	915.18
$b_T$	55.69
SSE	19.27
$R^2$	0.9736

The A-BC exhibited maximum monolayer adsorption capacity of 424.66 mg/g, which was larger than different adsorbents (Table S2.1). The previous works have reported that SMX adsorption capacity showed positive correlation with surface areas of different adsorbents (Jang et al., 2018c). Thus, in this study, the high  $Q_e$  value of A-BC may be ascribed to its high surface area (1991.59 m<sup>2</sup>/g) after the NaOH activation. Moreover, for figuring out potential of A-BC for commercial application, three commercial ACs (Calgon F400, Darco® G-60 and Norit® GAC) were also used for SMX adsorption. Surprisingly, the  $Q_e$  value of A-BC was higher than those of Calgon F400 (312.14 mg/g), Darco® G-60 (328.83 mg/g) and Norit® GAC (377.5 mg/g) which demonstrated the great potential of A-BC for the treatment of SMX in wastewater.

### 2.3.5 Thermodynamic study

The thermodynamic parameters were determined based on the impact of temperature (293-313 K) on SMX adsorption onto A-BC. The  $\Delta G^0$  values were negative under all investigated temperatures and initial concentrations, implying the spontaneous adsorption of SMX onto A-BC (Table 2.4) (Pezoti et al., 2016). In addition, the  $\Delta G^0$  value decreased with increase in temperature, revealing the affinity of SMX onto A-BC also increased at higher temperature. Furthermore, the absolute values of  $\Delta G^0$  obtained at the initial concentration of 50 mg/L were higher than those of 100 mg/L, indicating that SMX adsorption might be more spontaneous at lower initial concentration. This would be explained by that higher initial SMX concentration could cause higher competition of SMX molecules onto available active sites at the surface of A-BC. The positive values of  $\Delta H^0$  (2.120-6.184 kJ/mol) evidenced that the adsorption process was endothermic and inclined to chemisorption as physisorption often shows exothermic reactions (Pezoti et al., 2016). Meanwhile, the values of  $\Delta S^0$  (23.372-49.682 J/mol·K) were positive, suggesting that the randomness was enhanced at the contact area of solid-liquid and the adsorption was spontaneous in nature (Shin & Kim, 2016).

**Table 2.4** Thermodynamic parameters for the adsorption of SMX on A-BC.

Concentration(mg/L)	$\Delta H$ (kJ/mol)	$\Delta S$ (J/mol·K)	$\Delta G$ (kJ/mol)		
			T=293 K	T=303 K	T=313 K
<b>100</b>	2.120	23.372	-4.732	-4.965	-5.199
<b>50</b>	6.184	49.682	-8.380	-8.877	-9.374

### **2.3.6 Applications of A-BC for treatment of other emerging contaminants and wastewater**

While the A-BC was used for adsorption of SMX in this study, the adsorption capacities of A-BC for tetracycline and bisphenol A in water were also evaluated. The adsorption capacity of A-BC for tetracycline under the selected condition (0.01 g of BC, 100 mL of 100 mg/L tetracycline, initial pH 6, and 3 d) was 307 mg/g which was higher than those of commercial activated carbons and activated BCs (96-290 mg TC/g BC) and other BCs reported in the previous study (Jang et al., 2018b). The adsorption capacity of A-BC for bisphenol A under the selected condition (0.01 g of BC, 100 mL of 70 mg/L bisphenol A, initial pH of 6, 3 d) was also estimated to be 356 mg bisphenol A/g BC which was greater than those of commercial activated carbons (130-263 bisphenol A mg/g) and other BCs reported in the previous study (Choi & Kan, 2019).

In order to see practical feasibility of A-BC for treatment of antibiotics (SMX) in real wastewater containing multiple pollutants, SMX was added to the wastewater taken from the 2<sup>nd</sup> lagoon at the dairy farm of Southwest Dairy Center, Tarleton State University (Stephenville, TX). Please see multiple pollutants in the dairy wastewater which are listed in Table S2.7. Under the same adsorption conditions, compared to SMX adsorption onto A-BC in DI water, the adsorption capacity of A-BC for SMX in the dairy wastewater was reduced by 38.47% (Figure S2.7). This result clearly supports the presence of various organic and inorganic contaminants in the wastewater (Table S2.7) could compete with SMX for the active adsorption sites of A-BC although understanding of effects of individual pollutant is extremely challenging.

### **2.3.7 Regeneration study**

The regeneration of adsorbents is of great importance for development of cost-effective processes. Thus, it is important for A-BC to be effectively regenerated for long term reuse for removal of SMX in water. In this study, the NaOH-driven desorption was selected as one of possible

desorption methods although the previous studies also reported other desorption agents for regeneration of contaminant-saturated carbon adsorbents such as KOH, methanol and ethanol (Han et al., 2016; Reguyal et al., 2017b). Various concentrations of NaOH solution were used to regenerate A-BC after A-BC was fully saturated with SMX. As presented in Figure S2.8, the readsorption capacity was highest (397.65 mg/g) after regeneration using 0.2 M NaOH, and the NaOH concentration higher than 0.2 M resulted in the decrease of readsorption capacity. Previous studies also reported that the high regeneration capacity of biochars was observed using 0.1 M NaOH as the dilute NaOH could result in the formation of more interconnected pore structure (Jang & Kan, 2019c; Zhou et al., 2017). However, the carbon structure might be damaged or deformed under high concentration of NaOH, leading to the lower readsorption capacity. In addition, four cycles of adsorption-desorption were also conducted using 0.2 M NaOH in the present study. As shown in Figure 2.3, the regeneration efficiency remained at 91.19% and 64.60% after first and fourth cycles, indicating high potential of NaOH-driven regeneration of A-BC under optimization of regeneration conditions.

Therefore, owing to its inexpensive feedstock, high adsorption and regeneration capacities as well as possible adsorption of various contaminants, A-BC can be one of highly effective adsorbents for treatment of various organic contaminants in water and wastewater.

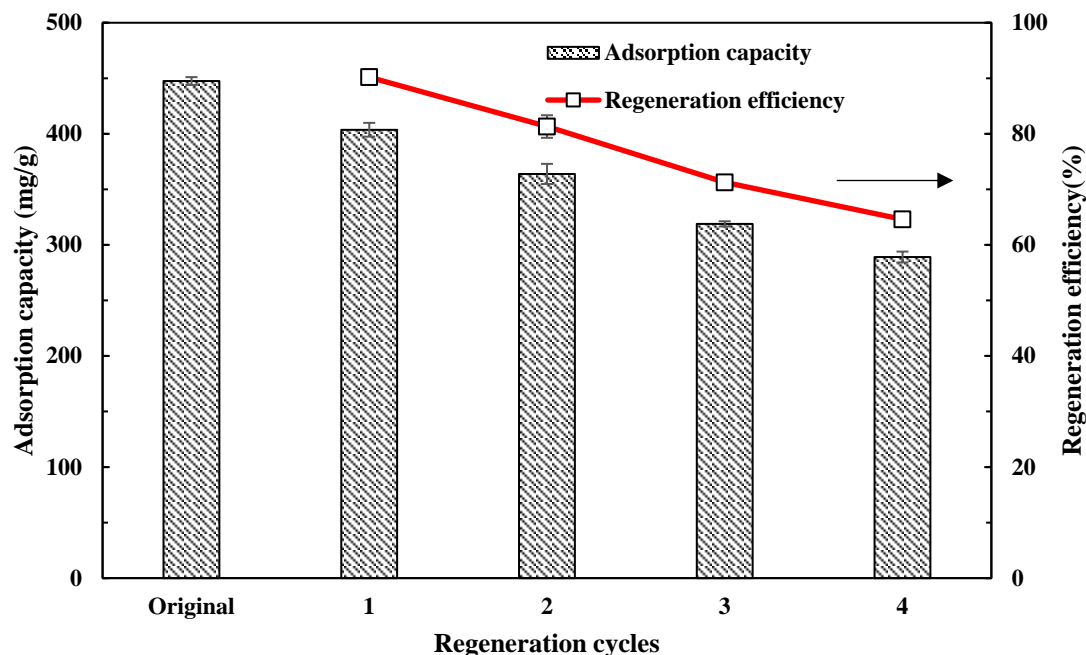


**Figure 2.3.** Reusability test of A-BC using 0.2 M NaOH.

## 2.4 Conclusions

The NaOH-activated BC made from forage Bermudagrass showed high surface area ( $1991.59 \text{ m}^2/\text{g}$ ) and adsorption capacity for SMX ( $425 \text{ mg/g BC}$ ), which was higher than various adsorbents including commercial ACs. The experimental results were well fitted by PSO and Elovich kinetic and Temkin isotherm models, revealing the strong chemisorptive interaction between SMX and A-BC. Moreover, both intraparticle diffusion and film diffusion affected the rate-limiting steps in the adsorption process. Additionally, the thermodynamic parameters implied the spontaneity and endothermic characteristic of SMX adsorption on A-BC. Furthermore, the regeneration of A-BC via the NaOH-driven desorption revealed the great potential for practical application of A-BC.

## CHAPTER III

# IRON-ACTIVATED BERMUDAGRASS-DERIVED BIOCHAR FOR ADSORPTION OF AQUEOUS SULFAMETHOXAZOLE: EFFECTS OF IRON IMPREGNATION RATIO ON BIOCHAR PROPERTIES, ADSORPTION, AND REGENERATION\*

### 3.1 Introduction

As mentioned in Chapter II, BC has been considered as an effective adsorbent for the treatment of antibiotic sulfamethoxazole (SMX). In addition, activation has been considered as an effective method to improve the functionality, porosity, and surface area of BCs for the enhancement of adsorption capacities of contaminants.

Compared with other activating agents,  $\text{FeCl}_3$  is inexpensive and environmentally friendly and can drastically enhance pore structure and surface area of BC. In addition, the size of ferric cation is smaller than other activators such as zinc cation, which can produce activated BCs with more smaller pore sizes (Theydan & Ahmed, 2012). Therefore, after  $\text{FeCl}_3$  activation, adsorption capacity of BCs can be significantly improved. So far, various works have been conducted on the preparation and applications of  $\text{FeCl}_3$ -activated BCs for adsorption of the pollutants in water (Bombuwala Dewage et al., 2018; Chen et al., 2017; Cho et al., 2017; Oliveira et al., 2009; Theydan & Ahmed, 2012; Wang et al., 2017d; Yang et al., 2016a; Zhu et al., 2014b). Theydan and Ahmed (2012) prepared and applied  $\text{FeCl}_3$ -activated date pit-derived BC for removing methylene blue with a maximum adsorption capacity of 259 mg/g calculated from Sips isotherm model.  $\text{FeCl}_3$

---

\*Reprinted with permission from “Iron-activated bermudagrass-derived biochar for adsorption of aqueous sulfamethoxazole: Effects of iron impregnation ratio on biochar properties, adsorption, and regeneration.” by Shengquan Zeng, Yong-Keun Choi, and Eunsung Kan, 2021, Science of The Total Environment, 750 (1), 141691, Copyright 2020 by ELSEVIER.

activated sawdust-derived BC and coffee husk-derived BC were used for the adsorption of aqueous *p*-nitrophenol and phenol with maximum adsorption capacities of 122 and 65 mg/g, respectively (Oliveira et al., 2009; Wang et al., 2017d). Cho et al. (2017) and Yang et al. (2016a) made and used FeCl<sub>3</sub>-activated BCs from coffee grounds and sawdust for adsorption of heavy metals arsenic and mercury in water. Chen et al. (2017) and Zhu et al. (2014b) also prepared FeCl<sub>3</sub>-activated BCs made from sawdust and *Salix psammophila* to adsorb tetracycline (Chen et al., 2017; Zhu et al., 2014b). Moreover, separation of powder BCs from aqueous phase was difficult, limiting their practical application in the treatment of real wastewater. However, after FeCl<sub>3</sub> activation, iron-activated BCs possess magnetic iron oxides (i.e., Fe<sub>3</sub>O<sub>4</sub>), which enable them to be easily separated under magnetic field for recycling the iron-activated BCs (Bombuwala Dewage et al., 2018; Yang et al., 2016a). Additionally, iron oxides in iron-activated BCs can serve as catalysts for Fenton and persulfate oxidation, which can be used for regeneration of contaminant-saturated BCs. More specifically, iron oxides can activate H<sub>2</sub>O<sub>2</sub> (for Fenton oxidation) and persulfate (for persulfate oxidation) to produce ·OH and SO<sub>4</sub>·<sup>-</sup> radicals, respectively, which can effectively oxidize contaminants adsorbed on BCs.

However, there have been no studies to report the impacts of iron impregnation ratio (g FeCl<sub>3</sub>/g feedstock for BC) during FeCl<sub>3</sub> activation on the properties of BCs, adsorption capacities of BCs, and regeneration of contaminant-spent BCs. More specifically, no studies have reported the correlations between functional groups of SMX and properties of iron-activated BCs. Moreover, cost-effective regeneration of contaminant-spent adsorbents is of prime importance for practical application of adsorbents for wastewater and water treatment. Only a few works have reported the impacts of iron impregnation ratio on BC properties, and adsorption of Hg and roxarsone (Yang et al., 2016a; Zhu et al., 2016). These works did not investigate possible effects of iron



impregnation ratio on adsorption of target contaminants and regeneration of contaminant-spent BC (Yang et al., 2016a; Zhu et al., 2016).

As mentioned in Chapter II, bermudagrass (BG) can be considered as a cost-effective feedstock for BC production. This work studied the impacts of various iron impregnation ratios (FeCl<sub>3</sub> to BG) on the physicochemical characteristics of iron-activated bermudagrass-derived biochars (IA-BCs), adsorption of sulfamethoxazole (SMX) on IA-BCs, and various regeneration techniques for SMX-spent IA-BCs. The IA-BCs were produced through one-step pyrolysis of FeCl<sub>3</sub>-laden BG at various iron impregnation ratios (g FeCl<sub>3</sub>/g BG). The physicochemical properties of IA-BCs at various iron impregnation ratios were determined. To understand the possible adsorption capacities and mechanisms, detailed adsorption experiments considering the effects of initial pH, kinetic studies, isotherm analysis, and thermodynamics studies were carried out. Furthermore, various regeneration experiments of the SMX-spent IA-BCs via NaOH desorption, thermal oxidation and Fenton oxidation were conducted over multiple cycles.

## **3.2 Materials and methods**

### **3.2.1 Materials**

SMX (C<sub>10</sub>H<sub>11</sub>N<sub>3</sub>O<sub>3</sub>S), ferric chloride (FeCl<sub>3</sub>), and other chemicals were obtained from Sigma-Aldrich (St. Louis, MO, USA). The physicochemical characteristics of SMX are provided in the Table S2.4 of Chapter II (Jang et al., 2018c). Bermudagrass (BG) was acquired from a local hay store (Stephenville, TX, USA).

### **3.2.2 Production of iron-activated BCs**

BG was dried, ground, sieved (< 500 μm), and used as the substrate for biochar production. Three grams of BG was mixed with 20 mL ferric chloride solution with various impregnation ratios (g of FeCl<sub>3</sub>/g of BG) of 0.5, 1.0, 2.0, and 3.0. The mixtures were stirred for 120 min and dried at 373

K. Then, dry mixtures were loaded to a tubular furnace (MTI Corp., Richmond, USA) and heated at 1073.15 K (800 °C) for 2 h in the heating rate of 8 K/min and N<sub>2</sub> flow of 2 L/min. The pyrolysis temperature (1073.15 K) used in this study was determined from the preliminary tests for SMX removal by the FeCl<sub>3</sub>-activated BG-derived BCs at 773.15-1073.15 K (with impregnation ratio of 2) (Figure S3.1). The resulting BCs were denoted as IA-BC<sub>x</sub>, where x in IA-BC<sub>x</sub> represents the FeCl<sub>3</sub> impregnation ratio. For comparison, BG without the addition of FeCl<sub>3</sub> was also pyrolyzed under the same abovementioned conditions. The BC resulting from this preparation was denoted as “BC800”. Acid washing could remove impurities and minerals in BCs (Choi & Kan, 2019; Jang & Kan, 2019a). Therefore, each BC (20 g) was mixed with 3 M HCl solution (1 L), stirred for 24 h, and then filtered with DI water until the filtrate pH was neutral. In the end, BCs were dried at 373 K and milled until the particle size was below 106 μm (140 mesh). The yields of BCs were defined according to the following equation (Eq. (3.1)):

$$\text{Yield (\%)} = \frac{W_{BC}}{W_{BG}} \times 100 \quad (3.1)$$

where W<sub>BC</sub> and W<sub>BG</sub> represent the weight of the initial BG and final BCs after washing and drying, respectively.

### 3.2.3 Characterization of BCs

Methods for the analyses of proximate, elemental, and mineral compositions, surface area, FT-IR, X-ray diffraction (XRD), and pH of zero point charge (pH<sub>PZC</sub>) of BCs were described in Sec. 2.2.3 of Chapter II. The surface morphologies of BCs were observed via a scanning electron microscope (SEM) connected to an energy-dispersive X-ray (EDX) instrument (S-4800, Hitachi Co., JPN).

### 3.2.4 SMX adsorption tests

For understanding the possible impacts of the initial solution pH on SMX adsorption, batch tests were performed at different pH values (1-11). BC (0.01 g) was added into 100 mL of 100 mg/L

SMX solution for 48 h at 150 rpm and 293 K to reach adsorption equilibrium. All adsorption tests in the current work were performed in duplicate. The adsorption of SMX onto BC ( $Q_e$ , mg SMX/g BC) at equilibrium was determined based on the below equation (Eq. (3.2)):

$$Q_e = \frac{(C_i - C_e) \times V}{M_b} \quad (3.2)$$

where  $C_i$  and  $C_e$  represent the initial and equilibrium SMX concentrations (mg/L), respectively,  $V$  represents the volume (L) of the SMX solution, and  $M_b$  represents the BC amount (g).

The empirical equation below (Eq. (3)) was applied for calculating the contribution of an individual SMX species to total adsorption at different pH values (Teixido et al., 2011):

$$K_d = K_d^- \alpha^- + K_d^0 \alpha^0 + K_d^+ \alpha^+ \quad (3.3)$$

where  $\alpha^-$ ,  $\alpha^0$ , and  $\alpha^+$  are the percentage of  $SMX^-$ ,  $SMX^0$ , and  $SMX^+$ , respectively, and  $K_d$ ,  $K_d^-$ ,  $K_d^0$ , and  $K_d^+$  (L/kg) are the adsorption coefficients of the entire,  $\alpha^-$ ,  $\alpha^0$ , and  $\alpha^+$ , respectively. The contribution percentage of each SMX species was evaluated through  $K_d^- \alpha^- / K_d$  for  $SMX^-$ ,  $K_d^0 \alpha^0 / K_d$  for  $SMX^0$ , and  $K_d^+ \alpha^+ / K_d$  for  $SMX^+$ .

The kinetics study was examined via stirring 0.01 g BC with 100 mL of 50 mg/L or 100 mg/L SMX solution at pH 3, which was proved to be the optimal pH in the above tests. For the adsorption isotherm study, adsorption experiments were performed through adding 0.01 g BC into 100 mL of various concentrations of SMX solution for 48 h. In this study, six kinetic models and four isotherm models, as listed in Table S2.2 (Chapter II), were applied for fitting the experimental results. The values for various parameters were derived from the kinetic and isotherm models. The physical meaning of each parameter value was also listed in the Table S2.2 (Chapter II).

In the thermodynamic study, the mixtures of 0.01 g BC and 100 mL of SMX solution at 100 mg/L were shaken for 48 h at various temperatures (303-323 K). The thermodynamic parameters,

including the standard enthalpy change ( $\Delta H^0$ ), standard entropy change ( $\Delta S^0$ ), and standard Gibbs free energy change ( $\Delta G^0$ ), were determined through thermodynamic equations (Table S2.2, Chapter II) (Pezoti et al., 2016).

The SMX concentration was measured by an HPLC instrument (LC-2030C model, SHIMADZU Corp., Torrance, CA, U.S.) connected to a PDA detector and a C18 column (3.6  $\mu\text{m}$  XB-C18). The running conditions for HPLC contained a mobile phase (33% methanol and 67% water containing 0.1% formic acid) and a flow rate of 0.6 mL/min.

In this study, the correlation between physicochemical characteristics of IA-BCs and adsorption ability for SMX was evaluated by the Minitab 16 Statistical Software (Minitab Inc., State College, PA). Pearson correlation analysis was applied for the statistical evaluation with significance levels of  $p < 0.05$ , 0.01, and 0.001.

### **3.2.5 Regeneration study**

In this study, NaOH desorption, thermal oxidation, and Fenton oxidation were used to regenerate and reuse SMX-saturated IA-BC<sub>2.0</sub>. For NaOH-driven desorption, after 48 h adsorption to reach equilibrium, SMX-saturated IA-BC<sub>2.0</sub> was separated and added into 0.1 L of 0.1-1 M NaOH solution under the shaking time of 24 h. After NaOH desorption, IA-BC<sub>2.0</sub> was separated again and oven-dried at 338 K. The readsorption conditions were the same as those described in the above experiments. For thermal oxidation, SMX-saturated IA-BC<sub>2.0</sub> was thermally treated in a furnace at various temperatures (373-573 K) for 3 h and then used for readsorption experiments. The desorption at 0.1 M NaOH and thermal oxidation at 573 K were performed to monitor possible cyclic adsorption-regeneration-readsorption over multiple cycles. For Fenton oxidation-driven regeneration, 0.01 g of IA-BC<sub>2.0</sub> was saturated with SMX, separated, and mixed with 100 mL of

400, 1600, and 4000 mg/L H<sub>2</sub>O<sub>2</sub> (pH 3) for 48 h. Then, readsorption experiments were conducted as mentioned above. The regeneration efficiency was determined by the following equation:

$$\text{Regeneration efficiency(\%)} = \frac{Q_n}{Q_0} \times 100 \quad (3.4)$$

where Q<sub>0</sub> and Q<sub>n</sub> represent the initial adsorption capacity and the adsorption capacity after n generation cycles, respectively.

### **3.2.6 Fixed bed experiment**

Fixed bed experiments were carried out by a down-flow column filled with 1 g of BC in the middle of column and 4 g of sand (100 mesh) (Jang & Kan, 2019a). The SMX influent concentration was 100 mg/L at pH 3. The flow rate was 1.28 mL/min, which was maintained by vacuum. Two breakthrough models (Thomas and Yoon-Nelson models) (Table S3.1) were used to fit the breakthrough curves obtained from the fixed bed experiments with BC800 and IA-BC<sub>2.0</sub>

## **3.3 Results and discussion**

### **3.3.1 Characterization of all BCs**

Table 3.1 displays the physicochemical characteristics of feedstock (Bermudagrass, BG) and all BCs (raw biochar and IA-BCs) produced in this study. Table 3.1 indicates that FeCl<sub>3</sub> activation caused a drastic enhancement in the surface area of IA-BCs with various impregnation ratios of FeCl<sub>3</sub> to BG (g FeCl<sub>3</sub>/g BG). Compared to BC800 (85.82 m<sup>2</sup>/g), IA-BC<sub>1.0</sub> to IA-BC<sub>3.0</sub> exhibited a greatly enhanced BET surface areas of 1014-1035 m<sup>2</sup>/g, which were higher than those of thermally and chemically activated BCs derived from other feedstocks and commercial activated carbons (Gauden et al., 2006; Rufford et al., 2011; Theydan & Ahmed, 2012) (Table S2.1, Chapter II).

**Table 3.1** Physicochemical properties of bermudagrass and IA-BCs at various iron impregnation ratios.

Material	Ultimate analysis (%)				O/C (mol/mol)	(N+O)/C (mol/mol)	H/C (mol/mol)	Proximate analysis (%)			SSA (m <sup>2</sup> g <sup>-1</sup> )	pH <sub>PZC</sub>	Fe content (%)
	C	H	O	N				VC	FC	Ash			
BG	47.43	6.30	35.66	2.50	0.564	0.609	1.594	85.71	6.60	7.69	0.63		0.02
BC800	68.02	1.58	12.94	3.37	0.143	0.185	0.279	18.04	67.92	14.04	85.82	4.19	0.04
IA-BC <sub>0.5</sub>	68.26	0.72	14.28	2.45	0.157	0.188	0.127	20.27	65.44	14.29	823.23	4.36	7.29
IA-BC <sub>1.0</sub>	70.56	0.62	12.12	2.80	0.129	0.163	0.105	20.58	65.52	13.90	1013.70	4.62	3.87
IA-BC <sub>2.0</sub>	71.60	0.49	10.07	2.42	0.105	0.134	0.082	22.05	63.19	14.76	1013.40	4.24	5.80
IA-BC <sub>3.0</sub>	68.31	0.35	9.81	2.32	0.108	0.137	0.061	21.99	58.80	19.21	1034.81	4.83	7.27

BG: Bermudagrass feedstock

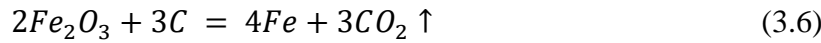
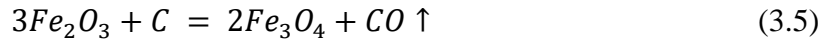
BC800: Bermudagrass biochar produced at 800 °C.

IA-BC<sub>x</sub>: iron (FeCl<sub>3</sub>)-activated BC, x represents the mass ratio of FeCl<sub>3</sub> to BG.

VC: Volatile carbon

FC: Fixed carbon

FeCl<sub>3</sub> has been considered an effective activator for carbonaceous materials to increase the surface areas and develop the micropores (Theydan & Ahmed, 2012). In the low-temperature treatment (< 673 K), decomposition processes happen and Fe species undergo some changes: FeCl<sub>3</sub> → FeOCl·H<sub>2</sub>O → FeOOH → Fe<sub>2</sub>O<sub>3</sub> (Rufford et al., 2011). However, at higher temperatures, amorphous carbon can convert Fe<sub>2</sub>O<sub>3</sub> to Fe<sub>3</sub>O<sub>4</sub>, Fe, CO<sub>2</sub>, and CO, as displayed in the below equations (Zhang et al., 2015; Zhu et al., 2016):



Thus, reactions between the carbon surface and iron oxides along with the evolution of CO and CO<sub>2</sub> would result in the pores development and the improvement of surface area of BCs. As shown in Table 3.1, the increase of iron impregnation ratio (g FeCl<sub>3</sub>/g BG) from 0.5 to 1 enhanced the surface areas of IA-BCs from 823 to 1014 m<sup>2</sup>/g due to FeCl<sub>3</sub> activation. However, at higher iron impregnation ratios (1-3), the intense chemical attack from excess FeCl<sub>3</sub> might destroy the existing pores, and also some iron oxides could cause the micropore blockage, which counteracted the positive effect of FeCl<sub>3</sub> activation. Similar results were also observed in the previous studies (Fu et al., 2017; Zhang et al., 2015). Furthermore, the high surface area of IA-BCs achieved in this study can provide more active sites for the adsorption of contaminants.

The elemental analysis indicated that the total C content of all IA-BCs slightly increased, and the highest C content was observed for IA-BC<sub>2.0</sub> compared to that of BC800 (Table 3.1). However, both total C content and fixed carbon content decreased with improving impregnation ratio from 2.0 to 3.0 due to the overactivation from excess FeCl<sub>3</sub> and reaction between carbon and excess iron oxides. Conversely, the O and H contents in the IA-BCs decreased significantly with a higher

impregnation ratio, which confirmed that FeCl<sub>3</sub> accelerated the decomposition of O and H and the loss of surface functional groups. With increasing impregnation ratio, the elemental ratio of H/C significantly dropped, indicating the increased aromaticity of BC (Mandal et al., 2017). However, the ratios of O/C and (N+O)/C were reduced with the increase of impregnation ratio, and increased slightly when the ratio exceeded 2.0, indicating that IA-BC<sub>2.0</sub> had the highest hydrophobicity and the lowest polarity in this study (Mandal et al., 2017). Such high aromaticity and hydrophobicity of IA-BC<sub>2.0</sub> could be beneficial for adsorption of organic contaminants in water.

After FeCl<sub>3</sub> activation, the IA-BCs showed different crystal phases compared to that of BC800. The peak at  $2\theta = 22^\circ$  indicated the presence of graphitized carbon, which resulted from aromatized and graphitized organic matter in BG (Luo et al., 2018) (Figure S3.2). Compared to BC800, the graphitization degree of all IA-BCs increased, suggesting that FeCl<sub>3</sub> could increase the graphitization degree of BC during the pyrolysis process. A previous study also reported that iron oxides produced by the decomposition of FeCl<sub>3</sub> could be inserted into a carbon matrix to form Fe carbide to improve the graphitization degree (Zhu et al., 2016). The peaks at about  $30.0^\circ$ ,  $54.0^\circ$ , and  $57.0^\circ$  corresponded to Fe<sub>3</sub>O<sub>4</sub>, confirming the presence of crystalline magnetite Fe<sub>3</sub>O<sub>4</sub>, which was from the redox reaction between carbon and Fe<sub>2</sub>O<sub>3</sub> (Eq. (5)) (Bombuwala Dewage et al., 2018; Cheng et al., 2010; Ghamkhari et al., 2020). The XRD patterns of all IA-BCs also showed diffraction peaks at  $2\theta = 24.1^\circ$ ,  $33.1^\circ$ ,  $35.0^\circ$ ,  $40.8^\circ$ ,  $49.4^\circ$ ,  $62.5^\circ$ , and  $64.0^\circ$ , which matched well with the peaks of  $\alpha$ -Fe<sub>2</sub>O<sub>3</sub>, confirming a previous report that the phase transformation of  $\gamma$ -Fe<sub>2</sub>O<sub>3</sub> to  $\alpha$ -Fe<sub>2</sub>O<sub>3</sub> can occur at 1073 K (Bombuwala Dewage et al., 2018; Zhu et al., 2014a). According to mineral composition results and EDX analysis (Table 3.1 and Figure S3.3), iron contents of all IA-BCs ranged from 3-9%, in contrast to only 0.04% for BC800, further indicating that iron was deposited onto the IA-BCs during FeCl<sub>3</sub> activation. From the SEM analysis (Figure S3.4),



compared to BC800, there were some small white particles on the surface of IA-BCs, which were iron oxides produced from FeCl<sub>3</sub> activation, indicating that iron were successfully attached onto the surface of IA-BCs. In addition, IA-BCs possessed rougher surface and increased small pores, which supported high surface area of IA-BCs. Furthermore, the presence of Fe<sub>3</sub>O<sub>4</sub> on IA-BCs provided excellent magnetic separation, which could facilitate the practical reuse of IA-BCs in wastewater and water treatment (Figure S3.5).

As shown in Figure S3.2, the functional groups of BC800 and IA-BCs were investigated using FT-IR, and all BCs showed similar peaks. In addition, there were no peaks in the region of 2858 cm<sup>-1</sup> to 3032 cm<sup>-1</sup>, which are usually ascribed to the C-H stretching vibration, indicating that feedstock (BG) was fully carbonized under the conditions of high temperature (1073.15 K) and FeCl<sub>3</sub> activation (Cui et al., 2019). Compared to BC800, the intensities of peaks centered at about 1556 cm<sup>-1</sup> and 2120 cm<sup>-1</sup>, corresponding to the stretching of C=C and C≡C groups, significantly increased for IA-BCs, indicating that FeCl<sub>3</sub> activation enhanced the aromatization degree of BCs (Ahmed et al., 2017a; Ahmed et al., 2017c). This also confirms that IA-BCs can provide more electron-donor sites for π-π EDA interaction between BCs and organic compounds. Another peak of IA-BCs at 1075 cm<sup>-1</sup> represented the stretching vibration of C-O (hydroxyl, ester, or ether) groups, whose oxygen functional groups are beneficial for the generation of hydrogen bond between BC surface and contaminants (Zhu et al., 2014b). Additionally, after the adsorption of SMX onto the IA-BCs, the peaks at 1075 cm<sup>-1</sup> (C-O), 1556 cm<sup>-1</sup> (C=C), and 2120 cm<sup>-1</sup> (C≡C) moved to 1085 cm<sup>-1</sup>, 1589 cm<sup>-1</sup>, and 2118 cm<sup>-1</sup>, respectively, and their intensities also decreased, confirming that these functional groups in IA-BC<sub>2.0</sub> contributed to the adsorption of SMX.

### **3.3.2 Statistical analysis: impregnation ratio of FeCl<sub>3</sub> to BG, properties and adsorption capacities of BCs**

The Pearson correlation analysis (Table S3.2) showed that the impregnation ratio of FeCl<sub>3</sub> to BG positively affected the properties (i.e., volatile carbon, ash and Fe content, and surface area) of the IA-BCs, while other properties appeared to be negatively correlated. In addition, some physicochemical properties (volatile carbon, surface area, H/C, P, K, Mg, and Na) of the IA-BCs influenced the adsorption capacity of SMX onto the IA-BCs. Particularly, surface area and H/C revealed a high correlation ( $p < 0.01$ ) with SMX adsorption capacity, implying that the improvement of surface area and decrease of H/C might result in the higher SMX adsorption capacity, similar to the results from previous literature (Choi & Kan, 2018).

### **3.3.3 Effects of initial pH and possible adsorption mechanisms**

Generally, adsorption properties of adsorbents for adsorbates are mainly affected by their characteristics and environmental conditions. SMX possesses amine (-NH<sub>2</sub>) and amide groups (-NH-) with two pKa values 1.6 and 5.7 (Choi & Kan, 2019). When solution pH is lower than 1.6 or higher than 5.7, SMX is positively or negatively charged, making electrostatic interaction a significant role for SMX adsorption. Moreover, groups -NH<sub>2</sub> and -NH- in SMX can form hydrogen bonding with various O-containing functional groups on BCs (Ahmed et al., 2017a; Ahmed et al., 2017b). The methyl group in SMX is considered as a hydrophobic group, which can play an important part in the hydrophobic interaction between SMX and BCs (Reguyal et al., 2017a). Besides, powerful electron withdrawing ability of the sulfonamide group and high electro negativity of the O atom in SMX make aromatic rings become electron deficient, which can serve as a  $\pi$  electron acceptor (Peiris et al., 2017). Due to the presence of graphitized surface in BCs ( $\pi$

electron donor), SMX can react with BCs by  $\pi$ - $\pi$  electron donor acceptor (EDA) interaction (Zheng et al., 2013).

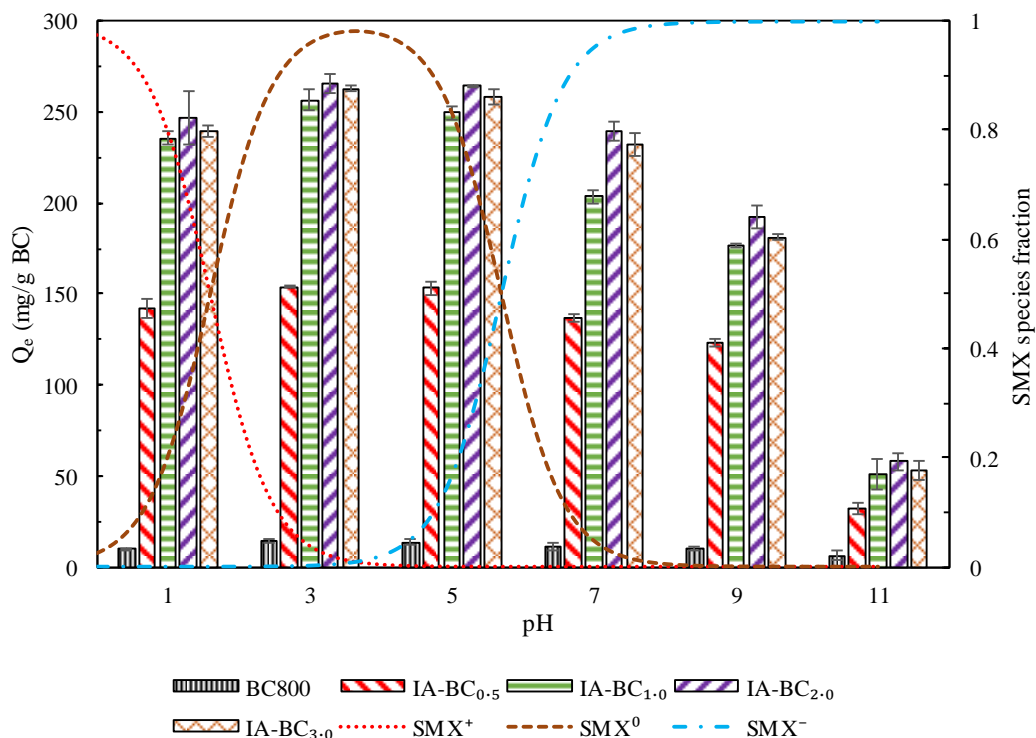


**Figure 3.1.** Effects of initial pH on adsorption of SMX onto BC800 and IA-BCs and pH-dependent SMX species. Experimental conditions: 100 mL of 100 mg/L SMX, 0.01 g of BC, initial pH of 1-11, and 48 h.

As mentioned earlier, the initial solution pH has substantial impacts on SMX adsorption onto BCs (Jang et al., 2018c). The pH dependence of SMX adsorption on all BCs exhibited the same pattern: the SMX adsorption ability was improved from pH 1 to 3 and then reduced from 3 to 11 (Figure 3.1). The maximum SMX adsorption capacities ( $Q_e$ ) of all BCs were obtained at pH 3. The  $Q_e$  values of all IA-BCs were much higher than that of BC800, possibly ascribed to the higher surface area and hydrophobicity of IA-BCs. Moreover, for all pH values investigated in this study, the  $Q_e$

value increased with increased impregnation ratio ( $\text{FeCl}_3/\text{BG}$ ) from 0.5 to 2, but slightly decreased at the ratio from 2 to 3. This result indicated that  $\text{FeCl}_3$  activation can increase the surface area and hydrophobicity, resulting in a higher adsorption capacity. However, for IA-BC<sub>3.0</sub>, excess  $\text{FeCl}_3$  could decrease the hydrophobicity of IA-BC, which would lower the hydrophobic interactions between SMX and IA-BC<sub>3.0</sub>.

The  $\text{pH}_{\text{PZC}}$  values of all IA-BCs were between 4 and 5 (Figure S3.6), and the surface charge of IA-BCs was positive at  $\text{pH} < \text{pH}_{\text{PZC}}$ ; otherwise, it was negative. SMX, which contains amine ( $-\text{NH}_2$ ) and amide groups ( $-\text{NH}-$ ), is considered an amphoteric molecule with two  $\text{pK}_a$  values (1.6 and 5.7); hence, the dominant species of SMX are  $\text{SMX}^+$ ,  $\text{SMX}^0$ , and  $\text{SMX}^-$  at  $\text{pH} < 1.6$ ,  $1.6 < \text{pH} < 5.7$ , and  $\text{pH} > 5.7$ , respectively (Choi & Kan, 2019; Jang et al., 2018c). Therefore, at pH 1, both SMX and IA-BCs were positively charged, and electrostatic repulsion would reduce SMX adsorption onto IA-BCs. Nevertheless, a high  $Q_e$  (larger than 90% of  $Q_e$  at pH 3.0) of the IA-BCs for SMX was still observed at pH 1.0, revealing that other interactions are also involved in the adsorption process.  $\pi$ - $\pi$  electron donor-acceptor (EDA) interactions have been identified as the most significant driving force between SMX and BCs (Peiris et al., 2017). Moreover, over 70% of the absorbed SMX came from  $\text{SMX}^+$  at pH 1.0 (Figure S3.7). Thus, at pH 1.0,  $\pi^+$ - $\pi$  EDA interaction could occur between the protonated aniline ring of  $\text{SMX}^+$  ( $\pi$  electron acceptor) and the  $\pi$  electron-rich graphitized surface of IA-BCs attached with  $\text{C}=\text{C}$  and  $\text{C}\equiv\text{C}$  groups ( $\pi$  electron donor), as shown in FTIR and XRD analysis (Ahmed et al., 2017a; Zheng et al., 2013).

At pH 1.6-5.7, the SMX molecule is electrically neutral ( $\text{SMX}^0$ ); hence, electrostatic interactions were not significant between  $\text{SMX}^0$  and IA-BCs. In addition to being attributed to  $\pi$ - $\pi$  EDA interaction, the high  $Q_e$  of IA-BCs for SMX observed at pH 3 and 5 could be attributed to hydrophobic interactions and hydrogen bonds. A previous report showed that SMX solubility was

lowest at pH 3.22 and increased with increasing solution pH value (Reguyal et al., 2017a). In our data, it can be observed that the  $Q_e$  value of the IA-BCs for SMX was negatively influenced by SMX solubility, supporting that hydrophobic interactions could occur between the  $SMX^0$  molecule and IA-BCs. In addition, as shown in the FT-IR spectra (Figure S3.2), some oxygenous functional groups appeared on the surface of the IA-BCs, which could form hydrogen bonds with  $-NH_2$  and  $-NH-$  groups of SMX. These results are consistent to previous data indicating that hydrophobic interactions and hydrogen bonds participate in the SMX adsorption process onto BCs (Ahmed et al., 2017a; Choi & Kan, 2019; Reguyal et al., 2017a).

At solution  $pH > 5.7$ , electrostatic repulsion could occur between negatively charged SMX ( $SMX^-$ ) and IA-BCs, which negatively impacted the adsorption capacity of SMX on IA-BCs. In addition, SMX is deprotonated at high pH, and the  $\pi$  electron acceptor capacity and hydrophobicity of  $SMX^-$  significantly decrease, thus inhibiting  $\pi$ - $\pi$  EDA interaction with the IA-BCs surface (Yao et al., 2018). However, except at pH 11.0, a considerable amount of SMX molecules were still adsorbed onto the IA-BCs in this pH range. This result could be ascribed to negative charge-assisted hydrogen bond (CAHB) interactions, which occurred because the  $SMX^-$  molecule captured a proton from a water molecule to produce neutral  $SMX^0$ , which further interacted with oxygen functional groups on IA-BCs (Ahmed et al., 2017a; Zheng et al., 2013). Previous reports also mentioned that negatively charged  $SMX^-$  molecules could be adsorbed onto negatively charged BCs via CAHB interactions (Ahmed et al., 2017b).

Iron oxides ( $Fe_2O_3$  and  $Fe_3O_4$ ) showed low adsorption capacity for SMX (less than 10 mg/g, data not shown). Moreover, Fe contents in IA-BCs ranged from 3.87% to 7.29%, which were a small portion of IA-BCs. Therefore, most of SMX adsorption occurred on carbon surface, rather than Fe compounds in IA-BCs. In overall, the elimination of SMX by IA-BCs was regulated through  $\pi^+-\pi$

EDA,  $\pi$ - $\pi$  EDA, hydrophobic, hydrogen bond, and negative CAHB interactions at various solution pH values (Figure S3.8).

### 3.3.4 Adsorption kinetics

Since IA-BC<sub>2.0</sub> showed the highest SMX adsorption capacities at various solution pH values (Figure 3.1), IA-BC<sub>2.0</sub> was selected for detailed analysis of adsorption characteristics. To determine the possible adsorption mechanism and rate-limiting step, the adsorption kinetics of SMX onto IA-BC<sub>2.0</sub> were investigated (Figure 3.2). Similar to the studies described by Jang et al. (2018c) and Yao et al. (2018), adsorption occurred rapidly, and 80% of the maximum adsorption capacity was achieved within 3 h.

The results from adsorption kinetics were also fitted to various models (Figure 3.2 and Table S3.3). Compared to the pseudo-first order (PFO) model, the pseudo-second order (PSO) model, which had a higher  $R^2$  (0.98) and lower SSE (9.28-9.92), better fitted the experimental data, revealing that chemical adsorption was the main mechanism for SMX adsorption onto IA-BC<sub>2.0</sub> (Jang & Kan, 2019c). Additionally, the calculated  $Q_e$  value in the PSO model was closer than that in the PFO model to the experimental  $Q_e$  value. The rate constants  $K_1$  and  $K_2$  were both far below 1, indicating that the adsorption process was very fast. Furthermore, the Elovich model best represented the adsorption kinetics (Table S3.3), supporting chemical interactions between IA-BC and SMX on the energetically heterogeneous surface of IA-BC (Jang et al., 2018b). Moreover, the two-compartment first-order (TCFO) model also fit the kinetics results well (Figure 3.2 and Table S3.3). The significantly higher rate constant of fast adsorption than that of slow adsorption suggested that fast adsorption was the dominant process, which highly supported the fast adsorption of SMX on IA-BC<sub>2.0</sub> in the first few hours, as seen in Figure 3.2.

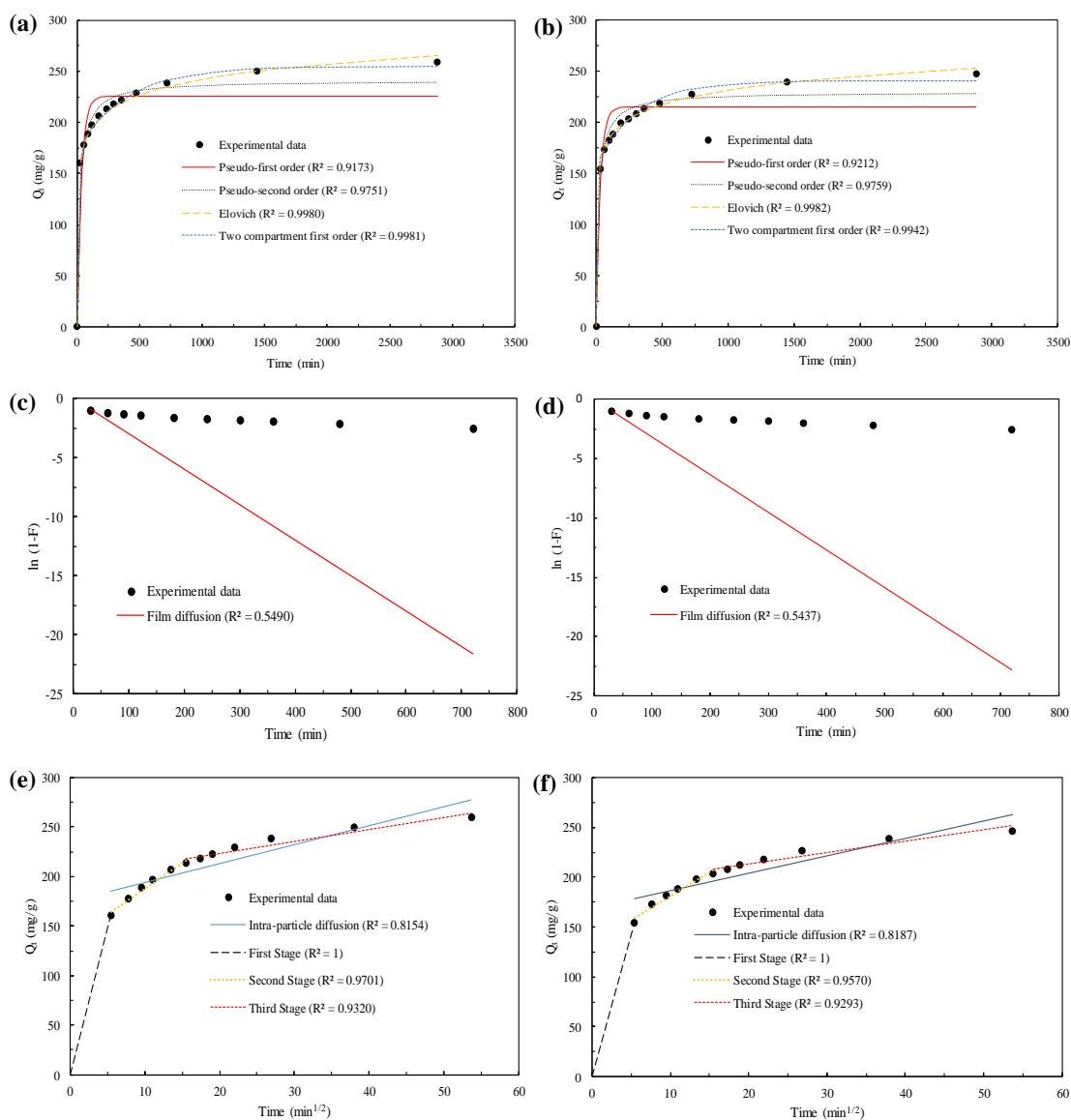


**Figure 3.2.** Adsorption kinetics of SMX on IA-BC<sub>2.0</sub>. by fitting the pseudo-first order, pseudo-second order, two compartment first order and Elovich ((a) and (b)), film diffusion model ((c) and (d)), and intra-particle diffusion model ((e) and (f)) under two different initial concentrations of 50 mg/L((a), (c) and (e)) and 100 mg/L((b), (d) and (f)). Experimental conditions: 100 mL of 50 and 100 mg/L SMX, 0.01 g of BC, and initial pH of 3.

To explore the possible rate-limiting step during the adsorption process, intraparticle diffusion and film diffusion models were fitted to the adsorption kinetics results (Figure 3.2 and Table S3.3). The intraparticle diffusion model was better fitted than the film diffusion model to the adsorption of SMX onto IA-BC<sub>2.0</sub>, emphasizing that adsorption could be controlled by intraparticle diffusion. Moreover, the plot of  $Q_t$  against  $t^{1/2}$  was divided into three linear segments including the SMX molecules diffusion into the external surface of IA-BC<sub>2.0</sub>, diffusion into the internal pore structure, and the achievement of adsorption equilibrium on the active sites of the internal pore surface (Jang et al., 2018b; Martins et al., 2015). In addition,  $K_{i1}$  was much higher than  $K_{i2}$  and  $K_{i3}$ , indicating that fast adsorption occurred at the beginning of the adsorption process, which accorded with the TCFO model. However, neither the second nor the third segment intersected with the origin, implying that intraparticle diffusion was not the sole rate-controlling process (Martins et al., 2015).

### 3.3.5 Adsorption isotherm

To further understand the interactions between IA-BCs and SMX molecules, the adsorption isotherm results were fitted to various isotherm models (Table 3.2 and Figure S3.9). The Freundlich model was better fitted than the Langmuir model to the experimental results, implying multilayer SMX molecules adsorption onto the heterogeneous IA-BC<sub>2.0</sub> surface (Jang & Kan, 2019c; Tang et al., 2018). In addition, the separation factor  $R_L$  (0.58) and heterogeneity factor  $1/n$  (0.11) calculated from the Langmuir and Freundlich models ranged from 0 to 1, revealing a favorable adsorption process (Tang et al., 2018). The Temkin model exhibited the best fit to isotherm results ( $R^2$  of 0.97 and lowest SSE of 8.16), which indicates that the adsorption heat of SMX onto IA-BC<sub>2.0</sub> decreases linearly with the coverage of the IA-BC<sub>2.0</sub> surface and that chemical interactions are the main adsorption mechanism (Martins et al., 2015). Moreover, the  $b_T$  value (104.44) in the Temkin model was much higher than 1, suggesting that SMX adsorption onto IA-



BC<sub>2.0</sub> is an exothermic process (Jang & Kan, 2019c; Martins et al., 2015). Furthermore, the results of the Dubinin-Radushkevich model ( $R^2$  of 0.83) also supported that adsorption happened on the heterogeneous surface (Tang et al., 2018).

**Table 3.2** Summary of isotherm parameters of SMX adsorption on IA-BC<sub>2.0</sub>. Experimental conditions: 100 mL of 10-100 mg/L SMX, 0.01 g of BC, initial pH of 3, and 48 h.

Langmuir model		Dubinin-Radushkevich model	
$Q_m$	252.81	$q_D$	250.73
$K_L$	7.29	$b_D$	$1.83 \times 10^{-8}$
$R_L$	0.58	E	5.21
SSE	17.43	SSE	20.74
$R^2$	0.8813	$R^2$	0.8319
Temkin model		Freundlich model	
$K_T$	1627.18	$K_f$	170.74
$b_T$	104.44	n	8.79
SSE	8.16	SSE	13.30
$R^2$	0.9732	$R^2$	0.9308

The maximum adsorption capacity of IA-BC<sub>2.0</sub> for SMX ( $Q_m$ , mg SMX/g BC; calculated from Langmuir isotherm model) was 253 mg/g, which was higher than those of various adsorbents displayed in Table S2.1 (Chapter II), including commercial activated carbons, thermally and chemically activated biochars, carbon nanotubes, and graphene oxide. Therefore, IA-BC<sub>2.0</sub> showed great potential for the elimination of the antibiotic SMX from water.

### 3.3.6 Thermodynamic study

Based on the adsorption of SMX onto IA-BC<sub>2.0</sub> at various temperatures, thermodynamic parameters ( $\Delta G^0$ ,  $\Delta H^0$ , and  $\Delta S^0$ ) were calculated (Table 3.3). The negative  $\Delta G^0$  values of 303-323 K indicated that SMX adsorption onto IA-BC<sub>2.0</sub> is spontaneous. The  $\Delta G^0$  value decreased with the increase of temperature, implying a more favorable adsorption process at elevated temperature (Pezoti et al., 2016). The negative  $\Delta H^0$  value indicated the exothermic adsorption process, which

coincided with the analysis of the Temkin isotherm model (Zhu et al., 2014b). Additionally, the positive value of  $\Delta S^0$  suggested the enhanced randomness at the solid-liquid interface for the adsorption of SMX onto IA-BC<sub>2.0</sub> (Tang et al., 2018).

**Table 3.3** Thermodynamic parameters for the adsorption of SMX on IA-BC<sub>2.0</sub>. Experimental conditions: 100 mL of 100 mg/L SMX, 0.01 g of BC, initial pH of 3, temperature of 303-323 K, and 48 h.

Temperature (K)	$K_d$ (L/g)	$\Delta G^0$ (J/mol)	$\Delta H^0$ (J/mol)	$\Delta S^0$ (J/mol·K)
303	3.74	-3329	-676.85	8.75
313	3.72	-3416		
323	3.68	-3504		

### 3.3.7 Regeneration study

Cost-effective regeneration of SMX-saturated IA-BC can enable the practical application of IA-BC for the SMX removal from water. NaOH desorption, thermal oxidation, and Fenton oxidation were used for the regeneration of SMX-saturated IA-BC<sub>2.0</sub>. NaOH-driven desorption at various NaOH concentrations indicated that 0.1 M NaOH was more effective than other concentrations of NaOH (Figure S3.10). NaOH-driven desorption with 0.1 M NaOH resulted in high regeneration efficiencies (72–97%) in the 1<sup>st</sup>-2<sup>nd</sup> cycles (Figure 3.3a). The result also corresponds with a previous finding that high pH with 0.1 M NaOH resulted in the effective desorption of antibiotics from BCs (Zhou et al., 2017). However, repeated NaOH-driven desorption during the 3<sup>rd</sup>-4<sup>th</sup> cycles led to decreased regeneration efficiencies (54-62%) owing to the possible accumulation of SMX on the BC surface and deterioration of the biochar surface exposed to NaOH solution for a longer period of time.

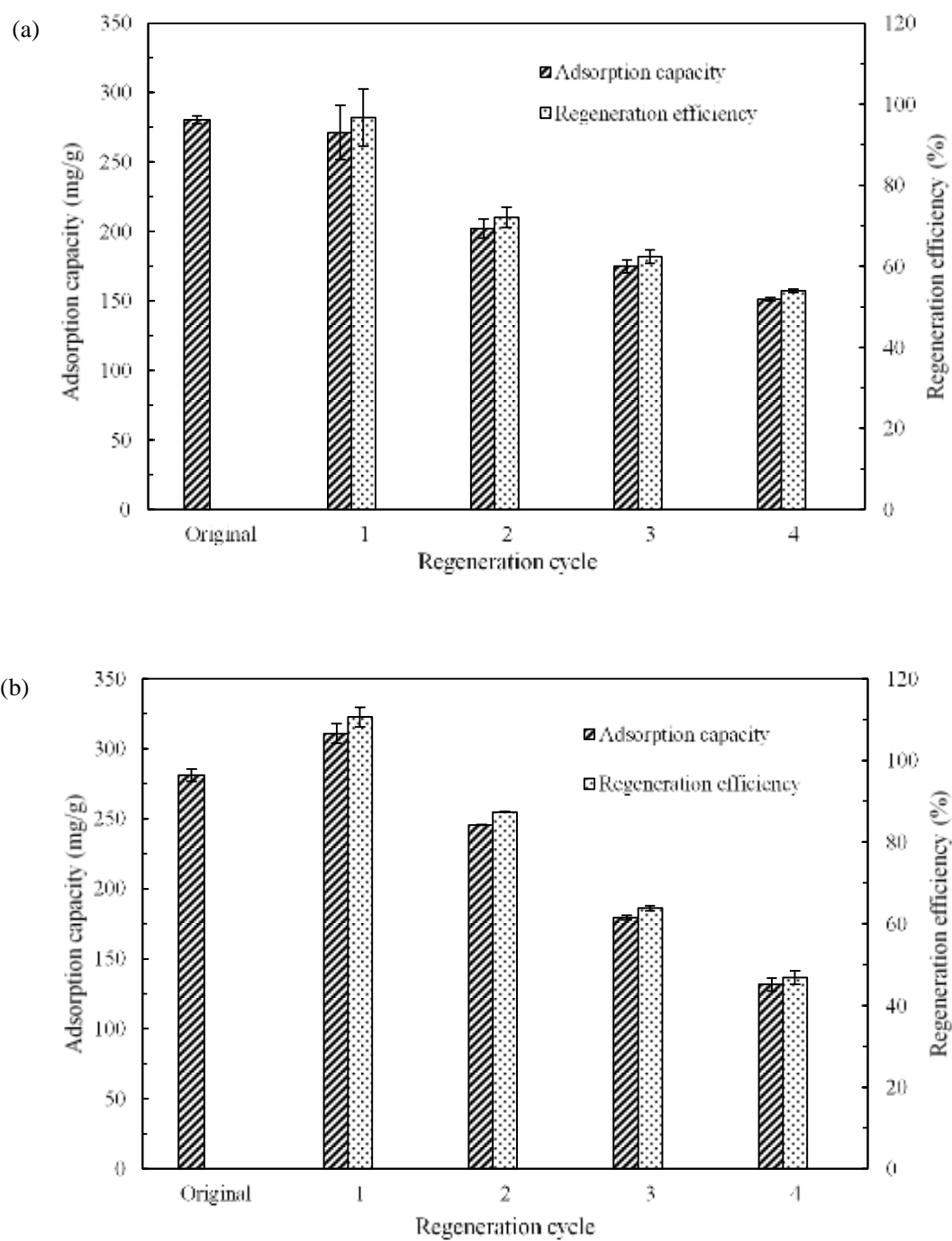


**Figure 3.3.** Regeneration experiments for the SMX-spent IA-BC2.0 using 0.1 M NaOH (a) and thermal oxidation at 573 K and 3 h (b).

It has been reported that thermal oxidation-driven regeneration is a fast and effective method for the regeneration of contaminant-spent absorbents (Carratalá-Abril et al., 2010). SMX-saturated IA-BC<sub>2.0</sub> was treated by thermal oxidation at 573 K for 3 h in a furnace, resulting in almost 100% regeneration efficiency (Figure 3.3b). Please note that thermal oxidation at 373 K and 473 K was not effective for the regeneration of SMX-saturated IA-BC<sub>2.0</sub> (Figure S3.11). A previous study also revealed that thermal oxidation at 573 K for 0.5 h could effectively regenerate dye-saturated activated carbon (Li et al., 2011). However, after 2-4 cycles of thermal regeneration at 573 K, regeneration efficiencies dropped to 87% and 46% (Figure 3.3b) owing to possible alterations in surface chemistry and a reduced surface area with damage to the pore structure after repeated thermal oxidation, as reported by Ledesma et al. (2014). After 4 cycles of thermal regeneration, the intensity of C-O vibrations increased significantly, which indicated an improvement in O-containing functional groups and the hydrophilicity of IA-BC<sub>2.0</sub> (Figure S3.12). This effect resulted in a decrease in hydrophobic interactions between SMX molecules and IA-BC<sub>2.0</sub>, which was the dominant mechanism at pH 3.

Since IA-BC<sub>2.0</sub> possessed various iron oxides (Fe<sub>2</sub>O<sub>3</sub> and Fe<sub>3</sub>O<sub>4</sub>) (from the XRD results), Fenton oxidation could possibly work to regenerate SMX-spent IA-BC<sub>2.0</sub>. Therefore, Fenton oxidation was conducted to regenerate SMX-spent IA-BC<sub>2.0</sub>. However, compared to the results of thermal oxidation and NaOH-driven desorption, the regeneration efficiency obtained via Fenton oxidation was unsatisfactory (below 40%) (Figure S3.13). Moreover, as shown in Figure S3.14, the desorption efficiency of SMX-spent IA-BC<sub>2.0</sub> was below 10%, which could explain the poor regeneration efficiency due to the strong interactions and limited diffusion of SMX in the inside pores of IA-BC<sub>2.0</sub>.

Therefore, both NaOH-driven desorption and thermal treatment could be cost-effective regeneration methods for SMX-saturated BCs after optimization of the regeneration conditions and cycles. The adsorption of SMX using IA-BC in this study has high potential for practically treating water and wastewater contaminated with SMX and other organic compounds.

### **3.3.8 Fixed bed experiment**

Fixed bed experiments were performed to investigate adsorption behaviors of BC800 and IA-BC<sub>2.0</sub> under dynamic conditions. Table S3.4 shows that breakthrough time ( $t_b$ ) for BC800 and IA-BC<sub>2.0</sub> were 60 and 1680 min, indicating that FeCl<sub>3</sub> activation resulted in significant increase of breakthrough time and treatment volume of SMX-contaminated water using the column filled with BC under the same operating conditions. In this study, Thomas and Yoon-Nelson models were applied to fit the SMX breakthrough curves in the fixed bed columns with BC<sub>800</sub> and IA-BC<sub>2.0</sub> (Figure 3.4 and Table S3.5). The  $q_0$  (adsorption capacity) calculated from Thomas model for IA-BC<sub>2.0</sub> was remarkably higher than that for BC800, which was related to the drastic improvement of BC surface area and hydrophobicity after FeCl<sub>3</sub> activation. Moreover, IA-BC<sub>2.0</sub> also showed higher  $\tau$  value (time required for 50% SMX breakthrough, 1961 min) than BC800 (106 min). Therefore, both higher  $q_0$  and  $\tau$  for IA-BC<sub>2.0</sub> indicated that IA-BC<sub>2.0</sub> has high capacity for treating SMX-contaminated water under dynamic conditions.

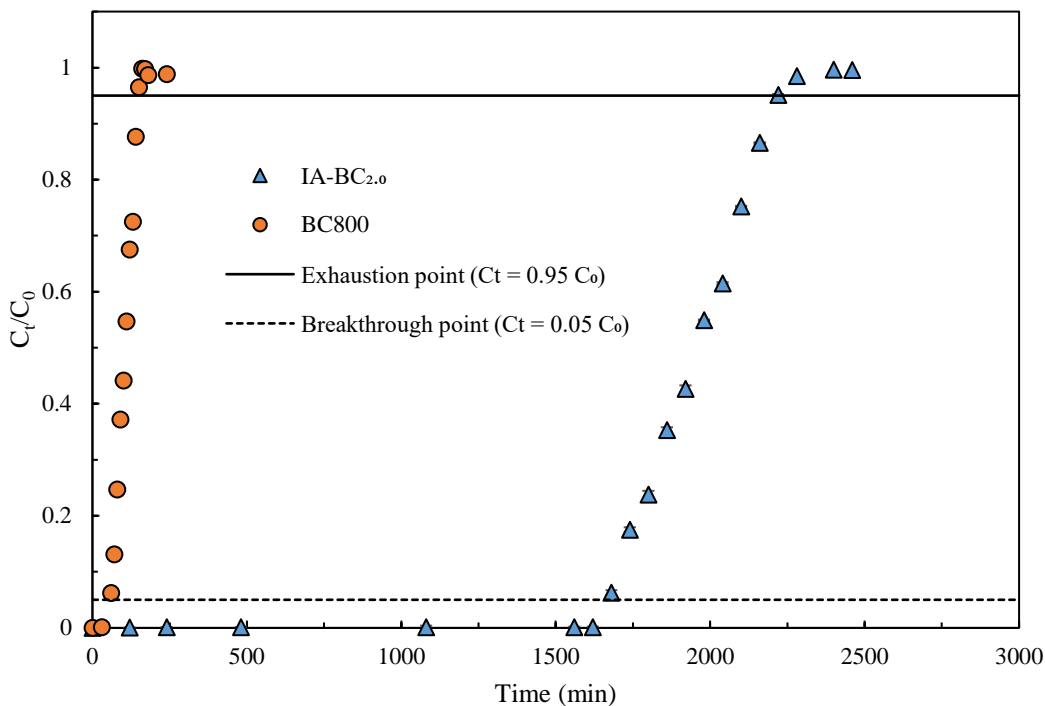


**Figure 3.4.** Comparison of the fraction of SMX in effluent of fixed bed experiment using BC800 and IA-BC<sub>2.0</sub>. The influent concentration of SMX and flow rate were 100 mg/L and 1.28 mL/min ( $C_0$  = SMX concentration in influent and  $C_t$  = SMX in effluent at time  $t$  (min)).

Further works will include optimization and scale-up of cyclic adsorption-regeneration process with the IA-BC. Following scale-up of the process, accurate cost evaluation of the process for biochar production and applications for wastewater treatment will be made and compared with those of current activated carbon adsorption processes.

### 3.4 Conclusions

One-step iron ( $\text{FeCl}_3$ )-assisted activation of bermudagrass-derived BCs (IA-BCs) exhibited great surface area and adsorption capacity for SMX, and IA-BC<sub>2.0</sub> showed the highest adsorption of SMX. The adsorption data were best fitted to the Elovich and Temkin models, implying strong chemisorptive interactions between SMX and IA-BC<sub>2.0</sub>. Additionally, intraparticle diffusion mainly controlled the adsorption rate. The thermodynamic study results implied that SMX

adsorption onto IA-BC<sub>2.0</sub> was spontaneous and exothermic. Additionally, the effective regeneration of SMX-saturated IA-BC<sub>2.0</sub> via NaOH-driven desorption and thermal oxidation indicated that iron-activated BC could be a cost-efficient material for treating SMX from water.

**CHAPTER IV**

**SIMULTANEOUS ADSORPTION AND HETEROGENEOUS FENTON OXIDATION  
FOR REMOVAL OF ANTIBIOTIC SULFAMETHOXAZOLE BY IRON-ACTIVATED  
BERMUDAGRASS-DERIVED BIOCHAR**

**4.1 Introduction**

As mentioned in Chapter II, it is pressing for the development of effective treatment methods to remove antibiotic sulfamethoxazole (SMX).

Various techniques have been developed for the treatment of SMX, such as adsorption, advanced oxidation, membrane, and biological treatment (Jang et al., 2018c; Larcher & Yargeau, 2012; Liu et al., 2018b; Sheng et al., 2020). Biological methods usually require a long reaction time and show low removal efficiency of contaminants while membrane technique need complex preparation process and suffer from the problem of membrane fouling (Chang et al., 2012; Larcher & Yargeau, 2012; Zeng et al., 2017). Adsorption has been considered as an easily operated, nontoxic, and highly efficient method to eliminate SMX from water (Jang et al., 2018c). Among various adsorbents, biochar (BC), obtained from the pyrolysis of biomass under oxygen limited conditions, has been recognized as an effective, environmentally friendly, and low-cost adsorbent for the treatment of SMX (Zeng & Kan, 2020a). However, the adsorption of SMX onto raw BCs were often limited by their limited surface areas and poor porous structures (Choi & Kan, 2019; Yao et al., 2018). Therefore, for the improvement of adsorption ability for contaminants, it is significant to increase surface areas and optimize pore structures of raw BCs.

Advanced oxidation processes (AOPs), including Fenton oxidation, ozonation, photocatalysis, persulfate oxidation, and so on, can achieve high removal efficiency and deep mineralization of



organic contaminants via the generation of free radicals with powerfully destructive ability (Tu et al., 2020b). Among AOPs, Fenton oxidation has been extensively applied for the degradation of organic contaminants including SMX (Liu et al., 2018b). Fenton oxidation process can produce  $\cdot\text{OH}$  radicals with high redox potential (2.8 V), which can non-selectively attack various organic compounds (Ozbey Unal et al., 2019). In the traditional Fenton oxidation process (homogeneous Fenton),  $\cdot\text{OH}$  radicals are produced from the reaction between  $\text{H}_2\text{O}_2$  and ferrous ion (Park et al., 2018b). However, a lot of iron sludge are produced and iron salt cannot be reused during homogeneous Fenton process, in which separation and disposal of sludge after reaction can result in additional costs (Park et al., 2018b; Rubeena et al., 2018). Therefore, in order to overcome the above-mentioned disadvantages, active studies have focused on heterogeneous Fenton oxidation process, which uses the iron-based solid materials as catalysts for Fenton oxidation (Park et al., 2018b). So far, most of iron-based solid catalysts are prepared by attaching iron compounds onto solid supports and used for the degradation tests of contaminants via Fenton-like oxidation. Compared to other expensive carbon materials such as carbon nanotube, graphene oxide, and activated carbon, BC can be a cost-effective and environmentally friendly support for heterogeneous Fenton oxidation due to the cheap feedstocks including industrial and agricultural wastes (Ge et al., 2019; Nguyen et al., 2011; Rubeena et al., 2018; Wang et al., 2020). For example, Rubeena et al. (2018) attached  $\text{Fe}_2\text{O}_3$ ,  $\text{Fe}_3\text{O}_4$  and  $\text{FeOOH}$  onto rice husk-derived BC as a heterogeneous Fenton catalyst for the removal of acid red 1 dye and achieved dye removal efficiency of 98% under the optimal conditions. Deng et al. (2018) prepared the zero-valent iron amended BC for the heterogeneous Fenton oxidation of antibiotic sulfamethazine, and found that 74% of sulfamethazine (10 mg/L) was oxidized at optimal conditions. Ngankam et al. (2020) also immobilized  $\text{Fe}_3\text{O}_4$  onto banana peel-derived BC and used it to degrade methylene blue (MB) via

heterogeneous Fenton oxidation, and reported that higher than 90% of MB was removed under the MB concentrations of 40-120 mg/L. However, BC-based heterogeneous Fenton catalysts described above were prepared via two-step process including the production of raw BC via pyrolysis and attachment of iron oxides onto the BC via chemical precipitation or calcination, which requires much time and energy input.

FeCl<sub>3</sub> has been considered as an effective activator to prepare activated BCs. After FeCl<sub>3</sub> activation, the surface area and porosity of BCs were significantly increased, which favored the improvement of adsorption ability for contaminants (Cho et al., 2017; Zhu et al., 2016). Moreover, FeCl<sub>3</sub> activation also resulted in the attachment of various iron species onto BCs (Zhu et al., 2016). In addition, magnetic iron compounds (e.g. Fe<sub>3</sub>O<sub>4</sub>) appeared on the surface of FeCl<sub>3</sub> activated BCs, which enable them to have magnetism and can be separated from the reaction solution by the magnet (Cho et al., 2017). So far, various FeCl<sub>3</sub> activated BCs have been prepared and used to remove various contaminants including arsenic, methylene blue, roxarsone, and tetracycline through the adsorption process (Cho et al., 2017; Theydan & Ahmed, 2012; Zhu et al., 2014b; Zhu et al., 2016). However, there are no studies about using FeCl<sub>3</sub> activated BCs as heterogeneous Fenton catalysts to degrade antibiotics including SMX.

In this study, to overcome the current limitations of BC as the adsorbent and support of heterogeneous Fenton catalysts, for the first time, iron (FeCl<sub>3</sub>) activated BC (FA-BC) was prepared by one-step pyrolysis/activation of bermudagrass and used for antibiotic SMX removal via adsorption and heterogeneous Fenton oxidation. Additionally, bermudagrass (BG), one of the most productive forage grasses in U.S, can be used as an inexpensive feedstock for BC (Zeng & Kan, 2020a). The specific objectives of this study were: (1) preparation and characterization of FA-BCs; (2) studying SMX adsorption kinetics and isotherm on FA-BC; (3) investigation of effects

of operational parameters (initial pH, H<sub>2</sub>O<sub>2</sub> concentration, and temperature) on Fenton oxidation of SMX by FA-BC; (4) exploring removal mechanisms of SMX via adsorption and Fenton oxidation by FA-BC; (5) application of FA-BC for SMX removal in real wastewater; and (6) reusability of FA-BC for the heterogeneous Fenton oxidation of SMX.

## **4.2 Materials and methods**

### **4.2.1 Materials**

Sulfamethoxazole (SMX, C<sub>10</sub>H<sub>11</sub>N<sub>3</sub>O<sub>3</sub>S), ferric trichloride (FeCl<sub>3</sub>), and hydrogen peroxide (H<sub>2</sub>O<sub>2</sub>, 30%) were supplied by Sigma-Aldrich (St. Louis, MO, USA). All chemicals utilized in the current study were of analytical grade. Bermudagrass was provided by Southwest Dairy Center (Stephenville, TX, USA).

### **4.2.2 Preparation and characterization of FeCl<sub>3</sub> activated biochars**

Bermudagrass (BG) was dried, ground, and sieved through a 35-mesh. BG (3 g) and various weights of FeCl<sub>3</sub> were stirred in 20 mL of DI water for 2 h, and then oven-dried at 105 °C for 4 h. The impregnation ratio of FeCl<sub>3</sub> to BG (mass ratio) was set to 0.5, 1, 2, and 3 in this study. Then, the dry solids were pyrolyzed in a tube furnace at 800 °C for 2 h and a heating rate of 8 °C/min under nitrogen flow. The produced FeCl<sub>3</sub> activated BCs were denoted as FA-BCs. For comparison, BG was also pyrolyzed at the same above-mentioned conditions without addition of FeCl<sub>3</sub>, which was referred to as Raw-BC. In addition, in order to evaluate the effect of acid washing on FA-BCs, the FA-BC at the impregnation ratio of 2 was washed by 3 M HCl. All BCs were dried at 80 °C, ground, and sieved to the size below 106 μm for further experiments.

The chemical state of elements of BCs was determined using an X-ray photoelectron spectrometer (XPS) (Perkin-Elmer Phi 560, USA). The analyses of X-ray diffraction (XRD), FT-IR, surface

area, mineral composition, and elemental composition of BCs were described in Chapter II (Sec. 2.2.3).

#### 4.2.3 Adsorption experiments

For batch adsorption tests, 0.01 g of BC was added into 100 mL of 100 mg/L of SMX solution at pH 3 and 150 rpm for 2 d, and SMX concentration was measured at various time intervals for the adsorption kinetic study. The adsorption isotherm study was carried out by mixing 0.01 g of BC with 100 mL of various concentrations (5-100 mg/L) of SMX solution at pH 3 for 2 d. In this study, two kinetic models (Pseudo-first order and Pseudo-second order) and two isotherm models (Langmuir and Freundlich) were applied to explain the experimental data (Table S2.2, Chapter II).

The adsorption capacity  $Q_e$  (mg/g) of BCs for SMX was calculated as the following equation:

$$Q_e = \frac{(C_i - C_e) \times V}{M} \quad (4.1)$$

where  $C_i$  and  $C_e$  (mg/L) are the SMX concentrations at initial and equilibrium time,  $V$  (L) is the solution volume, and  $M$  (g) is the BC mass.

#### 4.2.4 Fenton oxidation experiments

Heterogeneous Fenton oxidation experiments were performed through adding the  $H_2O_2$  into 100 mL of 100 mg/L SMX solution with 0.01 g of BC at 300 rpm. Effects of initial pH (3-7), reaction temperature (20-50 °C), and  $H_2O_2$  concentration (25-300 mg/L) on SMX oxidation were evaluated in this study. SMX and  $H_2O_2$  concentrations were measured at various time intervals. Kinetic constants  $k$  ( $h^{-1}$ ) of SMX oxidation and  $H_2O_2$  decomposition were calculated using the first-order equation. The removal efficiency of SMX was determined using the following equation:

$$SMX \text{ removal efficiency (\%)} = \left(1 - \frac{C_t}{C_i}\right) \times 100 \quad (4.2)$$

where  $C_i$  (mg/L) is the initial SMX concentration and  $C_t$  (mg/L) is the SMX concentration at time  $t$ .

Various concentrations (0 - 5 M) of ethanol as the scavenger were used to evaluate the contribution of  $\cdot\text{OH}$  radical to SMX oxidation under the conditions of 0.01 g of FA-BC, 100 mL of 100 mg/L SMX, initial pH of 3, 200 mg/L  $\text{H}_2\text{O}_2$ , and reaction temperature of 20 °C. To evaluate the reusability of FA-BC for SMX degradation, after Fenton reaction, FA-BC was magnetically separated from the reaction solution and added into 100 mL of fresh SMX solution (100 mg/L) for 3 cycles. For the application of FA-BC in the treatment of real wastewater, the lagoon wastewater was obtained from Southwest Dairy Center (Stephenville, TX, USA) and water quality parameters were presented in Table S2.7 (Chapter II). Then, 100 mL of lagoon wastewater was spiked with 100 mg/L SMX and mixed with 200 mg/L  $\text{H}_2\text{O}_2$  at pH 3 and 20 °C. All adsorption and Fenton degradation experiments in this study were performed in duplicate.

#### **4.2.5 Analytical methods**

The SMX concentration in the aqueous phase after adsorption or Fenton oxidation was measured by an HPLC (Shimadzu LC-2030C, Shimadzu Co., JP) connected to a C18 column (Phenomenex Inc., CA, USA) and a PDA detector. The mobile phase consisted of 33% methanol and 67% water containing 0.1% formic acid, and the flow rate was 0.6 mL/min. The  $\text{H}_2\text{O}_2$  concentration was determined through the peroxytitanic acid colorimetric method reported in the previous study (Cleveland et al., 2014). The COD,  $\text{NH}_4^+$ ,  $\text{NO}_3^-$ , and Fe concentrations in the aqueous phase were evaluated by commercial test kits from Hach company (Loveland, CO, USA).

## 4.3 Results and discussion

### 4.3.1 Effects of acid washing and impregnation ratio (g FeCl<sub>3</sub>/g BG) on the iron activated BCs performance based on the adsorption and heterogeneous Fenton oxidation ability of SMX

Acid washing can remove some impurities and minerals such as metal salts in BCs, which can expose more carbon surface for contaminants attachment (Chen et al., 2018; Choi & Kan, 2019). As seen in Figure S4.1, acid washing resulted in higher SMX adsorption and lower SMX Fenton oxidation ability of iron activated BC (impregnation ratio of 2). After acid washing, the SMX removal efficiency by Fenton oxidation was reduced from 99.99% to 46.34%, however, the SMX removal efficiency by adsorption was improved from 20.51% and 27.72%. The previous study indicated that BC surface area exhibited positive correlation with SMX adsorption ability (Jang et al., 2018c). In this study, Figure S4.2 shows that surface area was significantly improved from 835.1 to 1013.4 m<sup>2</sup>/g after acid washing, which is because that minerals and impurities might block the BC pores and were eliminated by acid washing. Moreover, iron compounds are significant for Fenton oxidation, which can react with H<sub>2</sub>O<sub>2</sub> to produce ·OH radicals for SMX oxidation. However, acid washing can remove some iron compounds in BC and caused the decrease of total iron content from 30.0% to 5.8% (Figure S4.2), which explains the lower Fenton oxidation ability. Therefore, considering that adsorption only accounted for a small portion of total SMX removal and Fenton oxidation ability was significantly decreased, acid washing was not recommended for the preparation of iron activated BCs.

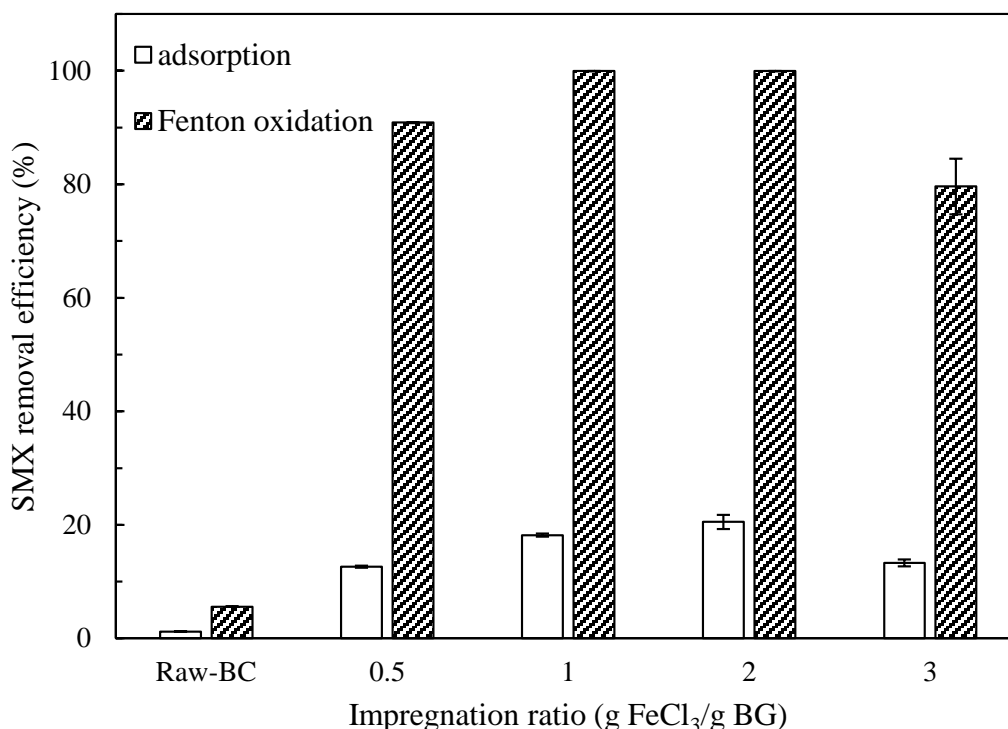


**Figure 4.1.** Effect of FeCl<sub>3</sub>/BG impregnation ratio on the performance of iron activated BCs for the adsorption and Fenton oxidation of SMX. Adsorption conditions: 0.01 g of BC, 100 mL of 100 mg/L SMX, initial pH of 3, temperature of 20 °C, and 24 h. Fenton oxidation conditions: 0.01 g of BC, 200 mg/L H<sub>2</sub>O<sub>2</sub>, 100 mL of 100 mg/L SMX, initial pH of 3, temperature of 20 °C, and 24 h.

Effects of FeCl<sub>3</sub>/BG impregnation ratio on the adsorption and Fenton oxidation ability of iron activated BCs (without acid washing) for SMX were displayed in Figure 4.1. Compared to Raw-BC (without iron activation), iron activated BCs with various impregnation ratios (0.5-3) showed significantly increased SMX adsorption and Fenton oxidation ability. This is because that FeCl<sub>3</sub> activation resulted in the increase of surface area, which could provide more activate sites for adsorption, and attachment of various iron compounds, which could serve as catalysts for heterogeneous Fenton oxidation (mentioned in the section 3.2). Interestingly, in this study, Raw-BC without iron attachment also exhibited SMX Fenton oxidation ability while it was relatively

weak. The reason is probably that the pyrolysis of feedstocks containing some organic compounds and minerals resulted in the formation of persistent free radicals, which could also activate the  $\text{H}_2\text{O}_2$  to produce  $\cdot\text{OH}$  radicals to oxidize organic contaminants (Huang et al., 2019). The optimal impregnation ratio based on the SMX adsorption ability was observed at 2. Moreover, both impregnation ratios of 1 and 2 showed the similar and highest SMX Fenton oxidation ability. In addition, COD removal efficiency (an indicator of removal of SMX, intermediates, and products) by Fenton oxidation was also the highest at the impregnation ratio of 2 (Figure S4.3). However, when the impregnation ratio was improved from 2 to 3, the performance of iron activated BC for SMX treatment was markedly decreased. The possible reasons have been described in the previous studies, which indicated that excessive iron loading resulted in the hyper-activation, which could cause the blockage of pores and aggregation of iron compounds (Yang et al., 2016a; Yang et al., 2016b). Therefore, iron activated BC at the impregnation ratio of 2 without acid washing, denoted as FA-BC, was selected for further characterization and experiments of SMX treatment in this study.

#### **4.3.2 Characterization of FA-BC**

The surface properties of FA-BC were evaluated via the XPS analysis. The XPS patterns displayed in Figure 2a indicated the presence of elements C, O, and Fe in FA-BC. In the C 1s spectrum (Figure 2b), the binding energy at 284.6 eV was ascribed to the groups of C-C/C=C, which can provide  $\pi$  electrons for the formation of  $\pi$ - $\pi$  interaction between FA-BC and organic contaminants (Zhang et al., 2018b). In addition, the binding energies at 285.8 and 286.8 eV were attributed to the groups of C-O and C=O, in which O-containing functional groups can participate in the generation of hydrogen bonding between FA-BC and organic contaminants (Zhang et al., 2018b). For the Fe 2p spectrum (Figure 2c), the peaks at 710.3 and 724.2 eV suggested the presence of  $\alpha$ -



Fe<sub>2</sub>O<sub>3</sub> (Bombuwala Dewage et al., 2018; Grosvenor et al., 2004). Moreover, the peaks with binding energies of 712.4, 713.9, and 725.0 eV were assigned to Fe<sub>3</sub>O<sub>4</sub> (Hu et al., 2011; Xu et al., 2019a). Small peaks at 707.0 and 720.2 eV corresponded to Fe<sup>0</sup> (Zhang et al., 2020). All Fe<sup>0</sup>, α-Fe<sub>2</sub>O<sub>3</sub>, and Fe<sub>3</sub>O<sub>4</sub> can be used as catalysts for the Fenton oxidation of contaminants. As for the O 1s spectrum (Figure 2d), two peaks at 533.8 and 531.8 eV were associated with O-containing functional groups of C-O-C and -OH/C=O (Chen et al., 2020; Tu et al., 2020b; Yi et al., 2020). The other peak at 530.2 eV was attributed to the group of Fe-O, which supported the analysis of Fe 2p spectrum (Chen et al., 2020).

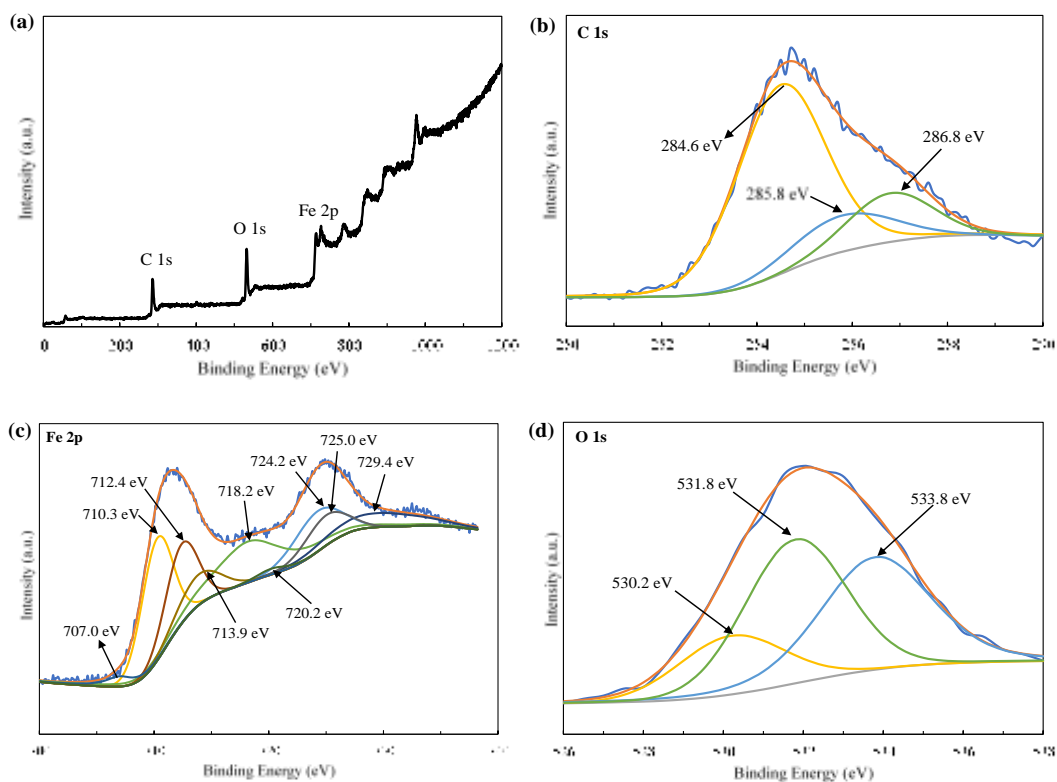


**Figure 4.2.** XPS spectra of FA-BC: full survey (a), C 1s (b), Fe 2p (c), and O 1s (d).

The XRD pattern of FA-BC, displayed in Figure S4.4, suggested the presence of  $\alpha$ -Fe<sub>2</sub>O<sub>3</sub> ( $2\theta = 33.3^\circ$  and  $62.6^\circ$ ), Fe<sub>3</sub>O<sub>4</sub> ( $2\theta = 30.4^\circ$ ,  $35.7^\circ$ ,  $43.3^\circ$ , and  $57.2^\circ$ ) and Fe<sup>0</sup> ( $2\theta = 44.8^\circ$ ) (Bombuwala Dewage et al., 2018; Su et al., 2013; Zhang et al., 2011c). In addition, the analysis of FT-IR spectrum in Fig.S5 also implied that the formation of C=C ( $1552\text{ cm}^{-1}$ ), C $\equiv$ C ( $2122\text{ cm}^{-1}$ ), C-O ( $1052\text{ cm}^{-1}$ ), and Fe-O ( $557\text{ cm}^{-1}$ ) groups in FA-BC (Ahmed et al., 2017a; Ahmed et al., 2017c; Yi et al., 2020; Zhu et al., 2014b). Both results from XRD and FT-IR analyses are consistent with that from the XPS study. The previous study has pointed out that carbon could react with Fe<sub>2</sub>O<sub>3</sub>, resulting in the formation of Fe<sup>0</sup>, Fe<sub>3</sub>O<sub>4</sub> and gases (CO and CO<sub>2</sub>), during the FeCl<sub>3</sub> activation at high temperature (Zhang et al., 2015; Zhu et al., 2016). Moreover, from the analysis of BC properties (Table S4.1), FA-BC ( $835.10\text{ m}^2/\text{g}$ ) exhibited higher surface area than BC800 ( $85.82\text{ m}^2/\text{g}$ ), indicating that FeCl<sub>3</sub> activation favored the improvement of BC surface area, which is due to the pore enlargement resulting from the release of produced gases (CO and CO<sub>2</sub>). Table S4.1 also indicates that, compared to BC800 without activation, the ratios of H/C, O/C, and (N+O)/C of FA-BC were significantly reduced, implying that FeCl<sub>3</sub> activation can increase the BC hydrophobicity, which favored the hydrophobic interaction between FA-BC and SMX. Additionally, the presence of Fe<sub>3</sub>O<sub>4</sub> in FA-BC enabled the FA-BC to possess the magnetic ability. Hence, the FA-BC could be easily separated from the aqueous solution by the magnet (Figure S4.6), which would reduce the separation cost during the application in the treatment of real wastewater.

### 4.3.3 SMX adsorption performance on FA-BC

In the heterogeneous Fenton reaction with the coexistence of adsorption and catalysis, the adsorption study is significant since absorbed contaminant molecules are more easily attacked by hydroxyl radicals produced on the surface of catalyst (Gu et al., 2013). Figure 4.3a indicates that SMX adsorption on FA-BC was a fast process and about 80% of  $Q_e$  (adsorption capacity at equilibrium time) was achieved within 2 h. Based on the correlation coefficient ( $R^2$ ), Pseudo-second order (PSO) model better fitted to adsorption kinetics data than Pseudo-first model (PFO) model (Figure 4.3a and Table S4.2), suggesting that chemical adsorption mainly controlled the adsorption process (Yang et al., 2016b). In addition, PFO model also exhibited high  $R^2$  (0.9558), implying that physical adsorption also participated in the SMX adsorption on FA-BC (Yang et al., 2016b). For the isotherm study, Langmuir and Freundlich models were applied to fit the experimental data. As shown in Figure 4.3b and Table S4.3, Langmuir model showed higher  $R^2$  than Freundlich model, implying that SMX adsorption onto FA-BC was mainly monolayer adsorption. Additionally, the heterogeneity  $1/n_f$  (0.13) was in the range of 0 to 1, suggesting that the adsorption process was favorable (Tang et al., 2018). According to the Langmuir model, the maximum adsorption capacity ( $Q_m$ ) of SMX on FA-BC was 194.58 mg/g, which was higher than various carbonaceous materials including activated carbon, carbon nanotube, and BCs from other sources (Table S2.1, Chapter II), suggesting the great potential of FA-BC as the adsorbent for the treatment of SMX in water. Furthermore, based on the previous studies, hydrophobic, hydrogen bonding, and  $\pi$ - $\pi$  interactions were main adsorption mechanisms for SMX on FA-BC when SMX molecules were neutrally charged at pH 3 used in this study (Choi & Kan, 2019; Jang et al., 2018c; Zeng & Kan, 2020a).

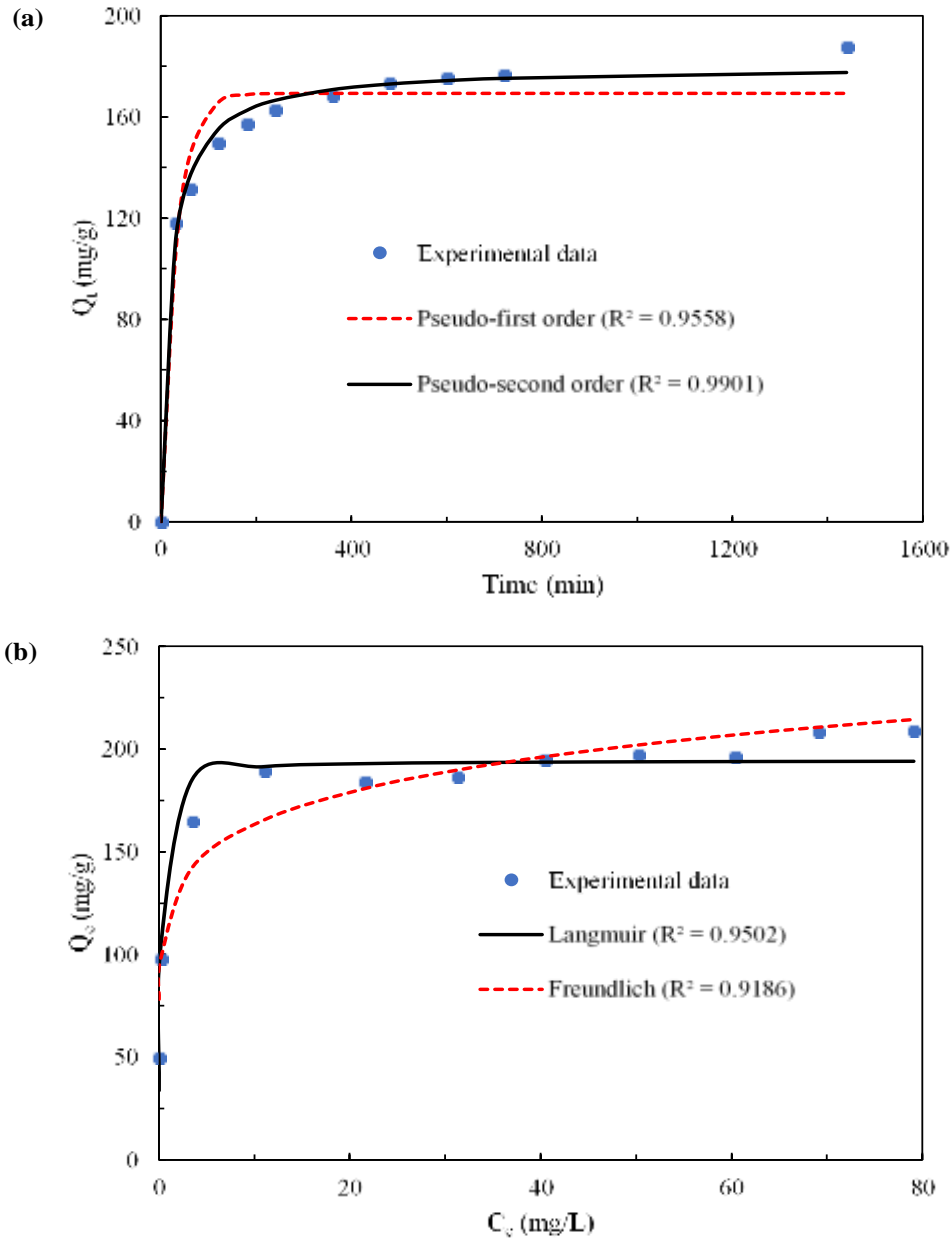


**Figure 4.3.** (a) Adsorption kinetics for SMX on FA-BC. Conditions: 0.01 g of FA-BC, 100 mL of 100 mg/L SMX, temperature of 20°C, and initial pH of 3. (b) Adsorption isotherm for SMX on FA-BC. Conditions: 0.01 g of FA-BC, 100 mL of 5-100 mg/L SMX, initial pH of 3, temperature of 20°C, and 2 d.

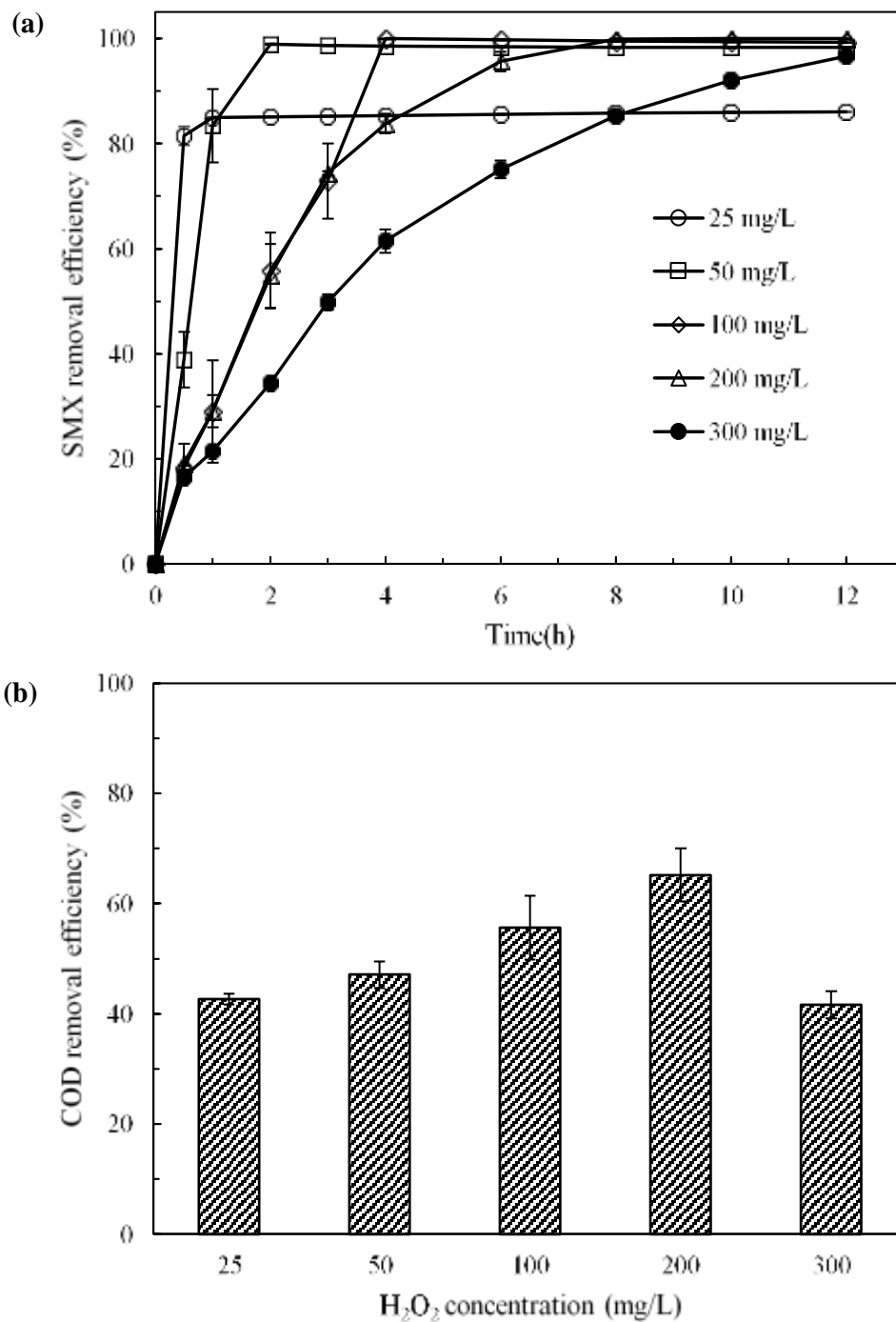


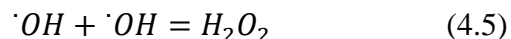
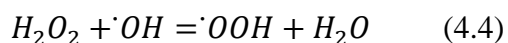
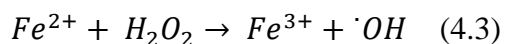
**Figure 4.4.** Effect of H<sub>2</sub>O<sub>2</sub> concentration on the removal efficiency of SMX and COD. Conditions: 0.01 g of FA-BC, 100 mL of 100 mg/L SMX, initial pH of 3, temperature of 20°C, and reaction time of 12 h.

#### 4.3.4 Effect of initial pH and H<sub>2</sub>O<sub>2</sub> concentration on Fenton oxidation of SMX

The effect of initial pH on the Fenton oxidation of SMX was evaluated by varying the initial pH from 3 to 7. As displayed in Figure S4.7. The optimal pH for the Fenton oxidation of SMX using FA-BC was 3 while the SMX removal efficiency was significantly decreased from pH 3 to 7. The previous studies have indicated that the increase of pH resulted in the decrease of production of  $\cdot\text{OH}$  radicals, which was due to the generation of ferric hydroxide precipitate on the surface of FA-BC and instability of H<sub>2</sub>O<sub>2</sub> at high pH (Li et al., 2019; Rubeena et al., 2018). In addition, Rubeena et al. (2018) also reported that the removal efficiency of acid red 1 dye was markedly reduced from 97.6% to 41.3% with the increase of pH from 3 to 9 using iron amended rice husk-derived BC as the catalyst of heterogeneous Fenton oxidation. Cleveland et al. (2014) found that the optimum pH was 3 for the heterogeneous Fenton oxidation of BPA by the Fe<sub>3</sub>O<sub>4</sub>/carbon nanotube. Therefore, further experiments about Fenton oxidation of SMX were performed at pH 3 in this study.

The H<sub>2</sub>O<sub>2</sub> concentration can affect the treatment efficiency and operation costs during the process of Fenton oxidation (Cleveland et al., 2014). In this study, the SMX and COD removal efficiencies under various H<sub>2</sub>O<sub>2</sub> concentrations were shown in Figure 4.4. It could be seen that the SMX removal efficiency was improved from 86.06% to 98.31% within 12 h when the H<sub>2</sub>O<sub>2</sub> concentration was increased from 25 to 50 mg/L. As shown in Eq. (3), the increase of H<sub>2</sub>O<sub>2</sub> concentration was beneficial for the generation of more  $\cdot\text{OH}$  radicals, which could attack more SMX molecules. Figure 4.4a also shows that 50-200 mg/L of H<sub>2</sub>O<sub>2</sub> caused the almost complete removal of SMX (98.31%-99.94%). However, with the increase of H<sub>2</sub>O<sub>2</sub> concentration from 50 to 200 mg/L, the COD removal efficiency was significantly improved from 47.10% to 65.19% (Figure 4.4b), which is probably because more  $\cdot\text{OH}$  radicals resulted in the complete oxidation of more intermediates and products to inorganic compounds. Additionally, the improvement of H<sub>2</sub>O<sub>2</sub>

concentration from 200 to 300 mg/L led to the decrease of SMX and COD removal efficiencies from 99.94% and 65.18% to 96.63% and 41.64% (Figure 4.4). These results are consistent with the previous reports indicating that high H<sub>2</sub>O<sub>2</sub> concentration showed negative effect on the Fenton oxidation efficiency (Ge et al., 2019; Hu et al., 2011; Rubeena et al., 2018). This is because excess H<sub>2</sub>O<sub>2</sub> would react with ·OH radicals to produce the less reactive perhydroxyl radicals (·OOH) (Eq. (4)) (Ge et al., 2019; Rubeena et al., 2018). In addition, high amount of ·OH radicals resulting from high H<sub>2</sub>O<sub>2</sub> concentration could be recombined as the Eq. (5), which could reduce the efficiency of Fenton oxidation (Rubeena et al., 2018). Hence, 200 mg/L was considered as the optimal H<sub>2</sub>O<sub>2</sub> concentration for Fenton oxidation of SMX in this study.



#### 4.3.5 Effect of temperature on Fenton oxidation of SMX

The reaction temperature is an important factor in the chemical reaction process. The effect of temperature on SMX treatment efficiency by the heterogeneous Fenton oxidation of FA-BC was evaluated under various temperatures (20-50 °C). Figure 4.5a indicates that all reaction temperatures from 20 to 50 °C resulted in the nearly complete removal of SMX (more than 99%) within 12 h. However, SMX oxidation rate was dramatically increased from 0.4610 h<sup>-1</sup> to 1.0424 h<sup>-1</sup> with the improvement of reaction temperature from 20 °C to 50 °C (Table 4.1). This is because the increase of reaction temperature could increase the collision frequency between SMX molecules and ·OH radicals (Chen et al., 2020; Rubeena et al., 2018).

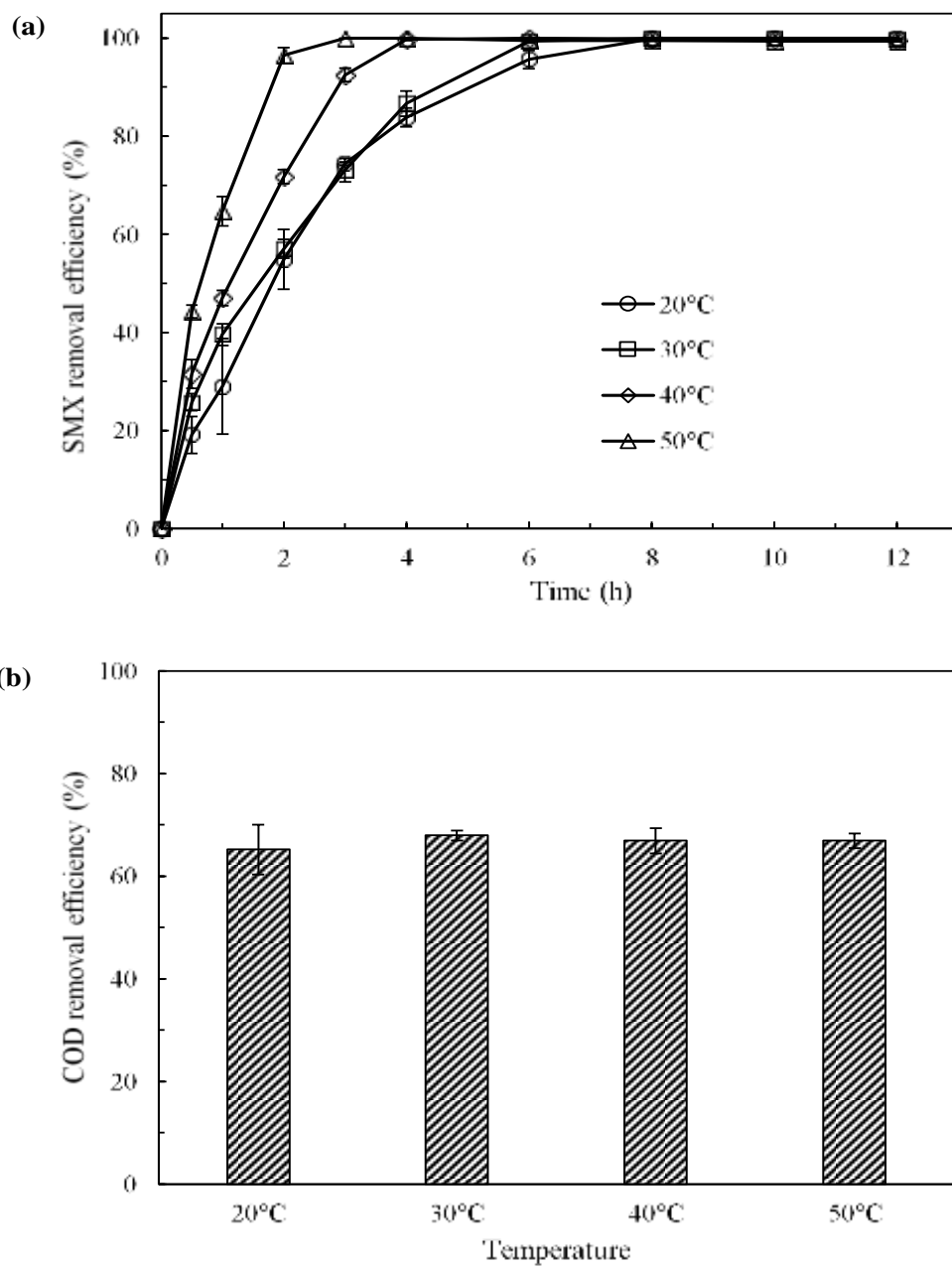


**Figure 4.** Effect of reaction temperature on the removal efficiency of SMX and COD. Conditions: 0.01 g of FA-BC, 100 mL of 100 mg/L SMX, initial pH of 3, 200 mg/L H<sub>2</sub>O<sub>2</sub>, and reaction time of 12 h.



Moreover, as displayed in Table 4.1, H<sub>2</sub>O<sub>2</sub> decomposition rate was also markedly improved from 0.1359 h<sup>-1</sup> to 0.4792 h<sup>-1</sup> with the increase in reaction temperature from 20 °C to 50 °C, indicating that the increase of temperature resulted in the increase of reaction rate in Eq. (3) and production of more ·OH radicals, which caused the rapid oxidation of SMX at high temperature. Additionally, the COD removal efficiency showed no significant difference when the reaction temperature was changed from 20 °C to 50 °C. Therefore, in this study, the increase of reaction temperature mainly favored the increase of SMX oxidation rate and reduction of reaction time. Similar conclusions are also indicated in the previous studies. For example, Chen et al. (2020) used the Fe<sub>2</sub>O<sub>3</sub>-TiO<sub>2</sub> amended BC as the catalyst for the heterogeneous Fenton oxidation of methylene blue, and found that high temperature favored the diffusion of H<sub>2</sub>O<sub>2</sub> and methylene blue molecules, and the increase of temperature from 30 °C to 50 °C caused the enhancement of oxidation rate by a factor of 1.32.

**Table 4.1** SMX oxidation rate and H<sub>2</sub>O<sub>2</sub> decomposition rate under various temperatures. Conditions: 0.01 g of FA-BC, 100 mL of 100 mg/L SMX, initial pH of 3, 200 mg/L H<sub>2</sub>O<sub>2</sub>, and reaction time of 12 h.

Temperature	SMX oxidation rate (h <sup>-1</sup> )	H <sub>2</sub> O <sub>2</sub> decomposition rate (h <sup>-1</sup> )
20 °C	0.4610	0.1359
30 °C	0.4741	0.1972
40 °C	0.6216	0.2907
50 °C	1.0424	0.4792

In addition, the activation energy E<sub>a</sub> (J/mol) was determined based on the Arrhenius equation as shown in the following equation (Ge et al., 2019):

$$\ln k = \ln A - \frac{E_a}{RT} \quad (4.6)$$

where  $k$  ( $\text{h}^{-1}$ ) represents the reaction rate constant of SMX oxidation,  $A$  represents the Arrhenius factor ( $\text{g}/\text{mg}\cdot\text{min}$ ),  $R$  ( $8.314 \text{ J}/\text{mol}\cdot\text{K}$ ) represents the ideal gas constant, and  $T$  ( $\text{K}$ ) represents the absolute temperature. In this study, the  $E_a$  calculated from the Arrhenius equation was  $21.13 \text{ kJ}/\text{mol}$ , which was higher than common  $E_a$  values ( $10\text{-}13 \text{ kJ}/\text{mol}$ ) in the reaction controlled by the molecular diffusion (Tang & Wang, 2018). This result indicated that SMX removal by the heterogeneous Fenton oxidation using FA-BC was mainly controlled by the chemical reaction, not the diffusion of SMX molecules (Tang & Wang, 2018).

#### **4.3.6 Reusability and stability of FA-BC for the heterogeneous Fenton oxidation of SMX**

The analysis of reusability and stability of FA-BC was carried out through 3 successive cycles of heterogeneous Fenton oxidation of SMX. As shown in Figure 4.6, SMX removal efficiency was 99.70% after the first cycle, and 89.58% of removal efficiency was still achieved after the third cycle. In addition, with 3 successive cycles, the COD removal efficiency was reduced from 65.19% to 30.38%. The decrease of removal efficiency was probably because the accumulation of intermediates and products on the surface of FA-BC, which might be attached on active catalytic sites of FA-BC (Cleveland et al., 2014). In addition, as displayed in Table S4.4, a small amount of iron in FA-BC was released into the reaction solution during the Fenton oxidation process, which could decrease the catalytic activity of FA-BC. However, iron concentrations in the reaction solution were very low (less than  $2 \text{ mg}/\text{L}$ ), which was not enough for homogeneous Fenton oxidation (Nidheesh et al., 2013; Rubeena et al., 2018). Therefore, SMX oxidation was mainly attributed to the heterogeneous Fenton oxidation by FA-BC.

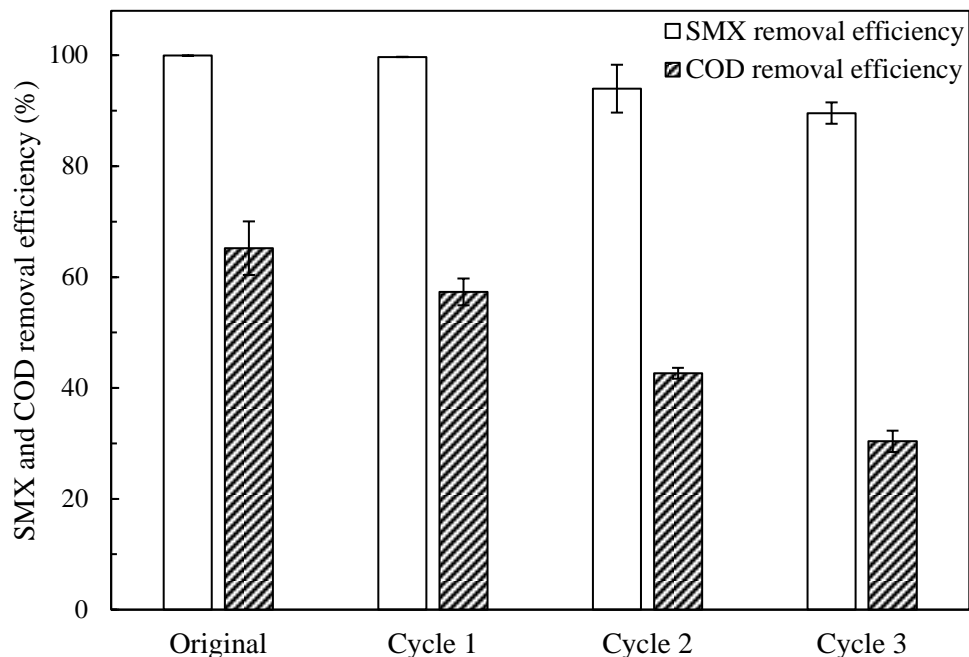


**Figure 4.6.** Reusability of FA-BC for Fenton oxidation of SMX. Conditions: 0.01 g of FA-BC, 100 mL of 100 mg/L SMX, initial pH of 3, 200 mg/L H<sub>2</sub>O<sub>2</sub>, and reaction temperature of 20 °C.

Additionally, Figure S4.4 shows that the XRD pattern of FA-BC after Fenton oxidation of SMX was similar to original FA-BC while peak intensities slightly decreased, indicating that the structure of FA-BC was not significantly changed after Fenton oxidation. Besides, the peak of Fe-O group in FA-BC from the FT-IR spectrum exhibited no significant change after Fenton oxidation (Figure S4.5). Hence, considering the excellent stability and recyclability, FA-BC showed great potential for the treatment of SMX contaminated wastewater by Fenton oxidation.

#### 4.3.7 SMX removal mechanisms of FA-BC

The ethanol has been considered as a scavenger for ·OH radicals (Cleveland et al., 2014). As shown in Figure S4.8, the addition of 1 M ethanol resulted in the significant reduction of SMX removal

efficiency from 99.94% to 17.13%, indicating that  $\cdot\text{OH}$  was the major radical participating in the Fenton oxidation of SMX by FA-BC.

The detailed degradation pathway of SMX by  $\cdot\text{OH}$  radicals from Fenton oxidation has been proposed in previous studies (Du et al., 2017; Liu et al., 2018b; Wang & Wang, 2017). Therefore, the present study did not focus on the detailed analysis of intermediates and products. Figure S4.9 shows the SMX degradation pathway by Fenton oxidation reported by Du et al. (2017). 2-Aminophenol, one of important intermediates of Fenton oxidation of SMX, was generated via the electrophilic replacement of aromatic ring followed by the cleavage of -C-S- and -S-N- bonds under the attack of  $\cdot\text{OH}$  radicals (Du et al., 2017). HPLC chromatograms in Figure S4.10 indicate that 2-Aminophenol concentration was firstly increased and then decreased with the increase of reaction time, suggesting that longer reaction time resulted in the more complete oxidation of intermediates. In addition, Figure S4.11 shows that the increase of  $\text{H}_2\text{O}_2$  concentration resulted in the decrease of concentration of 2-Aminophenol, indicating that higher  $\text{H}_2\text{O}_2$  concentration enhanced the conversion of intermediates to final products. Inorganic ions ( $\text{NH}_4^+$  and  $\text{NO}_3^-$ ) are major final products from Fenton oxidation of SMX (Figure S4.9). The change of concentrations of  $\text{NH}_4^+$  and  $\text{NO}_3^-$  in the reaction solution during the Fenton oxidation of SMX by FA-BC are shown in Figure S4.12. The concentrations of  $\text{NH}_4^+$  and  $\text{NO}_3^-$  increased in the Fenton oxidation process and 6.15 mg/L of  $\text{NH}_4^+\text{-N}$  and 2.81 mg/L of  $\text{NO}_3^-\text{-N}$  were detected after reaction of 12 h, implying that nitrogen in SMX were primarily transformed to ammonium after Fenton oxidation. This result supports the previous study showing the higher concentration of  $\text{NH}_4^+$  than that of  $\text{NO}_3^-$  after Fenton oxidation of SMX (Liu et al., 2018b).

In summary, as shown in Figure 4.7, FA-BC with high surface area could absorb SMX molecules. Meanwhile,  $\cdot\text{OH}$  radicals, generated from the reaction between  $\text{H}_2\text{O}_2$  and iron compounds, would

attack absorbed SMX molecules on the surface of FA-BC and convert them into intermediates and end products.

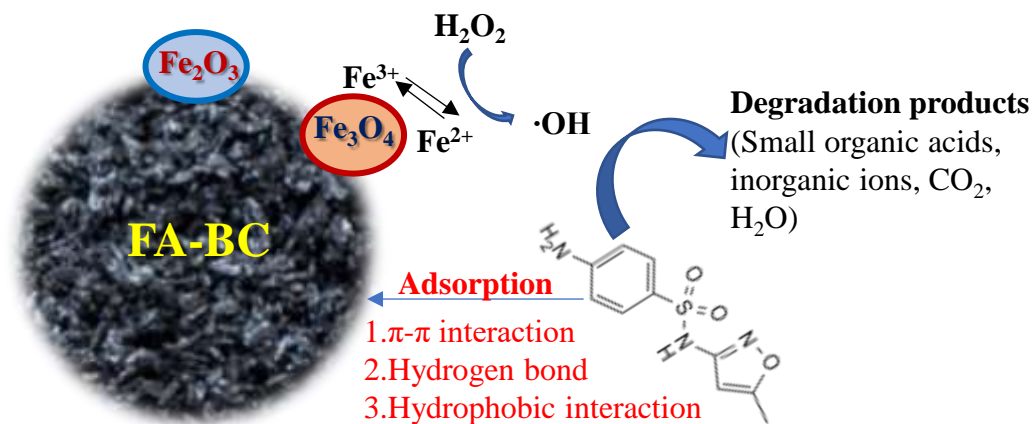


**Figure 4.7.** SMX removal mechanisms of FA-BC via adsorption and Fenton oxidation.

#### 4.3.8 Application in real wastewater

Generally, real wastewater has complex compositions, which can affect the processes of adsorption and Fenton oxidation and reduce the treatment efficiency of contaminants (Xu et al., 2019a). In this study, Fenton oxidation of SMX by FA-BC was also carried out in real wastewater from the lagoon in the dairy farm (Stephenville, TX, USA). As displayed in Figure 4.8, compared to DI water, SMX removal efficiency in wastewater was decreased from 99.94% to 82.65% within 12 h under the same reaction conditions. This is because that lagoon wastewater contains some organic and inorganic matters (Table S2.7, Chapter II), which could consume  $\cdot\text{OH}$  radicals.

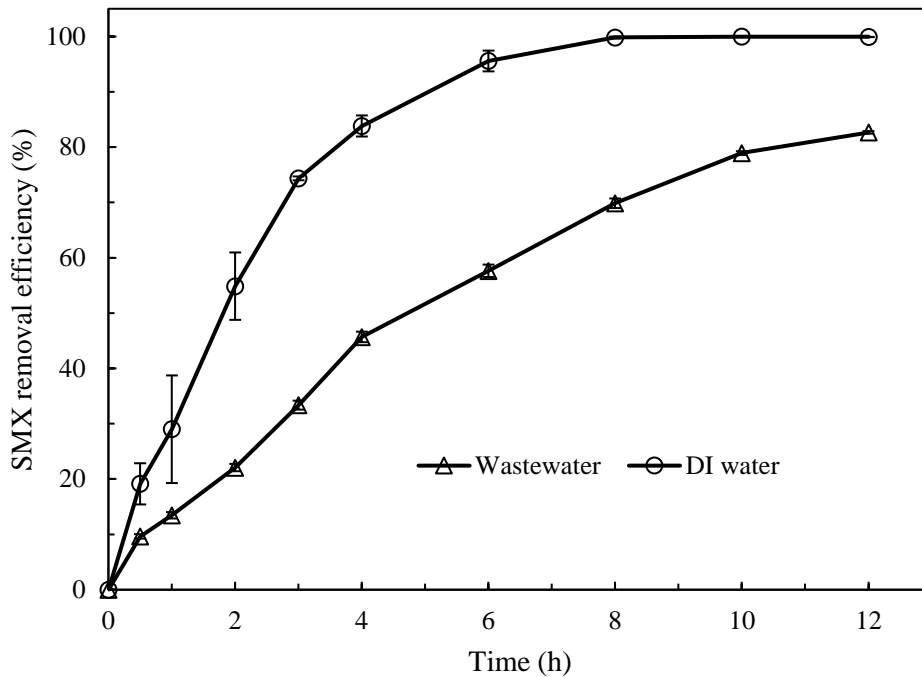


**Figure 4.8.** Fenton oxidation of SMX by FA-BC in DI water and real wastewater. Conditions: 0.01 g of FA-BC, 100 mL of 100 mg/L SMX, initial pH of 3, 200 mg/L H<sub>2</sub>O<sub>2</sub>, and reaction temperature of 20 °C.

#### 4.4 Conclusions

FA-BC was successfully prepared via one-step activation/pyrolysis of bermudagrass (BG). FA-BC at the FeCl<sub>3</sub> to BG mass ratio of 2 showed excellent surface area (835 m<sup>2</sup>/g) and adsorption capacity (195 mg/g). The optimal pH and H<sub>2</sub>O<sub>2</sub> concentration for heterogeneous Fenton oxidation of SMX were 3 and 200 mg/L, respectively. The increase of reaction temperature from 20 °C to 50 °C resulted in the improvement of SMX oxidation rate from 0.46 h<sup>-1</sup> and 1.04 h<sup>-1</sup>. SMX and COD removal efficiencies were 99.94% and 65.19%, respectively, under the optimal conditions. ·OH radicals mainly participated in the process of Fenton oxidation of SMX. After 3 cycles, 89.58% of SMX removal efficiency via Fenton oxidation was still achieved. This study confirms that FA-

BC has great potential for treatment of SMX contaminated wastewater through adsorption and Fenton oxidation.

**CHAPTER V**  
**CHARACTERIZATION, MECHANISM, AND REGENERATION OF IRON**  
**ACTIVATED BERMUDAGRASS-DERIVED BIOCHAR FOR MICROCYSTIN-LR**  
**ADSORPTION**

### **5.1 Introduction**

Microcystins (MCs), produced from cyanobacteria during the algal blooms in eutrophic waters, are the most abundant and typical cyanotoxins in nature waters (Pavagadhi et al., 2013). MCs can make the aquatic organisms subjected to acute liver failure, cancer, and internal hemorrhage (Liu et al., 2018a). Microcystin-LR (MC-LR), one of the most toxic MCs, is frequently detected in water samples, which can create a great risk to the ecosystem and impair the human health by the food-chain accumulation and drinking water (Liu et al., 2018a; Zhang et al., 2011a). Based on the significant environmental impacts, the World Health Organization (WHO) has stipulated that the safe concentration of MC-LR in drinking water is below 1 µg/L (Park et al., 2018a). In addition, MC-LR exhibits good chemical stability, large molecule size, water-soluble ability, and complex structure (He et al., 2020). Therefore, the traditional technologies of wastewater treatment, including flocculation, chlorination, and coagulation, cannot effectively eliminate the MC-LR from water (He et al., 2020; Pavagadhi et al., 2013).

To date, many techniques have been developed for the treatment of wastewater polluted by the MC-LR, including ozonation, biofiltration, TiO<sub>2</sub> photocatalysis, Fenton oxidation, photo-Fenton oxidation, zero-valent iron, and UV/H<sub>2</sub>O<sub>2</sub> (Bandala et al., 2004; Eke et al., 2018; He et al., 2012; Pinho et al., 2015; Wang et al., 2016). However, these methods usually require the input of a large number of chemicals and complex instruments, and also some toxic by-products might be formed



during the treatment process. Compared to the above-mentioned techniques, adsorption has been considered as an effective, quick, simply operated, and nontoxic method for the elimination of organic contaminants from water (Jang et al., 2018b). So far, various adsorbents have been prepared and applied for the adsorption of MC-LR in water, such as graphene oxide, carbon nanotube, activated carbon, iron oxides, Fe<sub>3</sub>O<sub>4</sub>/chitosan, and kaolinite (He et al., 2020; Huang et al., 2007; Lee & Walker, 2011; Liu et al., 2019; Pavagadhi et al., 2013; Yan et al., 2006). Nonetheless, high cost for preparation and regeneration and potential environmental risks after disposal still limit their practical applications for MC-LR adsorption. Therefore, it is urgent to find a cost-effective and environmentally friendly adsorbent to solve the problem of MC-LR contamination.

Biochar (BC), produced from the pyrolysis of agro-industrial wastes under the oxygen-limited conditions, has been considered as a promising adsorbent for the treatment of various contaminants due to the cheaper feedstock and better environmental friendliness (Jang & Kan, 2019c; Jang et al., 2018b). However, the studies about MC-LR adsorption onto BCs were quite limited (Li et al., 2018; Li et al., 2014a; Liu et al., 2018a). Li et al. (2014a) reported that wood chips-derived BCs could effectively adsorb the MC-LR with the adsorption capacity of 0.926-4.197 mg/g via the electrostatic attraction and hydrogen bonding, and surface functional groups were significant for MC-LR adsorption. Li et al. (2018) found that chicken manure-derived BCs showed better performance for MC-LR adsorption than sawdust-derived BCs and maize straw-derived BCs due to the higher ash content, mesopore volume, and surface functionality. Liu et al. (2018a) used the giant reed-derived BCs with various pyrolysis temperatures for MC-LR adsorption. They found that the increase of pyrolysis temperature resulted in the increase of MC-LR adsorption capacity owing to the increase of mesopores, and minerals in the high-temperature BC were very important

for MC-LR adsorption. However, the above-mentioned studies only focused on the MC-LR adsorption onto pristine BCs. They did not conduct the regeneration tests of MC-LR spent BCs and apply the BCs in the treatment of real wastewater, which are usually important studies for the practical application of adsorbents.

For improving the surface area, pore structures, and surface functional groups, many studies have focused on the BCs activation to improve the adsorption capacity and functionality of BCs (Braghiroli et al., 2018; Jang et al., 2018b). Activated BCs have been proved to have excellent adsorption performance for various contaminants (Braghiroli et al., 2018). However, to our knowledge, there are still no reports about large molecule MC-LR adsorption onto activated BCs. Compared to other common activators (NaOH, KOH, ZnCl<sub>2</sub>, and H<sub>3</sub>PO<sub>4</sub>), FeCl<sub>3</sub> exhibited lower toxicity and more environmental friendliness (Xu et al., 2019b). In addition, after FeCl<sub>3</sub> activation, BCs can be attached with magnetic particles (iron oxides) and magnetically separated after adsorption, which can solve the problem of separation of powder BCs (Yang et al., 2016a). For example, Yang et al. (2016a) reported that, after FeCl<sub>3</sub> activation of sawdust, Fe<sub>3</sub>O<sub>4</sub> particles were attached onto sawdust-derived BC. Moreover, the surface area and oxygen-containing functional groups were significantly enhanced, resulting in the higher mercury removal performance. Zhu et al. (2014b) used the FeCl<sub>3</sub> to activate the hydrochar and found that FeCl<sub>3</sub> activation could result in the formation of magnetic BCs and improved the surface area from 7.16 to 349 m<sup>2</sup>/g.

In this study, novel iron (FeCl<sub>3</sub>) activated biochars (FA-BCs) were prepared via one-step pyrolysis and activation of FeCl<sub>3</sub>-laden BG. The FA-BC was characterized and applied for MC-LR adsorption. Based on the studies of pH effect, kinetics, isotherm, and thermodynamics, the detailed adsorption mechanisms of MC-LR adsorption onto FA-BC were proposed. In addition, various

regeneration methods were applied to reuse the MC-LR spent FA-BC. Furthermore, the FA-BC was applied for the treatment of MC-LR from real lake water.

## **5.2 Materials and methods**

### **5.2.1 Materials**

Microcystin-LR (MC-LR,  $C_{48}H_{72}N_{10}O_{12}$ ) was acquired from Enzo Life Sciences (Farmingdale, NY, U.S.). The chemical structure of MC-LR was displayed in Figure S5.1. Ferric chloride ( $FeCl_3$ ), hydrogen peroxide ( $H_2O_2$ , 30%), ammonium persulfate, and all other chemicals used in the present study were purchased from Sigma-Aldrich (St.Louis, Missouri, U.S.) and of analytical grade. Bermudagrass (BG) was sourced from a local hay store (Stephenville, TX, U.S.)

### **5.2.2 Preparation and characterization of $FeCl_3$ -activated BCs**

Methods for preparation and characterization of  $FeCl_3$ -activated BCs were described in sec. 4.2.2 (Chapter IV).

### **5.2.3 Adsorption experiments**

For batch adsorption experiments, 0.004 g of BC was added into 100 mL of 500  $\mu g/L$  of MC-LR solution at pH 6 and 150 rpm with room temperature (20 °C) for 2 d. In our preliminary tests, the adsorption equilibrium for MC-LR onto BCs can be achieved within 2 d. In order to evaluate the effect of initial pH on the adsorption of MC-LR onto FA-BC, adsorption tests were performed at various pH values from 2 to 9. Except for the study of various initial pH, all of adsorption experiments in this study were carried out at pH 6 for practical application in real lake water or wastewater. The kinetic experiments were carried out via mixing 0.004 g of FA-BC with 100 mL of 500  $\mu g/L$  and 1000  $\mu g/L$  of MC-LR solution at pH 6, and the concentrations of MC-LR were measured at different time intervals. For the isotherm study, the batch experiments were conducted with 0.004 g of FA-BC and various concentrations of MC-LR solution (200-1000  $\mu g/L$ ) at pH 6

for 2 d. For the thermodynamic experiments, the mixtures of 0.004 g of FA-BC and 100 mL of 500 ug/L of MC-LR solution at pH 6 were shaken at various temperatures from 20 °C to 40 °C for 2 d.

After adsorption, the MC-LR concentrations in the aqueous phase were determined via an HPLC (Shimadzu LC-2030C, Shimadzu Co., Kyoto, JP) connected with a C18 column (Phenomenex Inc., Torrance, CA, USA) and a PDA (photo-diode array) detector. The mobile phase was the mixtures (55:45, v/v) of methanol and phosphate buffer (0.05 M, pH 2.5). The HPLC analysis was conducted at the wavelength of 238 nm with the flow rate of 0.75 mL/min.

The adsorption capacity ( $Q_e$ ) of BCs for MC-LR was calculated according to the following equation:

$$Q_e = \frac{(C_i - C_e) \times V}{W} \quad (5.1)$$

where  $C_i$  and  $C_e$  represent the initial and equilibrium MC-LR concentrations (mg/L) in the aqueous phase, respectively,  $V$  represents the MC-LR solution volume (L), and  $W$  represents the BC weight (g).

In the current study, six kinetic models and four isotherm models were applied to fit the experimental data (Table S2.2, Chapter II). The thermodynamic parameters were determined by thermodynamic equations (Table S2.2, Chapter II). In this study, the determination coefficients ( $R^2$ ) and the sum of squared error (SSE) were used to determine which model best fit the experimental data:

$$R^2 = 1 - \frac{\sum(Q_{exp} - Q_{cal})^2}{\sum(Q_{exp} - Q_{mean})^2} \quad (5.2)$$

$$SSE = \sqrt{\frac{\sum(Q_{exp} - Q_{cal})^2}{N}} \quad (5.3)$$

where  $Q_{\text{exp}}$ ,  $Q_{\text{cal}}$  and  $Q_{\text{mean}}$  are the experimental value, calculated value and mean of experimental value, respectively, and  $N$  is the number of measurements.

#### **5.2.4 Regeneration study**

The regeneration of MC-LR saturated FA-BC was evaluated. Firstly, 0.004 g of BC was saturated with 100 mL of 500  $\mu\text{g/L}$  of MC-LR solution at pH 6. Then, the MC-LR saturated FA-BC was magnetically separated via the magnet. For the regeneration by the thermal oxidation, the MC-LR saturated FA-BC was treated in the furnace at 300  $^{\circ}\text{C}$  for 3h. Four cycles of adsorption/thermal oxidation were carried out in this study. For the regeneration by the NaOH desorption, the MC-LR saturated FA-BC was mixed with 100 mL of 0.1 M and 1 M of NaOH solution for 24 h. For the regeneration by the Fenton oxidation, the MC-LR saturated FA-BC was stirred with 40 mL of 400 and 2000 mg/L of  $\text{H}_2\text{O}_2$  solution for 24 h. For the regeneration by the persulfate oxidation, the MC-LR saturated FA-BC was stirred with 40 mL of 200 and 400 mg/L of persulfate solution for 24 h. All readsorption experiments were performed under the same conditions with initial adsorption experiments.

#### **5.2.5 Application to the real lake water**

The lake water was obtained from the Proctor Lake (Dublin, TX, U.S.). The water quality parameters of lake water were displayed in Table S5.1. Before adsorption experiments, the lake water was filtered through filters (GF/C grade, 1.2  $\mu\text{m}$ ). For the first set of experiments, the lake water was spiked with 250  $\mu\text{g/L}$  of MC-LR. Then, 0.002 g of FA-BC was mixed with 100 mL of lake water for 2 d without the pH adjustment. For comparison, the relative adsorption experiments were also conducted in the DI water with the same conditions. For the second set of experiments, 0.004 g of FA-BC was stirred with 100 mL of lake water with various concentrations of MC-LR (5-50  $\mu\text{g/L}$ ) for 2 d.

## **5.3 Results and discussion**

### **5.3.1 Determination of optimal impregnation ratio (FeCl<sub>3</sub>/BG) for production of FA-BCs based on the adsorption capacity of MC-LR**

The impact of impregnation ratio (FeCl<sub>3</sub>/BG) on the adsorption capacity of MC-LR was displayed in Figure 5.1. Compared to the impregnation ratio of 0 (no activation), FeCl<sub>3</sub> activation resulted in the significant increase of MC-LR adsorption capacity. Moreover, with the increase of impregnation ratio from 0 to 2, the MC-LR adsorption capacity was significantly increased from 0.76 to 9.00 mg/g. This is due to that FeCl<sub>3</sub> activation caused the change of BC properties, which are beneficial for MC-LR adsorption (mentioned in section 3.2). However, the MC-LR adsorption capacity decreased with increasing in the impregnation ratio from 2 to 3. Excess ferric activator could result in the hyper-activation, which would reduce the surface area and damage the pore structure of BCs (Yang et al., 2016b). In addition, Yang et al. (2016a) also indicated that excess FeCl<sub>3</sub> activation caused the decrease of mercury adsorption onto FeCl<sub>3</sub> activated sawdust-derived BC due to the aggregation of iron oxides on the BC surface and the decrease of BC surface area. Therefore, in this study, FeCl<sub>3</sub> activated BC (FA-BC), produced from the optimal impregnation ratio of 2, was used for further characterization and adsorption experiments.

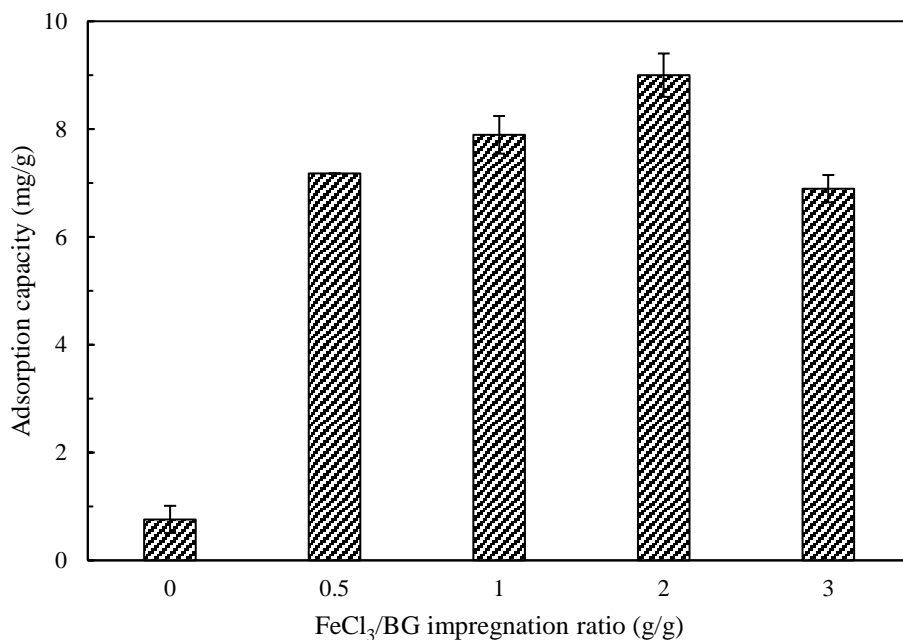


**Figure 5.1.** Effect of FeCl<sub>3</sub>/BG impregnation ratio on MC-LR adsorption capacity.

**Table 5.1** The physicochemical properties of feedstock and BCs.

	Elemental analysis (wt. %)				O/C	H/C	(N+O)/C	Proximate analysis (% dry basis)		
	C	H	O	N				FC	VC	Ash
BG	47.43	6.30	35.66	2.50	0.564	1.594	0.609	6.60	85.71	7.69
R-BC	68.02	1.58	12.94	3.37	0.143	0.279	0.185	67.92	18.04	14.04
FA-BC	55.34	0.90	8.17	1.93	0.111	0.195	0.141	43.16	23.18	33.66
	Mineral composition (wt. %)						BET surface area (m <sup>2</sup> /g)	pH <sub>pzc</sub>		
	P	K	Ca	Mg	Na	Fe				
BG	0.20	1.98	0.41	0.31	0.03	0.02	0.63			
R-BC	0.43	0.80	0.71	0.53	0.08	0.04	85.82	4.19		
FA-BC	0.45	0.02	0.38	0.13	0.00	30.0	835.10	7.36		

BG: Bermudagrass.

R-BC: Raw biochar; biochar produced at 800 °C with the FeCl<sub>3</sub>/BG impregnation ratio of 0.

FA-BC: FeCl<sub>3</sub> activated BC; biochar produced at 800 °C with the FeCl<sub>3</sub>/BG impregnation ratio of 2.

FC: Fixed carbon.

VC: Volatile carbon.

### 5.3.2 Characterization of BCs

The analyses of surface area, XRD, and XPS of R-BC and FA-BC was detailedly described in Sec. 4.3.2 (Chapter IV).

Compared to feedstock (BG), the contents of total carbon and fixed carbon of R-BC significantly increased from 47.43% and 6.60% to 68.02% and 67.92% due to the decomposition of volatile carbon and carbonization of BG at high temperature (Table 5.1). However, compared with R-BC, the carbon content of FA-BC decreased from 68.02% to 55.34% owing to the consumption of carbon via the reaction with iron oxide. In addition, the O and H contents of FA-BC were markedly lower than those of R-BC, indicating that FeCl<sub>3</sub> activation enhanced the decomposition of O and H. The reduction of ratios of H/C, O/C, and (O+N)/C suggests that the aromaticity, hydrophobicity, and polarity of BC increased after FeCl<sub>3</sub> activation (Jang et al., 2018b; Zhao et al., 2017). Furthermore, as shown in Figure S5.2, the pHPZC increased from 4.19 to 7.36 after FeCl<sub>3</sub> activation, implying that the acidic functional groups were reduced under the activation conditions.

The surface morphologies of BCs were investigated by obtaining SEM images. As shown in Figure S5.3, compared to R-BC, the surface of FA-BC was rougher and showed some small white particles, which could be attributed to metallic iron and iron oxides produced from FeCl<sub>3</sub> activation. In addition, the total iron content of FA-BC from the mineral composition analysis was 30.0%, while there was only 0.04% iron for R-BC, indicating again that iron was successfully attached onto the surface of FA-BC during the FeCl<sub>3</sub> activation (Table 5.1). Furthermore, from the EDX analysis (Figure S5.4), the iron content on the surface of FA-BC was 40.14%, which was higher than the total iron content of FA-BC, implying that there are more iron existing on the surface of than inside the FA-BC.



The functional groups of R-BC, FA-BC, and MC-LR saturated FA-BC were presented in Figure S5.5. After FeCl<sub>3</sub> activation, the new peak at 557 cm<sup>-1</sup>, resulting from the vibration of Fe-O group (Yi et al., 2020), appeared on the FA-BC, which supported the analysis of XRD and mineral compositions. The intensity of peaks of FA-BC at about 1552 cm<sup>-1</sup> and 2122 cm<sup>-1</sup>, attributed to C=C and C≡C vibrations (Ahmed et al., 2017a; Ahmed et al., 2017c), was enhanced significantly compared with those of R-BC, indicating that FeCl<sub>3</sub> activation could improve the BC aromaticity and result in the increase of electron-donor sites, which are beneficial for π-π interactions between FA-BC and organic contaminants. The peak at about 1052 cm<sup>-1</sup> confirmed the presence of C-O groups in all BCs (Zhu et al., 2014b). In addition, FT-IR spectra of FA-BC after MC-LR adsorption was also examined. As seen in Figure S5.5, after MC-LR adsorption, the peaks at 1552 cm<sup>-1</sup> (C=C) and 557 cm<sup>-1</sup> (Fe-O) moved to 1529 cm<sup>-1</sup> and 545 cm<sup>-1</sup>, respectively, indicating that both functional groups interacted with MC-LR molecules during adsorption.

### **5.3.3 Effect of pH and adsorption mechanism**

Due to the impacts of initial pH on the properties of FA-BC and the ionic form of MC-LR, the adsorption tests were carried out at various pH from 2 to 9 to examine the effect of initial pH on the MC-LR adsorption by FA-BC. The optimal pH values for MC-LR adsorption were observed at pH 3 and pH 4, and the adsorption capacity ( $Q_e$ ) decreased with the increase or decrease of pH. The same trend was also reported in the previous studies, showing that high pH resulted in the decrease of MC-LR adsorption onto carbonaceous materials (Huang et al., 2007; Pavagadhi et al., 2013). However, the  $Q_e$  values at pH 2-9 were between 8.36 and 9.69 mg/g, and did not change remarkably, suggesting that FA-BC has great potential for the treatment of MC-LR from real wastewater or lake water with various pH values.

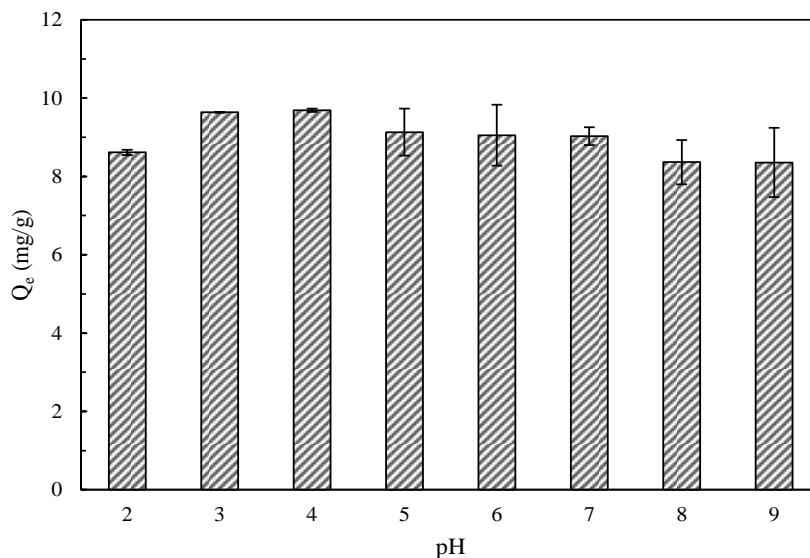


**Figure 5.2.** Effect of initial pH on adsorption of MC-LR onto FA-BC.

Due to the presence of functional groups of one  $\text{-NH}_2$  and two  $\text{-COOH}$  in the MC-LR molecule, MC-LR can exist in four different ionic forms under various pH values, such as  $\text{MC-LR}^+$  ( $\text{pH} < 2.09$ ),  $\text{MC-LR}^0$ , ( $2.09 < \text{pH} < 2.19$ ),  $\text{MC-LR}^-$  ( $2.19 < \text{pH} < 12.48$ ), and  $\text{MC-LR}^{2-}$  ( $\text{pH} > 12.48$ ) (Figure S5.6) (Li et al., 2014a). In addition, the  $\text{pH}_{\text{PZC}}$  of FA-BC was 7.36 (Figure S5.2), implying that FA-BC was positively charged when the solution pH was below 7.36, otherwise it was negatively charged. Therefore, the  $\text{MC-LR}^-$  molecule had the attractive electrostatic interaction with positively charged FA-BC at pH ranging from 3 to 7. Moreover, the FA-BC could carry more positive charges at lower pH, explaining that the lower pH resulted in the higher  $Q_e$  at pH 3-7. Additionally, owing to the existence of hydrophobic Adda and Leu residues in MC-LR (Figure S5.1), the hydrophobic interaction occurred between MC-LR and hydrophobic carbon surface of FA-BC (Park et al., 2020). The decrease of pH could cause the reduction of water solubility and hydrophilicity of MC-LR, which led to the enhancement of hydrophobic interaction between MC-

LR and FA-BC (Bajracharya et al., 2019). Moreover, the decrease of pH could also result in the decrease of MC-LR molecule dimensions due to the reduction of intramolecular electrostatic repulsion, which were beneficial for the transport of MC-LR molecules into inner pores of FA-BC (Bajracharya et al., 2019; Huang et al., 2007). Thus, both reasons can also explain the higher  $Q_e$  at lower pH. Nevertheless, the  $Q_e$  at pH 2 was significantly lower than that at pH 3, which was because that the proportion of MC-LR<sup>+</sup> increased from 1.6% to 42.8% when the pH decreased from 3 to 2 (Figure S5.6), suggesting that electrostatic repulsion was enhanced between MC-LR molecules and FA-BC.

As mentioned in the previous studies,  $\pi^+$ - $\pi$  electron donor-acceptor (EDA) interaction and hydrogen bond were also two of main mechanisms for MC-LR adsorption onto BCs (Li et al., 2018; Liu et al., 2018a). In this study, FA-BC can act as an electron donor due to the graphitized FA-BC attached with  $\pi$ -electron rich functional groups including -C=C- and -C $\equiv$ C- (Figure S5.5). Moreover, MC-LR can act as an electron acceptor because the guanidino group of MC-LR is easily protonated at pH below 12.48 and also the conjugation of N lone pairs and C atom of the guanidino group makes N atoms become electron-deficient (Li et al., 2018). Therefore,  $\pi^+$ - $\pi$  EDA interaction existed between the protonated guanidino group of MC-LR and FA-BC. What's more, -NH<sub>2</sub> and -COOH groups of MC-LR could form the hydrogen bond with O-containing functional groups of FA-BC. Additionally, as displayed in Figure 5.2, the  $Q_e$  values at pH 8 and 9 were significantly reduced due to the formation of electrostatic repulsion between MC-LR<sup>-</sup> and negatively charged FA-BC.

Moreover, due to about 30% of iron content in FA-BC, the adsorption capacity of MC-LR onto iron oxides was also evaluated under the same adsorption conditions for FA-BC. As indicated in Figure S5.7, the MC-LR adsorption capacities of Fe<sub>2</sub>O<sub>3</sub> and Fe<sub>3</sub>O<sub>4</sub> were 0.52 and 1.11 mg/g,

respectively. This result is consistent with FT-IR analysis, confirming that the group Fe-O was involved in the MC-LR adsorption. In addition, the previous studies also found that Fe<sub>2</sub>O<sub>3</sub> could adsorb the MC-LR via electrostatic, ligand exchange, and hydrophobic interactions (Gao et al., 2012; Lee & Walker, 2011). Therefore, in this study, the main mechanisms for MC-LR adsorption onto FA-BC were electrostatic,  $\pi^+ - \pi$  EDA, hydrogen bond, and hydrophobic interactions (Figure 5.3).

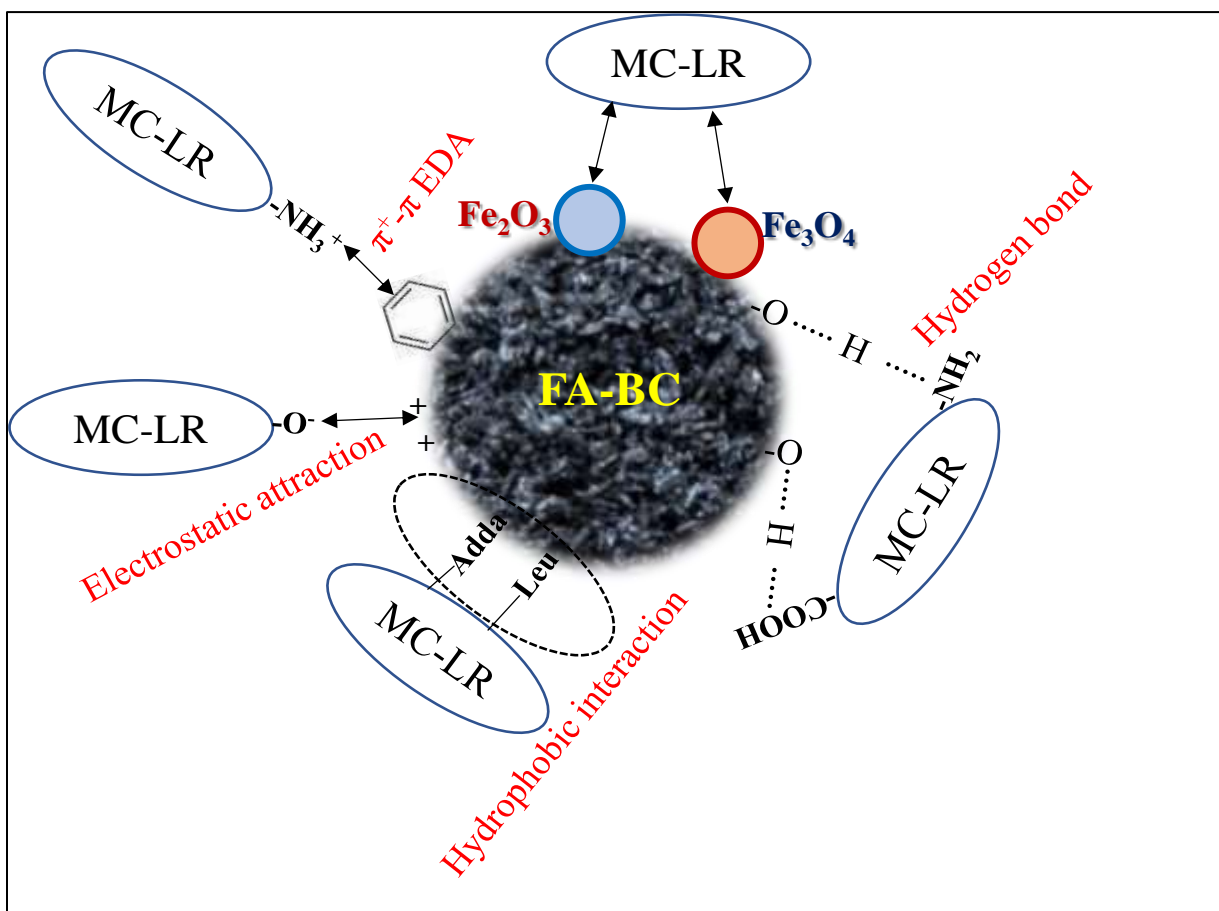


**Figure 5.3.** Proposed mechanisms of MC-LR adsorption onto FA-BC.

### 5.3.4 Kinetics study

To better evaluate the mechanisms of interactions between MC-LR and FA-BC, the adsorption kinetics was conducted in the present study. As displayed in Figure S5.8, the adsorption process of MC-LR onto FA-BC showed the same trend under two different initial MC-LR concentrations of 500 and 1000  $\mu\text{g/L}$ . More specifically, MC-LR adsorption capacity increased rapidly in the first hours and reached at equilibrium within 2 d. Pseudo-first order (PFO), pseudo-second order (PSO), Elovich, and two compartment first order (TCFO) models were applied to fit the kinetics data (Table 5.2 and Figure S5.8). Due to the higher  $R^2$  and lower SSE, the PSO model better fitted to experimental data than the PFO model, implying that FA-BC adsorbed the MC-LR mainly via the chemical interaction (Jang & Kan, 2019c). The high  $R^2$  (0.9923-0.9935) and low SSE (0.2422-0.2667) was also obtained from Elovich model fitting the kinetics data, supporting that chemisorption occurred on the FA-BC surface with energetic heterogeneity (Jang et al., 2018b). Moreover, the calculated  $Q_e$  from Elovich model was closer to the experimental  $Q_e$  compared with PFO and PSO models. The calculated a value from Elovich model at the initial concentration of 1000  $\mu\text{g/L}$  was higher than that of 500  $\mu\text{g/L}$ , indicating that the higher initial adsorption rate at the higher MC-LR concentration due to the higher concentration gradient between FA-BC surface and aqueous phase. Furthermore, the experimental results were also well fitted with TCFP model. The  $K_{\text{fast}}$  (333.0001-333.0024) was remarkably higher than  $K_{\text{slow}}$  (0.0019-0.0025), confirming that the fast adsorption controlled the process of MC-LR adsorption onto FA-BC.

**Table 5.2** Summary of kinetic parameters of MC-LR adsorption onto FA-BC.

	500 µg/L	1000 µg/L
$Q_e^a$	10.23	12.45
Pseudo-first order		
$Q_e^b$	8.75	10.35
$K_1$	0.0138	0.01873
SSE	1.1132	1.4270
$R^2$	0.8370	0.8144
Pseudo-second order		
$Q_e^b$	9.47	11.35
$K_2$	0.0022	0.0021
SSE	0.6897	0.9258
$R^2$	0.9375	0.9219
Elovich		
$Q_e^b$	10.17	12.30
a	2.1176	3.5221
b	0.8394	0.7237
SSE	0.2422	0.2667
$R^2$	0.9923	0.9935
Two compartment first-order		
$Q_e^b$	9.81	12.11
$F_{fast}$	0.4855	0.5255
$F_{slow}$	0.5145	0.4745
$K_{fast}$	333.0001	333.0124
$K_{slow}$	0.0025	0.0019
SSE	0.2002	0.1951
$R^2$	0.9947	0.9965
Liquid film diffusion		
$Q_e^b$	8.75	10.35
$K_{fd}$	0.0138	0.0187
SSE	1.1676	1.4967
$R^2$	0.5553	0.4558
Intra-particle diffusion		
$Q_e^b$	10.23	12.45
$K_i$	0.1037	0.1228
$K_{i1}$	0.9065	1.1603
$K_{i2}$	0.1899	0.1860
$K_{i3}$	0.0400	0.0623
$C_i$	5.1779	6.4448
SSE	0.5458	0.4863
$R^2$	0.9028	0.9425

<sup>a</sup>Experimental value<sup>b</sup>Calculated value

For better understanding the rate-limiting steps during the MC-LR adsorption into FA-BC, intra-particle diffusion and film diffusion models were also analyzed in this study (Table 5.2 and Figure S5.8). Compared with film diffusion model with low  $R^2$  (0.4558-0.5553) and high SSE (1.1676-1.4967), the intra-particle diffusion model showed higher  $R^2$  (0.9028-0.9025) and lower SSE (0.4863-0.5458), implying that the intra-particle diffusion was the rate-limiting step of the adsorption process. Figure S5.8 displays that the intra-particle diffusion was divided into three adsorption stages, including the rapid MC-LR adsorption from aqueous phase to FA-BC surface and macropores, the MC-LR diffusion inside the mesopores, and the final adsorption equilibrium (Mashile et al., 2018; Park et al., 2017). Additionally, the significantly lower diffusion rate constant  $K_{i2}$  and  $K_{i3}$  than  $K_{i1}$  indicated that pore diffusion mainly affected the entire adsorption rate. Furthermore, the  $C_i$  values were 5.1779-6.448, not close to zero, indicating that film diffusion also participated in the adsorption process (Tang et al., 2018).

### 5.3.5 Isotherm study

In this study, various isotherm models (Langmuir, Freundlich, Temkin, and Dubinin-Radushkevich (D-R) models) were also analyzed for further evaluating that how MC-LR molecules interacted with FA-BC (Table 5.3 and Figure S5.9). The adsorption data were better suited to Freundlich model ( $R^2 = 0.9308$ ) than Langmuir model ( $R^2 = 0.8011$ ), suggesting that multi-layer adsorption occurred on the heterogeneous surface of FA-BC (Martins et al., 2015). This result is consistent with the previous report showing that Freundlich model was well fitted with the data about MC-LR adsorption onto bamboo derived charcoal (Zhang et al., 2011a). Moreover, the separation factor ( $R_L = 0.85$ ) from the Langmuir model was in the range of 0 to 1, indicating that MC-LR adsorption onto FA-BC was a favorable process (Martins et al., 2015). The heterogeneity factor ( $1/n_f = 0.16$ ) was close to zero, implying that the FA-BC surface was greatly

heterogeneous (Martins et al., 2015). Additionally, the Temkin model was best suited with the experimental results based on the highest  $R^2$  (0.9732), demonstrating that the temperature could affect the adsorption heat of MC-LR adsorption onto FA-BC (Yan et al., 2020a). Furthermore, D-R models analysis also supported that MC-LR adsorption did not occur on the homogeneous surface (Tang et al., 2018).

**Table 5.3** Summary of isotherm parameters of MC-LR adsorption on FA-BC.

Langmuir model		Dubinin-Radushkevich model	
$Q_m$	10.12	$q_D$	10.70
$K_L$	179.49	$b_D$	$4.33 \times 10^{-9}$
$R_L$	0.85	E	4.30
SSE	0.8949	SSE	0.6847
$R^2$	0.8011	$R^2$	0.8319
Temkin model		Freundlich model	
$K_T$	14293.02	$K_f$	12.33
$b_T$	2011.20	$n_f$	6.43
SSE	0.5257	SSE	0.4960
$R^2$	0.9732	$R^2$	0.9308

The maximum adsorption capacity of MC-LR calculated from Langmuir model was 10.12 mg/g, which was higher than various adsorbents reported in the previous studies (Table S5.2), including carbon nanotube, graphene oxide, iron oxide, activated carbon, and other wastes derived BCs. Therefore, FA-BC exhibited great potential for the treatment of MC-LR in water.

### 5.3.6 Thermodynamics study

The thermodynamics analysis about MC-LR adsorption onto FA-BC was displayed in Table 5.4. The  $\Delta H^0$  value was positive (12.33 kJ/mol), suggesting the endothermic nature of MC-LR adsorption onto FA-BC. The previous study also showed that MC-LR adsorption onto wood chips derived BC was an endothermic process (Li et al., 2014a). In addition, the negative values of  $\Delta G^0$



confirmed that the adsorption process was spontaneous (Gao et al., 2012). Moreover, the increase of absolute values of  $\Delta G^0$  with the increase of temperature implied that the higher temperature resulted in a more favorable adsorption process. The positive  $\Delta S^0$  value (74.90 J/mol·K) demonstrated that the randomness was enhanced at the interface of FA-BC and MC-LR solution during the adsorption process (Li et al., 2014a).

**Table 5.4** Thermodynamic parameters for the adsorption of MC-LR on FA-BC.

Temperature (K)	$K_d$ (L/g)	$\Delta G^0$ (kJ/mol)	$\Delta H^0$ (kJ/mol)	$\Delta S^0$ (J/mol·K)
293	52.50	-9.63	12.33	74.90
303	60.08	-10.38		
313	72.57	-11.13		

### 5.3.7 Regeneration study

The regeneration study is significant for reducing the costs of the practical application of adsorbents in real wastewater treatment. So far, the thermal regeneration has been considered as an easy and effective method to regenerate the contaminants saturated activated carbon in an industrial scale (Carratalá-Abril et al., 2010). In this study, the MC-LR spent FA-BC was regenerated in the furnace at 300 °C for 3 h. As shown in Figure 5.4, after 4 successive regeneration cycles, the regeneration efficiency was still above 99%. The previous study reported by Carratalá-Abril et al. (2010), showing that organic compounds (benzene and toluene) saturated activated carbons could be effectively regenerated (about 100% regeneration efficiency) at 250-350 °C under oxygen-containing atmosphere. Moreover, Li et al. (2011) also reported that 300 °C treatment could result in the high regeneration efficiency (94.49%) after 3 successive cycles for methylene blue spent activated carbon.

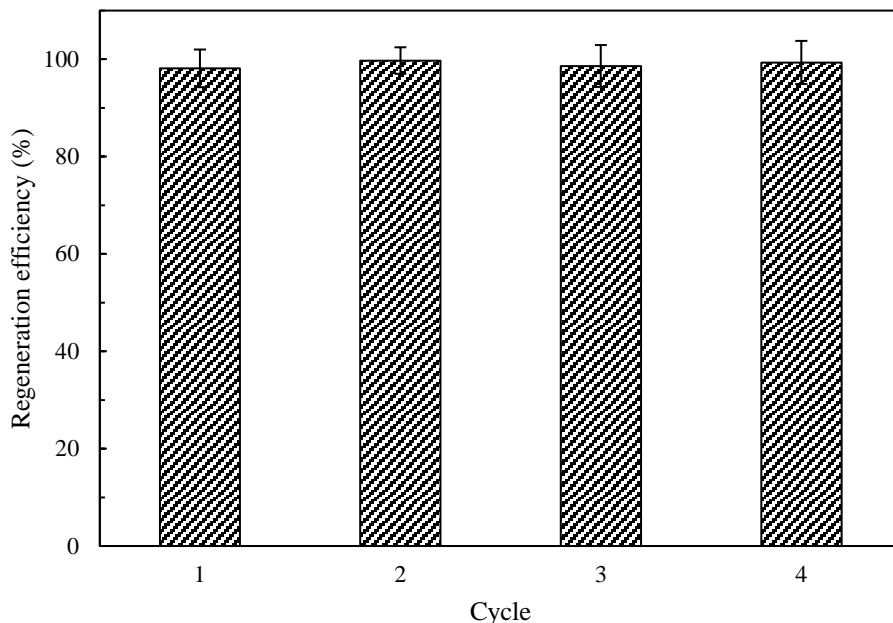


**Figure 5.4.** Thermal regeneration (300 °C) of MC-LR spent FA-BC for successive cycles.

Compared to thermal regeneration, NaOH desorption is a simple and cheaper method to regenerate the contaminants spent adsorbents. In this study, 31.19% and 86.69% of regeneration efficiencies were achieved for MC-LR spent FA-BC by 0.1 M and 1 M NaOH solution, respectively (Figure S5.10). However, the method of NaOH desorption could not destroy the MC-LR molecules and also produce a large amount of alkaline wastewater. Therefore, it is an unpractical method for the regeneration of MC-LR spent FA-BC.

The contaminants adsorbed on adsorbents can be degraded by the advanced oxidation to achieve the effective regeneration of contaminants spent adsorbents (Chemical regeneration). Based on the XRD analysis (Figure S5.3), FA-BC was attached with  $\text{Fe}^0$ ,  $\text{Fe}_2\text{O}_3$  and  $\text{Fe}_3\text{O}_4$ , which can act as the activators for Fenton oxidation and persulfate oxidation. Therefore, in this study, MC-LR spent FA-BC can be regenerated by Fenton oxidation or persulfate oxidation. As displayed in Figure S5.11 and Figure S5.12, persulfate oxidation showed better performance to regenerate the MC-LR

spent FA-BC than Fenton oxidation. This is because that sulfate radicals (2.5-3.1 V; 4 s) produced from persulfate oxidation have higher redox potential and lifetime than hydroxyl radicals (1.9-2.7 V; 20 ns) produced from Fenton oxidation (Wang et al., 2017c). Under the treatment of 400 mg/L persulfate, the regeneration efficiency was close to 100%, indicating that persulfate oxidation has great potential to regenerate the MC-LR spent FA-BC. Further studies following this work will focus on the optimization of parameters, reaction mechanisms, and toxicity evaluation for regeneration by the persulfate oxidation.

### **5.3.8 Application in real lake water**

In order to evaluate the feasibility of application of FA-BC in real wastewater treatment, the adsorption experiments were also performed in Proctor Lake water (Dublin, TX, USA). Compared to DI water, the adsorption capacity of MC-LR onto FA-BC in lake water was reduced by 49.31% (Figure S5.13). The main reason is that various organic and inorganic compounds in lake water (Table S5.1) could compete with MC-LR for available active sites in FA-BC. The MC-LR is usually detected in the natural water sources with the concentration of 0-50  $\mu\text{g/L}$  (Bajracharya et al., 2019; Park et al., 2018a; Park et al., 2017). Therefore, in this study, 40 mg/L of FA-BC was applied for the treatment of lake water with various MC-LR concentrations (5, 25, and 50  $\mu\text{g/L}$ ). The results in Figure S5.14 indicate that, after the FA-BC treatment, the final MC-LR concentrations could be reduced below 1  $\mu\text{g/L}$ , which is the guideline level from World Health Organization (WHO).

### **5.4 Conclusions**

The novel FA-BC was prepared by one-step pyrolysis and activation of  $\text{FeCl}_3$  pretreated BG, exhibiting excellent performance for MC-LR adsorption. The kinetics and isotherm studies indicated that MC-LR adsorption occurred on the heterogeneous surface of FA-BC by the chemical

interaction. The thermodynamics study suggested that MC-LR adsorption onto FA-BC was a spontaneous and endothermic process. Thermal oxidation and persulfate oxidation showed great performance for the regeneration of MC-LR spent FA-BC. This study indicates that FA-BC has great potential for the treatment of MC-LR in water.

## CHAPTER VI

### PERSULFATE OXIDATION-DRIVEN REGENERATION OF MICROCYSTIN-LR SPENT FECL<sub>3</sub>-ACTIVATED BIOCHAR

#### 6.1 Introduction

As mentioned in Chapter V, development of effective techniques for the treatment of MC-LR is of great importance. Various adsorbents including BCs has been applied to eliminate MC-LR from water. So far, however, no studies have been conducted for the regeneration of MC-LR spent adsorbents, which is of great importance for the industrial application of adsorbents.

Research about regeneration of contaminants spent BCs are quite limited. Contaminants spent BCs can be regenerated by the desorption and decomposition of contaminants on BCs (Dai et al., 2019). Thermal regeneration has been considered as an effective technique for the reuse of adsorbents through the decomposition of contaminants at high temperature (Dai et al., 2019; Wei et al., 2012). Zeng et al. (2021) regenerated the sulfamethoxazole spent BC under the treatment of 300 °C and achieved the 46% of regeneration efficiency after four cycles of adsorption-regeneration. In addition, solvent regeneration is also a good method to reuse the adsorbents by the desorption using inorganic reagents (such as acidic and alkali solution) and organic solvents (such as methanol and ethanol). For example, Zeng et al. (2021) and Jang and Kan (2019c) applied 0.1 M NaOH solution to effectively regenerate the sulfamethoxazole and tetracycline spent BCs. However, thermal treatment requires the high-energy input and causes the damage of structure and reduction of adsorption ability (Wei et al., 2012). In addition, for solvent regeneration, the treatment of large amounts of solvents containing high concentrations of contaminants is time-consuming and expensive (Du et al., 2016).

While chemical oxidation-driven regeneration using Fenton and persulfate reactions has been studied for carbonaceous adsorbents including activated carbon, carbon nanotube and graphene oxide (Kan & Huling, 2009; Liang et al., 2009; Naghizadeh et al., 2015; Qin et al., 2014), they have not been applied for contaminant-spent BC. Persulfate (PS) oxidation has been considered as an effective advanced oxidation process (AOP) for the degradation of organic compounds by  $\text{SO}_4^{\cdot-}$  radicals, which are produced from the activation of PS by heat, UV, transition metals, and so on (Song et al., 2019). In addition, due to higher redox potential and lifetime,  $\text{SO}_4^{\cdot-}$  exhibits higher stability and wider reactivity compared to  $\cdot\text{OH}$  (Wang et al., 2017c). So far, a few works have been carried out to study about regeneration of contaminants spent adsorbents by PS oxidation (Please see Supplementary materials, Table S6.1). For example, Huling et al. (2011) used activated PS to regenerate the methyl *tert*-butyl ether (MTBE) spent activated carbon and found that thermal activation of PS showed better performance for removing MTBE from activated carbon compared to alkali activation of PS. An et al. (2015) indicates that natural organic matter (NOM) spent activated carbon could be effectively regenerated by UV activation of PS. In addition, Liang et al. (2009) shows that  $\text{Fe}^{2+}$  activated PS oxidation could effectively degrade trichloroethylene absorbed on activated carbon. However, UV and thermal activation need the input of external energy, which can increase the regeneration costs (Song et al., 2019). Additionally, excess  $\text{Fe}^{2+}$  can react with  $\text{SO}_4^{\cdot-}$  radicals and reduce the reaction efficiency of PS oxidation (Yang et al., 2020). Moreover, large amounts of  $\text{Fe}^{3+}$  ions are accumulated in the reaction system of  $\text{Fe}^{2+}$  activated PS (An et al., 2015).

Various iron compounds, such as  $\text{Fe}_3\text{O}_4$ , zero-valent iron, and  $\text{CuFe}_2\text{O}_4$ , have been reported to be alternatives of  $\text{Fe}^{2+}$  to activate PS to produce  $\text{SO}_4^{\cdot-}$  to oxidize contaminants (Yan et al., 2011; Yang et al., 2020; Zhang et al., 2016). Moreover, Ouyang et al. (2017) and Yang et al. (2020) attached

$\text{Fe}_3\text{O}_4$  and zero-valent iron onto rice pine needle and stalk-derived BCs, and used them as catalysts to activate PS for the oxidation of 1,4-dioxane and monochlorobenzene, respectively. However, low concentrations of contaminants lead to the low reaction rate and efficiency by chemical oxidation and need a lot of oxidants due to the short lifetime of free radicals (Kim et al., 2015). Hence, a feasible method to overcome these disadvantages is that contaminants are firstly concentrated on adsorbents by adsorption and then degraded by chemical oxidation (Kim et al., 2015).

In addition,  $\text{FeCl}_3$  activation has been confirmed as a feasible method to simultaneously increase the surface area of BCs and attach iron compounds on the BCs (Yang et al., 2016a; Zhu et al., 2014b). Moreover, high surface area of BCs is beneficial to provide more active sites for adsorption and catalytic oxidation of contaminants. Therefore, this study suggests that  $\text{FeCl}_3$  activated BCs can be used to adsorb MC-LR from water and sequentially regenerated by PS oxidation.

To our knowledge, for the first time, this study used the PS oxidation to regenerate the contaminants spent BCs. The aims of this study were to: (1) produce the  $\text{FeCl}_3$  activated BC (FA-BC) by one-step  $\text{FeCl}_3$  activation/pyrolysis of bermudagrass; (2) evaluate the effects of temperature on the adsorption, desorption, diffusion, and oxidation of MC-LR on FA-BC; (3) investigate the effect of pH and PS concentration on the regeneration efficiency of MC-LR spent FA-BC by PS oxidation; (4) identify the main free radicals participating in the process of PS oxidation of MC-LR; (5) propose the mechanisms for PS oxidation of MC-LR on FA-BC; (6) regenerate the MC-LR spent FA-BC with multiple cycles by PS oxidation; and (7) apply the FA-BC in the treatment of MC-LR in real lake water.

## **6.2 Materials and methods**

### **6.2.1 Materials**

Bermudagrass (BG), used for biochar production, was provided by a hay store (Stephenville, Texas, USA), and then dried in the oven at 70 °C. Ferric chloride (FeCl<sub>3</sub>) and ammonium persulfate ((NH<sub>4</sub>)<sub>2</sub>S<sub>2</sub>O<sub>8</sub>) were obtained from Sigma-Aldrich (Saint Louis, Missouri, USA). Microcystin-LR (MC-LR, C<sub>48</sub>H<sub>72</sub>N<sub>10</sub>O<sub>12</sub>) was provided by Enzo Biochem (Farmingdale, New York, USA). All other chemicals used in the present study were of analytical grade.

### **6.2.2 Production of FeCl<sub>3</sub> activated biochar**

FeCl<sub>3</sub> activated BC with the mass impregnation ratio (FeCl<sub>3</sub>/BG) of 2 was produced and characterized as described in sec. 4.2.2 of Chapter IV.

### **6.2.3 MC-LR adsorption onto FA-BC**

The MC-LR adsorption performance onto FA-BC was evaluated by adsorption. For the adsorption kinetics tests, 0.004 g of FA-BC was mixed with 100 mL of 0.5 mg/L MC-LR solution at pH 6 under various temperatures (20, 35, and 50 °C). The MC-LR concentration was measured at various time intervals. The adsorption capacity ( $Q_t$ ) at time  $t$  was calculated according to the differences between initial and time  $t$  concentrations of MC-LR. Moreover, in this study, various kinetics models are applied for the fitting of experimental data (Table S2.2, Chapter II).

### **6.2.4 Persulfate oxidation-driven regeneration of MC-LR spent FA-BC**

0.004 g of FA-BC was saturated with MC-LR under the above-mentioned conditions (100 mL of 0.5 mg/L MC-LR, pH 6, 20 °C, and 2 d), and then magnetically separated by a magnet. Then, 0.004 g of MC-LR spent FA-BC was used for regeneration tests by persulfate (PS) oxidation. The effect of initial pH on the regeneration of MC-LR spent FA-BC by PS oxidation was carried out at different pH values ranging from 4 to 10 with the conditions of 40 mL of 200 mg/L PS and



20 °C. To investigate the effect of PS concentration on the regeneration of MC-LR spent FA-BC, 40 mL of various concentrations (100-400 mg/L) of PS solution at pH 6 and 20 °C was applied for the regeneration tests. The effect of reaction temperature was evaluated by mixing 0.004 g of MC-LR spent FA-BC with 40 mL of 200 mg/L PS solution at pH 6 and various temperatures ranging from 20 °C to 50 °C. After PS oxidation, the regenerated FA-BC was magnetically separated from the reaction solution and added into fresh MC-LR solution for the readsorption test under the same conditions for the initial adsorption test. The regeneration efficiency was calculated using the following equation:

$$\text{Regeneration efficiency (\%)} = \frac{Q_r}{Q_i} \times 100 \quad (6.1)$$

where  $Q_i$  (mg/g) and  $Q_r$  (mg/g) are the initial adsorption capacity and readsorption capacity, respectively.

In order to evaluate the MC-LR oxidation rate on FA-BC at various temperatures by persulfate oxidation, the residual MC-LR concentration on FA-BC was measured at various time intervals. The MC-LR content in FA-BC was evaluated by the desorption in 1 M NaOH solution for 2 h, and then the MC-LR concentration in desorption solution was analyzed. The MC-LR oxidation rate (mg MC-LR/g BC-h) was calculated as the weight of oxidized MC-LR in FA-BC divided by the weight of FA-BC and reaction time.

The MC-LR diffusion + desorption rate from MC-LR spent FA-BC at various temperatures was also evaluated by the desorption test in 40 mL of DI water at pH 6. The MC-LR concentration was measured at various time intervals. Then, the MC-LR diffusion + desorption rate (mg MC-LR/g BC-h) was calculated as the weight of desorbed MC-LR from FA-BC divided by the weight of FA-BC and reaction time.

Ethanol (10 and 50 mM) and tert butyl alcohol (TBA) (10 and 50 mM) as the radical scavengers were used to identify the main radicals participating in the process of PS oxidation under the conditions of 0.004 g of MC-LR spent FA-BC, 40 mL of 200 mg/L PS, initial pH of 6, and reaction temperature of 20 °C.

For evaluating the feasibility of practical application about persulfate-driven regeneration of MC-LR spent FA-BC, the adsorption-regeneration cycle was carried out 4 times. In addition, in this study, adsorption and regeneration tests were also performed in real lake water (Proctor Lake, Dublin, TX, USA). 100 mL of lake water was spiked with 0.25 mg/L MC-LR and mixed with 0.002 g of FA-BC at pH 8.25 (pH of lake water) for 2 d. After adsorption equilibrium, FA-BC was magnetically separated from the solution and regenerated by PS oxidation under the conditions of 20 mL of 200 mg/L PS, initial pH of 6, and reaction temperature of 50 °C. Four cycles of adsorption-regeneration tests in lake water were also conducted in this study.

### **6.2.5 Analytical methods**

The MC-LR concentration in solution was measured using an HPLC (Shimadzu LC-2030C, Shimadzu Co., JP) equipped with a C18 column (Phenomenex Inc., USA) and a PDA (photo-diode array) detector. The mobile phase consisted of methanol and phosphate buffer (0.05 M, pH 2.5) (55:45, v/v) with a flow rate of 0.75 mL/min. The wavelength used for MC-LR detection was 238 nm.

The iron concentration in the aqueous phase was determined by a commercial test kit (Hach company, Colorado, USA). The persulfate concentration was determined according to the method reported in the previous study (Wei et al., 2020). In brief, 0.04 mL of liquid sample was mixed with 1 mL of mixed solution consisting of 1 M KI and 0.15 mM NaHCO<sub>3</sub> for 20 min. Then, the reaction solution was measured via a UV-vis spectrophotometer (Hach company) at 352 nm.

## 6.3 Results and discussion

### 6.3.1 MC-LR adsorption performance onto FA-BC

Adsorption behaviors of MC-LR onto FA-BC were evaluated through adsorption kinetic and isotherm experiments in this study. As shown in Figure S6.1, FA-BC exhibited very rapid adsorption for MC-LR. The MC-LR adsorption amount increased with the increase of adsorption time at various temperatures and adsorption equilibrium was achieved within 2 d. For kinetics study, pseudo-first order and pseudo-second order models were applied for analyzing the experimental data. As shown in Table 6.1, the correlation coefficient ( $R^2$ ) at various temperatures indicated that the pseudo-second order model ( $R^2 = 0.94-0.97$ ) was better fitted with the adsorption kinetic data than the pseudo-first order model ( $R^2 = 0.84-0.89$ ), implying that MC-LR adsorption onto FA-BC was mainly dominated by the chemisorption (Zeng & Kan, 2020a). The previous studies conducted by Mashile et al. (2018) and Park et al. (2017) also showed that MC-LR adsorption onto carbonaceous materials well fitted with the pseudo-second order model. In addition,  $Q_e$  (mg/g, adsorption capacity at equilibrium time) derived from the pseudo-second order model increased with the improvement of temperature from 20 °C to 50 °C, suggesting that the increase of temperature favored the MC-LR adsorption onto FA-BC.

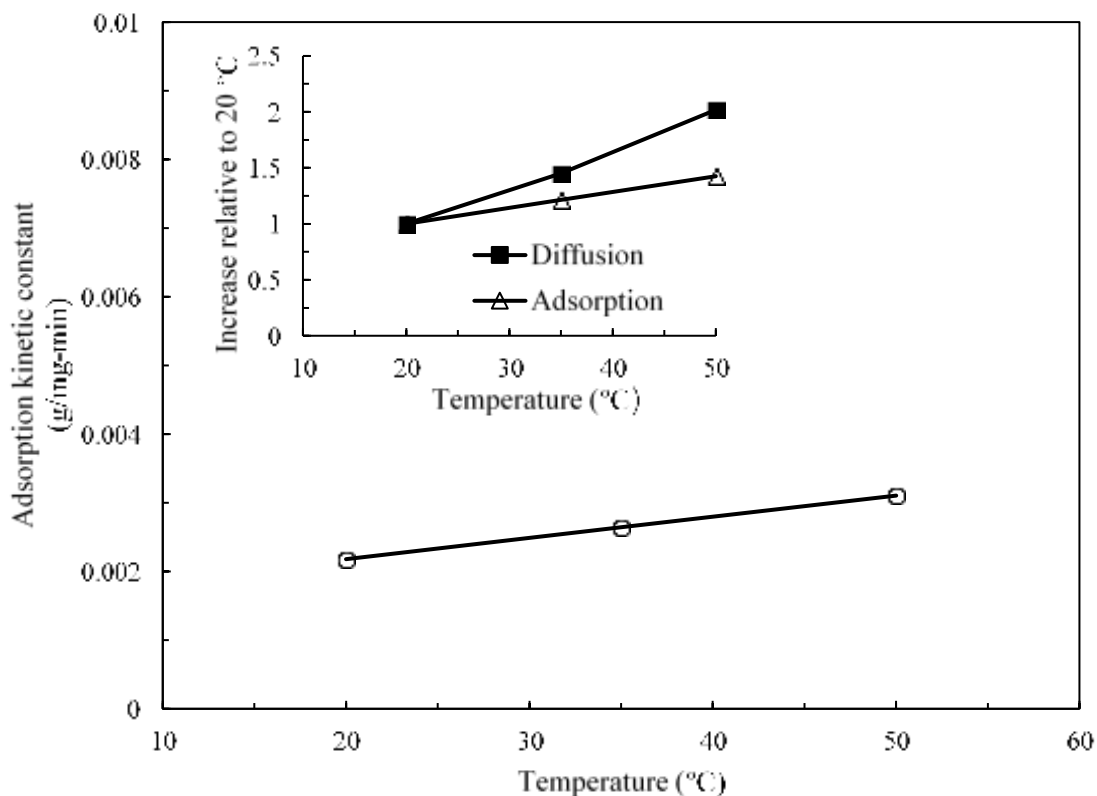


**Figure 6.1.** Adsorption kinetic constants (Pseudo-second order) of MC-LR onto FA-BC at various temperatures. Experimental conditions: 100 mL of 0.5 mg/L MC-LR, 0.004 g of FA-BC, and initial pH of 6.

**Table 6.1** Adsorption kinetic parameters of MC-LR adsorption onto FA-BC under various temperatures (20-50 °C). Experimental conditions: 100 mL of 0.5 mg/L MC-LR, 0.004 g of FA-BC, and initial pH of 6.

Temperature	Pseudo-first order			Pseudo-second order			Intra-particle diffusion		Film diffusion	
	$Q_e$ (mg/g)	$K_1$ ( $\text{min}^{-1}$ )	$R^2$	$Q_e$ (mg/g)	$K_2$ (g/mg/ min)	$R^2$	$K_i$ (mg/g/ $\text{min}^{0.5}$ )	$R^2$	$K_{fd}$ ( $\text{min}^{-1}$ )	$R^2$
20 °C	8.75	0.0138	0.84	9.47	0.0022	0.94	0.1037	0.90	0.0138	0.56
35 °C	8.95	0.0185	0.86	9.72	0.0026	0.95	0.1090	0.81	0.0185	0.55
50 °C	9.37	0.0220	0.89	10.10	0.0031	0.97	0.1141	0.80	0.0220	0.58

Table 6.1 and Figure 6.1 indicate that adsorption rate constant (pseudo-second order) of MC-LR adsorption onto FA-BC was remarkably improved from 0.0022 g/mg-min to 0.0031 g/mg-min with the increase of temperature from 20 °C to 50 °C. Generally, the Wike-Chang equation (Text S1, Supplementary materials) was applied for the evaluation of diffusivity of solute molecules in solution (Kan & Huling, 2009; Kim et al., 2015). The diffusivity of MC-LR and S<sub>2</sub>O<sub>8</sub><sup>2-</sup> in water at various temperature (20-50 °C) was calculated using the Wike-Chang equation (Kim et al., 2015):

$$D_{c,w} = T \times 7.4 \times 10^{-8} (\Phi_w M_w)^{0.5} / (\mu_w \times V_c^{0.6}) \quad (6.2)$$

where  $D_{c,w}$  = diffusivity of chemical C in water (cm<sup>2</sup>/s at 1 atm),  $\mu_w$  = viscosity of water (centipoise), T = absolute temperature (K),  $M_w$  = molecular weight of water,  $V_c$  = molar volume of a chemical at normal boiling point (1186.3 and 117.6 cm<sup>3</sup>/mol for MC-LR and S<sub>2</sub>O<sub>8</sub><sup>2-</sup>, respectively), and  $\Phi_w$  = association parameter for water (2.26, dimensionless).

As shown in Table 6.2, the increase of temperature resulted in the improvement of MC-LR diffusivity from 1.97×10<sup>-6</sup> cm<sup>2</sup>/s to 3.99×10<sup>-6</sup> cm<sup>2</sup>/s. Moreover, Table 6.2 also shows that the higher temperature caused the lower viscosity of water, which favored the molecular mass-transfer process in water. Thus, both above-mentioned reasons can explain the higher MC-LR adsorption rate resulting from the higher temperature. In addition, as displayed in the inset of Figure 6.1, the improvement of MC-LR diffusivity in water was linearly proportional with the enhancement of MC-LR adsorption rate onto FA-BC, implying that the diffusion mainly affected the process of MC-LR onto FA-BC.

**Table 6.2** MC-LR and S<sub>2</sub>O<sub>8</sub><sup>2-</sup> diffusivity at various temperatures.

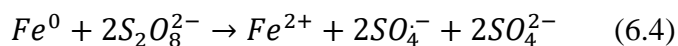
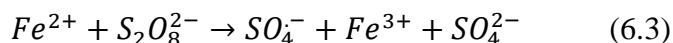
Temperature (°C)	Viscosity of water (centipoise)	MC-LR diffusivity in water (×10 <sup>-6</sup> cm <sup>2</sup> /s)	Overall increase in MC-LR diffusivity <sup>a</sup>	S <sub>2</sub> O <sub>8</sub> <sup>2-</sup> diffusivity in water (×10 <sup>-5</sup> cm <sup>2</sup> /s)	Overall increase in S <sub>2</sub> O <sub>8</sub> <sup>2-</sup> diffusivity <sup>a</sup>
20 °C	1.00	1.97	1.00	0.79	1.00
35 °C	0.73	2.86	1.45	1.15	1.45
50 °C	0.55	3.99	2.02	1.69	2.02

<sup>a</sup>Increase relative to 20 °C

In order to further figure out the rate-limiting step in the MC-LR adsorption process, intra-particle diffusion and film diffusion models were also applied to fit the adsorption kinetic data. Table 6.1 shows that the intra-particle diffusion model exhibited higher R<sup>2</sup> (0.80-0.90) at various temperatures compared to the film diffusion model (R<sup>2</sup> = 0.55-0.58), indicating that intraparticle diffusion played an important part in the process of MC-LR onto FA-BC. Moreover, the intra-particle diffusion rate constant increased with increasing temperature, which also favored the increase of MC-LR adsorption rate with the improvement of temperature.

### 6.3.2 Persulfate-driven regeneration of MC-LR spent FA-BC

As shown in EDX analysis (Figure S5.4, Chapter V), the iron content on the surface of FA-BC was 40.14%. In addition, from the XRD analysis (Figure S6.2), iron species on FA-BC mainly consisted of Fe<sup>0</sup>, α-Fe<sub>2</sub>O<sub>3</sub>, and Fe<sub>3</sub>O<sub>4</sub>. Both Fe<sup>0</sup> and Fe<sub>3</sub>O<sub>4</sub> can activate PS to generate SO<sub>4</sub><sup>-</sup> for the degradation of organic contaminants (Eqs. (6.3) and (6.4)) (Jonidi Jafari et al., 2017; Yang et al., 2020). Therefore, in this study, PS oxidation was applied for the regeneration of MC-LR spent FA-BC.



### 6.3.2.1 Effects of initial pH

Initial pH is a key factor during the PS oxidation process and can affect the  $\text{Fe}^{2+}$  dissolution from iron compounds, which is related to the PS oxidation rate and efficiency (Li et al., 2015c). Figure 6.2a shows that regeneration efficiency was reduced from 95.86% to 48.62% with the increase of pH from 4 to 10, indicating that acidic pH was more favorable for PS oxidation of MC-LR on FA-BC. As shown in Table S6.2, iron concentration in the reaction solution increased with the decrease of pH, suggesting that low pH favored the release of iron ions from FA-BC, which enhanced the activation of PS and generation of  $\text{SO}_4^-$  for oxidation of MC-LR on FA-BC. In addition, Table S6.3 also indicates that PS reaction rate was improved from  $0.0311 \text{ h}^{-1}$  to  $0.0709 \text{ h}^{-1}$  when the pH was decreased from pH 10 to 4. Moreover, at high pH, the electronic barrier can be formed due to the generation of Fe hydroxides on the surface of FA-BC, which could reduce the release of  $\text{Fe}^{2+}$  and inhibit the activation of PS (Jonidi Jafari et al., 2017; Li et al., 2015c). This is the reason that can explain the lowest regeneration efficiency at pH 10. However, as shown in Figure 6.2a, the regeneration efficiency at pH 8 was slightly higher than that at pH 6. The main MC-LR species at pH 4-10 is negatively charged  $\text{MC-LR}^-$  (Figure S5.6, Chapter V). Moreover, the  $\text{pH}_{\text{PZC}}$  of FA-BC was 7.36 (Figure S5.2, Chapter V), indicating that FA-BC was positively charged when the solution pH was less than 7.36, otherwise it was negatively charged. Therefore, electrostatic repulsion occurred between  $\text{MC-LR}^-$  and FA-BC at pH 8, which favored the release of MC-LR from FA-BC into the reaction solution, explaining the higher regeneration efficiency at pH 8.

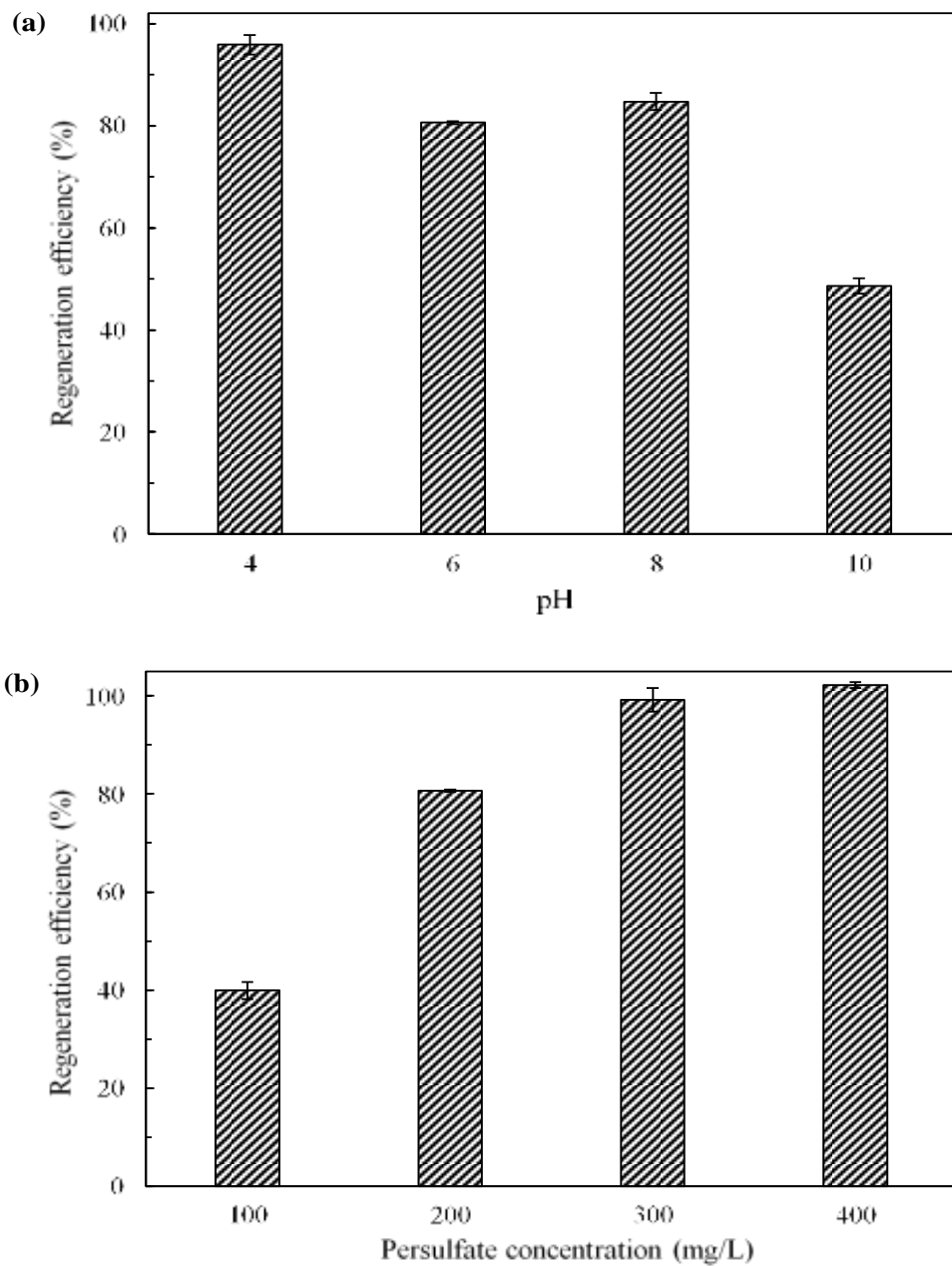


**Figure 6.2.** (a) Effect of initial pH on the regeneration efficiency of MC-LR spent FA-BC by PS oxidation. Regeneration conditions: 0.004 g of MC-LR spent FA-BC, 40 mL of 200 mg/L PS, and 20 °C. (b) Effect of PS concentration on the regeneration efficiency of MC-LR spent FA-BC by PS oxidation. Regeneration conditions: 0.004 g of MC-LR spent FA-BC, 40 mL of PS solution, pH 6, and 20 °C.



### 6.3.2.2 Effect of PS concentration

PS concentration is an important indicator for evaluating the cost for the regeneration of contaminants spent adsorbents by PS oxidation. Figure 6.2b shows that the regeneration efficiencies were 39.90%, 80.63%, 99.18%, and 102.24% at 100, 200, 300, and 400 mg/L of PS, respectively, indicating that the increase of PS concentration resulted in the increase of regeneration efficiency of MC-LR spent FA-BC by PS oxidation. This is because that, with the improvement of PS concentration, more PS ions reacted with  $\text{Fe}^{2+}$  on the surface of FA-BC to produce more  $\text{SO}_4^-$  radicals for the MC-LR oxidation.

### 6.3.2.3 Effect of temperature

Temperature is one of important parameters in the chemical reaction process. In this study, the effect of temperature on the regeneration of MC-LR spent FA-BC was investigated at 20-50 °C. Figure 6.3a indicates that the regeneration efficiency was increased from 80.63% to 97.45% with increasing temperature from 20 °C to 50 °C. The previous study also reported that the increase of reaction temperature resulted in the significant improvement of degradation efficiency of 2,4-dichlorophenol by the  $\text{Fe}^0/\text{PS}$  system. As shown in Figure 6.3b, the PS reaction rate constant was significantly improved from  $0.0634 \text{ h}^{-1}$  to  $0.2228 \text{ h}^{-1}$  with the increase of temperature from 20 °C to 50 °C. This is because the increase of temperature led to the enhancement of  $\text{S}_2\text{O}_8^{2-}$  diffusivity (Table 6.2) according to the Wike-Chang equation, which could enhance the collision frequency between  $\text{S}_2\text{O}_8^{2-}$  and FA-BC and thus improve the reaction rate. In addition, thermal activation of PS also resulted in the production of  $\text{SO}_4^-$ , which also explained that the higher temperature caused the higher PS reaction rate (Huling et al., 2011). Figure 6.3b also shows that MC-LR oxidation rate ( $\text{mg MC-LR/g BC-h}$ ) and PS reaction rate ( $\text{h}^{-1}$ ) were remarkably improved by the factor of

3.42 and 3.51 with increasing temperature from 20 °C to 50 °C. Therefore, the increase of temperature enhanced the PS reaction to improve  $\text{SO}_4^-$  production and MC-LR degradation.

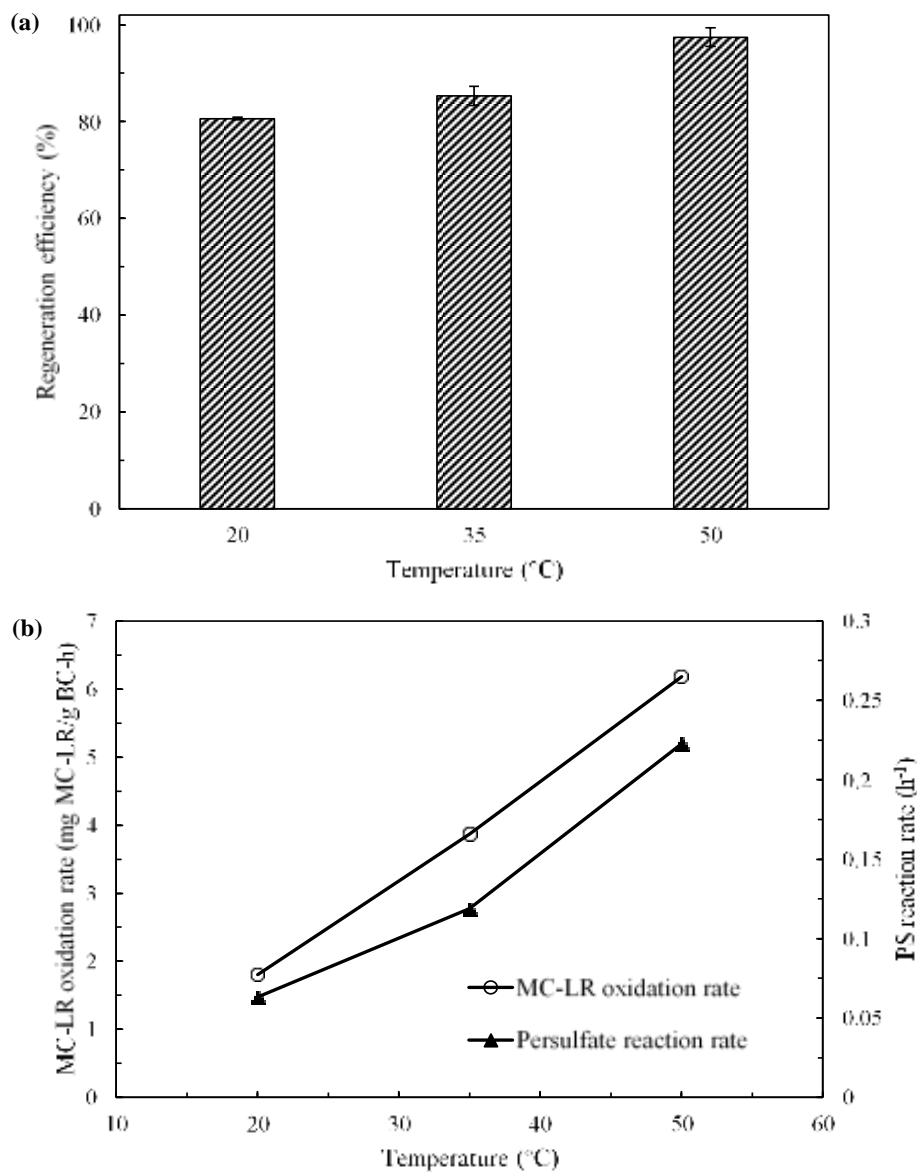


**Figure 6.3.** (a) Effect of temperature on the regeneration efficiency of MC-LR spent FA-BC by PS oxidation. (b) Effect of temperature on the MC-LR oxidation rate and PS reaction rate during the regeneration of MC-LR spent FA-BC by PS oxidation. Conditions: 0.004 g of MC-LR spent FA-BC, 40 mL of 200 mg/L PS, and pH 6.

For further figuring out the rate-limiting steps during the PS oxidation of MC-LR on FA-BC, as displayed in Figure 6.4, the diffusion rate, desorption + diffusion rate, and oxidation rate of MC-LR at various temperatures were compared. Figure 6.4 shows that MC-LR diffusion and desorption + diffusion rates were enhanced by the factor of 2.02 and 3.34 in the temperature range from 20 °C to 50 °C, suggesting that increasing temperature favored both desorption and diffusion of MC-LR. Moreover, higher MC-LR desorption + diffusion rate than diffusion rate also indicates that both desorption and diffusion are important steps for MC-LR mass transport from FA-BC. Additionally, MC-LR oxidation rate on the FA-BC showed a similar slope with MC-LR desorption + diffusion, implying that both diffusion and desorption of MC-LR from FA-BC controlled the MC-LR oxidation during the regeneration of MC-LR spent FA-BC by PS oxidation.

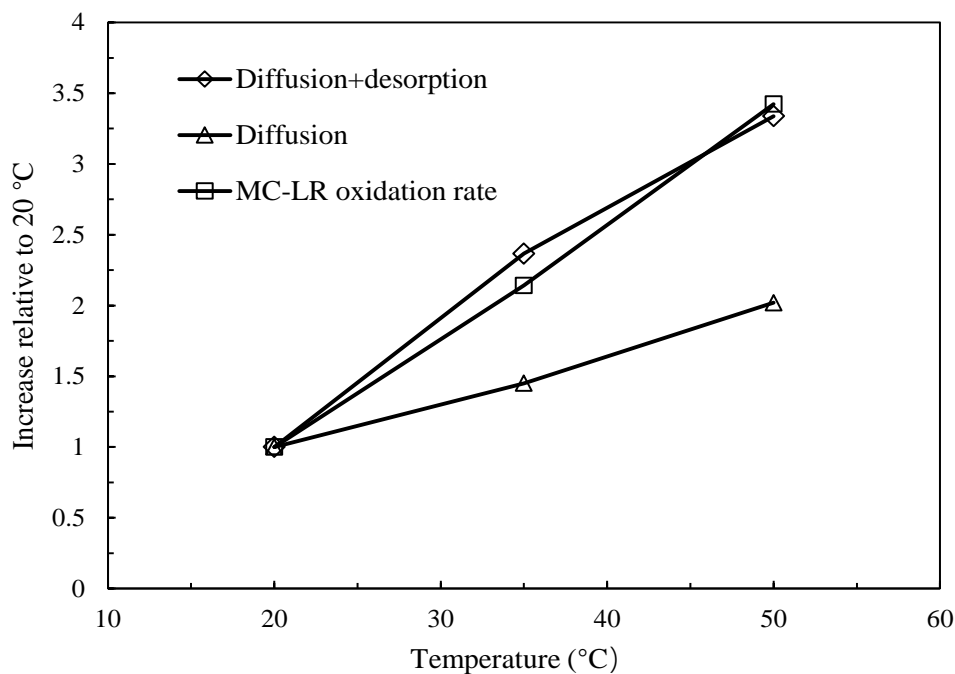


**Figure 6.4.** The temperature-dependent relative increase in the diffusion, diffusion + desorption, and oxidation rate of MC-LR during the regeneration of MC-LR spent FA-BC by PS oxidation.

#### **6.3.2.4 Effect of free radical scavengers**

For determining the main free radicals responsible for the PS oxidation of MC-LR on FA-BC, free radicals quenching tests using ethanol and TBA were carried out in this study. TBA is considered as a scavenger for  $\cdot\text{OH}$ , while ethanol is regarded as a scavenger for both  $\text{SO}_4^{\cdot-}$  and  $\cdot\text{OH}$  radicals (Ouyang et al., 2017; Wei et al., 2020). As indicated in Figure S6.3, the regeneration efficiency of MC-LR spent FA-BC was slightly decreased in the presence of TBA. However, with the addition of 10 mM and 50 mM ethanol, the regeneration efficiency was significantly reduced from 80.63% to 34.50% and 28.49%, respectively. Therefore, the results of radical scavenger tests indicated that  $\text{SO}_4^{\cdot-}$  was the main free radicals responsible for the destruction of MC-LR on the FA-BC during the PS oxidation.

#### **6.3.2.5 Mechanisms for PS oxidation of MC-LR on the FA-BC**

Based on the above-mentioned results and analyses, mechanisms about PS oxidation of MC-LR on FA-BC were proposed as displayed in Figure 6.5. During the regeneration of MC-LR spent FA-BC by PS oxidation, MC-LR was desorbed from the surface of FA-BC and went through the diffusive mass transport in the pores of FA-BC.  $\text{S}_2\text{O}_8^{2-}$  ions were also diffused into the FA-BC pores through the quiescent film surrounding the FA-BC and reacted with iron compounds on the FA-BC to produce  $\text{SO}_4^{\cdot-}$  to oxidize the MC-LR molecules. In addition, some  $\text{Fe}^{2+}$  ions could be released into the bulk solution from FA-BC and activate  $\text{S}_2\text{O}_8^{2-}$  ions in the bulk solution to produce  $\text{SO}_4^{\cdot-}$  for the oxidation of MC-LR released from the FA-BC.

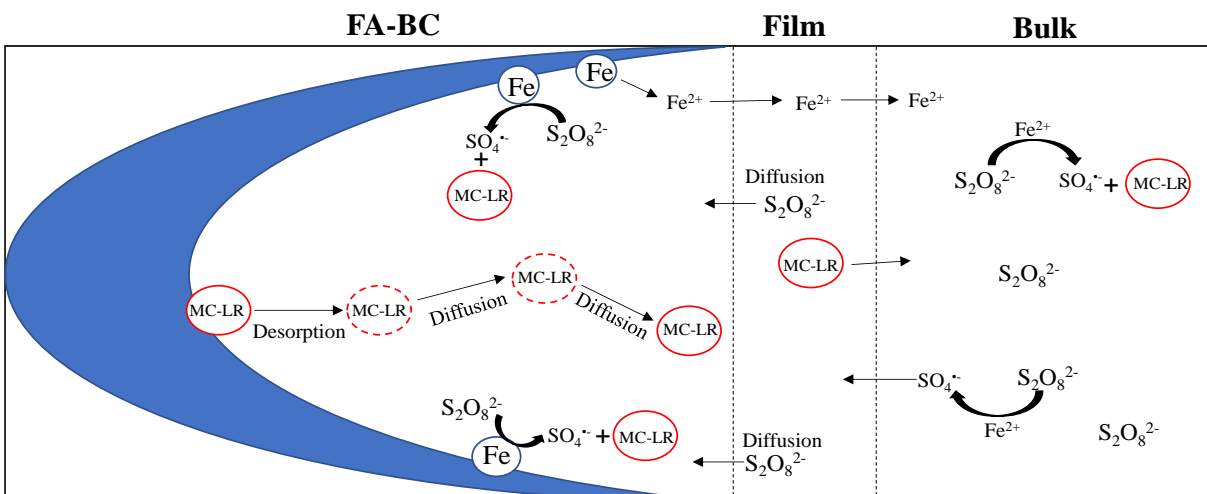


**Figure 6.5.** The proposed mechanisms for the PS oxidation of MC-LR on FA-BC.

### 6.3.3. Reusability and stability of FA-BC by PS oxidation regeneration

In this study, four cycles of successive adsorption and regeneration tests were performed to evaluate the reusability of FA-BC. Figure 6.6 shows that 98.56% and 92.81% of regeneration efficiencies were still achieved in the first and fourth cycles, Moreover, compared to previous reports about PS-driven regeneration of contaminants spent adsorbents (Table S6.1), FA-BC exhibited the excellent reusability of FA-BC for MC-LR adsorption by the regeneration of PS oxidation. The decrease of regeneration efficiency might be due to the accumulation of intermediates or byproducts on the active catalytic sites of FA-BC, negatively affecting the PS activation.

After 4 cycles of PS oxidation, the surface area of FA-BC was reduced from 835.1 m<sup>2</sup>/g to 413.3 m<sup>2</sup>/g, which is possibly due to the damage of pore structure of FA-BC by the attack of free radicals. This result corresponds to previous studies. Liang et al. (2009) indicated that the surface area of activated carbon was significantly decreased from 930 to 719 m<sup>2</sup>/g after 5 cycles of PS oxidation.

Wei et al. (2012) also reported that the surface area of activated carbon was reduced by about 15% after 7 cycles of PS-driven regeneration. In addition, from the XRD analysis (Figure S6.2), the FA-BC after PS oxidation exhibited the same peaks with original FA-BC, while the peak intensities slightly decreased, suggesting that crystalline structure of FA-BC was stable during the PS-driven regeneration process. Moreover, Table S6.2 indicates that iron concentrations were in the range of 0.02 – 1.25 mg/L after the regeneration of MC-LR spent FA-BC by PS oxidation at various pH ranging from 4 to 10. Considering the total iron content of FA-BC was about 30% (data not shown), less than 5% of iron on the FA-BC was released into the solution after PS oxidation, supporting the high regeneration efficiency after four cycles of adsorption-PS oxidation.

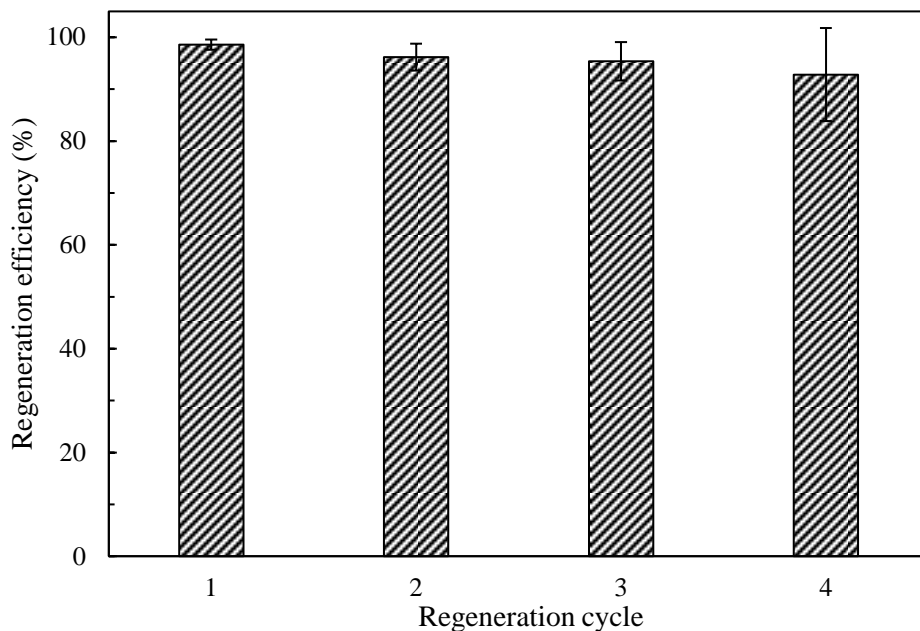


**Figure 6.6.** Reusability of FA-BC for MC-LR adsorption using PS oxidation regeneration. Adsorption conditions: 100 mL of 0.5 mg/L MC-LR, 0.004 g of FA-BC, pH 6, 20 °C and 2 d. Regeneration conditions: 0.004 g of MC-LR spent FA-BC, 40 mL of 200 mg/L PS, pH 6, and 50 °C.

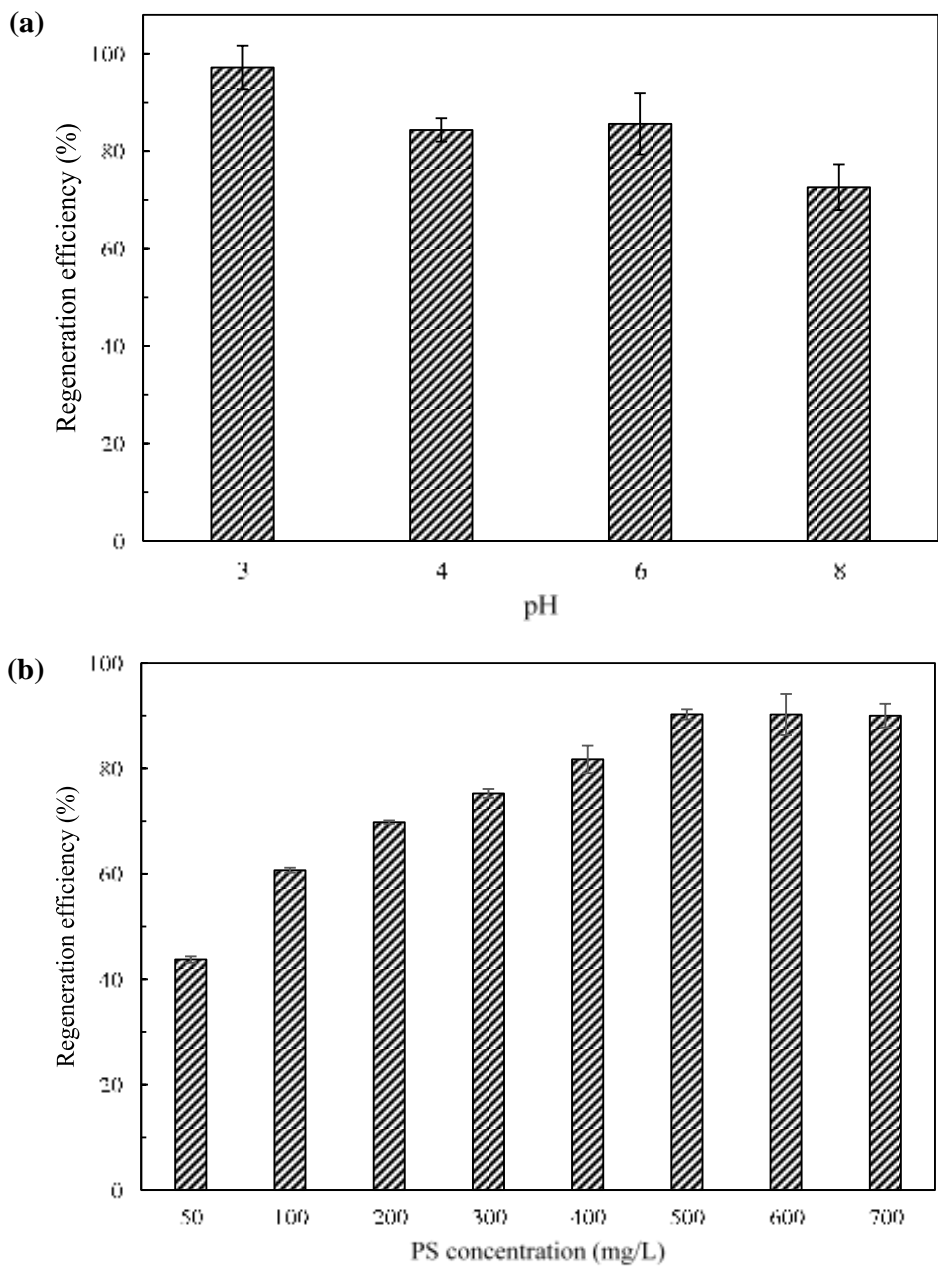


**Figure 6.7.** (a) PS-driven regeneration of tetracycline spent FA-BC at various pH. Regeneration conditions: 0.02 g tetracycline spent FA-BC, 100 mL of 300 mg/L PS, and 2 d. (b) PS-driven regeneration of tetracycline spent FA-BC at various PS concentrations. Regeneration conditions: 0.02 g tetracycline spent FA-BC, 100 mL of PS solution, pH 6, and 2 d.

#### **6.3.4. Application in real lake water**

For evaluating the feasibility of FA-BC for the application in the treatment of real wastewater, MC-LR adsorption tests by FA-BC were also conducted using lake water (Proctor Lake, Dublin, TX, USA). In addition, in this study, PS oxidation was also applied for the regeneration of FA-BC after MC-LR adsorption in lake water. As seen in Figure S6.4, 82.89% of regeneration efficiency was still achieved in the fourth cycle. The regeneration efficiency in lake water was lower than that in DI water, which is because that some organic compounds in lake water (Table S5.1, Chapter V) were adsorbed into FA-BC and might consume the  $\text{SO}_4^-$  radicals. Therefore, FA-BC can be considered as a feasible adsorbent for the treatment of MC-LR contaminated water or wastewater and effectively regenerated by PS oxidation.

#### **6.3.5 Comparison of regeneration of various contaminants spent FA-BC by PS or Fenton oxidation**

From the above analysis, MC-LR could be removed via FA-BC adsorption followed by PS-driven regeneration. In this study, FA-BC was also used to adsorb tetracycline or sulfamethoxazole followed by PS-driven regeneration. As shown in Figure 6.7, tetracycline spent FA-BC could be effectively regenerated by PS oxidation. The regeneration efficiency was about 73-97% in the pH ranging from 3 to 8. However, as shown in Figure 6.8, the regeneration efficiency of sulfamethoxazole spent FA-BC by PS oxidation was very limited and less than 20% under various regeneration conditions, indicating that PS oxidation could not effectively regenerate sulfamethoxazole spent FA-BC. Compared to MC-LR (water solubility: about 1-2 g/L) and tetracycline (water solubility: about 10 g/L), sulfamethoxazole is more hydrophobic and its water solubility is about 379 mg/L. Therefore, compared to sulfamethoxazole, MC-LR and tetracycline



are more easily released into aqueous phase from FA-BC, which might be easily attacked by free radicals.

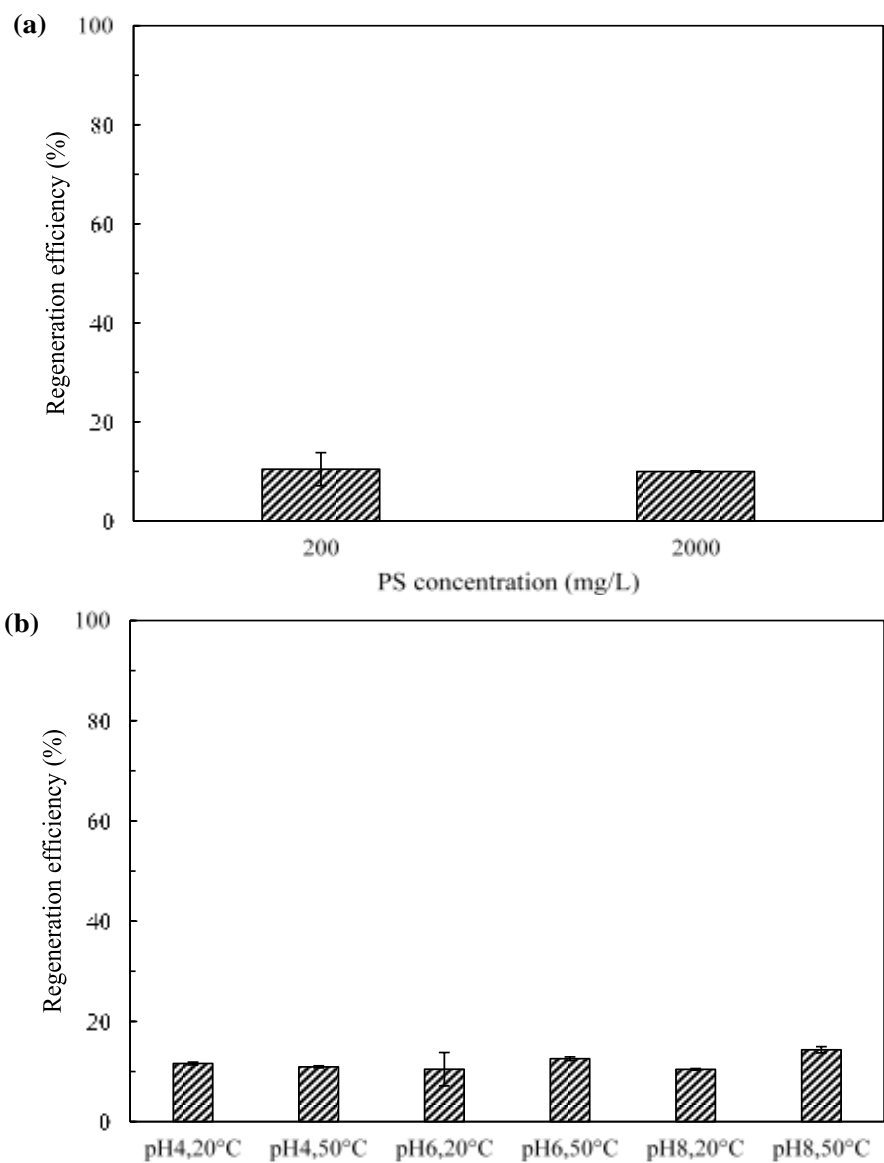


**Figure 6.8.** (a) PS-driven regeneration of sulfamethoxazole spent FA-BC at various PS concentrations. Regeneration conditions: 0.01 g sulfamethoxazole spent FA-BC, 100 mL of PS solution, pH 6, and 2 d. (2) PS-driven regeneration of sulfamethoxazole spent FA-BC at various pH and temperatures. Regeneration conditions: 0.01 g sulfamethoxazole spent FA-BC, 100 mL of PS solution, and 2 d.

Due to the presence of various Fe compounds ( $\text{Fe}_2\text{O}_3$ ,  $\text{Fe}_3\text{O}_4$ , and  $\text{Fe}^0$ ) on FA-BC, Fenton oxidation was also applied for the regeneration of various contaminants spent FA-BC in this study. As shown in Figure S6.5, the regeneration efficiency of sulfamethoxazole spent FA-BC by Fenton oxidation was very poor and less than 20%. The regeneration efficiency of tetracycline and MC-LR spent FA-BC was higher than that of sulfamethoxazole spent FA-BC and between 40% and 60% (Figure S6.6 and Figure S6.7). Therefore, persulfate oxidation showed better performance than Fenton oxidation for regeneration of contaminants spent FA-BC. This is possibly because that sulfate radicals (2.5-3.1 V; 4 s) produced from persulfate oxidation have higher redox potential and lifetime than hydroxyl radicals (1.9-2.7 V; 20 ns) produced from Fenton oxidation (Wang et al., 2017c).

#### **6.4 Conclusions**

$\text{FeCl}_3$  activated biochar (FA-BC) was used to adsorb MC-LR from water and then regenerated by PS oxidation. Pseudo-second order kinetics and Freundlich isotherm models well described the adsorption process onto FA-BC. The increase of temperature resulted in the increase of MC-LR adsorption rate and diffusivity. PS reaction rate and MC-LR oxidation rate on FA-BC were also enhanced with increasing temperature. MC-LR oxidation on FA-BC was mainly dominated by the desorption and diffusion of MC-LR from FA-BC.  $\text{SO}_4^{\cdot-}$  was the main free radical responsible for the degradation of MC-LR during the PS oxidation. In the fourth cycle of adsorption-regeneration, 92.81% and 82.89% of regeneration efficiencies by PS oxidation were still achieved in DI water and lake water.

**CHAPTER VII**

**EFFECT OF ALFALFA-DERIVED BIOCHAR ON ANAEROBIC DIGESTION OF**

**DAIRY MANURE**

**7.1 Introduction**

Anaerobic digestion (AD) is considered as an effective method for the conversion of various organic wastes (animal manures, sludge, food waste, agricultural waste, and so on) to biogas, which is regarded as the renewable energy (Romero-Güiza et al., 2016; Shen et al., 2020; Wang et al., 2018b). Besides easing the energy shortage, AD can solve the problems of environmental pollution resulting from wastes accumulation and reduce the emission of greenhouse gas from the burning of agricultural and industrial wastes (Pan et al., 2019a). Due to being rich in a variety of micronutrients, proteins, and organic matters, animal manures are regarded as the suitable substrates for AD to produce the biogas (Li et al., 2015a). In addition, a large quantity of animal manures (about 132 million metric tons of dried manure ) were annually produced in America (Dolliver et al., 2007). Therefore, AD of animal manure can attain the production of renewable energy biogas while decrease the manure contamination. Heretofore, a substantial number of works about AD of manure have been reported. Chae et al. (2008) investigated the impacts of digesting temperatures and feed loads on the performance of AD of manure and indicated that 35 °C was economical from the aspect of net energy balance. Li et al. (2015a) conducted the AD tests with four various animal manures and achieved the methane yields up to 323-410 mL/g VS<sub>added</sub> and also evaluated the impact of substrate concentration on methane production.

However, the AD process often suffered from the instability of pH, accumulation of toxic intermediates, and low methane production rate (Pan et al., 2019a). In order to improve the AD

performance, a variety of additives have been applied for the AD process, such as activated carbon (AC), carbon nanotube, graphene, iron oxides, and carbon cloth (Zhang et al., 2018a). Carbon nanotubes could improve the electrical conductance of substrates, and accelerate the substrate utilization and methane production rate in the AD reactors (Li et al., 2015b). Carbon cloth improved the AD performance by reducing the volatile fatty acids (VFAs) accumulation and preventing the pH drop (Lei et al., 2016). Graphene could enhance the direct interspecies electron transfer (DIET) between electron-active bacteria and methanogens, resulting in the improvement of methane yield in the AD of ethanol. Similarly, activated carbon also improved the methane production through enriching the *Methanosaeta/Methanosarcina* species on AC and accelerating the DIET in the AD of activated sludge (Yang et al., 2017b). Nevertheless, these additives exhibited the potential environmental risk and high production cost, limiting their practical application. Thus, development of cost-effective and environmentally friendly additives applied in the AD process is highly recommended.

Recently, biochar (BC), made from pyrolyzing the biomass in oxygen-limited conditions, has been considered to be an effective additive for improving the AD performance (Qiu et al., 2019). BC could offer the benign environment for microbial attachment and growth, resulting in the improvement of the activity of AD microorganism (Wang et al., 2018a). In addition, BC could relieve the pH drop from VFAs accumulation and also reduce the ammonia inhibition in the AD process (Pan et al., 2019b). Moreover, BC could act as a microbial supporter to immobilize the cell and also as a conductive medium for facilitating the DIET between VFAs-oxidative bacteria and methanogens (Qiu et al., 2019). So far, considerable research about the effects of BCs derived from various solid wastes on AD has been reported. For example, Pan et al. (2019a) reported that fruitwood-derived biochar could increase the methane yield up to 69% via reducing the ammonia

concentration and improving the buffering ability during the AD of chicken manure. Wang et al. (2017a) added the vermicompost-derived BC into the system of AD of easily acidified substrates and found that BC could offer the excellent buffering ability to hold back the pH drop and cause the significant increase of methane production. In addition, Jang et al. (2018a) mentioned that BC derived from cow manure could achieve a 24.90% increase of methane yield and a 36.84% reduction of lag phase in the mesophilic AD.

On the other hand, the grass alfalfa (AF) is extensively used as animal feed all over the world and is one of the most common hays in America (about 56 million tons per year) (Jang & Kan, 2019a). Hence, considering the amounts of AF production and low cost of AF, AF could be a viable biomass feedstock for BC production. Moreover, applying AF-derived BC in the AD process can become a good bridge linking the grass AF and bioenergy production. To our knowledge, this study firstly investigated the feasibility of the application of AF-derived BC in the AD of dairy manure. Firstly, the effects of AF-derived BC with different addition amounts on biogas and methane production were examined. Then the change of CO<sub>2</sub> during the AD of dairy manure was also analyzed. Finally, the potential roles of AF-derived BC during the AD process were determined on the basis of the analysis of changes of COD, ammonia, phosphate, VFAs, total alkalinity and pH.

## **7.2 Materials and methods**

### **7.2.1 Substrate and inoculum**

Dairy manure used in the present work was obtained from Tarleton dairy farm (Stephenville, Texas, USA). Before the experiments, the manure substrate was dried at 65 °C, ground, and sieved (less than 500 µm). The elemental compositions of dry dairy manure were: C (16.6%), H (2.3%), O (31.0%), N (1.1%), S (0.2%), and ash (48.8%). The inoculum sludge was collected from the lagoon

bottom of Tarleton dairy farm. After collection, the sludge was activated via cultivating with dry manure at mesophilic and anaerobic conditions for about a month (Jang et al., 2018a). Then the activated sludge was utilized as the inoculum for further AD experiments. The main characteristics of the inoculum obtained in the present work were: pH:  $7.72 \pm 0.07$ , total solids (TS):  $29.92 \pm 0.16$  g/L, volatile solids (VS):  $14.55 \pm 0.16$  g/L, total COD (TCOD):  $17.50 \pm 2.12$  g/L, soluble COD (SCOD):  $0.53 \pm 0.01$  g/L, total alkalinity (TA):  $939 \pm 53$  mg CaCO<sub>3</sub>/L, total volatile fatty acids (TVFAs):  $199 \pm 9$  mg/L.

### **7.2.2 Preparation and characterization of biochar**

The grass alfalfa (AF), obtained from a local hay store (Stephenville, Texas, USA), was used as the substrate for biochar production. After dried, ground, and sieved ( $< 500 \mu\text{m}$ ), 10 g of dry AF was introduced to the quartz-tube furnace (MTI corporation, Richmond, USA) for pyrolysis. The pyrolysis conditions were set at 350°C with the heating rate of 10°C/min and retention time of 120 min under the flow of nitrogen gas (2 L/min). The resulting BC was named as “AF-BC”. Then the AF-BC was milled and sieved until the particle size was below 106  $\mu\text{m}$ . The analysis of elemental and mineral compositions of AF and AF-BC were conducted at Robert Microlit Lab (Ledgewood, NJ, U.S.) and Soil, Forage and Water Testing Lab (College Station, TX, U.S.), respectively. Proximate analysis, including fixed carbon, volatile carbon, and ash, were determined according to ASTM D7582-12 (ASTM, 2012a). The surface functional groups of AF-BC were determined by a Fourier Transform Infrared Spectrometer (Bruker Optik GmbH, Ettlingen, Germany).

### **7.2.3 Anaerobic digestion of dairy manure**

BMP (Biochemical Methane Potential) tests were performed for evaluating the impact of BC on the AD of dairy manure. Briefly, 280-mL serum bottle was loaded with 130 mL of inoculum and dry dairy manure. The ratio of inoculum to manure was set to 1 (TS basis). The AF-BC was added

into the serum bottle with four various concentrations (0, 1, 5, and 10 g/L). After inoculation, each serum bottle was sealed with rubber plugs and screw caps. Then nitrogen gas was flushed into each bottle to remove the oxygen and ensure the anaerobic condition. All bottles, in duplicate, were incubated at mesophilic temperature (37 °C) and manually mixed every day. The experiment sets are referred as control, A1, A5, and A10, where control represents the experiment group without addition of AF-BC, and A1, A5, and A10 represent the experiment groups with addition of 1, 5, and 10 g/L of AF-BC.

#### **7.2.4 Analytical methods**

TS, VS, pH, TCOD, SCOD, NH<sub>3</sub>-N, PO<sub>4</sub><sup>3-</sup>, and TA were measured on the basis of APHA standard methods described in the previous report (Association, 2005). Biogas volume was evaluated via a 60-mL syringe, and biogas compositions including methane and carbon dioxide contents were determined through the gas chromatograph (GC) (GC-2014, Shimadzu Corp., Japan) fitted with a packed column and a thermal conductivity detector (TCD) and a flame ionization detector (FID). The operational temperatures of oven, TCD, and FID were set to 80, 110, and 250 °C, respectively. The concentrations of VFAs were also determined by the GC as previously described (Jang et al., 2018a). The FID temperature was also 250 °C and the carrier gas was helium.

#### **7.2.5 Modified Gompertz model**

For evaluating the effect of AF-BC addition on lag phase, maximum production potential and production rate during the AD of dairy manure in the current work, experimental data from BMP experiments were fitted with the modified Gompertz model described in the following equation (Jang et al., 2018a; Pan et al., 2019a):

$$M(t) = P \times \exp \left\{ -\exp \left[ \frac{R_{max} \times e}{P} (\lambda - t) + 1 \right] \right\} \quad (7.1)$$

where  $M(t)$  represents the methane yield in a time  $t$  ( $\text{mL/g VS}_{\text{removed}}$ ),  $P$  represents the maximum methane potential ( $\text{mL/g VS}_{\text{removed}}$ ),  $R_{\text{max}}$  represents the maximum methane production rate ( $\text{mL/g VS}_{\text{removed}} \cdot \text{d}$ ),  $\lambda$  represents the lag phase ( $\text{d}$ ) and  $e$  is the Euler's constant (2.7183). In the present study, the accuracy of prediction of the model was determined through the determination coefficient ( $R^2$ ):

$$R^2 = 1 - \frac{\sum(M_e - M_c)^2}{\sum(M_e - M_{\text{mean}})^2} \quad (7.2)$$

where  $M_e$ ,  $M_c$ , and  $M_{\text{mean}}$  represent the experimental value, calculated value and mean of experimental value, respectively.

## 7.3 Results and discussion

### 7.3.1 Effects of AF-BC addition on methane and biogas production

Biogas and methane production results from AD of dairy manure with different addition amounts of AF-BC were displayed in Figure 7.1. As shown in Figure 7.1, the highest cumulative biogas and methane volumes in the AD of dairy manure were achieved with the addition of 5 g/L (A5) of AF-BC. However, compared to the control, the addition of 1 g/L (A1) and 10 g/L (A2) of AF-BC into the AD of dairy manure showed the negative effects on cumulative biogas and methane volume. For biogas yield, compared with the control, A1 and A5 increased by 15.51% and 26.09%, from 625.99  $\text{mL/g VS}_{\text{removed}}$  to 723.08  $\text{mL/g VS}_{\text{removed}}$  and 789.34  $\text{mL/g VS}_{\text{removed}}$ , respectively. In addition, the methane yields in control, A1, and A5 were 300.01  $\text{mL/g VS}_{\text{removed}}$ , 343.84  $\text{mL/g VS}_{\text{removed}}$ , and 380.64  $\text{mL/g VS}_{\text{removed}}$ , respectively. Therefore, compared with the control, A1 and A5 increased the methane yield by 14.61% and 26.88%, respectively, indicating that the addition of AF-BC effectively improved the methane production in this study. These results are remarkably consistent to the positive impacts of BC on methane and biogas production in the AD process (Martínez et al., 2018; Pan et al., 2019a). Jang et al. (2018a) investigated the impacts of manure-



derived BC on the AD of cow manure and found that BC could significantly increase the methane production rate and potential, with 32.21% and 24.90% increase for cumulative methane volume and yield. Pan et al. (2019a) conducted the AD of chicken manure with addition of nine different kinds of BCs and the results showed that all of BCs significantly improved the methane yield and the addition of fruitwood BC achieved the maximum CH<sub>4</sub> yield of 294 mL/g VS. In addition, the AD of sewage sludge and orange peels carried out by Martínez et al. (2018) indicated that 10 g/L of vineyard pruning-derived BC increased the methane yield by 33% in the batch digestion system.

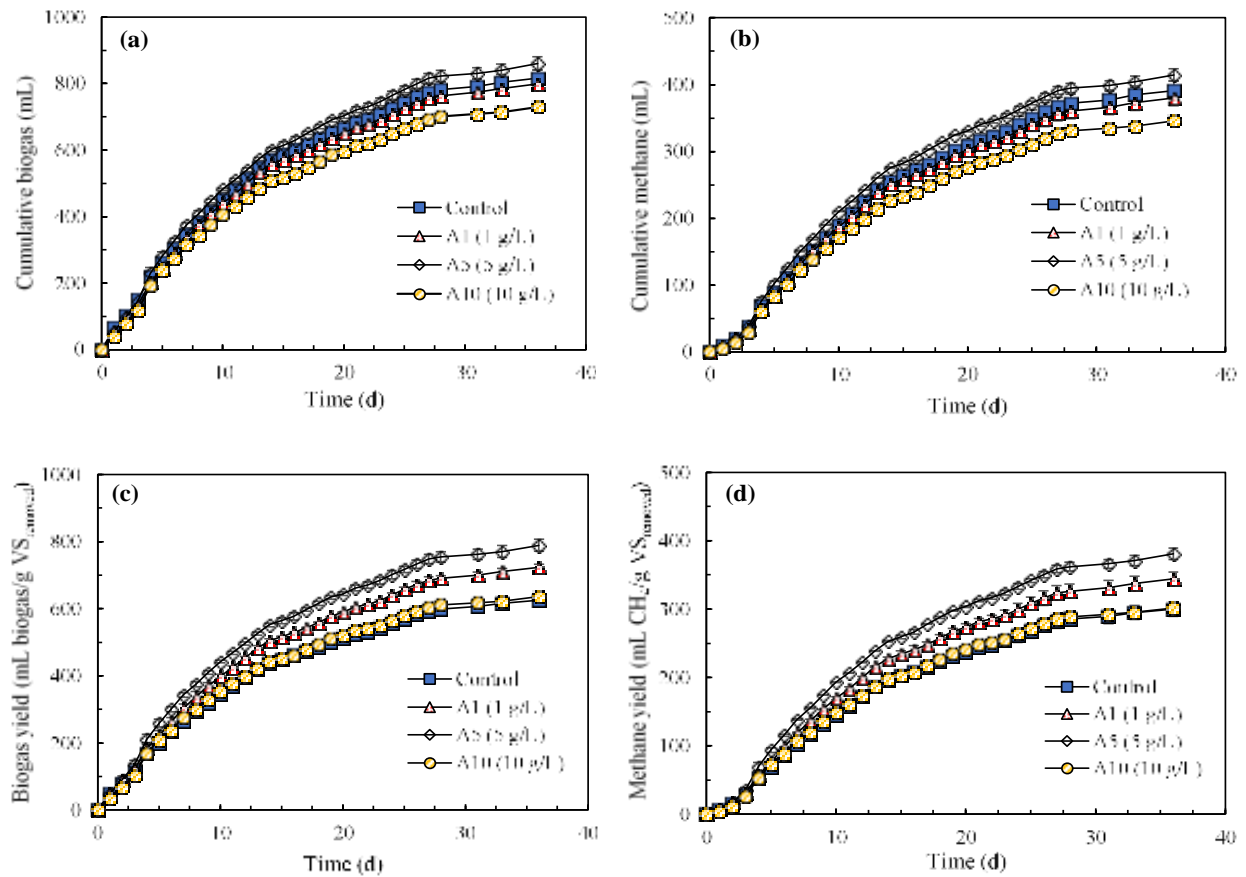


**Figure 7.1.** Cumulative biogas and methane volume (a,b) and yield (c,d) from AD of dairy manure with addition of different concentrations of AF-BC.

However, compared to the control, the addition of 10 g/L of AF-BC showed no obvious enhancement of biogas and methane yields. Figure 7.1 shows that biogas and methane yields were 641.70 mL/g VS<sub>removed</sub> and 301.68 mL/g VS<sub>removed</sub> in A10, and 625.99 mL/g VS<sub>removed</sub> and 300.01 mL/g VS<sub>removed</sub> in control, respectively, indicating that high addition amount of BC was not favorable for AD process. Similar observations have also been described by Shen et al. (2020). They found that methane production from AD of agriculture waste increased from 267.55 mL/g VS to 281.48 mL/g VS under the addition of 2% coconut shell BC, however, CH<sub>4</sub> yield was reduced to 271.50 mL/g VS with increase in BC loading up to 4%. Shen et al. (2016) also reported that the high amount of BC addition in the AD process showed no significant difference for methane production compared to the control. The possible reason is that excessive addition of BCs could inhibit the activity of AD microorganism. Moreover, Sunyoto et al. (2016) investigated the two-phase AD of food wastes with addition of sawdust-derived BC and reported that the cumulative methane production decreased with the increase of BC loading from 8.3 g/L to 33.3 g/L. They also found that excessive BC addition caused the accumulation of propionic acid, thus resulting in the lower methane production.

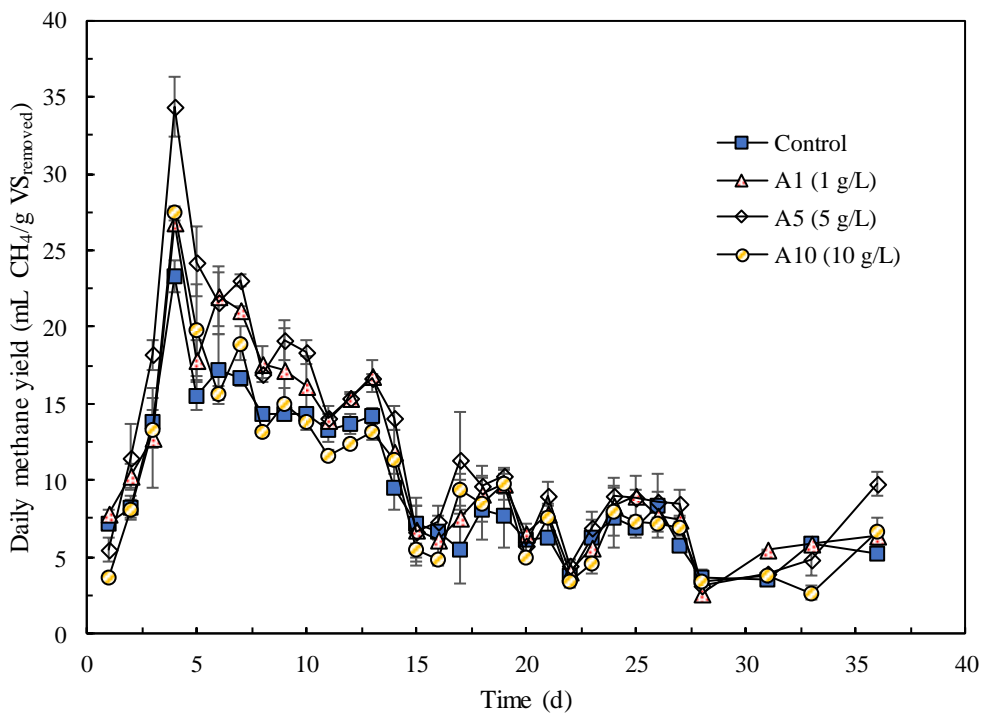


**Figure 7.2.** Daily methane yield from AD of dairy manure with addition of different concentrations of AF-BC.

As displayed in Figure 7.2, the first daily methane yield peak appeared on the fourth day of AD process for all of experiment groups, which might be caused by the consumption of easily degradable organic matters by anaerobic microorganism. The maximum daily methane yield in A1 (26.84 mL/g VS<sub>removed</sub>), A5 (34.35 mL/g VS<sub>removed</sub>), and A10 (27.45 mL/g VS<sub>removed</sub>) was obviously higher than in control (23.29 mL/g VS<sub>removed</sub>), indicating that AF-BC might enhance the utilization efficiency of organic substrates in the initial stage of AD. In addition, the second peak and third peak in A5 (17<sup>th</sup> and 24<sup>th</sup> day) appeared more earlier than those in control (18<sup>th</sup> and 26<sup>th</sup> day), revealing that AF-BC addition might be conducive to the degradation of complex intermediate in the middle and later stage, thus increasing the methane production (Pan et al., 2019a). Pan et al. (2019a) also observed three daily methane yield peaks during the AD of chicken manure and found

that BC addition could make the peaks occur earlier compared with the control without the BC addition.

**Table 7.1** Parameters values of modified Gompertz model fitted with the experimental data.

Biochar addition	Lag phase, $\lambda$ (d)	$R_{\max}$ (mL CH <sub>4</sub> /g VS <sub>removed</sub> ·d)	P (mL CH <sub>4</sub> /g VS <sub>removed</sub> )	R <sup>2</sup>
Control	0.99	15.20	295.78	0.99
A1 (1 g/L)	0.94	17.89	336.85	0.99
A5 (5 g/L)	0.76	19.89	371.51	0.99
A10 (10 g/L)	0.86	15.51	297.47	0.99

In this study, the experimental data were fitted to the Gompertz model to evaluate the impacts of AF-BC addition on microbial kinetics during the AD of dairy manure. As shown in Table 7.1, A1 and A5 achieved significantly higher  $R_{\max}$  (mL CH<sub>4</sub>/g VS<sub>removed</sub>·d) and P (mL CH<sub>4</sub>/g VS<sub>removed</sub>) than control. Compared with the control, both  $R_{\max}$  and P increased by 17.70% and 13.89% in A1, and 30.86% and 25.60% in A5, respectively. These results highly agrees with the previous reports about positive impact of BC addition on  $R_{\max}$  and P during the AD process (Cai et al., 2016; Jang et al., 2018a; Wang et al., 2018b). For example, Jang et al. (2018a) showed that both  $R_{\max}$  and P were improved by 32% and 25% when 10 g/L of manure derived-BC was applied in the process of AD of dairy manure. However, there are no significant differences between control and A10 for  $R_{\max}$  (15.20 vs. 15.51 mL/g VS<sub>removed</sub>·d) and P (295.78 vs. 297.47 mL/g VS<sub>removed</sub>). Shen et al. (2016) indicated that high concentration of BC (4.97 g/g dry sludge) resulted in the lower  $R_{\max}$  and P than low concentration of BC (2.49 g/g dry sludge). Moreover, Wang et al. (2018b) reported that, with improvement in BC concentration from 0 g/L to 6 g/L,  $R_{\max}$  and P significantly increased

during the AD of sludge and food waste, however, markedly decreased when the BC dosage exceeded 6 g/L. In addition, as noted in Table 1, lag phase ( $\lambda$ ) in the present AD process decreased after the addition of AF-BC. Compared to the control,  $\lambda$  was reduced by 5.05%, 23.23%, and 13.13% under the addition of 1, 5, and 10 g/L of AF-BC. Similarly, Fagbohunge et al. (2016) applied three kinds of BCs (Coconut shell BC, Rice husk BC, and wood BC) in the process of AD of citrus peel and indicated that all of BCs could lower the lag phase of AD. Jang et al. (2018a) also found that 1 and 10 g/L of manure derived-BC led to the decrease of lag phase by 10.10% and 26.92%. However, in this study, the lag phase in A10 was higher than that in A5. The possible reason might be that AD microorganism need more time to adapt to more external complex organic matters from high loading of AF-BC, counteracting the part of positive effect of AF-BC on reducing the lag phase.

### **7.3.2 Potential roles of AF-BC in AD**

#### **7.3.2.1 COD, ammonia, and phosphate**

The impacts of AF-BC addition on soluble COD, ammonia, and phosphate removal during the AD process were shown in Figure 7.3. As displayed in Figure 7.3a, the final COD in A1, A5, and A10 was lower than that in control. Compared to the control (47.52%), BC amended AD process achieved the COD removal efficiency of 56.64%, 64.60%, and 62.39% with addition of 1, 5, and 10 g/L of AF-BC, respectively, indicating that AF-BC addition improved the COD reduction during the AD of dairy manure. The possible reason was that microbial activity of AD might be enhanced by BC addition, resulting in higher consumption of organic compounds during the metabolic process of AD. The result is consistent with the previous work of Shanmugam et al. (2018), showing that switchgrass-derived BC could significantly improve the efficiency of COD removal by up to 16% during the AD of glucose. Moreover, Choe et al. (2019) added the bamboo-

derived hydrochar into the system of AD of fish processing waste and showed the significant positive effect of hydrochar on COD reduction. However, the COD removal efficiency in A10 was comparable to the A5, revealing that high dosage of AF-BC was not favorable for further COD reduction. One assumed explanation was that some toxic compounds might be released from excessive biochar and resulted in the negative effect on AD microorganism activity, which also explained the decrease of methane production in A10.

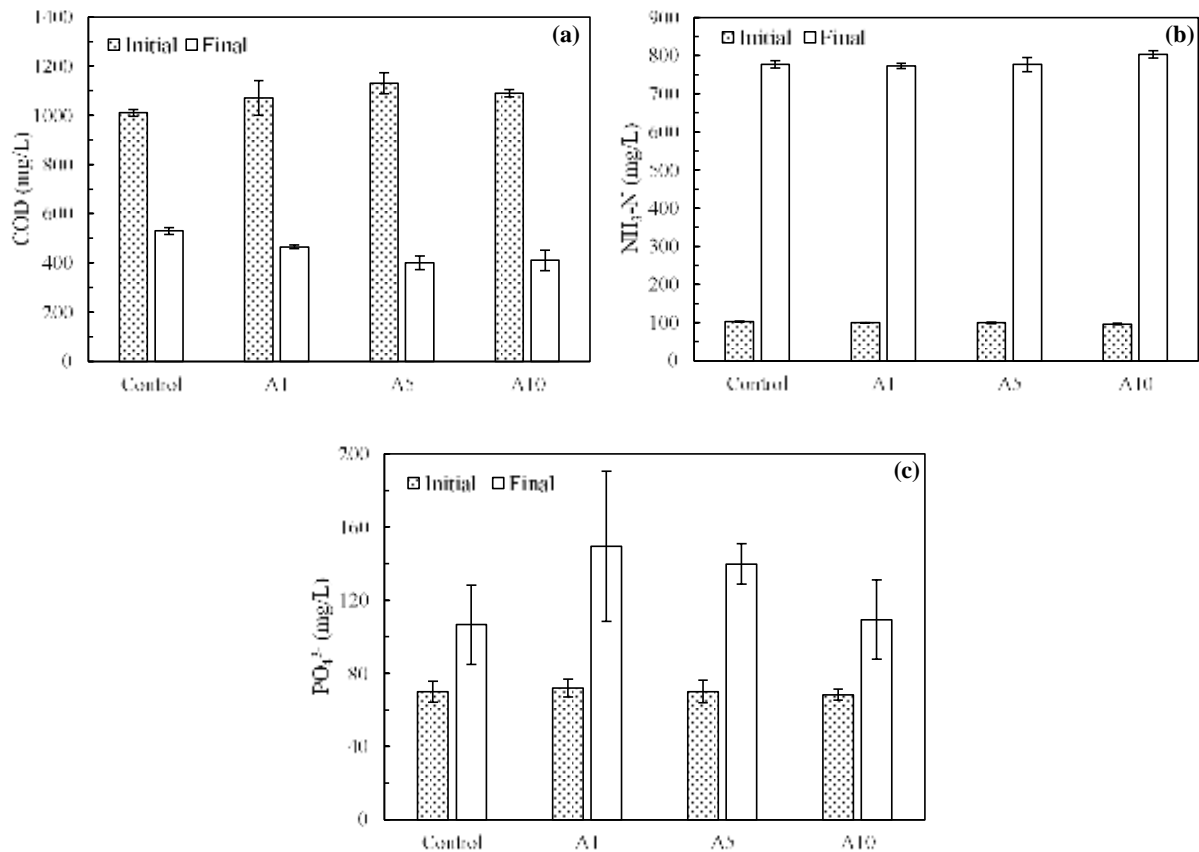


**Figure 7.3.** COD (a), ammonia (b), and phosphate (c) concentrations before and after AD of dairy manure with addition of different concentrations of AF-BC.

As shown in Figure 7.3b, after AD, ammonia concentrations were significantly increased in all of experiment groups, from 96.2-102.4 mg/L NH<sub>3</sub>-N to 773-803 mg/L NH<sub>3</sub>-N, which was from the degradation of nitrogen-containing organic matters by AD microorganism. Moreover, final ammonia concentration in A1 and A5 showed no significant difference with that in control. However, compared to the control, high dosage of AF-BC addition (A10) increased the final ammonia concentration from 777 mg/L to 803 mg/L. This is due to the higher increase of pH from high amount of AF-BC addition (mentioned in section 3.2.4), resulting in the conversion from NH<sub>4</sub><sup>+</sup> to NH<sub>3</sub> (Shen et al., 2015). Because the excess ammonia is toxic to AD microorganism and can cause the instability of AD process, it is one of the possible reasons that high dosage of AF-BC addition was not favorable for the increase of methane production (Shen et al., 2016). Similarly, Figure 7.3c indicated that AD process also improved the phosphate concentration due to the hydrolysis of organophosphorus compounds into inorganic forms. In addition, it is noted that AF-BC addition increased the phosphate concentration after AD process, however, the increase degree decreased with the increase of BC concentration, which might be due to the adsorption of AF-BC.

### **7.3.2.2 CO<sub>2</sub> content**

Biogas, produced from AD process, is mainly composed of methane, carbon dioxide, and other impurities. CO<sub>2</sub>, considered as the greenhouse gas, can cause the climate change. Moreover, higher CO<sub>2</sub> concentration will result in the lower energy value of biogas (Baltrėnas et al., 2019). Therefore, it is preferred to obtain the biogas with the low content of CO<sub>2</sub> during the AD process. Figure 7.4 shows that, after 36-day AD, CO<sub>2</sub> content of biogas in A1, A5, and A10 decreased from 48.59% to 41.98%, 38.57%, and 32.81% compared to the control, respectively, implying that AF-BC addition was favorable for the reduction of CO<sub>2</sub> content. In addition, it is obvious that CO<sub>2</sub> content was also reduced with increase in BC loading from 1 g/L to 10 g/L. It has been reported that BC

has the ability for CO<sub>2</sub> adsorption from biogas via the physisorptive interaction between acidic CO<sub>2</sub> and basic nitrogen functional groups of BC (Sethupathi et al., 2017). Creamer et al. (2014) also mentioned that nitrous groups played an important role in the CO<sub>2</sub> adsorption by the BC. As seen in Figure S7.1, there were some nitrogen-containing functional groups (C-N and N-O) on the surface of AF-BC, which was beneficial for CO<sub>2</sub> capture during the AD process. Similarly, Baltrėnas et al. (2019) conducted the AD of chicken manure with addition of wood BC and indicated that the BC showed no enhancement for biogas production, but reduced the average CO<sub>2</sub> content from 47.5% to 33.1%.

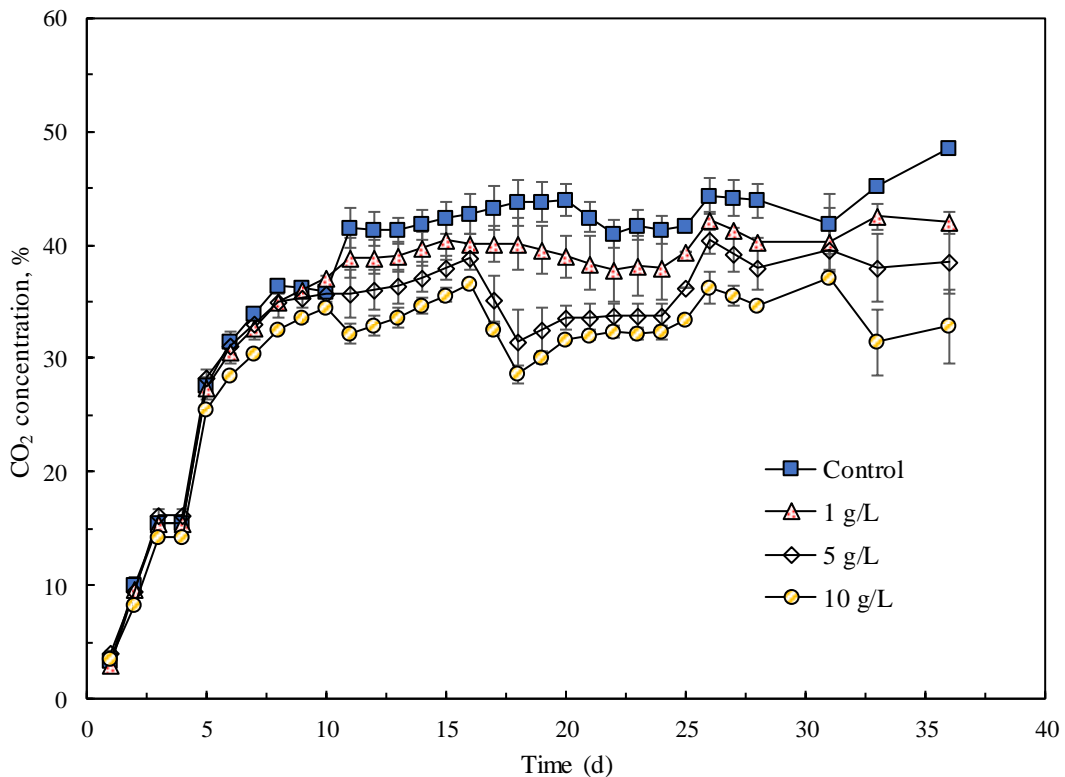


**Figure 7.4.** Change of CO<sub>2</sub> concentration during the AD of dairy manure with addition of different concentrations of AF-BC.



### 7.3.2.3 VFAs analysis

VFAs accumulation can cause the pH drop and inhibit the microbial activity, which frequently occurs in the AD process. Figure 7.5 indicates that all of experiment groups exhibited the similar trend of total VFAs concentration variation, and total VFAs concentration was the highest in the seventh day of AD and then decreased rapidly. This is due to the rapid hydrolysis of the easily degradable organic matters in the manure by the AD microorganism in the initial stage. Compared to the control, total VFAs concentration was significantly reduced with the addition of AF-BC. For instance, in the seventh day, total VFAs concentration in A1, A5, and A10 decreased from 214.66 mg/L (control) to 124.89 mg/L, 94.64 mg/L, and 153.69 mg/L, respectively. Wang et al. (2017a) and Sunyoto et al. (2016) both reported that vermicompost BC and sawdust BC addition could significantly reduce the VFAs accumulation and result in the increase of methane production. In addition, the previous report mentioned that excess BC could cause the excessive acceleration of hydrolysis and methanogenesis, resulting in the imbalance of AD system and the accumulation of intermediates, which finally reduced the methane production (Pan et al., 2019b). Therefore, in this study, it is also observed that total VFAs concentration in A10 was higher than that in A5, which supported the result that high concentration of AF-BC was not favorable for methane production.

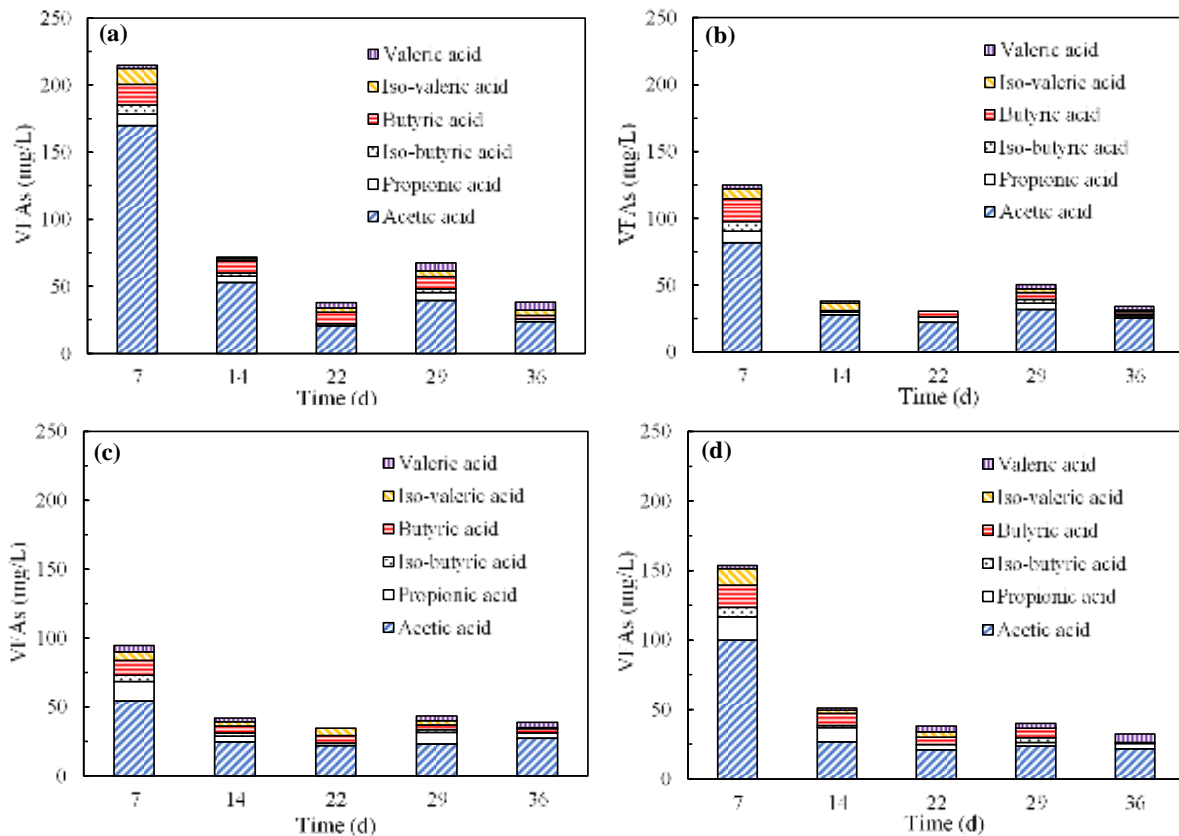


**Figure 7.5.** Changes of VFAs during the AD of dairy manure with addition of 0 g/L (a), 1 g/L (b), 5 g/L (c), and 10 g/L (d) of AF-BC.

As seen in Figure 7.5, acetic acid was the primary VFA from all experiment groups. Acetic acid was the main precursor for methane production and could be directly used by the acetotrophic methanogens for producing the methane (Qiu et al., 2019). Figure 7.5 also indicated that AF-BC addition resulted in the decrease of the concentration of acetic acid, implying that AF-BC can facilitate the transformation of acetic acid to methane and finally improve the methane yield. Lately, DIET has been recognized as the effective pathway to improve the methane production in the AD process (Pan et al., 2019b; Qiu et al., 2019). As shown in Figure S7.1, AF-BC was enriched

with several functional groups, including C-O, C-N, N-O, and C=C, which is favorable for the DITE (Shen et al., 2020). Thus, it can be inferred that AF-BC can enhance the metabolism of acetic acid via the DITE between acetogens and methanogens on the surface of AF-BC, which improved the efficiency of acetate-methanogenesis.

#### **7.3.2.4 Total alkalinity and pH**

Figure 7.6a indicated that TA in A1 was comparable to that in control, however, TAs in A5 and A10 were much higher than that in control during the AD process, implying that AF-BC addition could improve the TA value in the AD system. For example, at the end of AD experiments, compared with the control (1165 g CaCO<sub>3</sub>/L), TAs in A1, A5, and A10 was 1155, 1270, and 1625 g CaCO<sub>3</sub>/L, respectively. Moreover, as shown in Figure 7.6b, higher TA value also led to the increase of pH in the AD process. The reason for higher TA was that AF-BC contained various mineral elements such as N, P, K, Ca, and Mg (Table S7.1), which endowed the AF-BC with the alkalinity property and buffering ability in the AD system (Pan et al., 2019a; Wang et al., 2017a). Wang et al. (2017a) also reported that vermicompost BC addition increased the buffering ability and pH and reduced the VFAs accumulation during the AD of kitchen wastes and chicken manure, resulting in the increase of AD performance and methane production. In this study, higher TA value could cause the conversion of CO<sub>2</sub> into CO<sub>3</sub><sup>2-</sup> and HCO<sub>3</sub><sup>-</sup>, which could be directly utilized by hydrogenotrophic methanogens for methane production (Jang et al., 2018a). Moreover, the decrease of pH drop with AF-BC addition was more favorable for maintaining the activity of AD microorganism. To sum up, in this study, moderate AF-BC addition can significantly improve the performance of AD of dairy manure. Future work will focus on analyzing the compositions of microbial communities and further elucidate the mechanism about positive impact of AF-BC on the AD of manure.

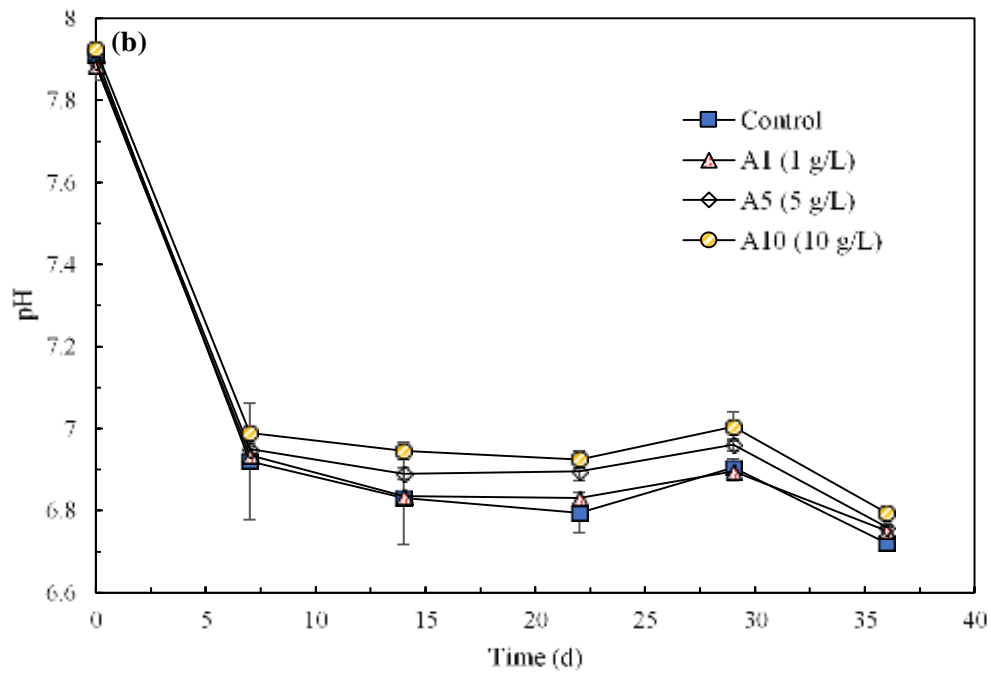
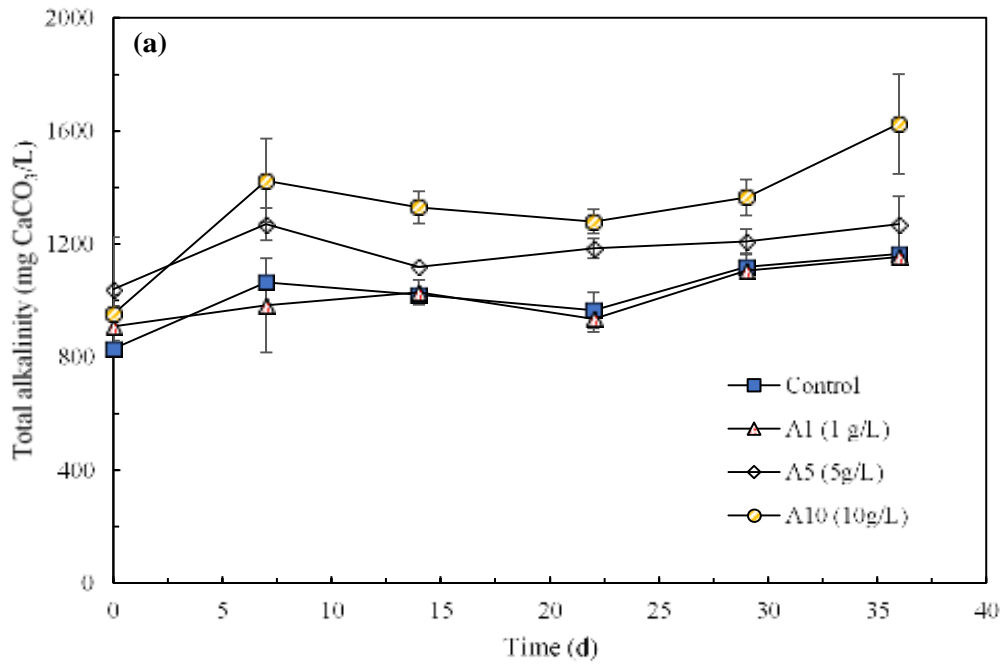


**Figure 7.6.** Changes of TA and pH during the AD of dairy manure with addition of different concentrations of AF-BC.

## **7.4 Conclusions**

The impact of AF-BC on the AD of dairy manure was examined in this study. The AD of dairy manure with AF-BC addition showed the significant enhancement of biogas and methane production compared with the control without AF-BC addition. The biogas and methane yields from the AD process increased by 15.51% and 14.61% with 1 g/L of AF-BC addition, and 26.09% and 26.88% with 5 g/L of AF-BC addition. However, high dosage (10 g/L) of AF-BC addition was not favorable for methane production. In the AD process, AF-BC addition reduced the lag phase and VFAs concentrations and improved the total alkalinity.

## CHAPTER VIII

### EFFECTS OF MECHANICAL REFINING ON ANAEROBIC DIGESTION OF DAIRY MANURE

#### 8.1 Introduction

As mentioned in Chapter VII, current (anaerobic digestion) AD of dairy manure has several shortcomings, such as low digestion and biogas production, fluctuating performance, and generation of significant amounts of undigested sludge (Jang et al., 2018a; Li et al., 2015a). In particular, approximately 40-50% of dairy manure is composed of biofibers, mainly consisting of lignin tightly associated with cellulose and hemicellulose, which is difficult to effectively degrade and hampers AD performance (Angelidaki & Ahring, 2000; Tsapekos et al., 2016).

To enhance the AD performance in dairy manure while effectively degrading biofibers in this manure, various physical, chemical, and biological pretreatments of dairy manure have been investigated. For instance, alkali (10% NaOH, 100°C) and acid (2% HCl, 37°C) pretreatments of dairy manure improved the methane production potential by 23.6% and 20.6% through the breakdown of fibers in manure (Passos et al., 2017). Moreover, Yang et al. (2017a) also reported that the pretreatment of dairy manure with 7% NaOH and 2% polyethylene glycol at 23 °C resulted in the improvement of methane yield by 33% during the AD of dairy manure, which was mainly due to the reduction of lignin in fiber after pretreatment. However, alkali or acid pretreatments often causes additional pollution from intermediates and byproducts generated by these pretreatments, and corrosion of AD reactors (Rodriguez et al., 2015). Ultrasonic treatment of dairy manure slurry with the amplitude of 160  $\mu\text{m}_{\text{pp}}$  and duration of 30 s disintegrated the manure and enhanced the methane yield by 62% during the AD process (Wu-Haan et al., 2010). However, high

energy input and difficult scale-up limited practical application of the ultrasonic pretreatment (Cesaro & Belgiorno, 2014; Rodriguez et al., 2015). The Fe-C microelectrolysis enhanced the electron transfer rate by the soluble redox shuttle secreted from the microorganism attached on the electrode (Qu et al., 2020). This improved the AD performance of dairy manure, methane yield by 81%, and diversity of microbial communities (Qu et al., 2020). Nonetheless, the high complexity of instruments offsets the advantages of Fe-C microelectrolysis (Qu et al., 2020). Furthermore, the combination of ozone and ammonia pretreatment for the AD of dairy manure improved the biogas production by 55-105% compared to the ammonia pretreatment alone, despite high capital costs and high numbers of ozone-associated health problems (Ai et al., 2019). Furthermore, Bruni et al. (2010) used laccase, cellulase, and hemicellulase to pretreat the biofibers from the digested cow manure and found that enzymatic pretreatments showed no effect on the methane yield in the AD of biofibers.

Compared to those chemical and biological pretreatment techniques, mechanical pretreatments have lower sensitivity of substrate specificities and can be easily scaled up for industrial applications (Carrere et al., 2016; Tsapekos et al., 2018). In addition, mechanical pretreatment does not generate any toxic intermediates and byproducts, which are often found during chemical pretreatment (Carrere et al., 2016; Tsapekos et al., 2018). In general, the main objectives of mechanical pretreatment are to lower the particle size and crystallinity and improve the surface area of biorecalcitrant substrates (i.e., lignocellulose), which makes them easily degraded by microorganisms during AD (Rodriguez et al., 2015). To date, considerable research has been conducted to apply the mechanical pretreatments of biomass for the AD process (Kang et al., 2019; Rodriguez et al., 2018; Rodriguez et al., 2017; Tsapekos et al., 2015; Tsapekos et al., 2018). For instance, Rodriguez et al. (2018) reported that the Hollander beater pretreatment of microalgae (*P.*

*canaliculata*) enhanced the methane yield by 45% (283 mL/g VS). Kang et al. (2019) used a grinder to evaluate the effect of particle size of substrate on the AD of grass (*Hybrid Pennisetum*), and achieved a maximum methane yield of 292 mL/g VS in the particle size of 0.25-0.38 mm. However, the application of mechanical pretreatment for the AD of dairy manure is notably limited. Angelidaki and Ahring (2000) reported that mechanical maceration using a mechanical blender reduced the size of biofibers in cattle manure and improved the methane yield by 20% for sizes less than 0.35 mm. In addition, Bruni et al. (2010) and Tsapekos et al. (2016) used kitchen blenders and commercially available heavy plates to pretreat the undigested manure containing biofibers and found that the mechanical pretreatment had a slightly positive impact on the biodegradability of fibers. Despite positive impacts of mechanical pretreatment on AD of dairy manure, high energy input and maintenance costs are still the main bottleneck facing the application of mechanical pretreatments (Cesaro & Belgiorno, 2014; Rodriguez et al., 2015).

Among the mechanical pretreatment methods, mechanical refining (MR) is extensively utilized in the pulp and paper industry. MR can open up the biomass structure via external fibrillation and internal delamination (Park et al., 2016), while most mechanical pretreatment methods require strong mechanical force to lower the particle size of substrates. Therefore, compared to other mechanical pretreatment methods, MR is cost-effective and requires reasonable energy consumption (Park et al., 2016). Recently, MR has been adopted in the biochemical conversion of biomass to overcome biomass recalcitrance by external fibrillation and internal delamination of biofibers; thus, the accessibility of biofibers was significantly enhanced (de Assis et al., 2018; Park et al., 2016). Nevertheless, to the best of our knowledge, the application of mechanical refining to any AD process has not been reported to date.



The major objective of the present work was to employ MR pretreatment of dairy manure to improve the production of biogas and methane from AD of dairy manure. To the best of our knowledge, the current study is the first to investigate the effects of MR on the AD performance of dairy manure. Moreover, the dairy manure containing biofibers was characterized to identify the change in manure morphologies before and after the MR pretreatment. Finally, the potential roles of MR in the AD process were elucidated.

## **8.2 Materials and methods**

### **8.2.1 Preparation of substrate and anaerobic inoculum**

The dairy manure used as the substrate for AD experiments in this study was prepared as described in Chapter VII (Sec. 7.2.1).

The inoculum in this study was obtained as described in Chapter VII (Sec. 7.2.1). The main characteristic parameters of the inoculum were pH:  $8.28 \pm 0.08$ , total solids (TS):  $137.65 \pm 10.11$  g/L, volatile solids (VS):  $27.17 \pm 0.17$  g/L, soluble COD (sCOD):  $2.09 \pm 0.01$  g/L, total alkalinity (TA):  $2.87 \pm 0.11$  g CaCO<sub>3</sub>/L, and total volatile fatty acids (TVFAs):  $9.4 \pm 0.9$  mg COD/L.

### **8.2.2 Mechanical refining of dairy manure**

Mechanical refining was used to pretreat the dry dairy manure by a PFI refiner (see Supplementary data, Figure S8.1), which is usually used for the treatment of pulp fibers. Before the refining, deionized water was mixed with the manure to obtain homogenous samples. The mixture was placed evenly on the wall of a rotating disk of a PFI mill. After that step, samples were refined at two different refining intensities (6,000 and 60,000 revolutions). During the PFI refining, the dairy manure slurry was thrown against the wall of milling housing by the rotation of the rotor. Then, the impacts of rotor bars resulted in the generation of shearing and compression forces, which led to intrafiber bond breakage, external fibrillation, and fiber cutting (Chen et al., 2013).

### **8.2.3 AD of unrefined and mechanically refined dairy manure**

BMP (Biochemical Methane Potential) tests were implemented to evaluate the effects of MR on the AD of dairy manure. The detailed methods for BMP tests was shown in Sec. 7.2.3 of Chapter VII. The experiment sets were referred as MR-control, MR-6K, and MR-60K, which represent the AD of unrefined, 6K (6,000 revolutions) and 60K (60,000 revolutions) refined dairy manure. The AD tests were performed in duplicate, and all bottles were mixed well once a day.

### **8.2.4 Analytical methods**

TS, VS, pH, sCOD, NH<sub>3</sub>-N, TN (total nitrogen), PO<sub>4</sub><sup>3-</sup>, TP (total phosphorus), TA, and TVFAs were measured on the basis of the standard methods for the evaluation of water and wastewater (Federation & Association, 2005). The soluble COD, TP, TN, ammonium, phosphate, and VFAs were conducted as follows: 1 g of dry manure was added to 100 mL of deionized water in a 250-mL conical flask and shaken for 24 h at 150 rpm. Then, the manure leachate was separated by centrifugation and used for measurement.

The biogas volume was determined using a 60-mL syringe, and the methane concentration of biogas and various VFA concentrations were measured by a gas chromatograph (GC) as described in Sec. 7.2.4 of Chapter VII.

To measure the particle size distribution, 1 g of dry manure sample was disintegrated in 1 L of distilled water to measure the manure particle length. Then, 200 ml of each disintegrated sample was added to the beaker and diluted to 600 ml to obtain manure particle frequency values under 15. Average manure particle length was measured by utilizing a Fiber Quality Analyzer (FQA). Optical microscopy images of each sample were obtained by a Nikon E200. The images of surface morphology of the manure were acquired using a Hitachi HT7700 field emission scanning electron microscope (SEM).

The unrefined, 6K and 60K refined samples were utilized to measure water retention value (WRV), which was described in the previous study (de Assis et al., 2018). Each sample slurry was placed in a water retention value vial, and samples were centrifuged for 30 min at 24 °C to remove free water from the samples. The speed of centrifugation was 900 G. Samples were weighed immediately after centrifugation to minimize evaporation loss. After that step, samples were dried at 105 °C overnight to calculate the amount of bound water in the sample. Then, the water retention value was calculated by using the equation:

$$WRV = \frac{W_{wet} - W_{dry}}{W_{dry}} \quad (8.1)$$

where  $W_{wet}$  is the wet sample weight and  $W_{dry}$  is the oven dried sample weight.

### **8.2.5 Kinetic study**

For evaluating the effects of MR on lag phase, maximum production potential and production rate during the AD experiments, the experimental data from BMP tests were fitted with the modified Gompertz model as described in Sec. 7.2.5 of Chapter VII.

## **8.3 Results and discussion**

### **8.3.1 Characterization of unrefined and mechanically refined dairy manure**

Both the arithmetic mean particle size and the length weighted mean particle size decreased with the increase of refining intensity (Table 8.1). Compared to the unrefined manure, the length weighted mean particle size of manure markedly decreased from 0.952 mm to 0.423 mm and 0.367 mm by MR at 6K and 60K revolutions. Moreover, as seen in the Supplementary data (Figure S8.2), considering the distribution of length weighted mean particle size, the length weighted mean particle size of manure refined at 60K revolutions was notably and evenly shortened compared to that refined at 6K revolutions. Similarly, previous studies have also found that size reduction of

biomass was one of the primary consequences of mechanical refining, and particle size decreased with improvement in the refining intensity (Chen et al., 2015b; de Assis et al., 2018).

**Table 8.1** Mean particle size of unrefined and mechanically refined dairy manure.

Revolution	Arithmetic (mm)	Length weighted (mm)
Unrefined	0.312	0.952
6K	0.201	0.423
60K	0.181	0.367

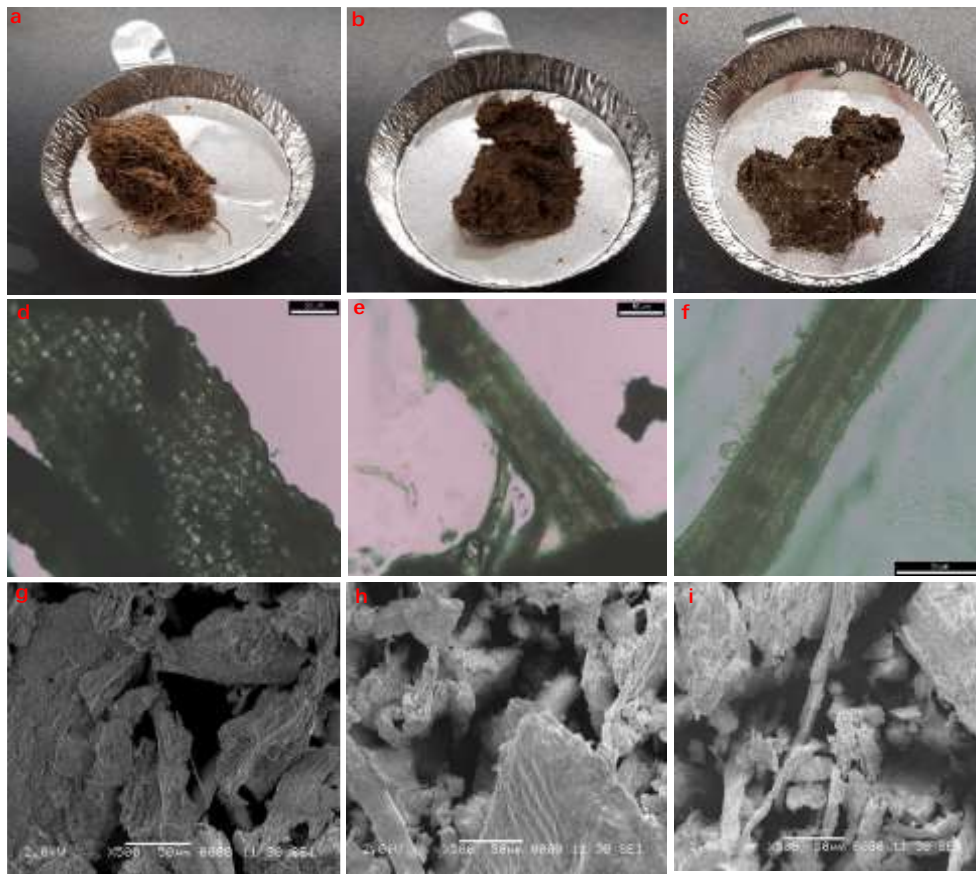


**Figure 8.1.** Photograph (a, b, c), optical microscope (d, e, f) and SEM (g, h, i) images of unrefined (a, d, g) and refined manure with 6K revolutions (b, e, h) and 60K revolutions (c, f, i).

The surface morphologies and texture of manure particles generated by MR at different revolutions were investigated using photographs, optical microscopy and SEM images (Figure 8.1). The morphology of manure became a slurry as the intensity of refining increased (Figure 8.1a-c). Some fibers were observed in the unrefined manure and refined manure at 6K revolutions, but few were observed in the refined manure at 60K revolutions. When fibers are subjected to MR, external fibrillation can occur on the surface of fibers and result in the production of small fibers (Park et al., 2016). Hairy features, resulting from small fibers, were observed in the images of refined manure at 6K and 60K revolutions (Figure 8.1d-f). Due to the production of small fibers, the surface area can increase after MR (Henn & Fraundorf, 1990). Moreover, Figure 8.1d-f also shows that the degree of fibrillation increased with increased refining intensity. From the SEM images (Figure 8.1g-i), the unrefined manure appeared as largely intact clusters that were aggregated; however, the MR produced smaller particles and increased the surface area, which may result from the disruption of manure structure and the delamination of the cell walls of fibers (de Assis et al., 2018). Similar observations were also mentioned by Chen et al. (2015b) and de Assis et al. (2018), which found the same change in biomass structure after MR.

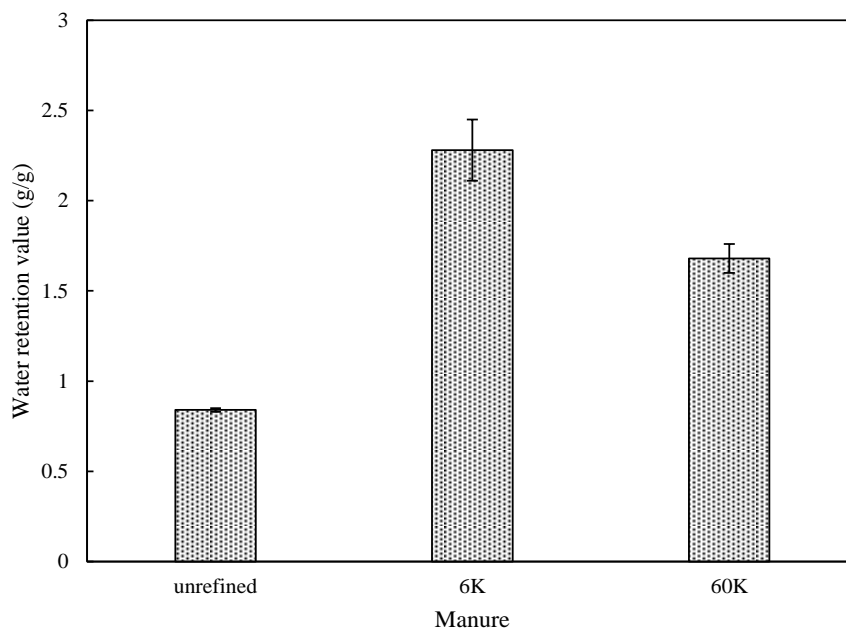


**Figure 8.2.** Water retention value (WRV) of unrefined and refined manure at 6K and 60K revolutions.

The effects of MR on the internal structure of manure were evaluated by measuring the water retention value (WRV). Figure 8.2 shows that the refined manure samples had higher WRVs than the unrefined samples. Compared to unrefined manure, the WRV values of refined manure at 6K and 60K revolutions increased from 0.84 g/g to 2.28 g/g and 1.68 g/g, respectively. In fact, the refining process induces internal delamination, which results from breakage of the crosslinking of interfibrillar matrices (Park et al., 2016). Thus, the cavities generated by internal delamination provide more opportunities for water molecules to stay within the internal structure of fibers. However, the WRV of refined manure at 60K revolutions was lower than that at 6K revolutions. This decrease may result from the collapsed pore structure, which decreased the water molecule accessibility to the internal structure of fibers. Chen et al. (2013) and Hui et al. (2009) also concluded that MR at high revolutions could destroy the pores and cause the loss of macropores.

Moreover, finely ground manure particles might aggregate and block the newly formed surface area of fibers.

**Table 8.2** Solubility of dairy manure before and after mechanical refining.

Revolution	sCOD (mg/kg TS)	TP-PO <sub>4</sub> <sup>3-</sup> (mg/kg TS)	TN-N (mg/kg TS)	PO <sub>4</sub> <sup>3-</sup> (mg/k g TS)	NH <sub>3</sub> -N (mg/kg TS)	TVFA (mg COD/kg TS)	Acetic acid (mg COD/kg TS)	Propionic acid (mg COD/kg TS)
unrefined	2300	3300	1800	217	11.4	1019	475	133
6K	3400	6670	4000	367	42.4	1943	744	134
60K	1200	1580	1100	119	6.2	1399	470	65

The effect of MR on manure solubility is shown in Table 8.2. Compared to the unrefined manure, the refined manure at 6K revolutions showed a drastic enhancement of water quality parameters and metabolites (i.e., soluble COD concentration by 47.83%, soluble total N by 122%, soluble total P by 102%, and soluble TVFA by 90.67%). This finding indicated that after MR at 6K revolutions, more organic and inorganic compounds from the manure were released to the liquid phase, due to the disintegration of the manure matrix and the disruption of fibers in the dairy manure. Low proportions of soluble phosphate in total P (5.50-7.53%) and soluble ammonia in total N (0.56-1.06%) revealed that the majority of soluble total N and P were bonded to organic compounds of manure, which anaerobic fermentative bacteria (acetogenic and acidogenic) would access and convert to biogas and small organic acid (i.e., acetic and butyric acids) as metabolites. Nah et al. (2000) also reported that after the mechanical pretreatment (via a collision-plate at 30 bar) of waste sludge for AD, the sCOD, TP and soluble protein concentrations were significantly increased. However, the manure with MR at 60K revolutions showed a reduction in most of the water quality parameters (sCOD, TP, TN, PO<sub>4</sub><sup>3-</sup> and ammonium) from the unrefined manure

(Table 8.2). This would come from the aggregation of finely ground manure particles, which could inhibit the release of organic and inorganic substances from the manure to the aqueous phase.

### **8.3.2 Effect of mechanical refining on biogas and methane production**

The cumulative biogas and methane volumes and yields from the unrefined and refined dairy manure are listed in Figure 8.3. Figure 8.3 indicates that AD of the manure with MR at 6K revolutions (MR-6K) achieved higher cumulative biogas and higher methane volume and yield than AD of the unrefined manure (MR-control). The cumulative gas volume and yield of MR-6K were 2342 mL and 1110.74 mL biogas/g VS<sub>removed</sub> for biogas, and 1289.29 mL and 611.47 mL CH<sub>4</sub>/g VS<sub>removed</sub> for methane, respectively. Compared to the MR-control, the cumulative gas volume and yield of MR-6K were improved by 32.02% and 6.35% for biogas and 33.65% and 7.66% for methane, respectively. The results strongly correspond with the beneficial effects of mechanical pretreatment of substrates on biogas and methane production during AD, as indicated by other researchers (Rodriguez et al., 2017; Tsapekos et al., 2015). Rodriguez et al. (2017) reported that the mechanical pretreatment of substrates using a Hollander beater improved the methane yield by 21% during mesophilic AD of waste paper. Tsapekos et al. (2015) also applied six mechanical pretreatment methods to meadow grass and evaluated their effects on biomass biodegradability. Compared with the untreated meadow grass, all the pretreatment methods resulted in increasing methane production by 8-25%.



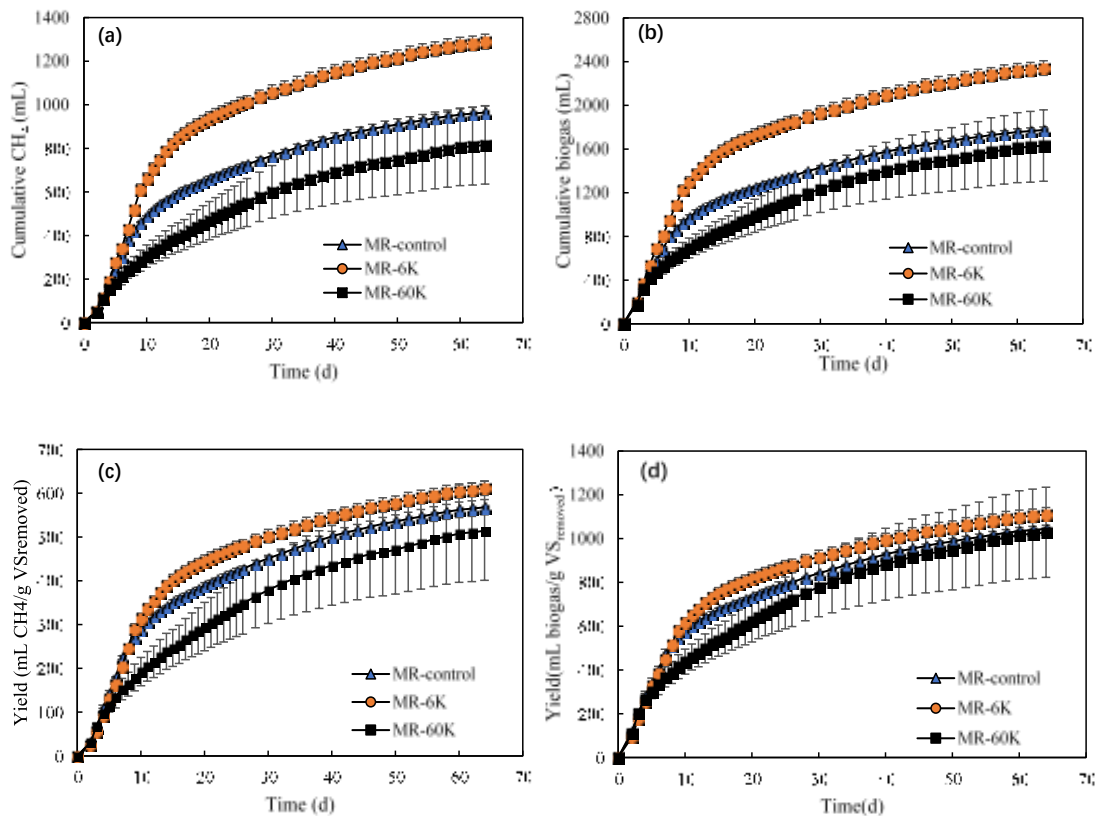


**Figure 8.3.** Cumulative methane and biogas volume (a,b) and yield (c,d) from AD of dairy manure.

Interestingly, MR-60K led to the decrease in biogas yield by 1.51% (from 1044.45 mL biogas/g VS<sub>removed</sub> to 1028.68 mL biogas/g VS<sub>removed</sub>) and methane yield by 9.45% (from 567.98 mL CH<sub>4</sub>/g VS<sub>removed</sub> to 514.21 mL CH<sub>4</sub>/g VS<sub>removed</sub>) compared to the MR-control (Figure 8.3). Tsapekos et al. (2018) also reported that biomass biodegradability increased by 20% through mechanical pretreatment under relatively gentle operation conditions (600 rpm); however, a higher methane yield was not achieved by more intense operation (1200 rpm). Izumi et al. (2010) also used bead milling to decrease the particle size of the substrates of AD for improving the methane yield. The researchers reported that excessive reduction of the particle size of the substrates led to a decrease in methane production during the AD process.

**Table 8.3** Parameters values of modified Gompertz model fitted with the experimental data.

Mechanical refining	Lag phase, $\lambda$ (d)	$R_{\max}$ (mL CH <sub>4</sub> /g VS <sub>removed</sub> ·d)	P (mL CH <sub>4</sub> /g VS <sub>removed</sub> )	R <sup>2</sup>
MR-control	0	24.11	520.53	0.9535
MR-6K	0	27.32	565.76	0.9719
MR-60K	0	15.05	490.90	0.9765

In this study, the modified Gompertz model was fitted to the experimental data to evaluate the effects of MR on microbial kinetics during AD. Table 8.3 shows that MR-6K achieved significantly higher  $R_{\max}$  (27.32 mL CH<sub>4</sub>/g VS<sub>removed</sub>·d) and P (565.76 mL CH<sub>4</sub>/g VS<sub>removed</sub>) than the MR-control. Compared to the MR-control, both  $R_{\max}$  and P were increased by 13.31% and 8.69%, respectively, in MR-6K. These results are highly consistent with previous studies that demonstrated the positive impact of mechanical pretreatment on  $R_{\max}$  and P in AD (Kang et al., 2019; Tsapekos et al., 2018). However, both  $R_{\max}$  and P of MR-60K decreased by 37.58% and 5.69% compared to the MR-control, and 44.91% and 13.23% compared to MR-6K, respectively. Similarly, Tsapekos et al. (2018) also found that compared to mechanical pretreatment operated at moderate rotating conditions (600 rpm) during AD of meadow grass, the P value significantly decreased with the highest rotating speeds (900 and 1200 rpm). In the previous study, Tsapekos et al. (2017) found that the full scale mechanical pretreatment caused significant damage to the surface of lignocellulosic biomass and augmented access to the organic matter, resulting in a decreased lag phase during AD. However, in this study,  $\lambda$  values in all AD experiments were zero because the inocula for all AD tests were highly activated and already fully adapted to mesophilic conditions before the AD experiments began.

### **8.3.3 Potential roles of mechanical refining in AD of dairy manure**

Mechanical stress on lignocellulosic biomass in the refining process can cause various alternations to biomass structure (Park et al., 2016). There are three mechanisms associated with the mechanical refining of biomass: cutting, external fibrillation, and internal delamination (de Assis et al., 2018; Park et al., 2016). Through cutting, refined manure at 6K revolutions had smaller particles, higher surface area, and easier access to bacteria and enzymes associated with AD, resulting in a higher production of biogas and methane during AD than unrefined manure (Park et al., 2016). Similar to cutting, MR also led to higher surface area and anaerobic biodegradability through external fibrillation of biofibers in the manure (Chen et al., 2015b). In addition, the internal delamination induced by MR caused the rupture of crosslinking of interfibrillar matrices and the generation of cavities inside the cell wall structure (Chen et al., 2013; Park et al., 2016). Thus, the approachability of cellulose in biofibers to enzyme and bacteria was significantly improved after MR, thereby enhancing the hydrolysis efficiency and methane production. However, MR at high revolutions (60K) caused the breakage of pore structure of biofibers in manure, which decreased the manure digestibility due to the reduced enzyme attack during the AD process.

From the AD parameters listed in Table 8.4, the initial concentrations of sCOD, TP and TN at MR-6K were higher than those of the MR-control. Moreover, as discussed above, the mechanical refining enhanced the release of organic P and N from manure to the liquid phase. Thus, it can be concluded that the MR resulted in higher soluble organic substances in the manure sample, which can be easily utilized by the microorganisms associated with AD for increasing methane production. However, MR-60K had lower sCOD, TP and TN compared to the MR-control and MR-6K, which might result from aggregation of finely ground manure particles, which would prevent the release of organic substances from the manure. In addition, MR-6K had a higher

consumption of sCOD (62%) than the MR-control (58%) and MR-60K (50%). Furthermore, the final NH<sub>3</sub>-N concentration from the MR-60K was lower than that from the MR-control and MR-6K, indicating lower degradation and conversion of refined manure at 60K revolutions to soluble ammonia. This also explains the lower production of methane from MR-60K than the MR-control and MR-6K.

**Table 8.4** Operation parameters for AD process with different dairy manure.

Operation parameters	MR-control		MR-6K		MR-60K	
	Initial	Final	Initial	Final	Initial	Final
sCOD (g/L)	6.94	2.89	9.18	3.48	4.16	2.09
TP-PO <sub>4</sub> <sup>3-</sup> (mg/L)	62.6	22.6	77.1	31.7	44.4	39.3
TN-N(mg/L)	810	1120	1020	1150	720	730
NH <sub>3</sub> -N(mg/L)	504	767	500	761	508	561
PO <sub>4</sub> <sup>3+</sup> (mg/L)	8.78	10.15	8.52	14.45	8.83	19.6
TA (mg CaCO <sub>3</sub> /L)	3900	4940	4090	5060	3100	3890
TVFA (mg COD/L)	38.4	70.1	131.2	64.0	107.4	35.5
Acetic acid (mg COD/L)	32.3	59.2	96.9	48.5	85.3	31.8
Propionic acid (mg COD/L)	6.1	10.9	24.1	9.8	14.0	3.7
pH	7.44	7.19	7.86	7.27	7.96	6.97
VS (g/L)	60.77	43.78	69.17	48.09	57.75	41.89

As listed in Table 8.4, the initial TVFAs concentration of MR-6K was higher than those of the MR-control and MR-60K. Although a high concentration of TVFAs would possibly inhibit methane production from AD, the inoculum used in this study was highly activated so that the high level of VFAs was directly consumed and converted to methane. Thus, a higher initial concentration of TVFAs in MR-6K would be beneficial for biogas and methane production in this study. However, similar to sCOD, TP and TN, MR-60K reduced the release of VFAs from the manure due to aggregation of finely ground manure particles. It is reported that acetic acid is the primary precursor for methane production, while propionic acid can be converted to acetic acid in

the absence of acetic acid (Izumi et al., 2010; Zheng et al., 2015). Thus, higher initial concentrations of acetic and propionic acid at MR-6K led to higher methane production than for the MR-control and MR-60K. Table 8.4 also shows the TA concentration of MR-6K before and after AD was higher than that of the MR-control and MR-60K. Having higher TA in MR-6K could provide higher buffering capacity during the AD of manure, which can improve the AD process stability by alleviating the pH drop from the accumulation of VFAs (Jang et al., 2018a). This could also enhance the methane production in MR-6K compared to the MR-control and MR-60K. Overall, the appropriate mechanical pretreatment of dairy manure containing biofiber (6K revolutions in this study) increased the release of organic substances and AD metabolites from the manure to enhance biogas and methane production. Future studies will focus on detailed optimization of mechanical refining (i.e., mechanical intensity, process time), achieving a continuous AD process with mechanically pretreated manure, and scale-up studies.

#### **8.4 Conclusions**

The effects of mechanical refining on anaerobic digestion of dairy manure were investigated in this study. MR-6K showed a significant enhancement of biogas and methane production due to the increase in manure solubilization, reduction in particle size, and external fibrillation and internal delamination of fibers in manure compared to the MR-control. The cumulative gas volume and yield from MR-6K increased to 33.7% and 7.7% for methane and to 32.0% and 6.4% for biogas, respectively. However, MR-60K exhibited even lower biogas and methane production than the MR-control and MR-6K due to the rupture of pore structure and aggregation of finely ground manure particles, which could prevent access and digestibility of microorganisms and enzymes associated with AD.

## CHAPTER IX

### SUMMARY AND CONCLUSIONS

In this dissertation, NaOH and FeCl<sub>3</sub> activated BCs derived from bermudagrass were successfully prepared, characterized, and applied for the removal of emerging contaminants in water. In addition, mechanical refining and biochar addition were also applied for the improvement of performance of anaerobic digestion (AD) of dairy manure.

After NaOH activation, high surface area (1992 m<sup>2</sup>/g) was observed with a significant increase in adsorption capacity for SMX (456 mg/g BC), which was higher than those of various adsorbents from previous studies as well as commercial activated carbons. The effect of initial pH, kinetic and isotherm studies indicated the strong chemisorptive interaction between SMX and activated BC via  $\pi$ - $\pi$  EDA, hydrophobic and hydrogen bond interactions. Good regeneration capacity for multiple cycles was achieved using NaOH as the desorption agent, indicating that NaOH activated BC had the high potential for SMX removal in water.

After FeCl<sub>3</sub> activation, activated BC produced from the impregnation mass ratio of 2.0 (FeCl<sub>3</sub>/BG) showed high surface area (1013 m<sup>2</sup>/g) and best adsorption ability (265 mg/g BC) for SMX, and can be separated by the magnet after adsorption. The rate-limiting step for SMX adsorption onto FeCl<sub>3</sub> activated BC was controlled by intraparticle diffusion. The thermodynamic parameters suggested that the adsorption process was spontaneous and exothermic. Both NaOH desorption and thermal oxidation methods can effectively regenerate SMX saturated FeCl<sub>3</sub> activated BC.

FeCl<sub>3</sub> activated BC without acid washing was applied for SMX removal through simultaneous adsorption and heterogeneous Fenton oxidation. Acid washing increased adsorption ability and decreased Fenton oxidation ability of FeCl<sub>3</sub> activated BC for SMX removal due to the

improvement of surface area and reduction of iron content. After  $\text{FeCl}_3$  activation,  $\text{Fe}_2\text{O}_3$ ,  $\text{Fe}^0$ , and  $\text{Fe}_3\text{O}_4$  were successfully attached onto  $\text{FeCl}_3$  activated BC without acid washing. Under the optimal conditions (100 mg/L of SMX, 100 mg/L of BC, pH 3, 200 mg/L of  $\text{H}_2\text{O}_2$ , and 20 °C), removal efficiencies of SMX and COD were up to 99.94% and 65.19%, respectively. The  $\cdot\text{OH}$  radicals were proved to be the dominant radicals during the SMX oxidation. Furthermore, the reusability tests showed that 89.58% of SMX removal efficiency was still achieved after 3 cycles under the optimal conditions.

$\text{FeCl}_3$  activated BC was also applied for the removal of microcystin-LR (MC-LR) in water. The kinetics and isotherm studies indicated that MC-LR adsorption occurred on the heterogeneous surface of  $\text{FeCl}_3$  activated BC by chemical interaction. The thermodynamics study suggested that MC-LR adsorption was a spontaneous and endothermic process. The thermal regeneration at 300 °C showed excellent regeneration efficiency (above 99%) of MC-LR spent  $\text{FeCl}_3$  activated BC after 4 successive cycles. In addition, persulfate oxidation showed better performance than Fenton oxidation to regenerate the MC-LR spent  $\text{FeCl}_3$  activated BC. Persulfate reaction rate and MC-LR oxidation rate on  $\text{FeCl}_3$  activated BC were enhanced with increasing temperature. MC-LR oxidation was mainly dominated by the desorption and diffusion of MC-LR from  $\text{FeCl}_3$  activated BC.  $\text{SO}_4^{\cdot-}$  was the main free radical responsible for the degradation of MC-LR during the PS oxidation. In the fourth cycle of adsorption-regeneration, 92.81% and 82.89% of regeneration efficiencies by persulfate oxidation were still achieved in DI water and lake water.

Mechanical refining (MR) at 6,000 revolutions showed a significant enhancement of biogas and methane production from AD of dairy manure due to the increase in manure solubilization, reduction in particle size, and external fibrillation and internal delamination of fibers in manure compared to that without MR pretreatment. . However, MR at 60,000 revolutions resulted in the

decrease of biogas and methane production due to the rupture of pore structure and aggregation of finely ground manure particles, which could prevent access and digestibility of microorganisms and enzymes associated with AD.

The AD of dairy manure with hay-derived BC addition showed the significant enhancement of biogas and methane production compared with the control without BC addition. The biogas and methane yields from the AD process increased by 15.51% and 14.61% with 1 g/L of BC addition, and 26.09% and 26.88% with 5 g/L of BC addition. However, high dosage (10 g/L) of BC addition was not favorable for methane production. In the AD process, hay-derived BC addition reduced the lag phase and VFAs concentrations and improved the total alkalinity.



## REFERENCES

- Ahmad, M., Rajapaksha, A.U., Lim, J.E., Zhang, M., Bolan, N., Mohan, D., Vithanage, M., Lee, S.S., Ok, Y.S. 2014. Biochar as a sorbent for contaminant management in soil and water: a review. *Chemosphere*, 99, 19-33.
- Ahmed, M.B., Zhou, J.L., Ngo, H.H., Guo, W., Johir, M.A.H., Belhaj, D. 2017a. Competitive sorption affinity of sulfonamides and chloramphenicol antibiotics toward functionalized biochar for water and wastewater treatment. *Bioresource Technology*, 238, 306-312.
- Ahmed, M.B., Zhou, J.L., Ngo, H.H., Guo, W., Johir, M.A.H., Sornalingam, K. 2017b. Single and competitive sorption properties and mechanism of functionalized biochar for removing sulfonamide antibiotics from water. *Chemical Engineering Journal*, 311, 348-358.
- Ahmed, M.B., Zhou, J.L., Ngo, H.H., Guo, W., Johir, M.A.H., Sornalingam, K., Sahedur Rahman, M. 2017c. Chloramphenicol interaction with functionalized biochar in water: sorptive mechanism, molecular imprinting effect and repeatable application. *Science of the Total Environment*, 609, 885-895.
- Ahmed, M.B., Zhou, J.L., Ngo, H.H., Guo, W., Thomaidis, N.S., Xu, J. 2017d. Progress in the biological and chemical treatment technologies for emerging contaminant removal from wastewater: A critical review. *Journal of Hazardous Materials*, 323(Pt A), 274-298.
- Ai, P., Zhang, X., Dinamarca, C., Elsayed, M., Yu, L., Xi, J., Mei, Z. 2019. Different effects of ozone and aqueous ammonia in a combined pretreatment method on rice straw and dairy manure fiber for enhancing biomethane production. *Bioresource Technology*, 282, 275-284.
- An, D., Westerhoff, P., Zheng, M., Wu, M., Yang, Y., Chiu, C.A. 2015. UV-activated persulfate oxidation and regeneration of NOM-Saturated granular activated carbon. *Water Research*, 73, 304-310.
- Angelidaki, I., Ahring, B.K. 2000. Methods for increasing the biogas potential from the recalcitrant organic matter contained in manure. *Water Science and Technology*, 41(3), 189-194.
- Association, A.P.H. 2005. APHA (2005) Standard methods for the examination of water and wastewater. APHA Washington DC, USA.
- ASTM, A. 2010. D7582–10. Standard Test Methods for Proximate Analysis of Coal and Coke by Macro Thermogravimetric Analysis. Annual Book of ASTM Standards. American Society for Testing and Materials, West Conshohocken, PA.
- ASTM, D. 2012a. 7582-12. Standard test methods for proximate analysis of coal and coke by macro thermogravimetric analysis. ASTM: West Conshohocken, PA.

- ASTM, D.J.A.W.C., PA. 2012b. 7582-12. Standard test methods for proximate analysis of coal and coke by macro thermogravimetric analysis.
- Atandi, E., Rahman, S. 2012. Prospect of anaerobic co-digestion of dairy manure: a review. *Environmental Technology Reviews*, 1(1), 127-135.
- Avisar, D., Lester, Y., Ronen, D. 2009. Sulfamethoxazole contamination of a deep phreatic aquifer. *Science of the Total Environment*, 407(14), 4278-4282.
- Bai, X., Acharya, K. 2016. Removal of trimethoprim, sulfamethoxazole, and triclosan by the green alga *Nannochloris* sp. *Journal of Hazardous Materials*, 315, 70-75.
- Bajracharya, A., Liu, Y.-L., Lenhart, J.J. 2019. The influence of natural organic matter on the adsorption of microcystin-LR by powdered activated carbon. *Environmental Science: Water Research & Technology*, 5(2), 256-267.
- Baltrėnas, P., Paliulis, D., Kolodynski, V. 2019. The experimental study of biogas production when digesting chicken manure with a biochar additive. *Greenhouse Gases: Science and Technology*, 9(4), 837-847.
- Bandala, E.R., Martinez, D., Martinez, E., Dionysiou, D.D. 2004. Degradation of microcystin-LR toxin by Fenton and Photo-Fenton processes. *Toxicon*, 43(7), 829-832.
- Bombuwala Dewage, N., Liyanage, A.S., Pittman, C.U., Jr., Mohan, D., Mlsna, T. 2018. Fast nitrate and fluoride adsorption and magnetic separation from water on alpha-Fe<sub>2</sub>O<sub>3</sub> and Fe<sub>3</sub>O<sub>4</sub> dispersed on Douglas fir biochar. *Bioresource Technology*, 263, 258-265.
- Braghiroli, F.L., Bouafif, H., Neculita, C.M., Koubaa, A. 2018. Activated Biochar as an Effective Sorbent for Organic and Inorganic Contaminants in Water. *Water, Air, & Soil Pollution*, 229(7), 230.
- Bruni, E., Jensen, A.P., Angelidaki, I. 2010. Comparative study of mechanical, hydrothermal, chemical and enzymatic treatments of digested biofibers to improve biogas production. *Bioresource Technology*, 101(22), 8713-8717.
- Cai, J., He, P., Wang, Y., Shao, L., Lu, F. 2016. Effects and optimization of the use of biochar in anaerobic digestion of food wastes. *Waste Management & Research*, 34(5), 409-16.
- Çalışkan, E., Göktürk, S. 2010. Adsorption Characteristics of Sulfamethoxazole and Metronidazole on Activated Carbon. *Separation Science and Technology*, 45(2), 244-255.
- Calisto, V., Ferreira, C.I., Oliveira, J.A., Otero, M., Esteves, V.I. 2015. Adsorptive removal of pharmaceuticals from water by commercial and waste-based carbons. *Journal of Environmental Management*, 152, 83-90.
- Carratalá-Abril, J., Lillo-Ródenas, M.A., Linares-Solano, A., Cazorla-Amorós, D. 2010. Regeneration of activated carbons saturated with benzene or toluene using an oxygen-containing atmosphere. *Chemical Engineering Science*, 65(6), 2190-2198.

- Carrere, H., Antonopoulou, G., Affes, R., Passos, F., Battimelli, A., Lyberatos, G., Ferrer, I. 2016. Review of feedstock pretreatment strategies for improved anaerobic digestion: From lab-scale research to full-scale application. *Bioresource Technology*, 199, 386-397.
- Cesaro, A., Belgiorno, V. 2014. Pretreatment methods to improve anaerobic biodegradability of organic municipal solid waste fractions. *Chemical Engineering Journal*, 240, 24-37.
- Chae, K.J., Jang, A., Yim, S.K., Kim, I.S. 2008. The effects of digestion temperature and temperature shock on the biogas yields from the mesophilic anaerobic digestion of swine manure. *Bioresource Technology*, 99(1), 1-6.
- Chang, E.E., Chang, Y.C., Liang, C.H., Huang, C.P., Chiang, P.C. 2012. Identifying the rejection mechanism for nanofiltration membranes fouled by humic acid and calcium ions exemplified by acetaminophen, sulfamethoxazole, and triclosan. *Journal of Hazardous Materials*, 221-222, 19-27.
- Chen, H., Gao, B., Li, H. 2015a. Removal of sulfamethoxazole and ciprofloxacin from aqueous solutions by graphene oxide. *Journal of Hazardous Materials*, 282, 201-207.
- Chen, J., Wang, C., Pan, Y., Farzana, S.S., Tam, N.F. 2018. Biochar accelerates microbial reductive debromination of 2,2',4,4'-tetrabromodiphenyl ether (BDE-47) in anaerobic mangrove sediments. *Journal of Hazardous Materials*, 341, 177-186.
- Chen, S.-Q., Chen, Y.-L., Jiang, H. 2017. Slow Pyrolysis Magnetization of Hydrochar for Effective and Highly Stable Removal of Tetracycline from Aqueous Solution. *Industrial & Engineering Chemistry Research*, 56(11), 3059-3066.
- Chen, X.-L., Li, F., Chen, H., Wang, H., Li, G. 2020. Fe<sub>2</sub>O<sub>3</sub>/TiO<sub>2</sub> functionalized biochar as a heterogeneous catalyst for dyes degradation in water under Fenton processes. *Journal of Environmental Chemical Engineering*, 8(4), 103905.
- Chen, X., Kuhn, E., Wang, W., Park, S., Flanagan, K., Trass, O., Tenlep, L., Tao, L., Tucker, M. 2013. Comparison of different mechanical refining technologies on the enzymatic digestibility of low severity acid pretreated corn stover. *Bioresource Technology*, 147, 401-408.
- Chen, X., Wang, W., Ciesielski, P., Trass, O., Park, S., Tao, L., Tucker, M.P. 2015b. Improving Sugar Yields and Reducing Enzyme Loadings in the Deacetylation and Mechanical Refining (DMR) Process through Multistage Disk and Szego Refining and Corresponding Techno-Economic Analysis. *ACS Sustainable Chemistry & Engineering*, 4(1), 324-333.
- Cheng, W., Tang, K., Qi, Y., Sheng, J., Liu, Z. 2010. One-step synthesis of superparamagnetic monodisperse porous Fe<sub>3</sub>O<sub>4</sub> hollow and core-shell spheres. *Journal of Materials Chemistry*, 20(9), 1799-1805.
- Cho, D.W., Yoon, K., Kwon, E.E., Biswas, J.K., Song, H. 2017. Fabrication of magnetic biochar as a treatment medium for As(V) via pyrolysis of FeCl<sub>3</sub>-pretreated spent coffee ground. *Environmental Pollution*, 229, 942-949.

- Choe, U., Mustafa, A.M., Lin, H., Xu, J., Sheng, K. 2019. Effect of bamboo hydrochar on anaerobic digestion of fish processing waste for biogas production. *Bioresource Technology*, 283, 340-349.
- Choi, Y.K., Kan, E. 2019. Effects of pyrolysis temperature on the physicochemical properties of alfalfa-derived biochar for the adsorption of bisphenol A and sulfamethoxazole in water. *Chemosphere*, 218, 741-748.
- Cleveland, V., Bingham, J.-P., Kan, E. 2014. Heterogeneous Fenton degradation of bisphenol A by carbon nanotube-supported Fe<sub>3</sub>O<sub>4</sub>. *Separation and Purification Technology*, 133, 388-395.
- Creamer, A.E., Gao, B., Zhang, M. 2014. Carbon dioxide capture using biochar produced from sugarcane bagasse and hickory wood. *Chemical Engineering Journal*, 249, 174-179.
- Cui, L., Chen, T., Yin, C., Yan, J., Ippolito, J.A., Hussain, Q.J.B. 2019. Mechanism of adsorption of cadmium and Lead ions by iron-activated biochar. *BioResources*, 14(1), 842-857.
- Dahlan, R., McDonald, C., Sunderland, V.B. 1987. Solubilities and intrinsic dissolution rates of sulphamethoxazole and trimethoprim. *Journal of Pharmacy and Pharmacology*, 39(4), 246-251.
- Dai, Y., Zhang, N., Xing, C., Cui, Q., Sun, Q. 2019. The adsorption, regeneration and engineering applications of biochar for removal organic pollutants: A review. *Chemosphere*, 223, 12-27.
- de Assis, T., Huang, S., Driemeier, C.E., Donohoe, B.S., Kim, C., Kim, S.H., Gonzalez, R., Jameel, H., Park, S. 2018. Toward an understanding of the increase in enzymatic hydrolysis by mechanical refining. *Biotechnology for Biofuels*, 11, 289.
- Deng, J., Dong, H., Zhang, C., Jiang, Z., Cheng, Y., Hou, K., Zhang, L., Fan, C. 2018. Nanoscale zero-valent iron/biochar composite as an activator for Fenton-like removal of sulfamethazine. *Separation and Purification Technology*, 202, 130-137.
- Dolliver, H., Kumar, K., Gupta, S. 2007. Sulfamethazine uptake by plants from manure-amended soil. *Journal of environmental quality*, 36(4), 1224-1230.
- Du, J., Guo, W., Li, X., Li, Q., Wang, B., Huang, Y., Ren, N. 2017. Degradation of sulfamethoxazole by a heterogeneous Fenton-like system with microscale zero-valent iron: Kinetics, effect factors, and pathways. *Journal of the Taiwan Institute of Chemical Engineers*, 81, 232-238.
- Du, J., Guo, W., Wang, H., Yin, R., Zheng, H., Feng, X., Che, D., Ren, N. 2018. Hydroxyl radical dominated degradation of aquatic sulfamethoxazole by Fe(0)/bisulfite/O<sub>2</sub>: Kinetics, mechanisms, and pathways. *Water Research*, 138, 323-332.
- Du, Z., Deng, S., Liu, D., Yao, X., Wang, Y., Lu, X., Wang, B., Huang, J., Wang, Y., Xing, B., Yu, G. 2016. Efficient adsorption of PFOS and F53B from chrome plating wastewater and

- their subsequent degradation in the regeneration process. *Chemical Engineering Journal*, 290, 405-413.
- Eke, J., Wagh, P., Escobar, I.C. 2018. Ozonation, biofiltration and the role of membrane surface charge and hydrophobicity in removal and destruction of algal toxins at basic pH values. *Separation and Purification Technology*, 194, 56-63.
- Epold, I., Dulova, N., Veressinina, Y., Trapido, M. 2012. Application of ozonation, UV photolysis, Fenton treatment and other related processes for degradation of ibuprofen and sulfamethoxazole in different aqueous matrices. *Journal of Advanced Oxidation Technologies*, 15(2), 354-364.
- Fagbohunge, M.O., Herbert, B.M., Hurst, L., Li, H., Usmani, S.Q., Semple, K.T. 2016. Impact of biochar on the anaerobic digestion of citrus peel waste. *Bioresource Technology*, 216, 142-149.
- Fan, Y., Zheng, C., Hou, H. 2019. Preparation of Granular Activated Carbon and Its Mechanism in the Removal of Isoniazid, Sulfamethoxazole, Thiamphenicol, and Doxycycline from Aqueous Solution. *Environmental Engineering Science*, 36(9), 1027-1040.
- Federation, W.E., Association, A.P.H. 2005. Standard methods for the examination of water and wastewater. American Public Health Association (APHA): Washington, DC, USA.
- Foo, K.Y., Hameed, B.H. 2012. Potential of jackfruit peel as precursor for activated carbon prepared by microwave induced NaOH activation. *Bioresource Technology*, 112, 143-150.
- Fu, K., Yue, Q., Gao, B., Wang, Y., Li, Q. 2017. Activated carbon from tomato stem by chemical activation with FeCl<sub>2</sub>. *Colloids and Surfaces A: Physicochemical and Engineering Aspects*, 529, 842-849.
- Gao, J., Pedersen, J.A. 2005. Adsorption of sulfonamide antimicrobial agents to clay minerals. *Environmental Science & Technology*, 39(24), 9509-9516.
- Gao, Y.Q., Gao, N.Y., Deng, Y., Gu, J.S., Shen, Y.C., Wang, S.X. 2012. Adsorption of microcystin-LR from water with iron oxide nanoparticles. *Water Environmental Research*, 84(7), 562-568.
- Gauden, P.A., Szmecchtig-Gauden, E., Rychlicki, G., Duber, S., Garbacz, J.K., Buczkowski, R. 2006. Changes of the porous structure of activated carbons applied in a filter bed pilot operation. *Journal of Colloid and Interface Science*, 295(2), 327-347.
- Ge, Y.-L., Zhang, Y.-F., Yang, Y., Xie, S., Liu, Y., Maruyama, T., Deng, Z.-Y., Zhao, X. 2019. Enhanced adsorption and catalytic degradation of organic dyes by nanometer iron oxide anchored to single-wall carbon nanotubes. *Applied Surface Science*, 488, 813-826.
- Ghamkhari, A., Mohamadi, L., Kazemzadeh, S., Zafar, M.N., Rahdar, A., Khaksefidi, R. 2020. Synthesis and characterization of poly(styrene-block-acrylic acid) diblock copolymer

- modified magnetite nanocomposite for efficient removal of penicillin G. *Composites Part B: Engineering*, 182.
- Gomez-Brandon, M., Lazcano, C., Dominguez, J. 2008. The evaluation of stability and maturity during the composting of cattle manure. *Chemosphere*, 70(3), 436-444.
- Gonçalves, A.G., Órfão, J.J.M., Pereira, M.F.R. 2013. Ozonation of sulfamethoxazole promoted by MWCNT. *Catalysis Communications*, 35, 82-87.
- Grosvenor, A.P., Kobe, B.A., Biesinger, M.C., McIntyre, N.S. 2004. Investigation of multiplet splitting of Fe 2p XPS spectra and bonding in iron compounds. *Surface and Interface Analysis*, 36(12), 1564-1574.
- Gu, L., Zhu, N., Guo, H., Huang, S., Lou, Z., Yuan, H. 2013. Adsorption and Fenton-like degradation of naphthalene dye intermediate on sewage sludge derived porous carbon. *Journal of Hazardous Materials*, 246-247, 145-53.
- Han, Y., Cao, X., Ouyang, X., Sohi, S.P., Chen, J. 2016. Adsorption kinetics of magnetic biochar derived from peanut hull on removal of Cr (VI) from aqueous solution: effects of production conditions and particle size. *Chemosphere*, 145, 336-341.
- He, J., Dai, J., Zhang, T., Sun, J., Xie, A., Tian, S., Yan, Y., Huo, P. 2016. Preparation of highly porous carbon from sustainable  $\alpha$ -cellulose for superior removal performance of tetracycline and sulfamethazine from water. *RSC Advances*, 6(33), 28023-28033.
- He, X., Pelaez, M., Westrick, J.A., O'Shea, K.E., Hiskia, A., Triantis, T., Kaloudis, T., Stefan, M.I., de la Cruz, A.A., Dionysiou, D.D. 2012. Efficient removal of microcystin-LR by UV-C/H<sub>2</sub>O<sub>2</sub> in synthetic and natural water samples. *Water Research*, 46(5), 1501-1510.
- He, Y., Wu, P., Li, G., Li, L., Yi, J., Wang, S., Lu, S., Ding, P., Chen, C., Pan, H. 2020. Optimization on preparation of Fe<sub>3</sub>O<sub>4</sub>/chitosan as potential matrix material for the removal of microcystin-LR and its evaluation of adsorption properties. *International Journal of Biological Macromolecules*, 156, 1574-1583.
- Henn, A.R., Fraundorf, P.B. 1990. A quantitative measure of the degree of fibrillation of short reinforcing fibres. *Journal of Materials Science*, 25(8), 3659-3663.
- Heo, J., Yoon, Y., Lee, G., Kim, Y., Han, J., Park, C.M. 2019. Enhanced adsorption of bisphenol A and sulfamethoxazole by a novel magnetic CuZnFe<sub>2</sub>O<sub>4</sub>-biochar composite. *Bioresource Technology*, 281, 179-187.
- Hu, X., Liu, B., Deng, Y., Chen, H., Luo, S., Sun, C., Yang, P., Yang, S. 2011. Adsorption and heterogeneous Fenton degradation of 17 $\alpha$ -methyltestosterone on nano Fe<sub>3</sub>O<sub>4</sub>/MWCNTs in aqueous solution. *Applied Catalysis B: Environmental*, 107(3-4), 274-283.
- Huang, D., Luo, H., Zhang, C., Zeng, G., Lai, C., Cheng, M., Wang, R., Deng, R., Xue, W., Gong, X., Guo, X., Li, T. 2019. Nonnegligible role of biomass types and its compositions on the

- formation of persistent free radicals in biochar: Insight into the influences on Fenton-like process. *Chemical Engineering Journal*, 361, 353-363.
- Huang, J., Zimmerman, A.R., Chen, H., Gao, B. 2020. Ball milled biochar effectively removes sulfamethoxazole and sulfapyridine antibiotics from water and wastewater. *Environmental Pollution*, 258, 113809.
- Huang, W.J., Cheng, B.L., Cheng, Y.L. 2007. Adsorption of microcystin-LR by three types of activated carbon. *Journal of Hazardous Materials*, 141(1), 115-122.
- Huang, X., An, D., Song, J., Gao, W., Shen, Y. 2017. Persulfate/electrochemical/FeCl<sub>2</sub> system for the degradation of phenol adsorbed on granular activated carbon and adsorbent regeneration. *Journal of Cleaner Production*, 165, 637-644.
- Huang, X., Hu, Q., Gao, L., Hao, Q., Wang, P., Qin, D. 2018. Adsorption characteristics of metal-organic framework MIL-101(Cr) towards sulfamethoxazole and its persulfate oxidation regeneration. *RSC Advances*, 8(49), 27623-27630.
- Hui, L., Liu, Z., Ni, Y. 2009. Characterization of high-yield pulp (HYP) by the solute exclusion technique. *Bioresource Technology*, 100(24), 6630-4.
- Huling, S.G., Ko, S., Park, S., Kan, E. 2011. Persulfate oxidation of MTBE- and chloroform-spent granular activated carbon. *Journal of Hazardous Materials*, 192(3), 1484-90.
- Izumi, K., Okishio, Y.-k., Nagao, N., Niwa, C., Yamamoto, S., Toda, T. 2010. Effects of particle size on anaerobic digestion of food waste. *International Biodeterioration & Biodegradation*, 64(7), 601-608.
- Jang, H.M., Choi, Y.K., Kan, E. 2018a. Effects of dairy manure-derived biochar on psychrophilic, mesophilic and thermophilic anaerobic digestions of dairy manure. *Bioresource Technology*, 250, 927-931.
- Jang, H.M., Kan, E. 2019a. Engineered biochar from agricultural waste for removal of tetracycline in water. *Bioresource Technology*, 284, 437-447.
- Jang, H.M., Kan, E. 2019b. A novel hay-derived biochar for removal of tetracyclines in water. *Bioresource Technology*, 274, 162-172.
- Jang, H.M., Yoo, S., Choi, Y.K., Park, S., Kan, E. 2018b. Adsorption isotherm, kinetic modeling and mechanism of tetracycline on Pinus taeda-derived activated biochar. *Bioresource Technology*, 259, 24-31.
- Jang, H.M., Yoo, S., Park, S., Kan, E. 2018c. Engineered biochar from pine wood: Characterization and potential application for removal of sulfamethoxazole in water. *Environmental Engineering Research*, 24(4), 608-617.
- Jonidi Jafari, A., Kakavandi, B., Jaafarzadeh, N., Rezaei Kalantary, R., Ahmadi, M., Akbar Babaei, A. 2017. Fenton-like catalytic oxidation of tetracycline by AC@Fe<sub>3</sub>O<sub>4</sub> as a heterogeneous

- persulfate activator: Adsorption and degradation studies. *Journal of Industrial and Engineering Chemistry*, 45, 323-333.
- Kan, E., Huling, S.G. 2009. Effects of temperature and acidic pre-treatment on Fenton-driven oxidation of MTBE-spent granular activated carbon. *Environmental science & technology*, 43(5), 1493-1499.
- Kang, X., Zhang, Y., Song, B., Sun, Y., Li, L., He, Y., Kong, X., Luo, X., Yuan, Z. 2019. The effect of mechanical pretreatment on the anaerobic digestion of Hybrid Pennisetum. *Fuel*, 252, 469-474.
- Kilic, M., Apaydin-Varol, E., Pütün, A.E. 2011. Adsorptive removal of phenol from aqueous solutions on activated carbon prepared from tobacco residues: equilibrium, kinetics and thermodynamics. *Journal of Hazardous Materials*, 189(1-2), 397-403.
- Kim, J.R., Huling, S.G., Kan, E. 2015. Effects of temperature on adsorption and oxidative degradation of bisphenol A in an acid-treated iron-amended granular activated carbon. *Chemical Engineering Journal*, 262, 1260-1267.
- Kim, J.R., Kan, E. 2016. Heterogeneous photocatalytic degradation of sulfamethoxazole in water using a biochar-supported TiO<sub>2</sub> photocatalyst. *Journal of Environmental Management*, 180, 94-101.
- Kim, S., Yun, Y.S., Choi, Y.E. 2018. Development of waste biomass based sorbent for removal of cyanotoxin microcystin-LR from aqueous phases. *Bioresource Technology*, 247, 690-696.
- Kim, Y., Choi, K., Jung, J., Park, S., Kim, P.-G., Park, J. 2007. Aquatic toxicity of acetaminophen, carbamazepine, cimetidine, diltiazem and six major sulfonamides, and their potential ecological risks in Korea. *Environment international*, 33(3), 370-375.
- Larcher, S., Yargeau, V. 2012. Biodegradation of sulfamethoxazole: current knowledge and perspectives. *Applied Microbiology and Biotechnology*, 96(2), 309-318.
- Ledesma, B., Román, S., Álvarez-Murillo, A., Sabio, E., González, J.F. 2014. Cyclic adsorption/thermal regeneration of activated carbons. *Journal of Analytical and Applied Pyrolysis*, 106, 112-117.
- Lee, J., Walker, H.W. 2011. Adsorption of microcystin-Lr onto iron oxide nanoparticles. *Colloids and Surfaces A: Physicochemical and Engineering Aspects*, 373(1-3), 94-100.
- Lei, Y., Sun, D., Dang, Y., Chen, H., Zhao, Z., Zhang, Y., Holmes, D.E. 2016. Stimulation of methanogenesis in anaerobic digesters treating leachate from a municipal solid waste incineration plant with carbon cloth. *Bioresource Technology*, 222, 270-276.
- Li, J., Cao, L., Yuan, Y., Wang, R., Wen, Y., Man, J. 2018. Comparative study for microcystin-LR sorption onto biochars produced from various plant- and animal-wastes at different



- pyrolysis temperatures: Influencing mechanisms of biochar properties. *Bioresource Technology*, 247, 794-803.
- Li, J., Pan, L., Yu, G., Xie, S., Li, C., Lai, D., Li, Z., You, F., Wang, Y. 2019. The synthesis of heterogeneous Fenton-like catalyst using sewage sludge biochar and its application for ciprofloxacin degradation. *Science of the Total Environment*, 654, 1284-1292.
- Li, K., Liu, R., Sun, C. 2015a. Comparison of anaerobic digestion characteristics and kinetics of four livestock manures with different substrate concentrations. *Bioresource Technology*, 198, 133-140.
- Li, L., Qiu, Y., Huang, J., Li, F., Sheng, G.D. 2014a. Mechanisms and Factors Influencing Adsorption of Microcystin-LR on Biochars. *Water, Air, & Soil Pollution*, 225(12), 2220.
- Li, L.L., Tong, Z.H., Fang, C.Y., Chu, J., Yu, H.Q. 2015b. Response of anaerobic granular sludge to single-wall carbon nanotube exposure. *Water Research*, 70, 1-8.
- Li, R., Jin, X., Megharaj, M., Naidu, R., Chen, Z. 2015c. Heterogeneous Fenton oxidation of 2,4-dichlorophenol using iron-based nanoparticles and persulfate system. *Chemical Engineering Journal*, 264, 587-594.
- Li, W.-H., Yue, Q.-Y., Gao, B.-Y., Ma, Z.-H., Li, Y.-J., Zhao, H.-X. 2011. Preparation and utilization of sludge-based activated carbon for the adsorption of dyes from aqueous solutions. *Chemical Engineering Journal*, 171(1), 320-327.
- Li, Y., Shao, J., Wang, X., Deng, Y., Yang, H., Chen, H. 2014b. Characterization of Modified Biochars Derived from Bamboo Pyrolysis and Their Utilization for Target Component (Furfural) Adsorption. *Energy & Fuels*, 28(8), 5119-5127.
- Liang, C., Lin, Y.T., Shin, W.H. 2009. Persulfate regeneration of trichloroethylene spent activated carbon. *Journal of Hazardous Materials*, 168(1), 187-92.
- Liu, G., Zheng, H., Zhai, X., Wang, Z. 2018a. Characteristics and mechanisms of microcystin-LR adsorption by giant reed-derived biochars: Role of minerals, pores, and functional groups. *Journal of Cleaner Production*, 176, 463-473.
- Liu, Y., Fan, Q., Wang, J. 2018b. Zn-Fe-CNTs catalytic in situ generation of H<sub>2</sub>O<sub>2</sub> for Fenton-like degradation of sulfamethoxazole. *Journal of Hazardous Materials*, 342, 166-176.
- Liu, Y.L., Walker, H.W., Lenhart, J.J. 2019. Adsorption of microcystin-LR onto kaolinite, illite and montmorillonite. *Chemosphere*, 220, 696-705.
- Liu, Z.-h., Kanjo, Y., Mizutani, S. 2009. Removal mechanisms for endocrine disrupting compounds (EDCs) in wastewater treatment—physical means, biodegradation, and chemical advanced oxidation: a review. *Science of the Total Environment*, 407(2), 731-748.

- Luo, J., Li, X., Ge, C., Muller, K., Yu, H., Huang, P., Li, J., Tsang, D.C.W., Bolan, N.S., Rinklebe, J., Wang, H. 2018. Sorption of norfloxacin, sulfamerazine and oxytetracycline by KOH-modified biochar under single and ternary systems. *Bioresource Technology*, 263, 385-392.
- Mandal, A., Singh, N., Purakayastha, T.J. 2017. Characterization of pesticide sorption behaviour of slow pyrolysis biochars as low cost adsorbent for atrazine and imidacloprid removal. *Science of the Total Environment*, 577, 376-385.
- Martínez, E.J., Rosas, J.G., Sotres, A., Moran, A., Cara, J., Sánchez, M.E., Gómez, X. 2018. Codigestion of sludge and citrus peel wastes: Evaluating the effect of biochar addition on microbial communities. *Biochemical Engineering Journal*, 137, 314-325.
- Martínez, F., Gómez, A. 2002. Estimation of the solubility of sulfonamides in aqueous media from partition coefficients and entropies of fusion. *Physics and Chemistry of Liquids*, 40(4), 411-420.
- Martins, A.C., Pezoti, O., Cazetta, A.L., Bedin, K.C., Yamazaki, D.A.S., Bandoch, G.F.G., Asefa, T., Visentainer, J.V., Almeida, V.C. 2015. Removal of tetracycline by NaOH-activated carbon produced from macadamia nut shells: Kinetic and equilibrium studies. *Chemical Engineering Journal*, 260, 291-299.
- Mashile, P.P., Mpupa, A., Nomngongo, P.N. 2018. Adsorptive removal of microcystin-LR from surface and wastewater using tyre-based powdered activated carbon: Kinetics and isotherms. *Toxicon*, 145, 25-31.
- Mohan, D., Sarswat, A., Ok, Y.S., Pittman, C.U., Jr. 2014. Organic and inorganic contaminants removal from water with biochar, a renewable, low cost and sustainable adsorbent--a critical review. *Bioresource Technology*, 160, 191-202.
- Mondal, S., Aikat, K., Halder, G. 2016. Ranitidine hydrochloride sorption onto superheated steam activated biochar derived from mung bean husk in fixed bed column. *Journal of Environmental Chemical Engineering*, 4(1), 488-497.
- Nah, I.W., Kang, Y.W., Hwang, K.-Y., Song, W.-K. 2000. Mechanical pretreatment of waste activated sludge for anaerobic digestion process. *Water Research*, 34(8), 2362-2368.
- Nasir, I.M., Mohd Ghazi, T.I., Omar, R. 2012. Anaerobic digestion technology in livestock manure treatment for biogas production: A review. *Engineering in Life Sciences*, 12(3), 258-269.
- Nawaz, M., Shahzad, A., Tahir, K., Kim, J., Moztahida, M., Jang, J., Alam, M.B., Lee, S.-H., Jung, H.-Y., Lee, D.S. 2020. Photo-Fenton reaction for the degradation of sulfamethoxazole using a multi-walled carbon nanotube-NiFe<sub>2</sub>O<sub>4</sub> composite. *Chemical Engineering Journal*, 382, 123053.
- Ngankam, E.S., Dai-Yang, L., Debina, B., Baçaoui, A., Yaacoubi, A., Rahman, A.N. 2020. Preparation and Characterization of Magnetic Banana Peels Biochar for Fenton Degradation of Methylene Blue. *Materials Sciences and Applications*, 11(06), 382-400.

- Nguyen, T.D., Phan, N.H., Do, M.H., Ngo, K.T. 2011. Magnetic Fe<sub>2</sub>MO<sub>4</sub> (M:Fe, Mn) activated carbons: fabrication, characterization and heterogeneous Fenton oxidation of methyl orange. *Journal of Hazardous Materials*, 185(2-3), 653-661.
- Nidheesh, P.V., Gandhimathi, R., Ramesh, S.T. 2013. Degradation of dyes from aqueous solution by Fenton processes: a review. *Environmental Science and Pollution Research*, 20(4), 2099-2132.
- Oliveira, L.C., Pereira, E., Guimaraes, I.R., Vallone, A., Pereira, M., Mesquita, J.P., Sapag, K. 2009. Preparation of activated carbons from coffee husks utilizing FeCl<sub>3</sub> and ZnCl<sub>2</sub> as activating agents. *Journal of Hazardous Materials*, 165(1-3), 87-94.
- Ouyang, D., Yan, J., Qian, L., Chen, Y., Han, L., Su, A., Zhang, W., Ni, H., Chen, M. 2017. Degradation of 1,4-dioxane by biochar supported nano magnetite particles activating persulfate. *Chemosphere*, 184, 609-617.
- Ozbey Unal, B., Bilici, Z., Ugur, N., Isik, Z., Harputlu, E., Dizge, N., Ocakoglu, K. 2019. Adsorption and Fenton oxidation of azo dyes by magnetite nanoparticles deposited on a glass substrate. *Journal of Water Process Engineering*, 32, 100897.
- Pal, A., Gin, K.Y.-H., Lin, A.Y.-C., Reinhard, M. 2010. Impacts of emerging organic contaminants on freshwater resources: review of recent occurrences, sources, fate and effects. *Science of the Total Environment*, 408(24), 6062-6069.
- Pan, J., Ma, J., Liu, X., Zhai, L., Ouyang, X., Liu, H. 2019a. Effects of different types of biochar on the anaerobic digestion of chicken manure. *Bioresource Technology*, 275, 258-265.
- Pan, J., Ma, J., Zhai, L., Luo, T., Mei, Z., Liu, H. 2019b. Achievements of biochar application for enhanced anaerobic digestion: A review. *Bioresource Technology*, 292, 122058.
- Park, J.-A., Kang, J.-K., Jung, S.-M., Choi, J.-W., Lee, S.-H., Yargeau, V., Kim, S.-B. 2020. Investigating Microcystin-LR adsorption mechanisms on mesoporous carbon, mesoporous silica, and their amino-functionalized form: Surface chemistry, pore structures, and molecular characteristics. *Chemosphere*, 247.
- Park, J., Hung, I., Gan, Z., Rojas, O.J., Lim, K.H., Park, S. 2013. Activated carbon from biochar: influence of its physicochemical properties on the sorption characteristics of phenanthrene. *Bioresource Technology*, 149, 383-9.
- Park, J., Jones, B., Koo, B., Chen, X., Tucker, M., Yu, J.H., Pschorn, T., Venditti, R., Park, S. 2016. Use of mechanical refining to improve the production of low-cost sugars from lignocellulosic biomass. *Bioresource Technology*, 199, 59-67.
- Park, J.A., Jung, S.M., Choi, J.W., Kim, J.H., Hong, S., Lee, S.H. 2018a. Mesoporous carbon for efficient removal of microcystin-LR in drinking water sources, Nak-Dong River, South Korea: Application to a field-scale drinking water treatment plant. *Chemosphere*, 193, 883-891.

- Park, J.A., Jung, S.M., Yi, I.G., Choi, J.W., Kim, S.B., Lee, S.H. 2017. Adsorption of microcystin-LR on mesoporous carbons and its potential use in drinking water source. *Chemosphere*, 177, 15-23.
- Park, J.H., Wang, J.J., Xiao, R., Tafti, N., DeLaune, R.D., Seo, D.C. 2018b. Degradation of Orange G by Fenton-like reaction with Fe-impregnated biochar catalyst. *Bioresource Technology*, 249, 368-376.
- Passos, F., Ortega, V., Donoso-Bravo, A. 2017. Thermochemical pretreatment and anaerobic digestion of dairy cow manure: Experimental and economic evaluation. *Bioresource Technology*, 227, 239-246.
- Pavagadhi, S., Tang, A.L., Sathishkumar, M., Loh, K.P., Balasubramanian, R. 2013. Removal of microcystin-LR and microcystin-RR by graphene oxide: adsorption and kinetic experiments. *Water Research*, 47(13), 4621-4629.
- Pego, M.F., Bianchi, M.L., Carvalho, J.A., Veiga, T.R. 2019. Surface modification of activated carbon by corona treatment. *Anais da Academia Brasileira de Ciências*, 91(1).
- Peiris, C., Gunatilake, S.R., Mlsna, T.E., Mohan, D., Vithanage, M. 2017. Biochar based removal of antibiotic sulfonamides and tetracyclines in aquatic environments: A critical review. *Bioresource Technology*, 246, 150-159.
- Peng, J., Wu, E., Wang, N., Quan, X., Sun, M., Hu, Q. 2019. Removal of sulfonamide antibiotics from water by adsorption and persulfate oxidation process. *Journal of Molecular Liquids*, 274, 632-638.
- Pezoti, O., Cazetta, A.L., Bedin, K.C., Souza, L.S., Martins, A.C., Silva, T.L., Santos Júnior, O.O., Visentainer, J.V., Almeida, V.C. 2016. NaOH-activated carbon of high surface area produced from guava seeds as a high-efficiency adsorbent for amoxicillin removal: Kinetic, isotherm and thermodynamic studies. *Chemical Engineering Journal*, 288, 778-788.
- Pinho, L.X., Azevedo, J., Brito, Â., Santos, A., Tamagnini, P., Vilar, V.J.P., Vasconcelos, V.M., Boaventura, R.A.R. 2015. Effect of TiO<sub>2</sub> photocatalysis on the destruction of *Microcystis aeruginosa* cells and degradation of cyanotoxins microcystin-LR and cylindrospermopsin. *Chemical Engineering Journal*, 268, 144-152.
- Qiu, L., Deng, Y.F., Wang, F., Davaritouchae, M., Yao, Y.Q. 2019. A review on biochar-mediated anaerobic digestion with enhanced methane recovery. *Renewable and Sustainable Energy Reviews*, 115.
- Qu, G., Lv, P., Cai, Y., Tu, C., Ma, X., Ning, P. 2020. Enhanced anaerobic fermentation of dairy manure by microelectrolysis in electric and magnetic fields. *Renewable Energy*, 146, 2758-2765, 109373.
- Rajapaksha, A.U., Vithanage, M., Ahmad, M., Seo, D.C., Cho, J.S., Lee, S.E., Lee, S.S., Ok, Y.S. 2015. Enhanced sulfamethazine removal by steam-activated invasive plant-derived biochar. *Journal of Hazardous Materials*, 290, 43-50.

- Reguyal, F., Sarmah, A.K., Gao, W. 2017a. Synthesis of magnetic biochar from pine sawdust via oxidative hydrolysis of FeCl<sub>2</sub> for the removal sulfamethoxazole from aqueous solution. *Journal of Hazardous Materials*, 321, 868-878.
- Rodríguez-Martínez, C.E., Gutiérrez Segura, E., Fall, C., Colín-Cruz, A. 2019. Removal of sulfamethoxazole in aqueous solution by two activated carbons from secondary sludge and biomass. *Desalination and Water Treatment*, 158, 67-78.
- Rodriguez-Narvaez, O.M., Peralta-Hernandez, J.M., Goonetilleke, A., Bandala, E.R. 2017. Treatment technologies for emerging contaminants in water: A review. *Chemical Engineering Journal*, 323, 361-380.
- Rodriguez, C., Alaswad, A., El-Hassan, Z., Olabi, A.G. 2018. Improvement of methane production from *P. canaliculata* through mechanical pretreatment. *Renewable Energy*, 119, 73-78.
- Rodriguez, C., Alaswad, A., El-Hassan, Z., Olabi, A.G. 2017. Mechanical pretreatment of waste paper for biogas production. *Waste Management*, 68, 157-164.
- Rodriguez, C., Alaswad, A., Mooney, J., Prescott, T., Olabi, A.G. 2015. Pre-treatment techniques used for anaerobic digestion of algae. *Fuel Processing Technology*, 138, 765-779.
- Romero-Güiza, M.S., Vila, J., Mata-Alvarez, J., Chimenos, J.M., Astals, S. 2016. The role of additives on anaerobic digestion: A review. *Renewable and Sustainable Energy Reviews*, 58, 1486-1499.
- Rubeena, K.K., Hari Prasad Reddy, P., Laiju, A.R., Nidheesh, P.V. 2018. Iron impregnated biochars as heterogeneous Fenton catalyst for the degradation of acid red 1 dye. *Journal of Environment Management*, 226, 320-328.
- Rufford, T.E., Hulicova-Jurcakova, D., Zhu, Z., Lu, G.Q. 2011. A comparative study of chemical treatment by FeCl<sub>3</sub>, MgCl<sub>2</sub>, and ZnCl<sub>2</sub> on microstructure, surface chemistry, and double-layer capacitance of carbons from waste biomass. *Journal of Materials Research*, 25(8), 1451-1459.
- Sethupathi, S., Zhang, M., Rajapaksha, A., Lee, S., Mohamad Nor, N., Mohamed, A., Al-Wabel, M., Lee, S., Ok, Y. 2017. Biochars as Potential Adsorbers of CH<sub>4</sub>, CO<sub>2</sub> and H<sub>2</sub>S. *Sustainability*, 9(1), 121.
- Shanmugam, S.R., Adhikari, S., Nam, H., Kar Sajib, S. 2018. Effect of bio-char on methane generation from glucose and aqueous phase of algae liquefaction using mixed anaerobic cultures. *Biomass and Bioenergy*, 108, 479-486.
- Sharma, V.K., Johnson, N., Cizmas, L., McDonald, T.J., Kim, H. 2016. A review of the influence of treatment strategies on antibiotic resistant bacteria and antibiotic resistance genes. *Chemosphere*, 150, 702-714.

- Shen, R., Jing, Y., Feng, J., Luo, J., Yu, J., Zhao, L. 2020. Performance of enhanced anaerobic digestion with different pyrolysis biochars and microbial communities. *Bioresource Technology*, 296, 122354.
- Shen, Y., Linville, J.L., Ignacio-de Leon, P.A.A., Schoene, R.P., Urgun-Demirtas, M. 2016. Towards a sustainable paradigm of waste-to-energy process: Enhanced anaerobic digestion of sludge with woody biochar. *Journal of Cleaner Production*, 135, 1054-1064.
- Shen, Y., Linville, J.L., Urgun-Demirtas, M., Schoene, R.P., Snyder, S.W. 2015. Producing pipeline-quality biomethane via anaerobic digestion of sludge amended with corn stover biochar with in-situ CO<sub>2</sub> removal. *Applied Energy*, 158, 300-309.
- Sheng, J., Yin, H., Qian, F., Huang, H., Gao, S., Wang, J. 2020. Reduced graphene oxide-based composite membranes for in-situ catalytic oxidation of sulfamethoxazole operated in membrane filtration. *Separation and Purification Technology*, 236.
- Shin, H.S., Kim, J.-H. 2016. Isotherm, kinetic and thermodynamic characteristics of adsorption of paclitaxel onto Diaion HP-20. *Process Biochemistry*, 51(7), 917-924.
- Song, W., Li, J., Wang, Z., Zhang, X. 2019. A mini review of activated methods to persulfate-based advanced oxidation process. *Water Science and Technology*, 79(3), 573-579.
- Sophia, A.C., Lima, E.C. 2018. Removal of emerging contaminants from the environment by adsorption. *Ecotoxicology and Environmental Safety*, 150, 1-17.
- Stackelberg, P.E., Gibs, J., Furlong, E.T., Meyer, M.T., Zaugg, S.D., Lippincott, R.L. 2007. Efficiency of conventional drinking-water-treatment processes in removal of pharmaceuticals and other organic compounds. *Science of the Total Environment*, 377(2-3), 255-272.
- Su, Y.F., Cheng, Y.L., Shih, Y.H. 2013. Removal of trichloroethylene by zerovalent iron/activated carbon derived from agricultural wastes. *Journal of Environment Management*, 129, 361-366.
- Sun, B., Lian, F., Bao, Q., Liu, Z., Song, Z., Zhu, L. 2016. Impact of low molecular weight organic acids (LMWOAs) on biochar micropores and sorption properties for sulfamethoxazole. *Environmental Pollution*, 214, 142-148.
- Sunyoto, N.M.S., Zhu, M., Zhang, Z., Zhang, D. 2016. Effect of biochar addition on hydrogen and methane production in two-phase anaerobic digestion of aqueous carbohydrates food waste. *Bioresource Technology*, 219, 29-36.
- Taheran, M., Naghdi, M., Brar, S.K., Knystautas, E.J., Verma, M., Ramirez, A.A., Surampalli, R.Y., Valero, J.R. 2016. Adsorption study of environmentally relevant concentrations of chlortetracycline on pinewood biochar. *Science of the Total Environment*, 571, 772-777.
- Tan, X., Liu, Y., Zeng, G., Wang, X., Hu, X., Gu, Y., Yang, Z. 2015. Application of biochar for the removal of pollutants from aqueous solutions. *Chemosphere*, 125, 70-85.

- Tang, J., Wang, J. 2018. Fenton-like degradation of sulfamethoxazole using Fe-based magnetic nanoparticles embedded into mesoporous carbon hybrid as an efficient catalyst. *Chemical Engineering Journal*, 351, 1085-1094.
- Tang, L., Yu, J., Pang, Y., Zeng, G., Deng, Y., Wang, J., Ren, X., Ye, S., Peng, B., Feng, H. 2018. Sustainable efficient adsorbent: Alkali-acid modified magnetic biochar derived from sewage sludge for aqueous organic contaminant removal. *Chemical Engineering Journal*, 336, 160-169.
- Teixido, M., Pignatello, J.J., Beltran, J.L., Granados, M., Peccia, J. 2011. Speciation of the ionizable antibiotic sulfamethazine on black carbon (biochar). *Environmental Science & Technology*, 45(23), 10020-10027.
- Theydan, S.K., Ahmed, M.J. 2012. Adsorption of methylene blue onto biomass-based activated carbon by FeCl<sub>3</sub> activation: Equilibrium, kinetics, and thermodynamic studies. *Journal of Analytical and Applied Pyrolysis*, 97, 116-122.
- Torres-Pérez, J., Gérente, C., Andrès, Y. 2012. Sustainable activated carbons from agricultural residues dedicated to antibiotic removal by adsorption. *Chinese Journal of Chemical Engineering*, 20(3), 524-529.
- Tsapekos, P., Kougias, P.G., Angelidaki, I. 2015. Biogas production from ensiled meadow grass; effect of mechanical pretreatments and rapid determination of substrate biodegradability via physicochemical methods. *Bioresource Technology*, 182, 329-335.
- Tsapekos, P., Kougias, P.G., Angelidaki, I. 2018. Mechanical pretreatment for increased biogas production from lignocellulosic biomass; predicting the methane yield from structural plant components. *Waste Management*, 78, 903-910.
- Tsapekos, P., Kougias, P.G., Egelund, H., Larsen, U., Pedersen, J., Trénel, P., Angelidaki, I. 2017. Mechanical pretreatment at harvesting increases the bioenergy output from marginal land grasses. *Renewable Energy*, 111, 914-921.
- Tsapekos, P., Kougias, P.G., Frison, A., Raga, R., Angelidaki, I. 2016. Improving methane production from digested manure biofibers by mechanical and thermal alkaline pretreatment. *Bioresource Technology*, 216, 545-552.
- Tu, B., Wen, R., Wang, K., Cheng, Y., Deng, Y., Cao, W., Zhang, K., Tao, H. 2020a. Efficient removal of aqueous hexavalent chromium by activated carbon derived from Bermuda grass. *Journl of Colloid and Interface Science*, 560, 649-658.
- Tu, Y., Peng, Z., Huang, J., Wu, X., Kong, L., Liang, Z., Yang, L., Lin, Z. 2020b. Preparation and Characterization of Magnetic Biochar Nanocomposites via a Modified Solvothermal Method and Their Use as Efficient Heterogeneous Fenton-like Catalysts. *Industrial & Engineering Chemistry Research*, 59(5), 1809-1821.

- Vona, A., Di Martino, F., Garcia-Ivars, J., Picó, Y., Mendoza-Roca, J.-A., Iborra-Clar, M.-I. 2015. Comparison of different removal techniques for selected pharmaceuticals. *Journal of Water Process Engineering*, 5, 48-57.
- Wang, D., Ai, J., Shen, F., Yang, G., Zhang, Y., Deng, S., Zhang, J., Zeng, Y., Song, C. 2017a. Improving anaerobic digestion of easy-acidification substrates by promoting buffering capacity using biochar derived from vermicompost. *Bioresource Technology*, 227, 286-296.
- Wang, F., Wu, Y., Gao, Y., Li, H., Chen, Z. 2016. Effect of humic acid, oxalate and phosphate on Fenton-like oxidation of microcystin-LR by nanoscale zero-valent iron. *Separation and Purification Technology*, 170, 337-343.
- Wang, G., Li, Q., Gao, X., Wang, X.C. 2018a. Sawdust-Derived Biochar Much Mitigates VFAs Accumulation and Improves Microbial Activities To Enhance Methane Production in Thermophilic Anaerobic Digestion. *ACS Sustainable Chemistry & Engineering*, 7(2), 2141-2150.
- Wang, G., Li, Q., Gao, X., Wang, X.C. 2018b. Synergetic promotion of syntrophic methane production from anaerobic digestion of complex organic wastes by biochar: Performance and associated mechanisms. *Bioresource Technology*, 250, 812-820.
- Wang, H., Chu, Y., Fang, C., Huang, F., Song, Y., Xue, X. 2017b. Sorption of tetracycline on biochar derived from rice straw under different temperatures. *PLoS One*, 12(8), e0182776.
- Wang, J., Liao, Z., Ifthikar, J., Shi, L., Du, Y., Zhu, J., Xi, S., Chen, Z., Chen, Z. 2017c. Treatment of refractory contaminants by sludge-derived biochar/persulfate system via both adsorption and advanced oxidation process. *Chemosphere*, 185, 754-763.
- Wang, P., Tang, L., Wei, X., Zeng, G., Zhou, Y., Deng, Y., Wang, J., Xie, Z., Fang, W. 2017d. Synthesis and application of iron and zinc doped biochar for removal of p-nitrophenol in wastewater and assessment of the influence of co-existed Pb(II). *Applied Surface Science*, 392, 391-401.
- Wang, S., Wang, J. 2017. Comparative study on sulfamethoxazole degradation by Fenton and Fe(ii)-activated persulfate process. *RSC Adv.*, 7(77), 48670-48677.
- Wang, W., Cao, Y., Hu, X., Zhou, S., Zhu, D., Qi, D., Deng, S. 2020. Granular reduced graphene oxide/Fe<sub>3</sub>O<sub>4</sub> hydrogel for efficient adsorption and catalytic oxidation of p-perfluorinated nonenoxybenzene sulfonate. *Journal of Hazardous Materials*, 386, 121662.
- Wang, Z., Keshwani, D.R., Redding, A.P., Cheng, J.J. 2010. Sodium hydroxide pretreatment and enzymatic hydrolysis of coastal Bermuda grass. *Bioresource Technology*, 101(10), 3583-3585.
- Wei, J., Liu, Y., Zhu, Y., Li, J. 2020. Enhanced catalytic degradation of tetracycline antibiotic by persulfate activated with modified sludge bio-hydrochar. *Chemosphere*, 247, 125854.



- Wei, M.-C., Wang, K.-S., Lin, I.C., Hsiao, T.-E., Lin, Y.-N., Tang, C.-T., Chen, J.-C., Chang, S.-H. 2012. Rapid regeneration of sulfanilic acid-sorbed activated carbon by microwave with persulfate. *Chemical Engineering Journal*, 193-194, 366-371.
- Wu-Haan, W., Burns, R.T., Moody, L.B., Grewell, D., Raman, R. 2010. Evaluation of ultrasonic pretreatment on anaerobic digestion of different animal manures. *Transactions of the ASABE*, 53(2), 577-583.
- Xia, D., Tan, F., Zhang, C., Jiang, X., Chen, Z., Li, H., Zheng, Y., Li, Q., Wang, Y. 2016. ZnCl<sub>2</sub>-activated biochar from biogas residue facilitates aqueous As(III) removal. *Applied Surface Science*, 377, 361-369.
- Xu, J., Wang, Z., Cheng, J.J. 2011. Bermuda grass as feedstock for biofuel production: a review. *Bioresource Technology*, 102(17), 7613-20.
- Xu, X., Chen, W., Zong, S., Ren, X., Liu, D. 2019a. Magnetic clay as catalyst applied to organics degradation in a combined adsorption and Fenton-like process. *Chemical Engineering Journal*, 373, 140-149.
- Xu, Z., Sun, Z., Zhou, Y., Chen, W., Zhang, T., Huang, Y., Zhang, D. 2019b. Insights into the pyrolysis behavior and adsorption properties of activated carbon from waste cotton textiles by FeCl<sub>3</sub>-activation. *Colloids and Surfaces A: Physicochemical and Engineering Aspects*, 582, 123934.
- Yakout, S.M. 2015. Monitoring the Changes of Chemical Properties of Rice Straw-Derived Biochars Modified by Different Oxidizing Agents and Their Adsorptive Performance for Organics. *Bioremediation Journal*, 19(2), 171-182.
- Yan, H., Gong, A., He, H., Zhou, J., Wei, Y., Lv, L. 2006. Adsorption of microcystins by carbon nanotubes. *Chemosphere*, 62(1), 142-8.
- Yan, J., Lei, M., Zhu, L., Anjum, M.N., Zou, J., Tang, H. 2011. Degradation of sulfamonomethoxine with Fe<sub>3</sub>O<sub>4</sub> magnetic nanoparticles as heterogeneous activator of persulfate. *Journal of Hazardous Materials*, 186(2-3), 1398-1404.
- Yan, L., Liu, Y., Zhang, Y., Liu, S., Wang, C., Chen, W., Liu, C., Chen, Z., Zhang, Y. 2020a. ZnCl<sub>2</sub> modified biochar derived from aerobic granular sludge for developed microporosity and enhanced adsorption to tetracycline. *Bioresource Technology*, 297, 122381.
- Yan, L., Liu, Y., Zhang, Y., Liu, S., Wang, C., Chen, W., Liu, C., Chen, Z., Zhang, Y. 2020b. ZnCl<sub>2</sub> modified biochar derived from aerobic granular sludge for developed microporosity and enhanced adsorption to tetracycline. *Bioresource technology*, 297, 122381.
- Yang, J., Zhao, Y., Ma, S., Zhu, B., Zhang, J., Zheng, C. 2016a. Mercury Removal by Magnetic Biochar Derived from Simultaneous Activation and Magnetization of Sawdust. *Environmental Science & Technology*, 50(21), 12040-12047.

- Yang, L., Chen, Y., Ouyang, D., Yan, J., Qian, L., Han, L., Chen, M., Li, J., Gu, M. 2020. Mechanistic insights into adsorptive and oxidative removal of monochlorobenzene in biochar-supported nanoscale zero-valent iron/persulfate system. *Chemical Engineering Journal*, 400,125811.
- Yang, Q., Wang, H., Larson, R., Runge, T.M. 2017a. Comparative study of chemical pretreatments of dairy manure for enhanced biomethane production. *BioResources*, 12(4), 7363-7375.
- Yang, S.F., Lin, C.F., Lin, A.Y., Hong, P.K. 2011. Sorption and biodegradation of sulfonamide antibiotics by activated sludge: experimental assessment using batch data obtained under aerobic conditions. *Water Research*, 45(11), 3389-97.
- Yang, X., Xu, G., Yu, H., Zhang, Z. 2016b. Preparation of ferric-activated sludge-based adsorbent from biological sludge for tetracycline removal. *Bioresource Technology*, 211, 566-573.
- Yang, Y., Zhang, Y., Li, Z., Zhao, Z., Quan, X., Zhao, Z. 2017b. Adding granular activated carbon into anaerobic sludge digestion to promote methane production and sludge decomposition. *Journal of Cleaner Production*, 149, 1101-1108.
- Yao, Y., Gao, B., Chen, H., Jiang, L., Inyang, M., Zimmerman, A.R., Cao, X., Yang, L., Xue, Y., Li, H. 2012. Adsorption of sulfamethoxazole on biochar and its impact on reclaimed water irrigation. *Journal of Hazardous Materials*, 209-210, 408-13.
- Yao, Y., Zhang, Y., Gao, B., Chen, R., Wu, F. 2018. Removal of sulfamethoxazole (SMX) and sulfapyridine (SPY) from aqueous solutions by biochars derived from anaerobically digested bagasse. *Environmental Science and Pollution Research*, 25(26), 25659-25667.
- Yi, Y., Tu, G., Eric Tsang, P., Fang, Z. 2020. Insight into the influence of pyrolysis temperature on Fenton-like catalytic performance of magnetic biochar. *Chemical Engineering Journal*, 380, 122518.
- Yu, F., Li, Y., Han, S., Ma, J. 2016. Adsorptive removal of antibiotics from aqueous solution using carbon materials. *Chemosphere*, 153, 365-385.
- Zeng, S., Choi, Y.-K., Kan, E. 2021. Iron-activated bermudagrass-derived biochar for adsorption of aqueous sulfamethoxazole: Effects of iron impregnation ratio on biochar properties, adsorption, and regeneration. *Science of The Total Environment*, 750, 141691.
- Zeng, S., Kan, E. 2020a. Chemical Activation of Forage Grass-Derived Biochar for Treatment of Aqueous Antibiotic Sulfamethoxazole. *ACS Omega*. 5(23), 13793-13801.
- Zeng, S., Qin, X., Xia, L. 2017. Degradation of the herbicide isoproturon by laccase-mediator systems. *Biochemical Engineering Journal*, 119, 92-100.
- Zhang, H., Schroder, J. 2014. Animal manure production and utilization in the US. in: *Applied manure and nutrient chemistry for sustainable agriculture and environment*, Springer, pp. 1-21.

- Zhang, H., Zhu, G., Jia, X., Ding, Y., Zhang, M., Gao, Q., Hu, C., Xu, S. 2011a. Removal of microcystin-LR from drinking water using a bamboo-based charcoal adsorbent modified with chitosan. *Journal of Environmental Sciences*, 23(12), 1983-1988.
- Zhang, J., Zhao, W., Zhang, H., Wang, Z., Fan, C., Zang, L. 2018a. Recent achievements in enhancing anaerobic digestion with carbon- based functional materials. *Bioresource Technology*, 266, 555-567.
- Zhang, K., Sun, P., Faye, M.C.A.S., Zhang, Y. 2018b. Characterization of biochar derived from rice husks and its potential in chlorobenzene degradation. *Carbon*, 130, 730-740.
- Zhang, L., Song, X., Liu, X., Yang, L., Pan, F., Lv, J. 2011b. Studies on the removal of tetracycline by multi-walled carbon nanotubes. *Chemical Engineering Journal*, 178, 26-33.
- Zhang, S., Wu, W., Xiao, X., Zhou, J., Ren, F., Jiang, C. 2011c. Preparation and characterization of spindle-like Fe<sub>3</sub>O<sub>4</sub> mesoporous nanoparticles. *Nanoscale Research Letters*, 6(1), 1-9.
- Zhang, X., Feng, M., Qu, R., Liu, H., Wang, L., Wang, Z. 2016. Catalytic degradation of diethyl phthalate in aqueous solution by persulfate activated with nano-scaled magnetic CuFe<sub>2</sub>O<sub>4</sub>/MWCNTs. *Chemical Engineering Journal*, 301, 1-11.
- Zhang, X., Li, Y., Li, G., Hu, C. 2015. Preparation of Fe/activated carbon directly from rice husk pyrolytic carbon and its application in catalytic hydroxylation of phenol. *RSC Advances*, 5(7), 4984-4992.
- Zhang, Y., Zhao, L., Yang, Y., Sun, P. 2020. Fenton-Like Oxidation of Antibiotic Ornidazole Using Biochar-Supported Nanoscale Zero-Valent Iron as Heterogeneous Hydrogen Peroxide Activator. *International Journal of Environmental Research and Public Health*, 17(4), 1324.
- Zhao, H., Liu, X., Cao, Z., Zhan, Y., Shi, X., Yang, Y., Zhou, J., Xu, J. 2016. Adsorption behavior and mechanism of chloramphenicols, sulfonamides, and non-antibiotic pharmaceuticals on multi-walled carbon nanotubes. *Journal of Hazardous Materials*, 310, 235-245.
- Zhao, N., Zhao, C., Lv, Y., Zhang, W., Du, Y., Hao, Z., Zhang, J. 2017. Adsorption and coadsorption mechanisms of Cr(VI) and organic contaminants on H<sub>3</sub>PO<sub>4</sub> treated biochar. *Chemosphere*, 186, 422-429.
- Zheng, H., Wang, Z., Zhao, J., Herbert, S., Xing, B. 2013. Sorption of antibiotic sulfamethoxazole varies with biochars produced at different temperatures. *Environmental Pollution*, 181, 60-67.
- Zheng, Z., Liu, J., Yuan, X., Wang, X., Zhu, W., Yang, F., Cui, Z. 2015. Effect of dairy manure to switchgrass co-digestion ratio on methane production and the bacterial community in batch anaerobic digestion. *Applied Energy*, 151, 249-257.
- Zhou, Y., Liu, X., Xiang, Y., Wang, P., Zhang, J., Zhang, F., Wei, J., Luo, L., Lei, M., Tang, L. 2017. Modification of biochar derived from sawdust and its application in removal of

tetracycline and copper from aqueous solution: Adsorption mechanism and modelling. *Bioresource Technology*, 245(Pt A), 266-273.

Zhu, X., Liu, Y., Luo, G., Qian, F., Zhang, S., Chen, J. 2014a. Facile fabrication of magnetic carbon composites from hydrochar via simultaneous activation and magnetization for triclosan adsorption. *Environmental Science & Technology*, 48(10), 5840-5848.

Zhu, X., Liu, Y., Qian, F., Zhou, C., Zhang, S., Chen, J. 2014b. Preparation of magnetic porous carbon from waste hydrochar by simultaneous activation and magnetization for tetracycline removal. *Bioresource Technology*, 154, 209-214.

Zhu, X., Qian, F., Liu, Y., Matera, D., Wu, G., Zhang, S., Chen, J. 2016. Controllable synthesis of magnetic carbon composites with high porosity and strong acid resistance from hydrochar for efficient removal of organic pollutants: An overlooked influence. *Carbon*, 99, 338-347.

Zhuan, R., Wang, J. 2019. Enhanced mineralization of sulfamethoxazole by gamma radiation in the presence of Fe<sub>3</sub>O<sub>4</sub> as Fenton-like catalyst. *Environmental Science and Pollution Research*, 26(27), 27712-27725.

## APPENDIX A

### SUPPORTING INFORMATION FOR CHAPTER II

**Table S2.1** Maximum adsorption capacity ( $Q_m$ ) of SMX and surface area of various adsorbents.

Adsorbents	Surface area ( $m^2/g$ )	$Q_m$ (mg/g)	Reference
Carbon nanotube	382	71.8 <sup>a</sup>	(Zhao et al., 2016)
Graphene oxide	-	240 <sup>a</sup>	(Chen et al., 2015a)
Commercial AC (ChemViron Carbon)	848	118 <sup>a</sup>	(Calisto et al., 2015)
Coal based AC	851	185.19 <sup>a</sup>	(Çalışkan & Göktürk, 2010)
Alfalfa BC	405	90.4 <sup>a</sup>	(Choi & Kan, 2019)
Giant reed BC (300 °C)	2.09	4.99 <sup>a</sup>	(Zheng et al., 2013)
Giant reed BC (600 °C)	58.75	1.93 <sup>a</sup>	
Pine Sawdust BC	125	13.8 <sup>a</sup>	(Reguyal et al., 2017a)
Rice-straw BC (300 °C)	5.76	4.21 <sup>a</sup>	(Sun et al., 2016)
Rice-straw BC (600 °C)	27.4	7.40 <sup>a</sup>	
Wheat-straw BC (300 °C)	7.62	6.75 <sup>a</sup>	
Wheat-straw BC (600 °C)	38.1	0.25 <sup>a</sup>	
Bamboo BC (H <sub>3</sub> PO <sub>4</sub> activated)	1.12	88.1 <sup>a</sup>	(Ahmed et al., 2017b)
Anaerobically digested BC	17.66	54.38 <sup>a</sup>	(Yao et al., 2018)
Cornstalk BC(steam activated)	944.71	36.93 <sup>a</sup>	(Fan et al., 2019)
Sludge BC (thermal activated)	266.18	30.43 <sup>a</sup>	(Rodríguez-Martínez et al., 2019)
Plant BC (thermal activated)	631.76	21.53 <sup>a</sup>	
CuZnFe <sub>2</sub> O <sub>4</sub> -Bamboo BC	61.48	212.8 <sup>a</sup>	(Heo et al., 2019)
Commercial AC (Darco® G-60)	933	328.83 <sup>b</sup>	(Jang et al., 2018c)
Commercial AC (Calgon F400)	816.3	312.14 <sup>b</sup>	
Commercial AC (Norit® GAC)	1200	377.5 <sup>b</sup>	

BC: Biochar

AC: Activated Carbon

<sup>a</sup>Derived from isotherm model

<sup>b</sup>Derived from experimental data

**Table S2.2** Adsorption isotherm, kinetic, and thermodynamic models used in this study.

Models	Names and Equations
Kinetics	Pseudo-first order: $Q_t = Q_e(1 - \exp(-K_1t))$
	Pseudo-second order: $Q_t = \frac{K_2Q_e^2t}{1+K_2Q_e t}$
	Elovich: $Q_t = \left(\frac{1}{b}\right) \ln ab + \left(\frac{1}{b}\right) \ln t, t_0 = \frac{1}{ab}$
	Intra-particle diffusion: $Q_t = K_i\sqrt{t} + C_i$
	Boyd equation: $B_t = -\ln\left(1 - \frac{Q_t}{Q_e}\right) - 0.4977$
	Liquid film diffusion: $\ln(1 - F) = -K_{fd}t, F = \frac{Q_t}{Q_e}$
Isotherm	Freundlich isotherm: $Q_e = K_f C_e^{\frac{1}{n_f}}$
	Langmuir isotherm: $Q_e = \frac{Q_m K_L C_e}{1 + K_L C_e}, R_L = \frac{1}{1 + K_L C_0}$
	Temkin isotherm: $Q_e = \frac{RT}{b_T} \ln(K_T C_e)$
	Dubinin-Radushkevich: $Q_e = K_{DR} \exp(-B_D \varepsilon_D^2) \quad \varepsilon_D = RT \ln\left(1 + \frac{1}{C_e}\right); E = \frac{1}{\sqrt{2B_D}}$
Thermodynamics	$K_d = \frac{Q_e}{C_e}$
	$\Delta G^o = -RT \ln(K_d)$
	$\ln(K_d) = -\frac{\Delta G^o}{RT} = \frac{\Delta S^o}{R} - \frac{\Delta H^o}{RT}$

$Q_t$ : adsorption capacity (mg g<sup>-1</sup>) at time t (min).

$Q_e$ : adsorption capacity (mg g<sup>-1</sup>) at equilibrium time.

$K_1$ : adsorption rate constant of Pseudo-first order (min<sup>-1</sup>).

$K_2$ : adsorption rate constant of Pseudo-second order (min<sup>-1</sup>).

a: initial adsorption rate (mg/g.min).

b: desorption constant (g/mg).

$K_i$ : Intra-particle diffusion rate constant (mg min<sup>0.5</sup> g<sup>-1</sup>).

$C_i$ : the intercept reflecting the boundary layer thickness.

$B_t$ : Boyd constant, predicting the adsorption rate-limiting step.

$K_{fd}$  = adsorption rate constant (h<sup>-1</sup>).

$C_e$ : equilibrium concentration at liquid phase (mg L<sup>-1</sup>).

$K_f$ : distribution coefficient (mg/g), it implies that the energy of adsorption on a homogeneous surface is independent of surface coverage.

$1/n_f$ : related to the surface heterogeneity, more close to zero means more heterogeneous surface.

$Q_m$ : maximum adsorption capacity (mg/g) from monolayer adsorption.

$K_L$ : Langmuir constant (L/g) describing the adsorption/desorption equilibrium for each reactant in contact with a surface.

$R_L$ : separation constant; the adsorption is irreversible  $R_L=0$ , favorable  $0 < R_L < 1$ , linear  $R_L=1$ , and unfavorable  $R_L > 1$ .

R: universal gas constant (8.314 J mol<sup>-1</sup>K<sup>-1</sup>).

T: temperature in terms of Kelvin.

$b_T$ : Temkin constant (J/mol), defined as variation of adsorption energy; the adsorption is exothermic ( $b_T > 1$ ) or endothermic ( $b_T < 1$ )

$K_T$ : equilibrium bond constant related to the maximum energy of bond (mg/L).

$K_{DR}$ : adsorption capacity (mg/g), multilayer adsorption

$B_D$ : mean free energy of sorption (mol<sup>2</sup>/kJ<sup>2</sup>).

E: bonding energy of the ion-exchange mechanism (kJ/mol).

$\epsilon_D$ : adsorption potential.

$\Delta H^\circ$  = standard enthalpy change.

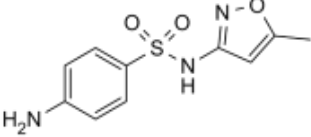
$\Delta S^\circ$  = standard entropy change.

$\Delta G^\circ$  = standard Gibbs free energy change.

**Table S2.3** Characteristics of various activated carbons.

Adsorbents	Surface area (m <sup>2</sup> /g)	Elemental compositions				O/C	H/C	Ash (%)	Reference
		C	H	O	N				
A-BC (This study)	1991.6	81.22	0.84	7.42	0.83	0.07	0.12	9.46	
Commercial activated carbon (Calgon F400)	1102	82.85	0.93	9.27	0.55	0.08	0.13	5.40	(Jang & Kan, 2019b)
Commercial activated carbon (Alphacarbo)	525.3	78.62	1.28	19.77	0.33	0.19	0.20	5.03	(Pego et al., 2019)
Commercial activated carbon (Steam activated coconut shell)	1138	90.1	0.2	9.0	-	0.07	0.03	0.4	(Torres-Pérez et al., 2012)
Commercial activated carbon (H <sub>3</sub> PO <sub>4</sub> activated wood)	1515	64.8	2.4	19.5	-	0.23	0.44	1.1	(Torres-Pérez et al., 2012)
Activated carbon (K <sub>2</sub> CO <sub>3</sub> activated tobacco residue)	1634	55.25	0.22	45.38	0.95	0.62	0.05	-	(Kilic et al., 2011)
Activated carbon (KOH activated tobacco residue)	1474	49.40	0.28	48.80	1.52	0.74	0.07	-	(Kilic et al., 2011)
Activated carbon (Steam activated beet pulp)	821	77.9	0.9	7.0	0.6	0.07	0.14	13.6	(Torres-Pérez et al., 2012)
Activated carbon (Steam activated peanut shell)	829	91.2	0.8	6.0	0.2	0.05	0.11	1.3	(Torres-Pérez et al., 2012)

**Table S2.4** Physicochemical characteristics of sulfamethoxazole (SMX) (Jang et al., 2018c; Martínez & Gómez, 2002).

Molecular structure	Formula	Molecular weight	Solubility <sup>a</sup>	pK <sub>a</sub>
	C <sub>10</sub> H <sub>11</sub> N <sub>3</sub> O <sub>3</sub> S	253.28	0.37 g/L	pK <sub>1</sub> = 1.6 pK <sub>2</sub> = 5.7

<sup>a</sup>At ambient temperature

**Table S2.5** Calculated sorption coefficients for three SMX species on A-BC at pH 1-12.

pH	K <sub>d</sub>	K <sub>d</sub> <sup>+</sup>	K <sub>d</sub> <sup>0</sup>	K <sub>d</sub> <sup>-</sup>
1	6402	7357	2597	1000
2	7762	4237	9167	1002
3	8229	1294	8519	1016
4	8139	1025	8306	1148
5	7145	998	8090	2423
6	6199	995	4105	7248
7	5478	994	1232	5690
8	5356	992	1020	5378
9	5561	992	1000	5563
10	2934	991	997	2934



**Table S2.6** Contribution of different SMX species to the overall sorption on A-BC.

pH	Contribution percent (%)		
	SMX <sup>+</sup>	SMX <sup>0</sup>	SMX <sup>-</sup>
1	91.86	8.14	<0.01
2	15.54	84.46	<0.01
3	0.60	99.38	0.02
4	0.05	99.68	0.28
5	<0.01	94.35	5.64
6	<0.01	22.11	77.89
7	<0.01	1.07	98.93
8	<0.01	0.10	99.90
9	<0.01	<0.01	99.99
10	<0.01	<0.01	99.99

\*Contribution percentage was calculated by  $K_d^+ \alpha^+ / K_d$  for SMX<sup>+</sup>,  $K_d^0 \alpha^0 / K_d$  for SMX<sup>0</sup>, and  $K_d^- \alpha^- / K_d$  for SMX<sup>-</sup>.

**Table S2.7** Characteristics of lagoon wastewater from dairy farm (Stephenville, TX, USA).

COD (ppm)	1050
Total N (ppm)	460
Total P (ppm)	57
Total K (ppm)	676
Total Ca (ppm)	227
Total Mg (ppm)	157
Total Na (ppm)	277

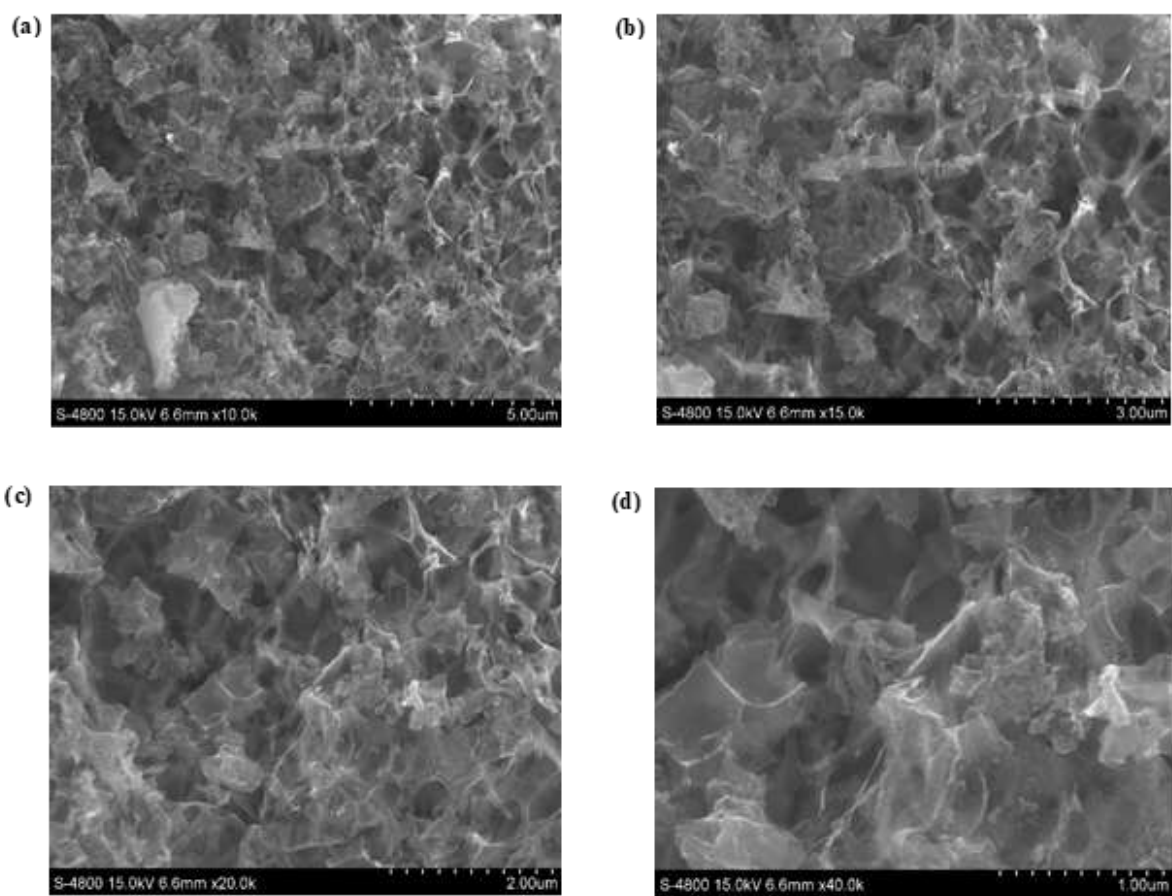


**Figure S2.1.** SEM images of A-BC at various magnifications (a:10,000; b:15,000; c:20,000; d:40,000)

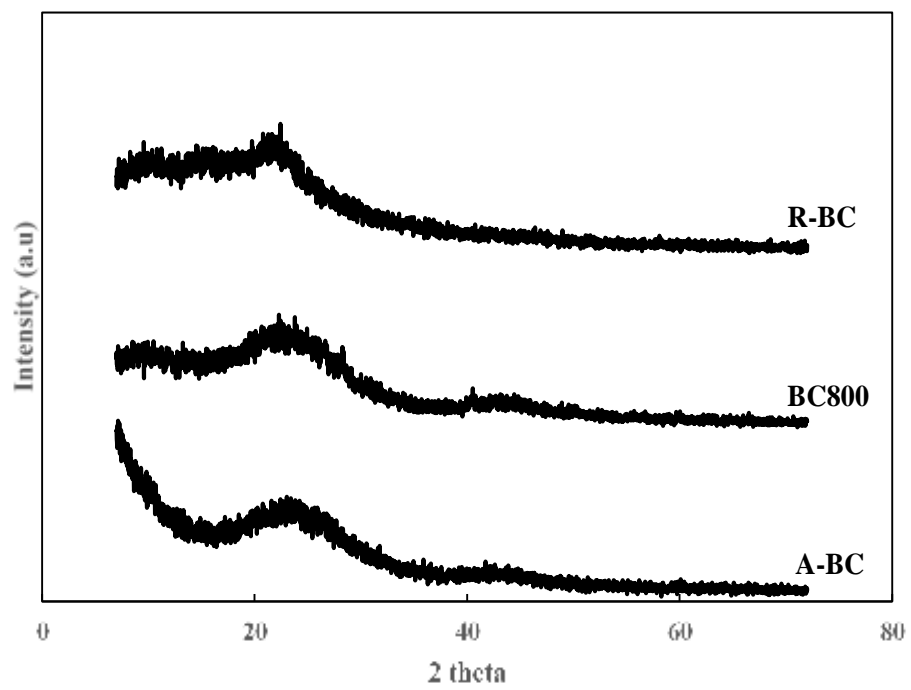


**Figure S2.2.** XRD pattern of all BCs.

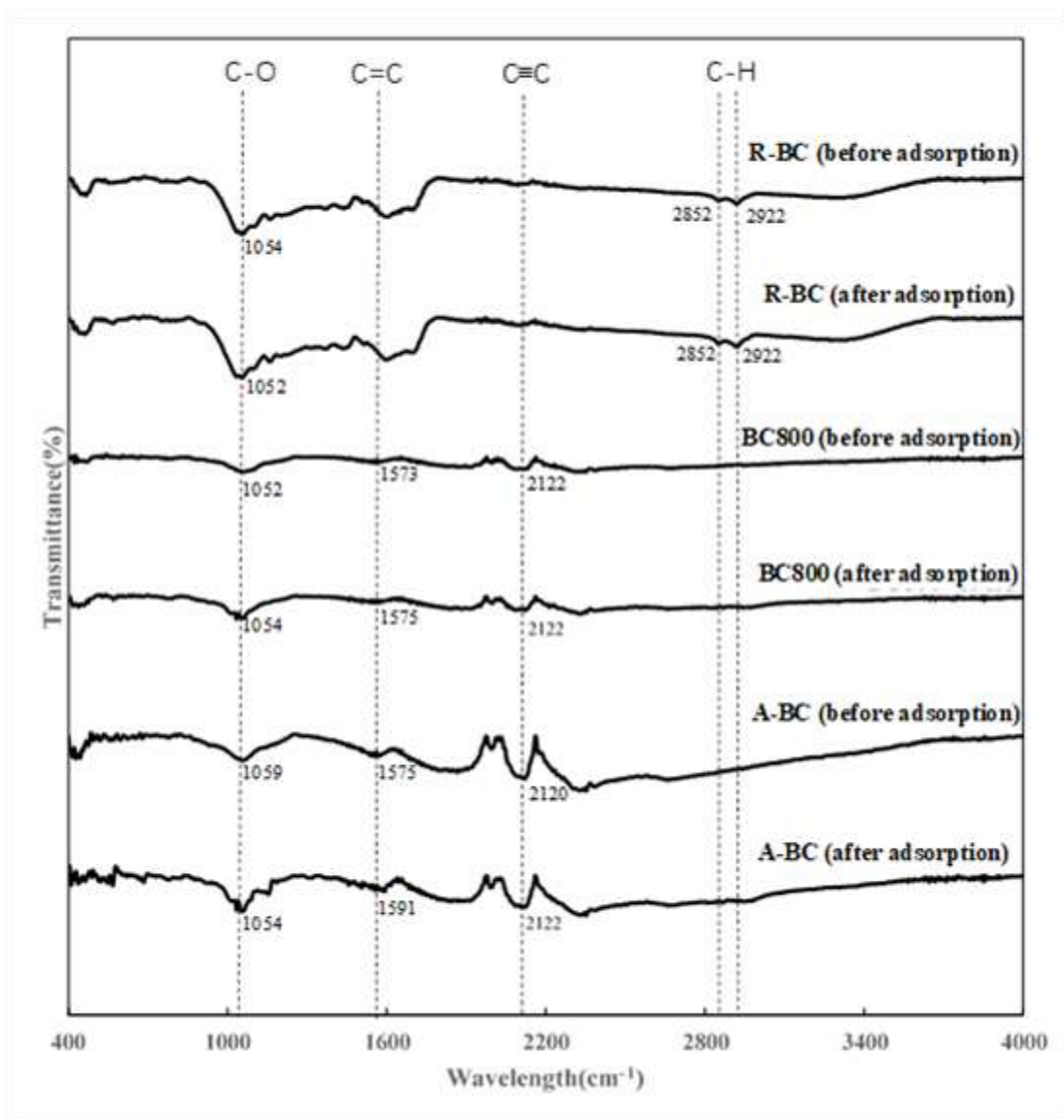


**Figure S2.3.** FT-IR spectrum of all BCs before and after SMX adsorption.

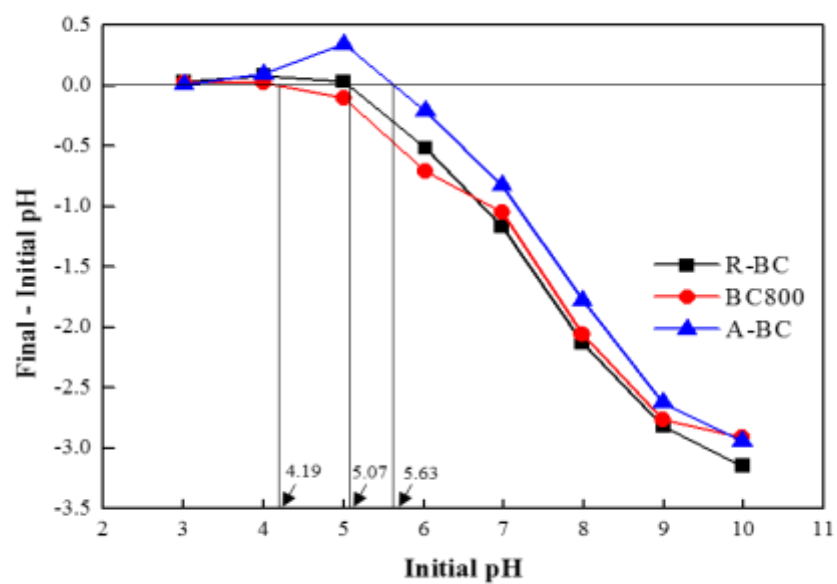


**Figure S2.4.** The pHzpc of all BCs.

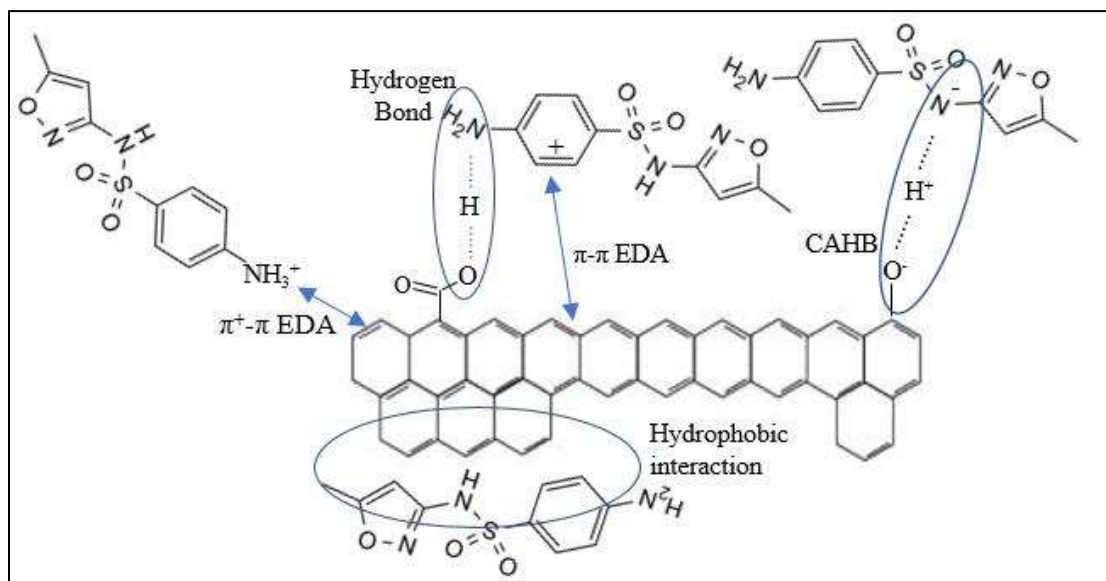


**Figure S2.5.** Proposed mechanisms for SMX adsorption on A-BC.

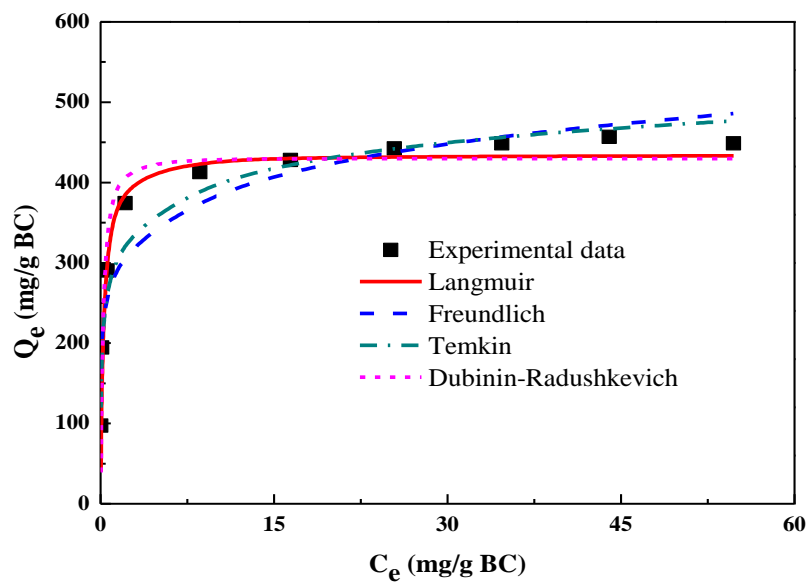


**Figure S2.6.** Adsorption isotherm of SMX on A-BC.

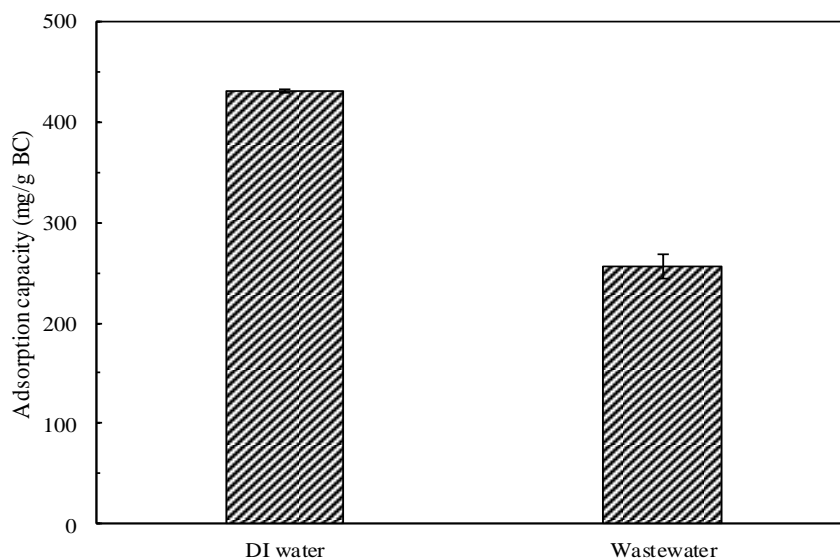


**Figure S2.7.** Adsorption of SMX onto A-BC in DI water and real wastewater. Adsorption conditions: 0.01 g of A-BC, initial pH of 6, 100 mL of 100 mg/L SMX, and 3 day.

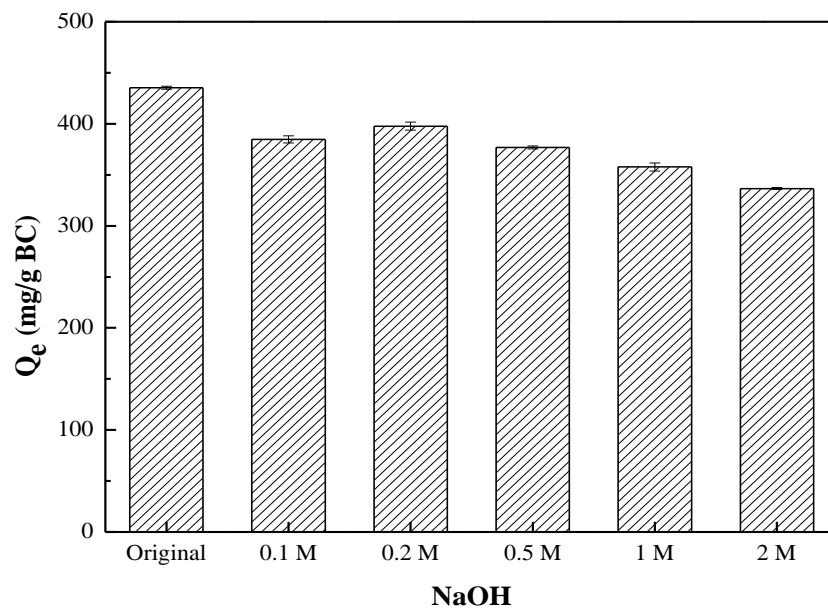


**Figure S2.8.** Effect of different NaOH concentration on the regeneration of A-BC.

## APPENDIX B

### SUPPORTING INFORMATION FOR CHAPTER III

**Table S3.1** Breakthrough models for fixed bed experiments.

Breakthrough model	Equation
Thomas	$\ln\left(\frac{C_0}{C_t} - 1\right) = k_{Th}q_0\frac{m}{Q} - k_{Th}C_0t$
Yoon-Nelson	$\ln\left(\frac{C_t}{C_0 - C_t}\right) = k_{YN}t - \tau k_{YN}$

$k_{Th}$ : Thomas rate constant (mL/min mg).

$q_0$ : adsorption capacity (mg/g).

$C_0$ : inlet SMX concentration (mg/L).

$C_t$ : outlet SMX concentration at time  $t$  (mg/L).

$m$ : mass of adsorbent (mg),  $Q$  is the flow rate (mL/min).

$t$ : the time (min).

$k_{YN}$ : Yoon–Nelson rate constant ( $\text{min}^{-1}$ ).

$\tau$ : time required for 50% SMX breakthrough (min).



**Table S3.2** Pearson correlation analysis (coefficients (*r*) and significance level) between physical and chemical properties of IA-BCs and SMX adsorption capacity.

Factors	Impregnation ratio of FeCl <sub>3</sub> to BG			SMX Q <sub>e</sub> (mg/g)		
	<i>r</i>	Significance level	<i>p</i> value	<i>r</i>	Significance level	<i>p</i> value
SMX Q <sub>e</sub> (mg/g)	0.789	NS	0.112	-	-	-
Ash (%)	0.845	NS	0.071	0.415	NS	0.487
Volatile Carbon (%)	0.886	*	0.046	0.946	*	0.015
Fixed Carbon (%)	-0.973	**	0.005	-0.721	NS	0.169
Surface area (m <sup>2</sup> /g)	0.714	NS	0.175	0.974	**	0.005
O/C (mol/mol)	-0.865	NS	0.058	-0.700	NS	0.188
H/C (mol/mol)	-0.804	NS	0.101	-0.967	**	0.007
N (%)	-0.745	NS	0.149	-0.811	NS	0.095
P (%)	-0.601	NS	0.284	-0.896	*	0.040
K (%)	-0.588	NS	0.297	-0.889	*	0.044
Ca (%)	-0.654	NS	0.231	-0.875	NS	0.052
Mg (%)	-0.627	NS	0.258	-0.893	*	0.041
Na (%)	-0.604	NS	0.281	-0.906	*	0.034
Fe (%)	0.666	NS	0.220	0.750	NS	0.145

\*, \*\*, and \*\*\* are significance level of <0.05, <0.01 and <0.001; NS= not significant.

**Table S3.3** Summary of kinetic parameters of SMX adsorption on IA-BC<sub>2.0</sub>. Experimental conditions: 100 mL of 50 and 100 mg/L SMX, 0.01 g of BC, initial pH of 3, and 48 h.

	50 mg/L	100 mg/L
$Q_e^a$	259.19	246.86
Pseudo-first order		
$Q_e^b$	225.08	214.80
$K_1$	0.03	0.03
SSE	18.07	16.79
$R^2$	0.9173	0.9212
Pseudo-second order		
$Q_e^b$	241.10	229.66
$K_2$	0.0002	0.0002
SSE	9.92	9.28
$R^2$	0.9751	0.9759
Elovich		
$Q_e^b$	265.81	252.87
a	1238.11	1634.91
b	0.05	0.05
SSE	2.84	2.55
$R^2$	0.9980	0.9982
Two compartment first-order		
$Q_e^b$	254.92	240.45
$F_{fast}$	0.68	0.65
$F_{slow}$	0.32	0.35
$K_{fast}$	4.25	333
$K_{slow}$	0.15	0.194
SSE	2.75	4.57
$R^2$	0.9981	0.9942
Liquid film diffusion		
$Q_e^b$	225.08	214.80
$K_{fd}$	0.03	0.03
SSE	18.80	17.47
$R^2$	0.5490	0.5437
Intra-particle diffusion		
$Q_e^b$	277.06	263.38
$K_i$	1.90	1.76
$K_{i1}$	29.2504	28.1811
$K_{i2}$	5.1993	4.7696
$K_{i3}$	1.1936	1.1276
$C_i$	175.24	169.14
SSE	12.03	11.01
$R^2$	0.8154	0.8187

<sup>a</sup>Experimental value

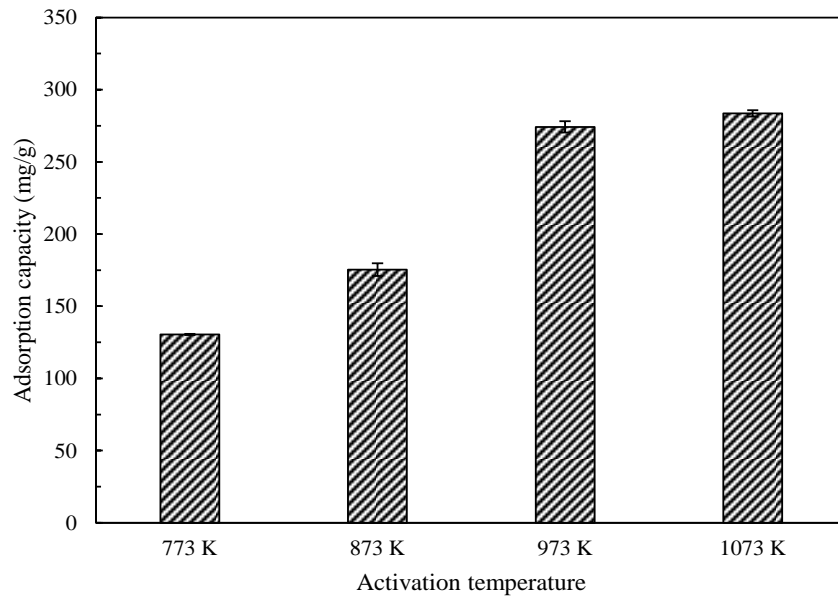
<sup>b</sup>Calculated value

**Table S3.4** Summary of breakthrough curves.

	Z (cm) <sup>a</sup>	F (mL/min) <sup>b</sup>	t <sub>b</sub> (min) <sup>c</sup>	t <sub>e</sub> (min) <sup>d</sup>	Z <sub>m</sub> (cm) <sup>e</sup>
BC800	1.88	1.28	60	150	1.13
IA-BC <sub>2.0</sub>	1.88	1.28	1680	2220	0.46

<sup>a</sup> Column height<sup>b</sup> Flow rate<sup>c</sup> Breakthrough time when the normalized effluent concentration (C<sub>t</sub>/C<sub>0</sub>) reaches 5%<sup>d</sup> Exhaustion time when C<sub>t</sub>/C<sub>0</sub> reaches 95%<sup>e</sup> Mass transfer zone where SMX is adsorbed onto IA-BC<sub>2.0</sub> in the column: Z<sub>m</sub> = Z (1 - t<sub>b</sub>/t<sub>e</sub>)**Table S3.5** Summary of Thomas and Yoon-Nelson model parameters for the fixed bed experiments.

	Thomas model			Yoon-Nelson model		
	k <sub>Th</sub> (L/min mg)	q <sub>0</sub> (mg/g)	R <sup>2</sup>	k <sub>YN</sub> (min <sup>-1</sup> )	τ (min)	R <sup>2</sup>
BC800	0.00053	13.52	0.98	0.053	105.62	0.98
IA-BC <sub>2.0</sub>	0.000084	251.03	0.98	0.0084	1961.19	0.98

**Figure S3.1.** Effect of activation temperature on the SMX adsorption capacity of IA-BC at the iron impregnation ratio of 2. Conditions: 0.01 g of BC, 100 mL of 100 mg/L of SMX solution, pH 5 and 2 d.

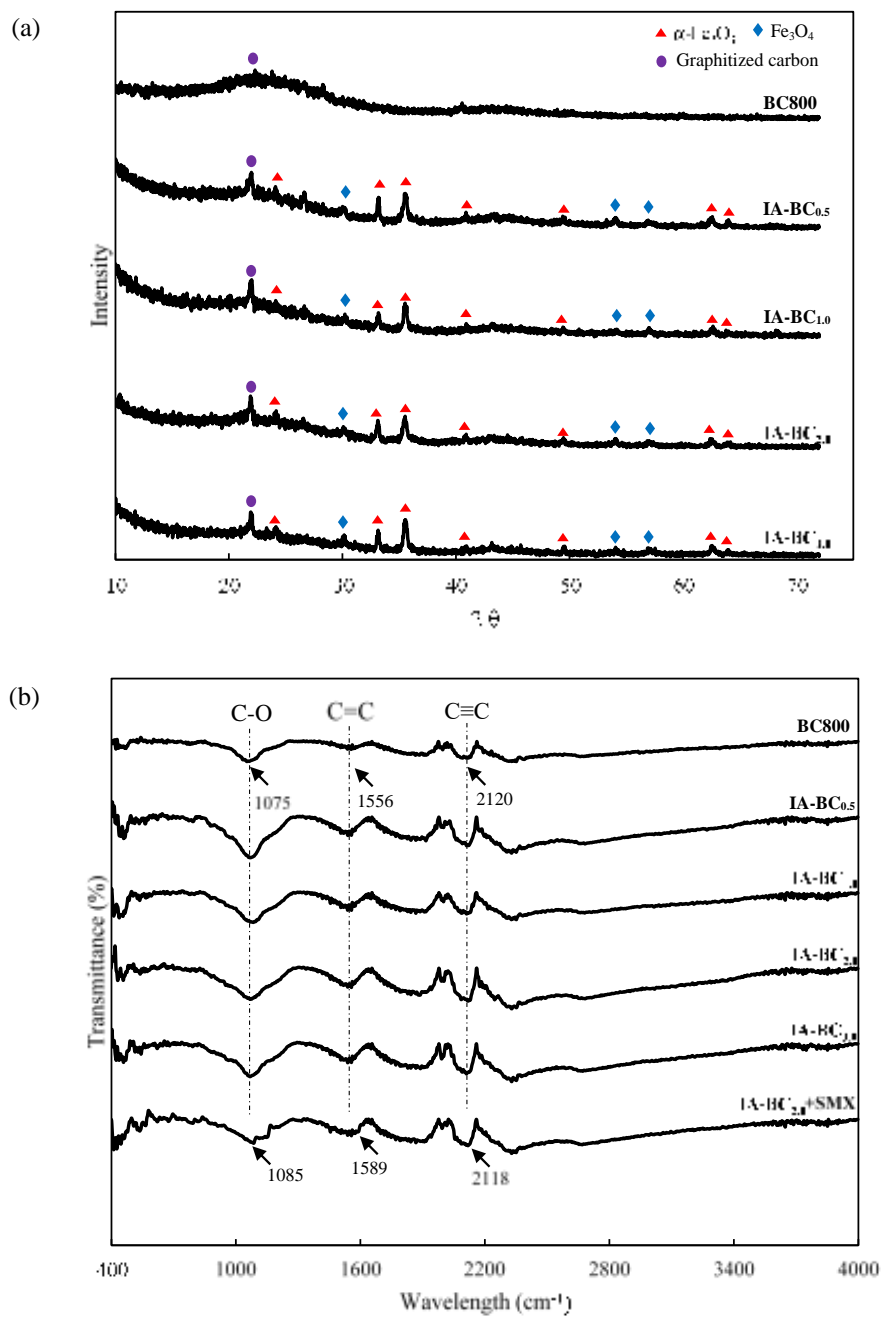


**Figure S3.2.** XRD patterns (a) and FT-IR spectrum (b) of all BCs.

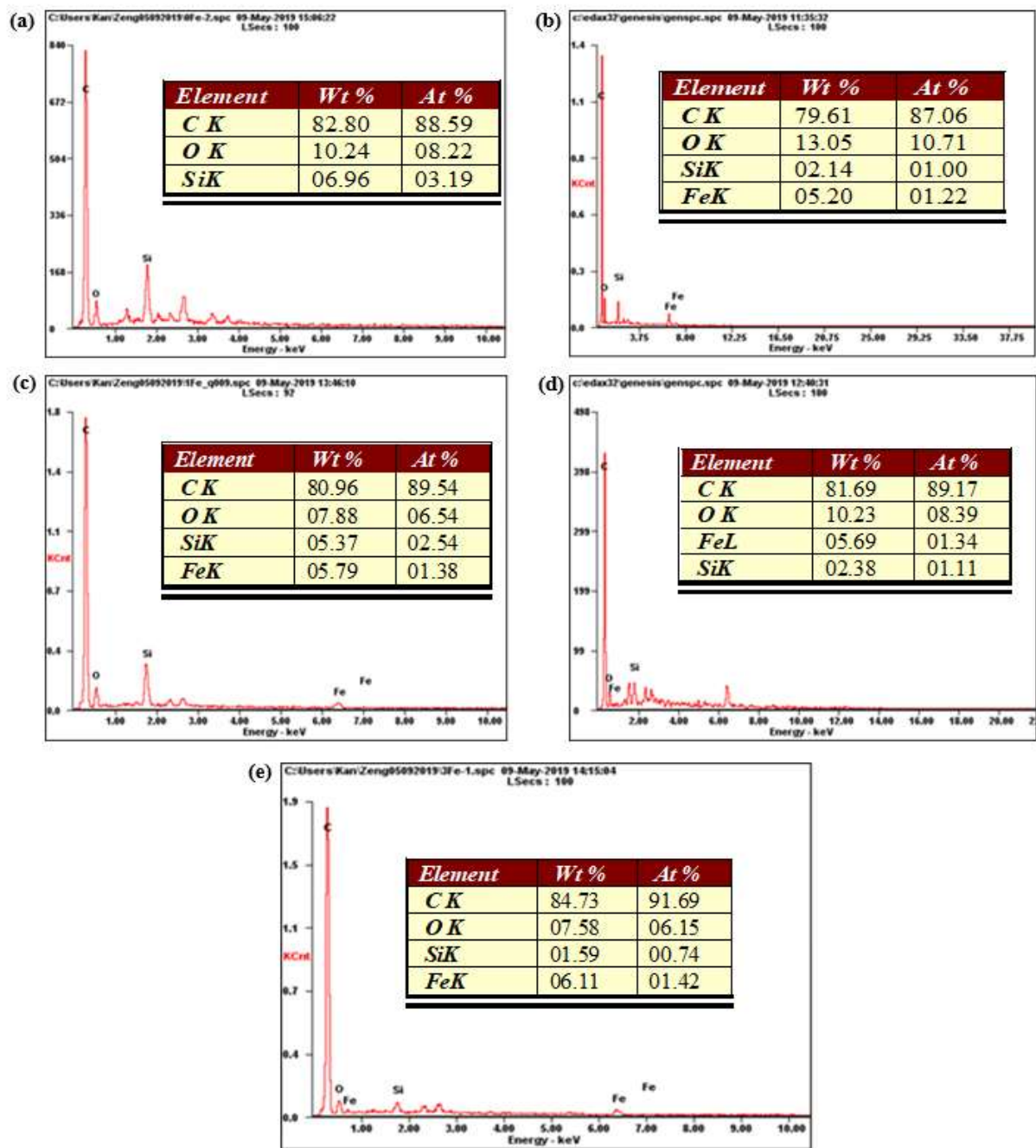


**Figure S3.3.** EDX analysis of all BCs. (a: BC800; b: IA-BC<sub>0.5</sub>; c: IA-BC<sub>1.0</sub>; d: IA-BC<sub>2.0</sub>; e: IA-BC<sub>3.0</sub>).

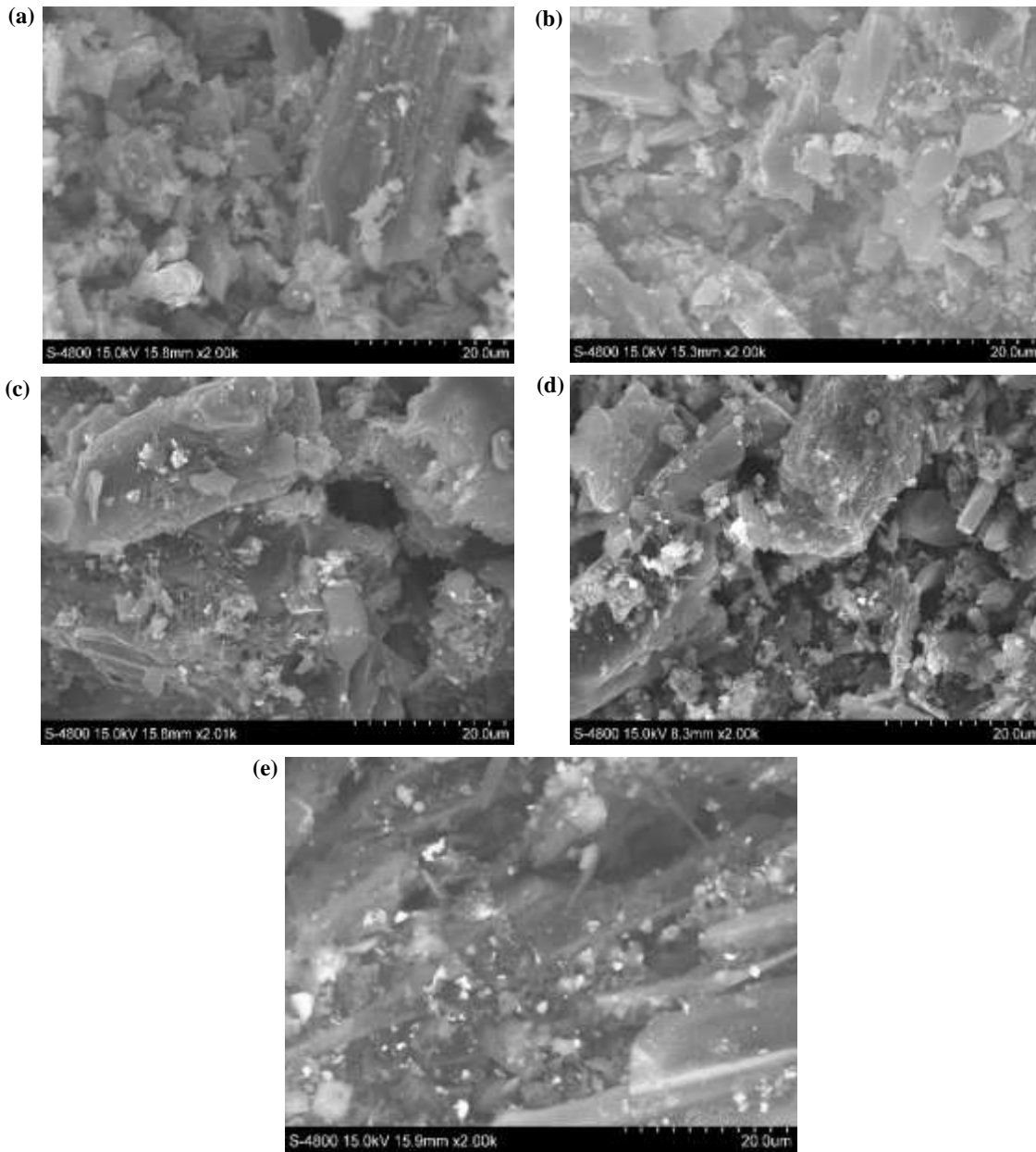


**Figure S3.4.** SEM images of all BCs. (a: BC800; b: IA-BC<sub>0.5</sub>; c: IA-BC<sub>1.0</sub>; d: IA-BC<sub>2.0</sub>; e: IA-BC<sub>3.0</sub>).



**Figure S3.5.** Magnetic separation of IA-BC<sub>2.0</sub> after SMX adsorption under an external magnetic field.

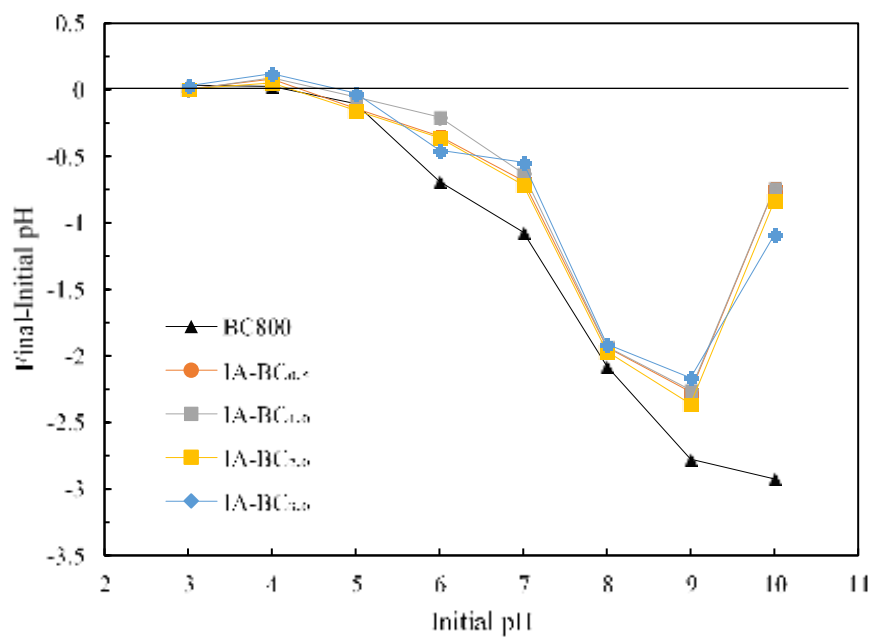


**Figure S3.6.** The pHPZC of all BCs.

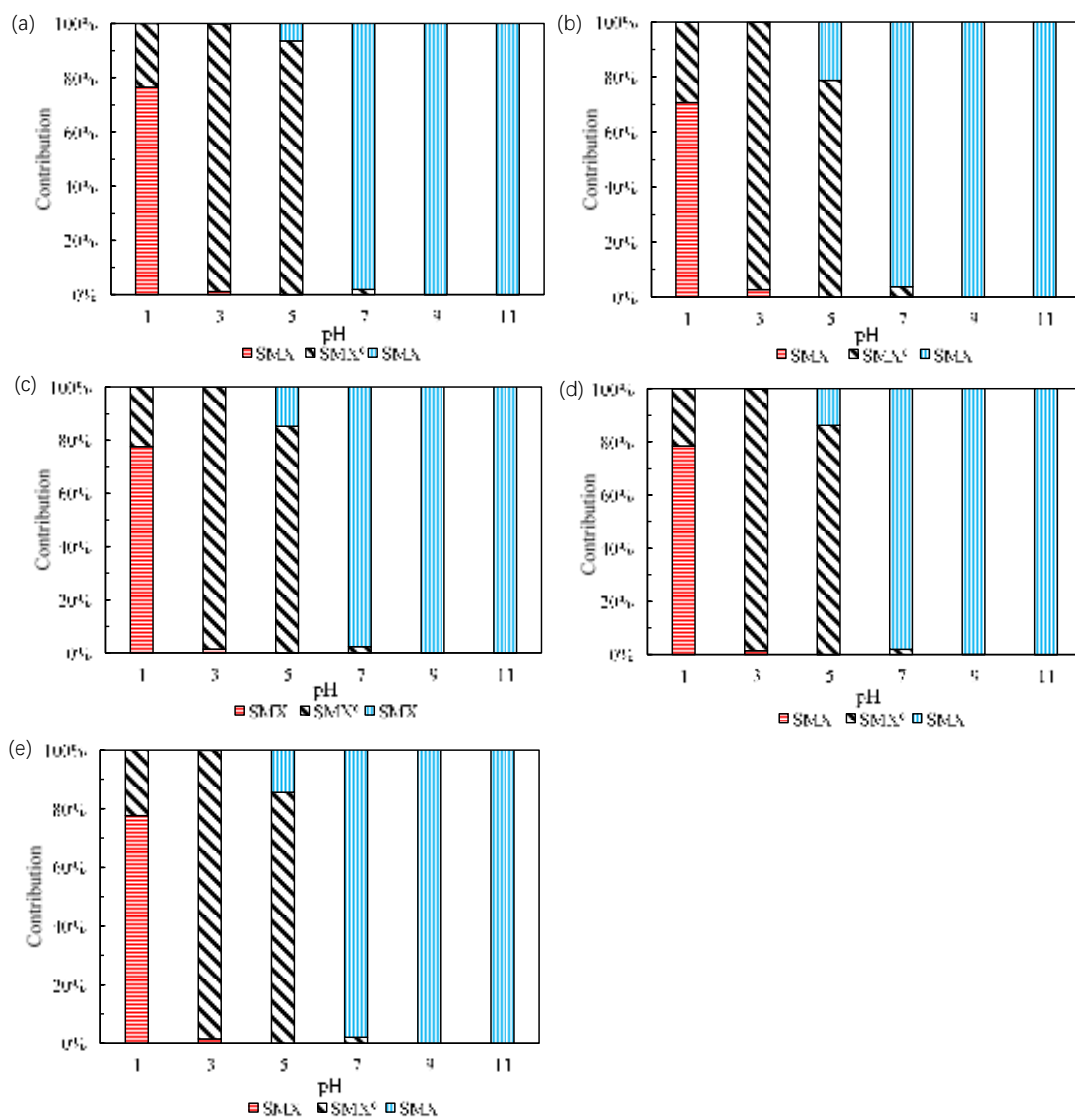


**Figure S3.7.** Contribution of different SMX species to the overall sorption on all BCs. Contribution percentage was calculated by  $K_d^+ \alpha^+ / K_d$  for  $SMX^+$ ,  $K_d^0 \alpha^0 / K_d$  for  $SMX^0$ , and  $K_d^- \alpha^- / K_d$  for  $SMX^-$ . (a: BC800; b: IA-BC<sub>0.5</sub>; c: IA-BC<sub>1.0</sub>; d: IA-BC<sub>2.0</sub>; e: IA-BC<sub>3.0</sub>)



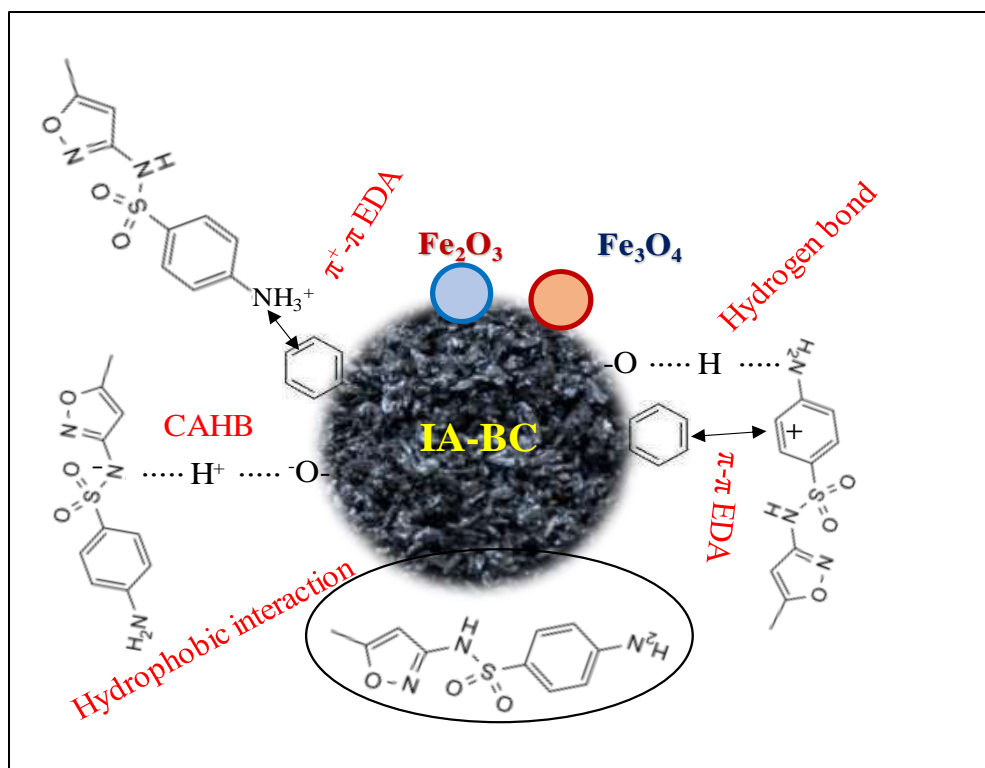


**Figure S3.8.** The proposed mechanism for SMX adsorption onto the IA-BC.

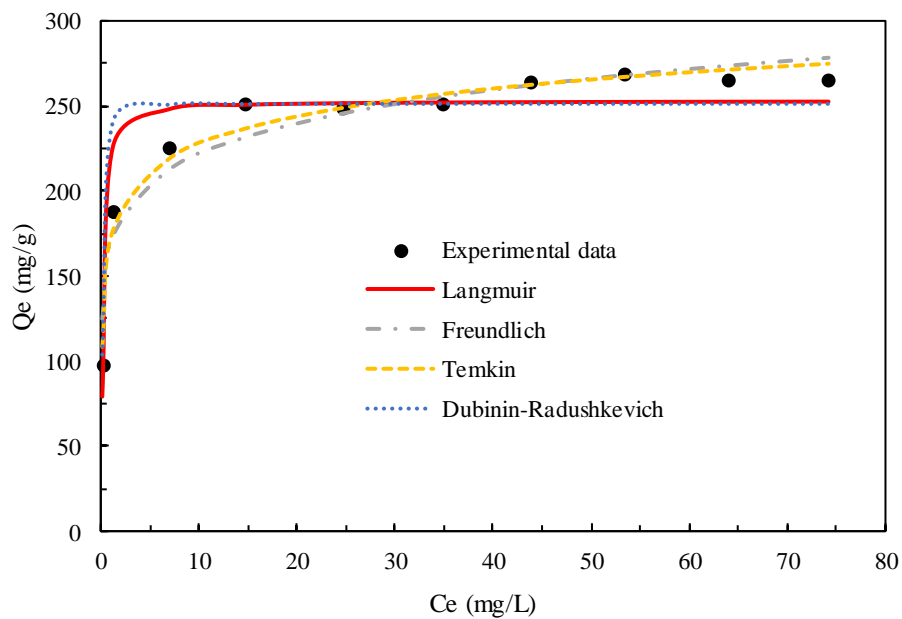


**Figure S3.9.** Adsorption isotherm of SMX on IA-BC<sub>2.0</sub>. Experimental conditions: 100 mL of 10-100 mg/L SMX, 0.01 g of BC, initial pH of 3, and 24 h.

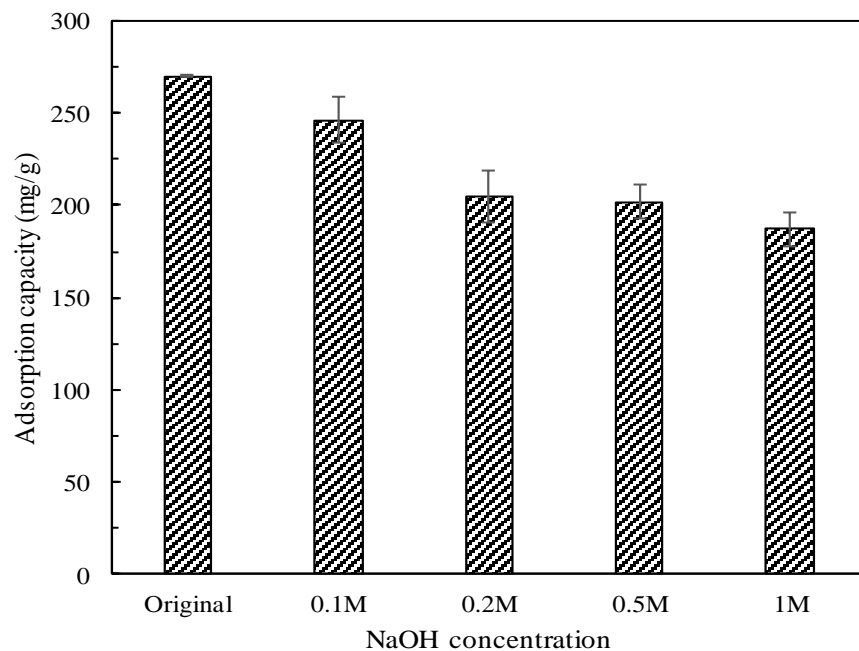


**Figure S3.10.** Effect of different NaOH concentration on the regeneration of IA-BC<sub>2.0</sub>.

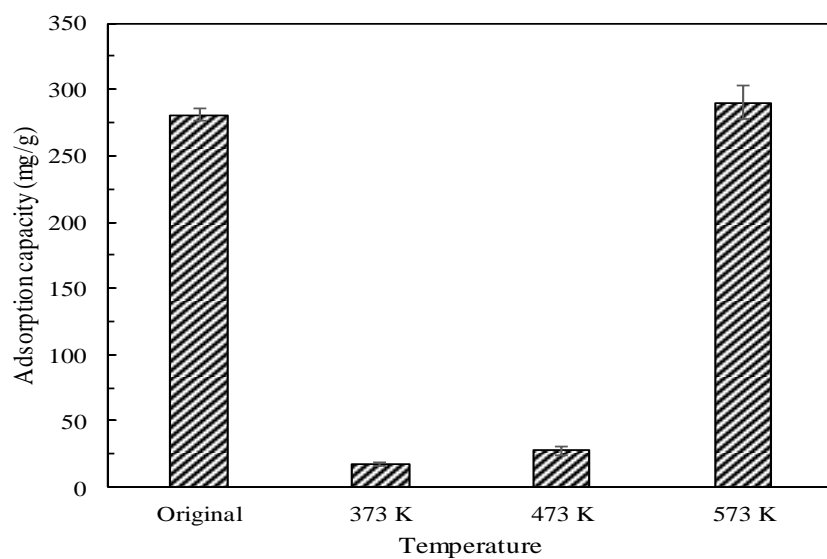


**Figure S3.11.** Effect of different treatment temperature on the regeneration of IA-BC<sub>2.0</sub>.

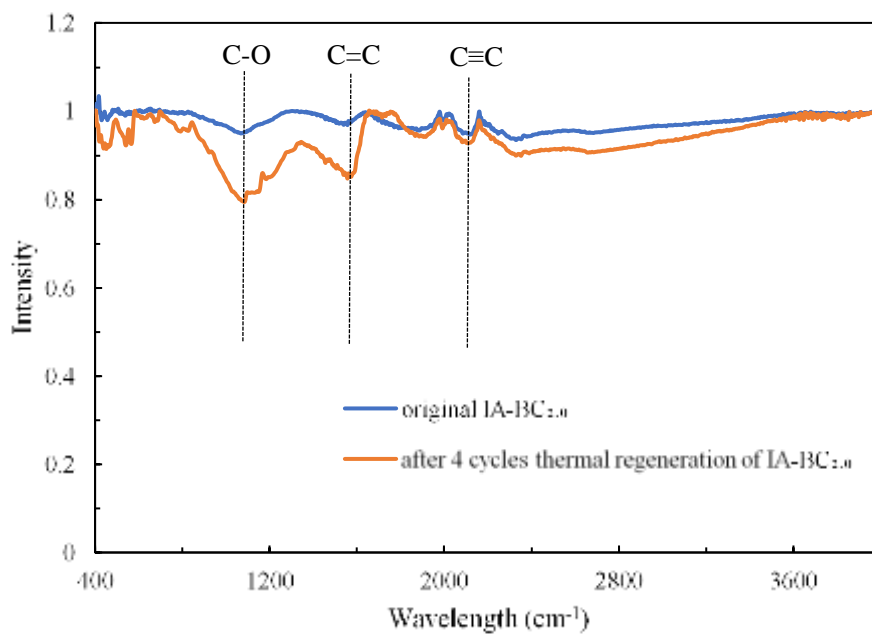


**Figure S3.12.** FT-IR spectrum of original IA-BC<sub>2.0</sub> and after 4 cycles thermal regeneration of IA-BC<sub>2.0</sub>.

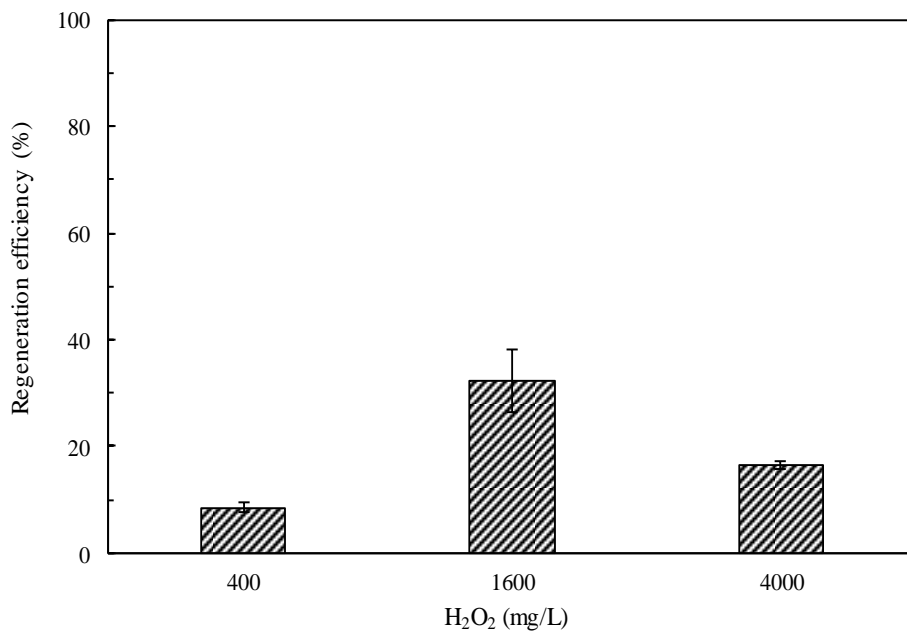


**Figure S3.13.** Effect of various H<sub>2</sub>O<sub>2</sub> concentration on the regeneration of IA-BC<sub>2.0</sub>.

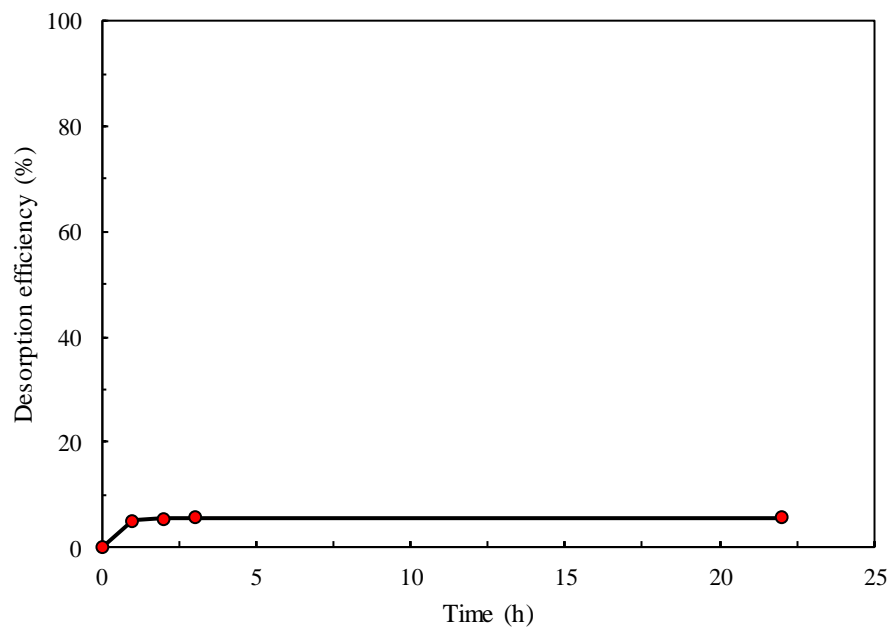


**Figure S3.14.** Desorption efficiency of SMX-spent IA-BC<sub>2.0</sub> at pH 3.

## APPENDIX C

### SUPPORTING INFORMATION FOR CHAPTER IV

**Table S4.1** The physicochemical properties of Raw-BC and FA-BC.

	Elemental analysis (wt.%)				O/C	H/C	(N+O)/C	BET surface area (m <sup>2</sup> /g)	Fe content (%)
	C	H	O	N					
Raw-BC	68.02	1.58	12.94	3.37	0.14	0.28	0.19	85.82	0.04
FA-BC	55.34	0.90	8.17	1.93	0.11	0.20	0.14	835.10	30.0

Raw-BC: Raw biochar; biochar produced at 800 °C without FeCl<sub>3</sub> activation.

FA-BC: FeCl<sub>3</sub> activated BC; biochar produced at 800 °C with the FeCl<sub>3</sub>/BG impregnation ratio of 2.

**Table S4.2** Summary of kinetic parameters for SMX on FA-BC.

BC	Q <sub>e</sub> <sup>a</sup>	Pseudo-first order			Pseudo-second order		
		Q <sub>e</sub> <sup>b</sup>	K <sub>1</sub>	R <sup>2</sup>	Q <sub>e</sub> <sup>b</sup>	K <sub>2</sub>	R <sup>2</sup>
FA-BC	187.77	169.34	0.03	0.9558	179.98	0.0003	0.9901

<sup>a</sup>Experimental value (mg/g)

<sup>b</sup>Calculated value (mg/g)

**Table S4.3** Summary of isotherm parameters for SMX on FA-BC.

BC	Langmuir model			Freundlich model		
	Q <sub>m</sub>	K <sub>L</sub>	R <sup>2</sup>	K <sub>f</sub>	n <sub>f</sub>	R <sup>2</sup>
FA-BC	194.58	5.68	0.9502	120.67	7.60	0.9186

**Table S4.4** Leaching of iron in solution under 3 successive cycles of Fenton oxidation.

	Iron concentration (mg/L)
Original	1.48
Cycle 1	0.62
Cycle 2	0.43
Cycle 3	0.24

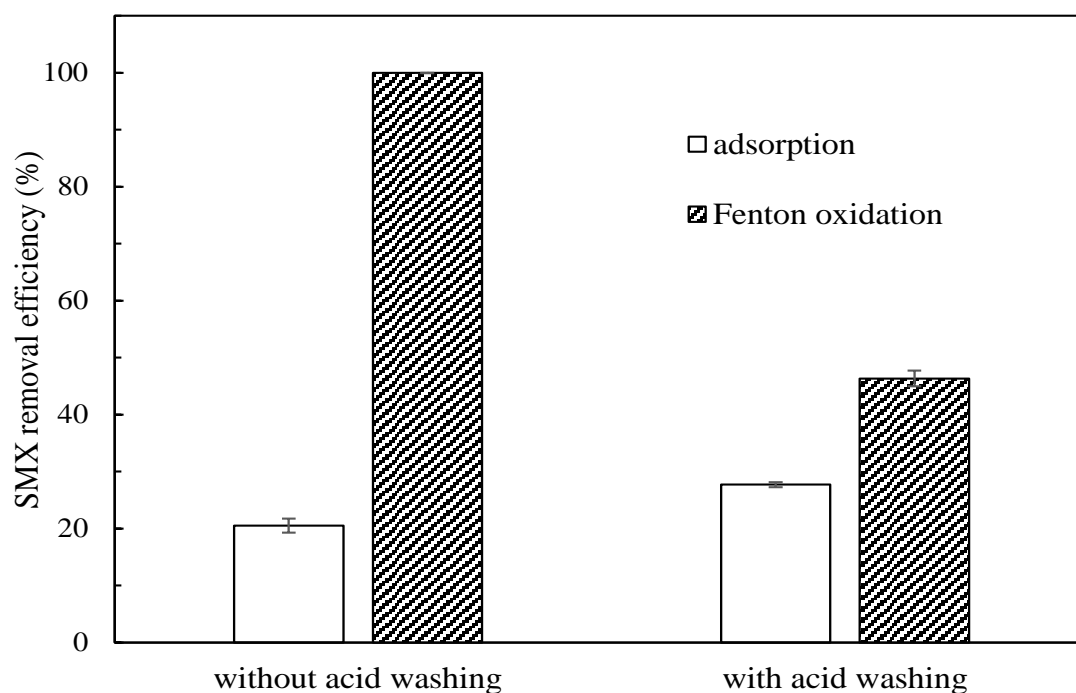


**Figure S4.1.** Effect of acid washing on SMX removal efficiency by iron activated BC (impregnation ratio of 2). Adsorption conditions: 0.01 g of BC, 100 mL of 100 mg/L SMX, initial pH of 3, temperature of 20°C, and 24 h. Fenton oxidation conditions: 0.01 g of BC, 200 mg/L H<sub>2</sub>O<sub>2</sub>, 100 mL of 100 mg/L SMX, initial pH of 3, temperature of 20°C, and 24 h.

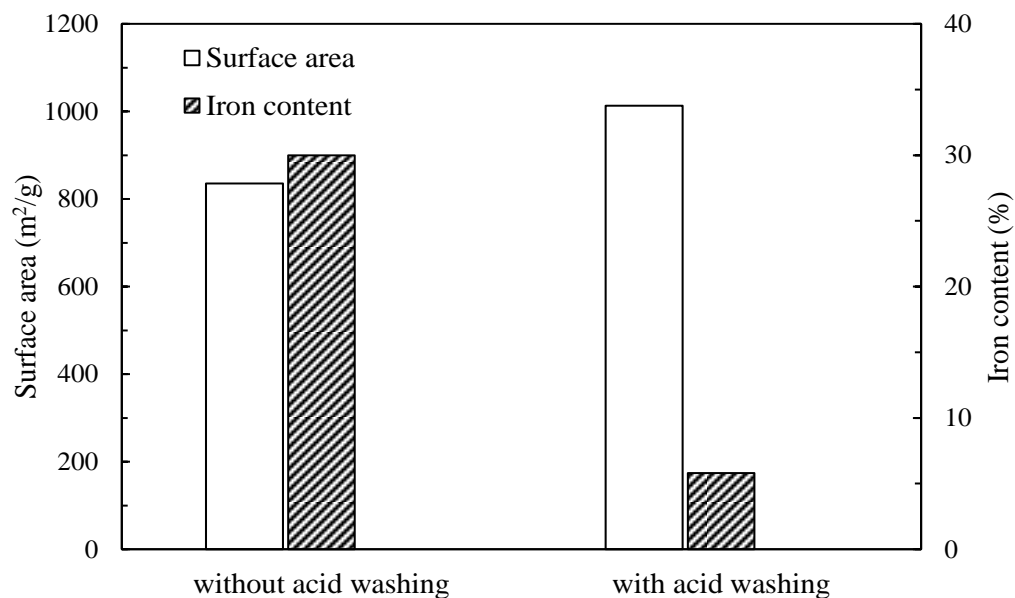


**Figure S4.2.** Effect of acid washing on surface area and iron content of iron activated BC (impregnation ratio of 2).

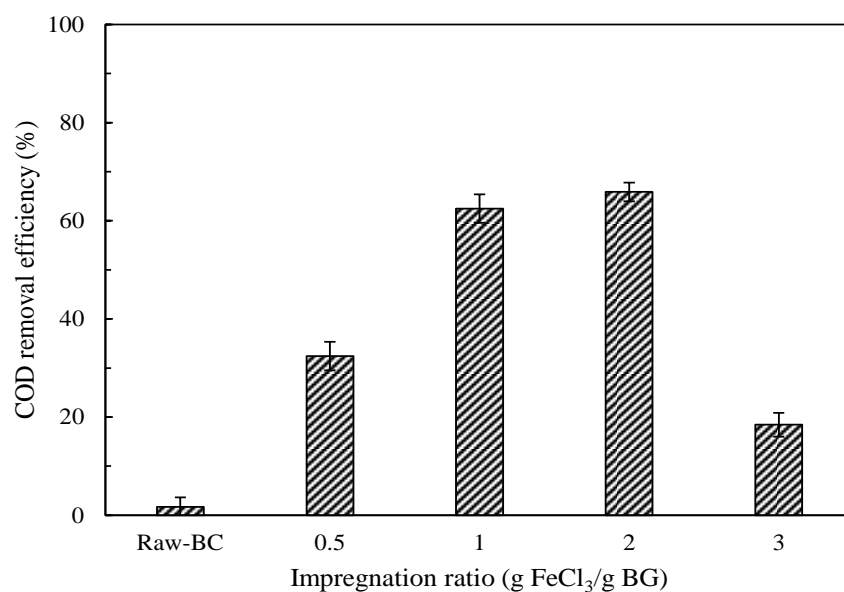


**Figure S4.3.** Effect of FeCl<sub>3</sub>/BG impregnation ratio on the COD removal efficiency by Fenton oxidation of iron activated BCs for SMX. Fenton oxidation conditions: 0.01 g of BC, 200 mg/L H<sub>2</sub>O<sub>2</sub>, 100 mL of 100 mg/L SMX, initial pH of 3, temperature of 20°C, and 24 h.



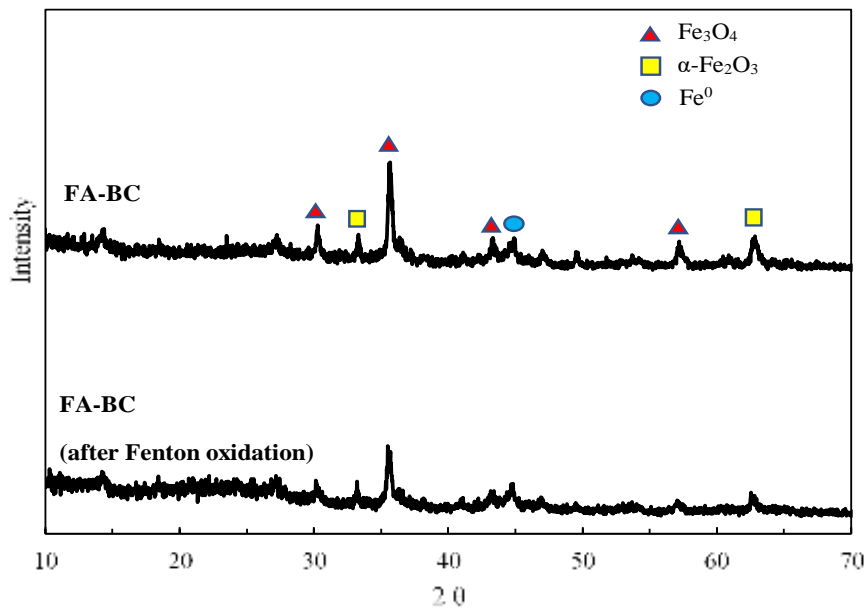


**Figure S4.4.** The XRD pattern of FA-BC before and after Fenton oxidation.

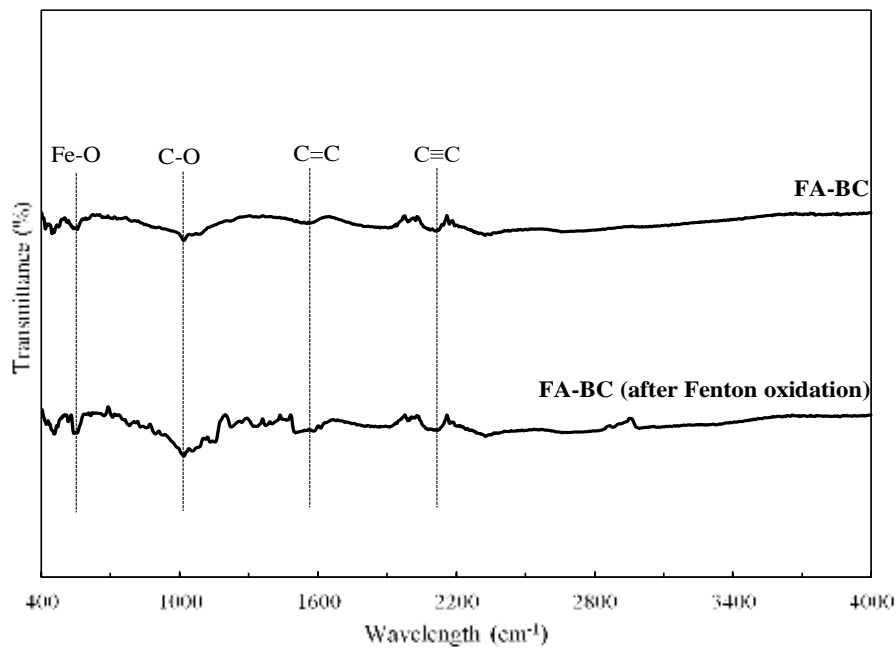


**Figure S4.5.** The FT-IR spectrum of FA-BC before and after Fenton oxidation.



**Figure S4.6.** Magnetic separation of FA-BC in the aqueous solution under an external magnetic field.

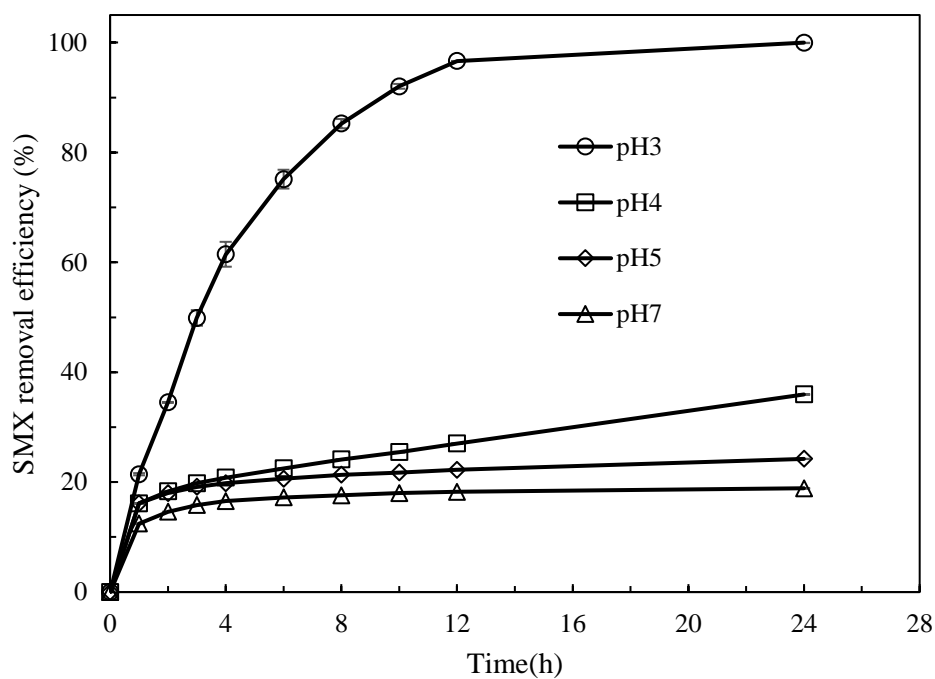


**Figure S4.7.** Effect of initial pH on Fenton oxidation of SMX. Conditions: 0.01 g of FA-BC, 300 mg/L  $H_2O_2$ , 100 mL of 100 mg/L SMX, and temperature of 20°C.

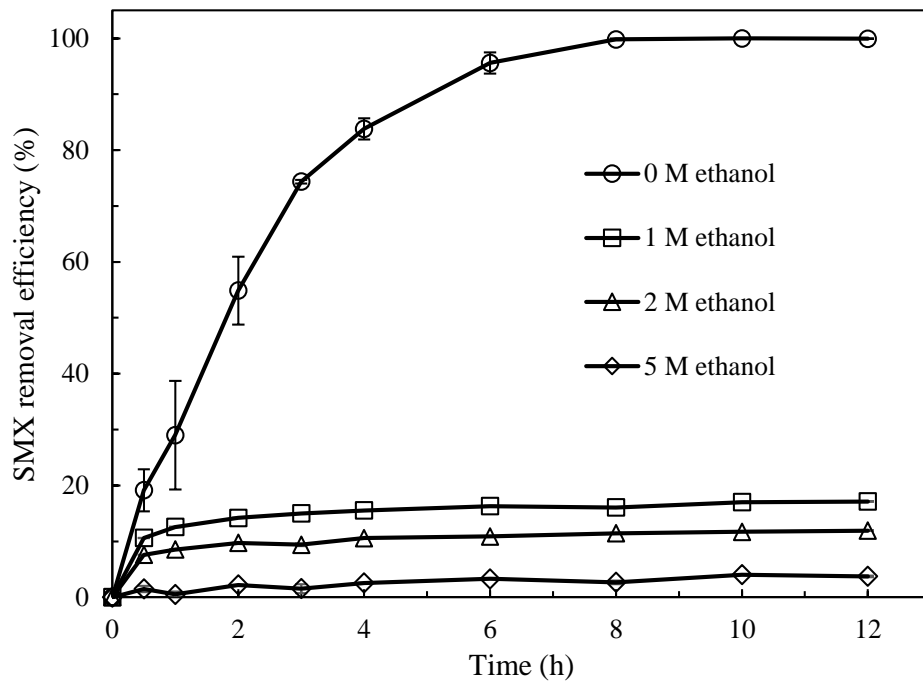


**Figure S4.8.** Effect of ethanol on Fenton oxidation of SMX. Conditions: 0.01 g of FA-BC, 200 mg/L H<sub>2</sub>O<sub>2</sub>, 100 mL of 100 mg/L SMX, initial pH of 3, and temperature of 20°C.

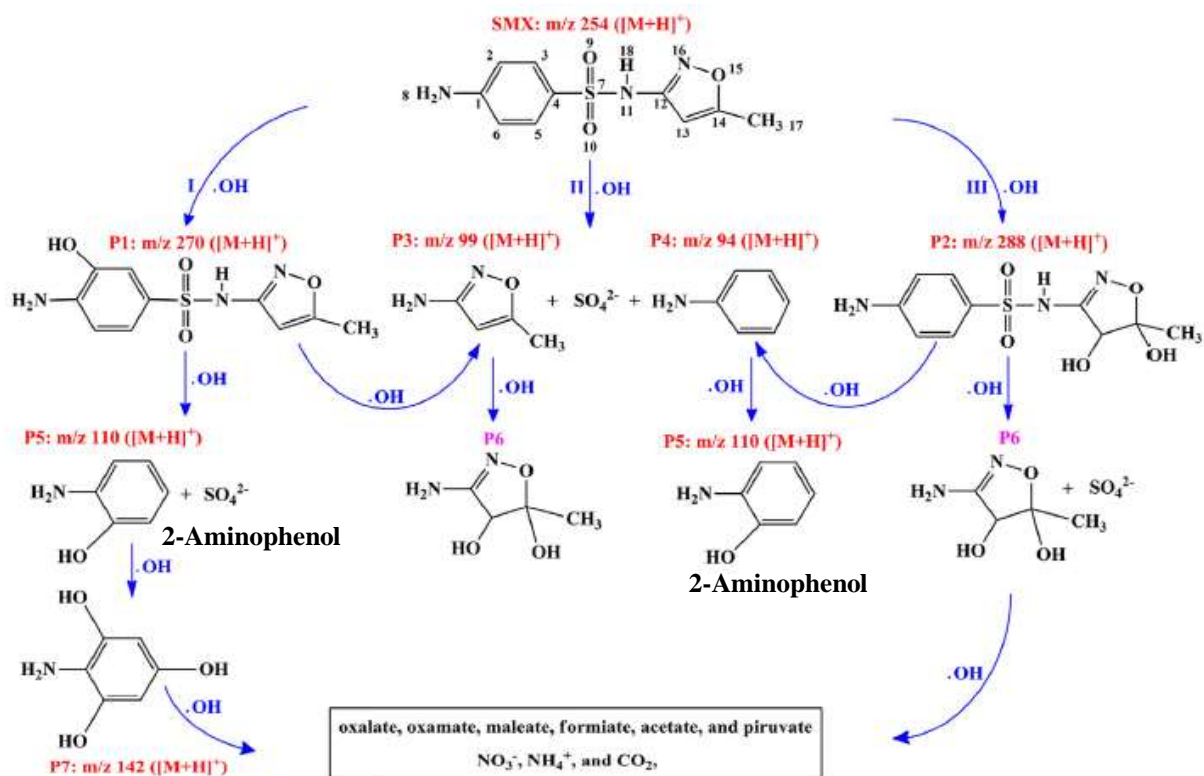


**Figure S4.9.** Proposed pathway of Fenton oxidation of SMX described by Du et al. (2017).

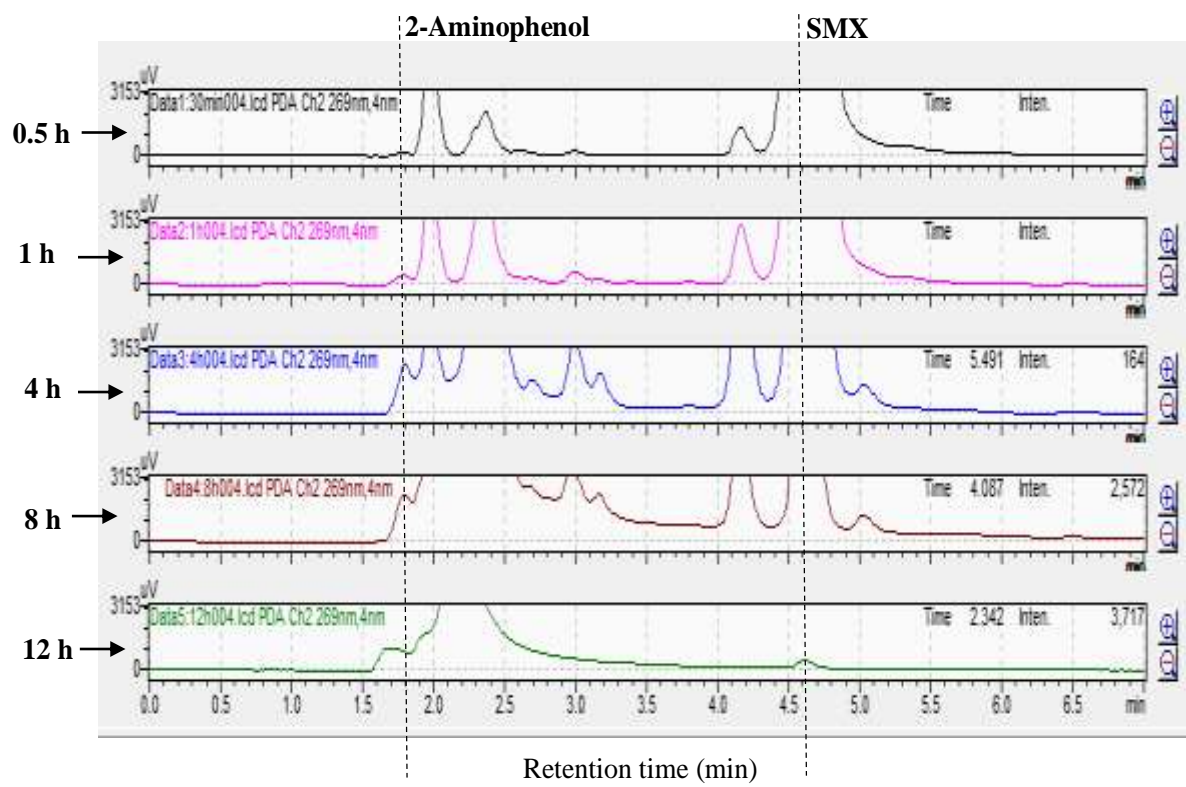


**Figure S4.10.** HPLC chromatograms under various reaction time during the Fenton oxidation of SMX. The peak positions of 2-Aminophenol and SMX were determined by matching with standard samples.

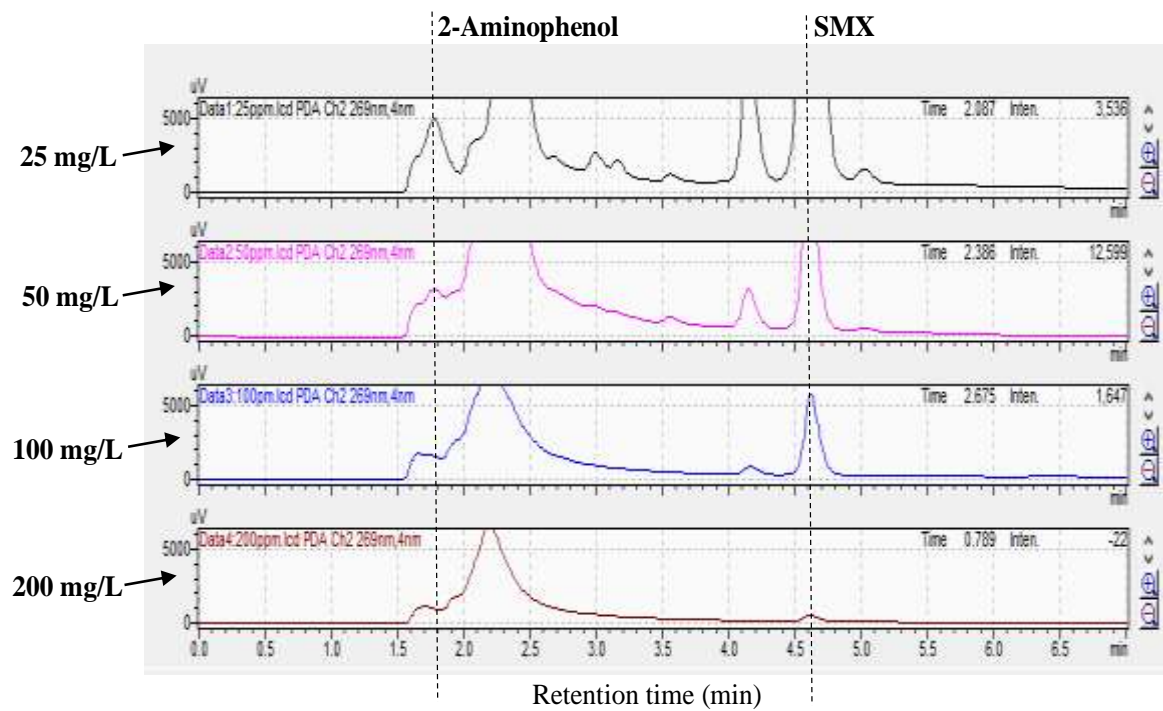


**Figure S4.11.** HPLC chromatograms of end products from the Fenton oxidation of SMX at various H<sub>2</sub>O<sub>2</sub> concentrations within 12 h of reaction time.

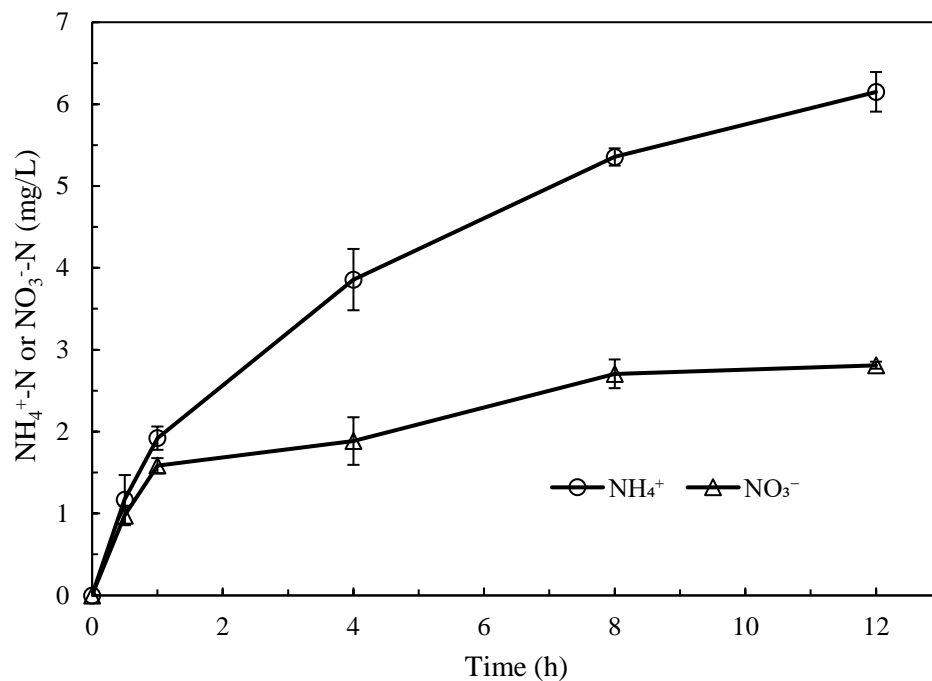


**Figure S4.12.** Change of concentration of  $\text{NH}_4^+$  and  $\text{NO}_3^-$  during the Fenton oxidation of SMX by FA-BC. Conditions: 0.01 g of FA-BC, 200 mg/L  $\text{H}_2\text{O}_2$ , 100 mL of 100 mg/L SMX, initial pH of 3, and temperature of 20 °C.

## APPENDIX D

### SUPPORTING INFORMATION FOR CHAPTER V

**Table S5.1** The water quality parameters of the Proctor Lake (Dublin, TX, USA).

COD (ppm)	136
pH	8.31
Total N (ppm)	92
Total P (ppm)	46
PO <sub>4</sub> <sup>3-</sup> -P (ppm)	24
NH <sub>3</sub> -N (ppm)	53

**Table S5.2** Comparison of MC-LR adsorption capacity ( $Q_m$ ) and surface area of various adsorbents.

Adsorbents	Surface area (m <sup>2</sup> /g)	$Q_m$ (mg/g)	Reference
Graphene oxide	-	1.700	(Pavagadhi et al., 2013)
Carbon nanotube	-	5.9	(Yan et al., 2006)
Iron oxide	-	0.618	(Gao et al., 2012)
Kaolinite	23.5	<0.09	(Liu et al., 2019)
Illite	21.7	<0.09	
Montmorillonite	13.1	<0.14	
Activated carbon	1111	0.357	(Mashile et al., 2018)
Wood chips biochar (300 °C)	4.1	0.926	(Li et al., 2014a)
Wood chips biochar (700 °C)	392.1	4.197	
Pine sawdust biochar (300 °C)	1.3	< 0.7	(Li et al., 2018)
Pine sawdust biochar (600 °C)	371.2	< 0.7	
Maize straw biochar (300 °C)	3.7	< 1.6	
Maize straw biochar (600 °C)	353.5	< 1.6	
Chicken manure biochar (300 °C)	4.0	< 1.8	
Chicken manure biochar (600 °C)	86.6	< 1.8	
Giant reed biochar (300°C)	2.6	0.14	(Liu et al., 2018a)
Giant reed biochar (350°C)	2.1	0.14	
Giant reed biochar (400°C)	3.0	0.71	
Giant reed biochar (500°C)	2.5	41.2	
Giant reed biochar (600°C)	58.8	42.4	



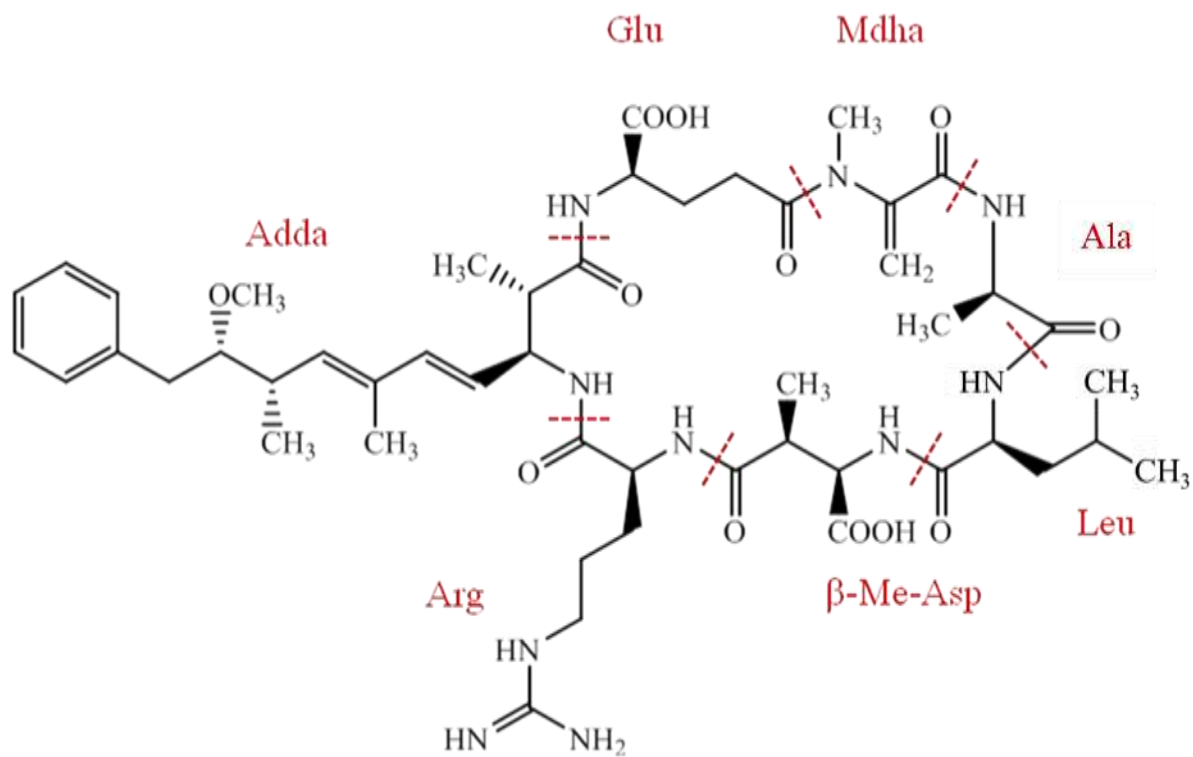


**Figure S5.1.** The chemical structure of microcystin-LR (Li et al., 2018).

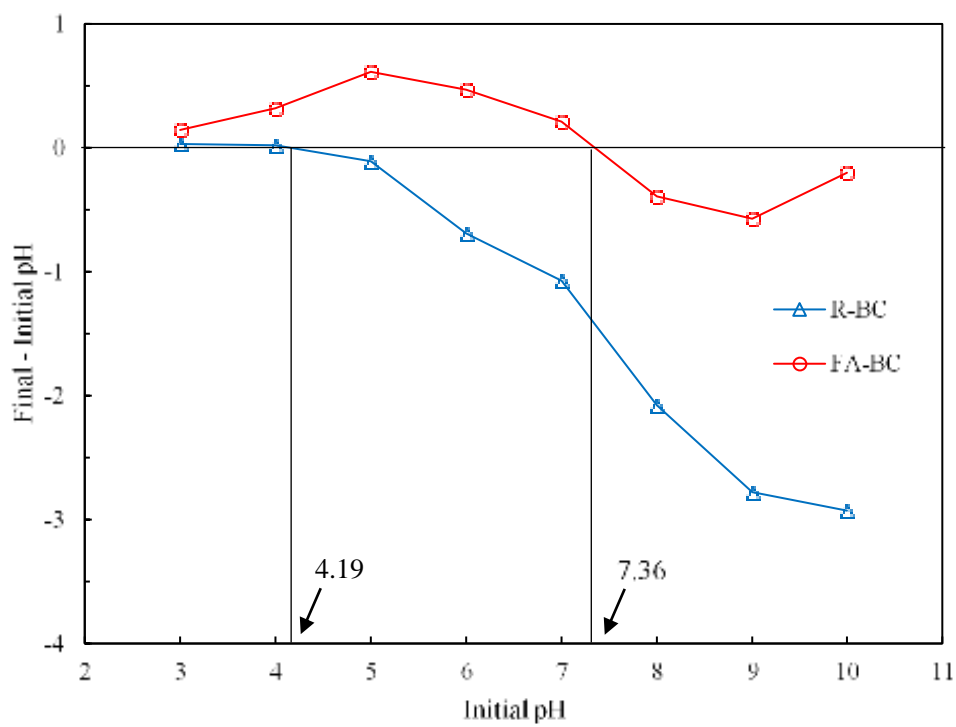


**Figure S5.2.** The pHPZC of BCs.

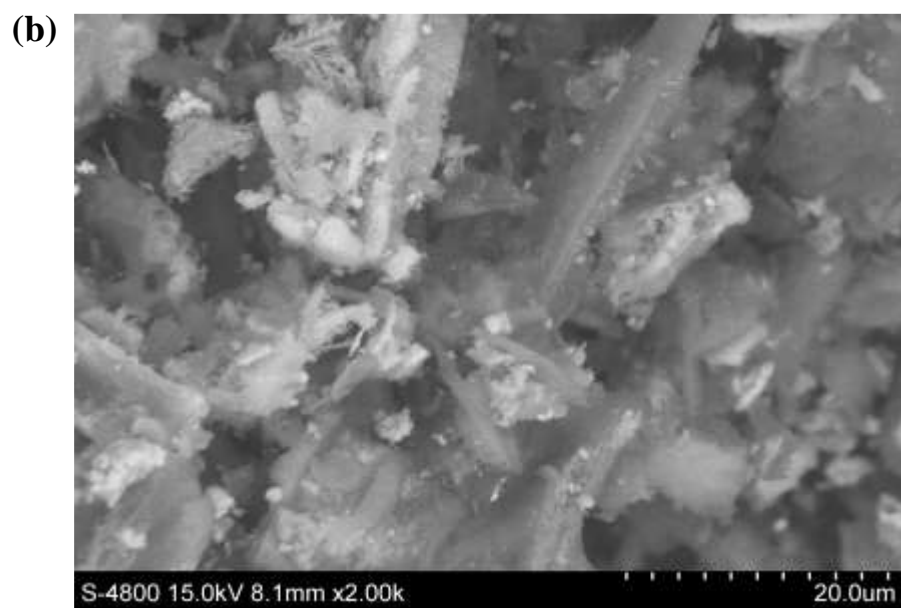
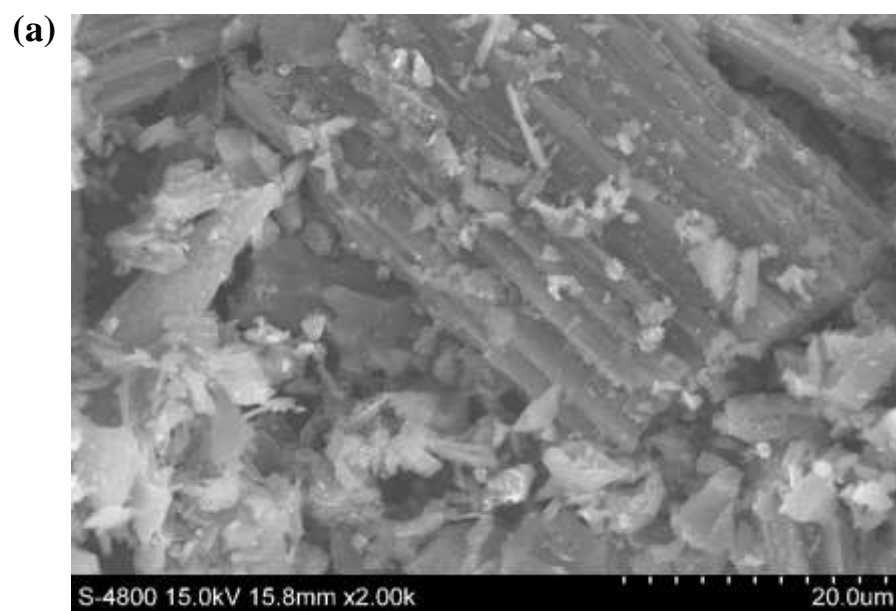
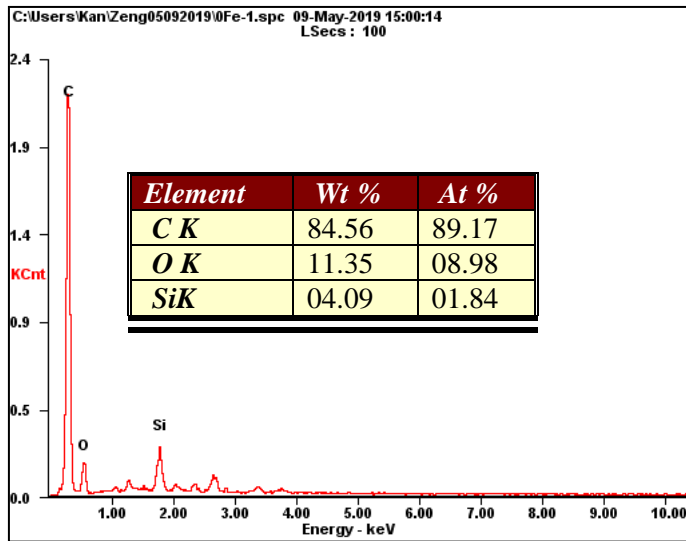


**Figure S5.3.** SEM images of BCs (a: R-BC; b: FA-BC).

(a)



(b)

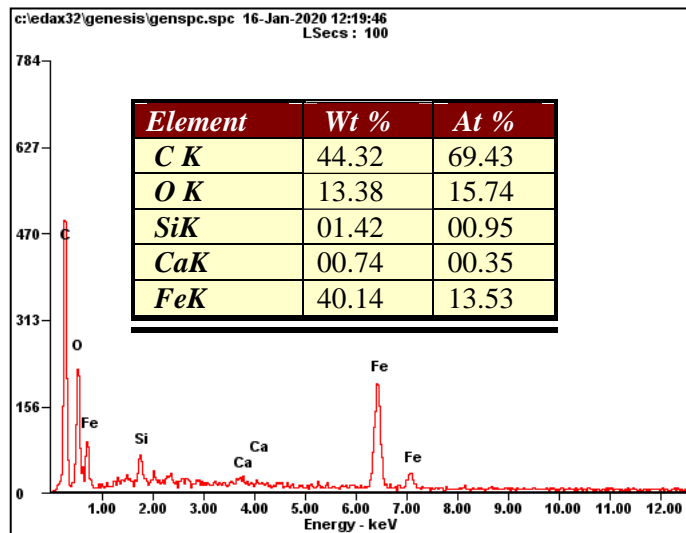
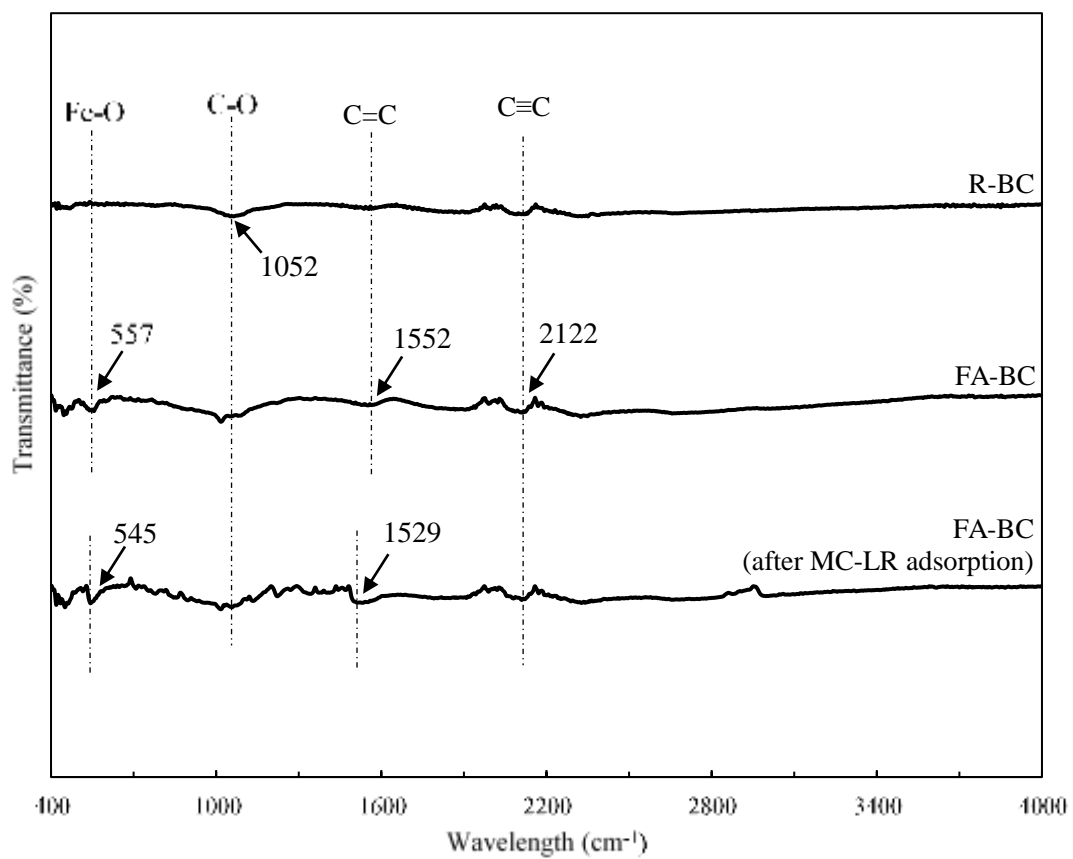
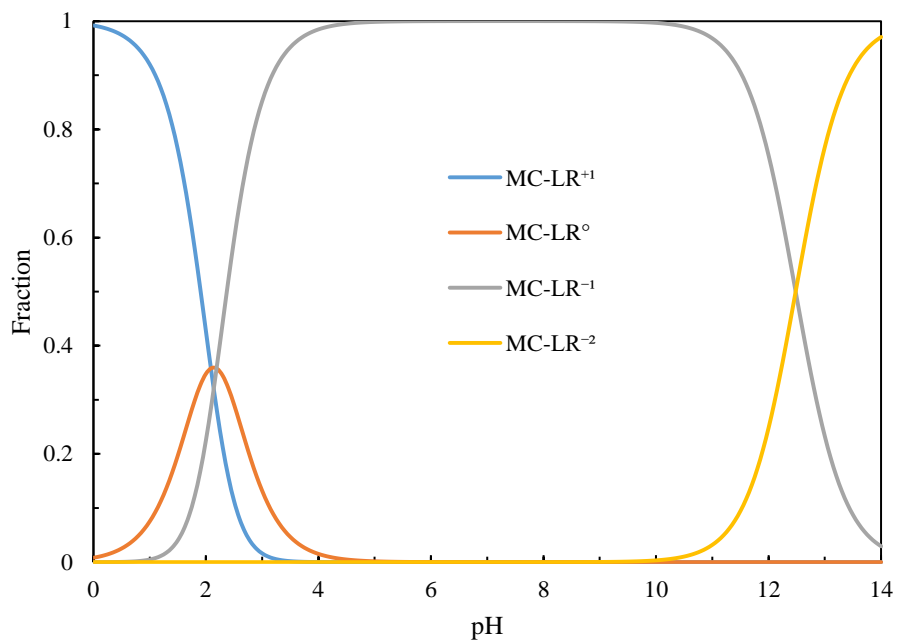


Figure S5.4. EDX analysis of BCs (a: R-BC; b: FA-BC).



**Figure S5.5.** FTIR spectra of BCs.



**Figure S5.6.** pH-dependent distribution of MC-LR species.

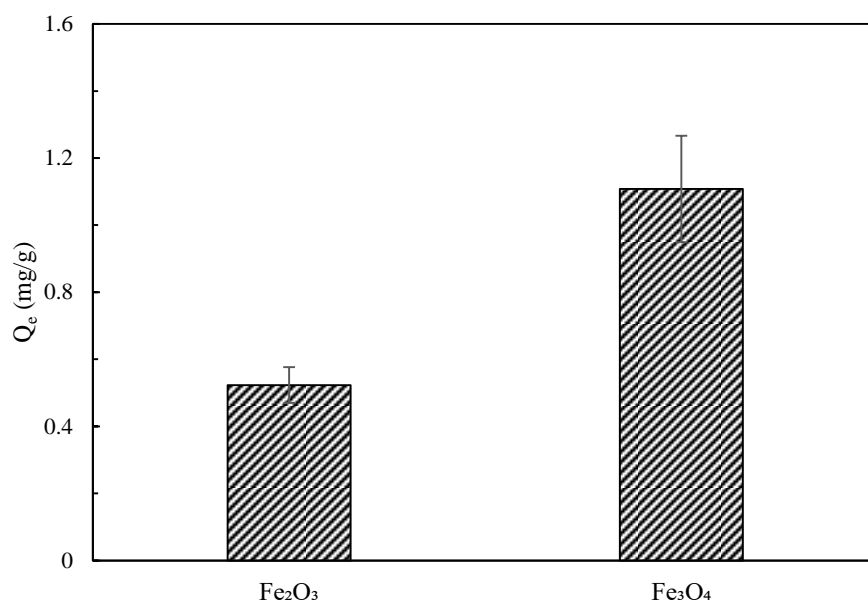


**Figure S5.7.** Adsorption capacity of MC-LR onto  $Fe_2O_3$  and  $Fe_3O_4$ .

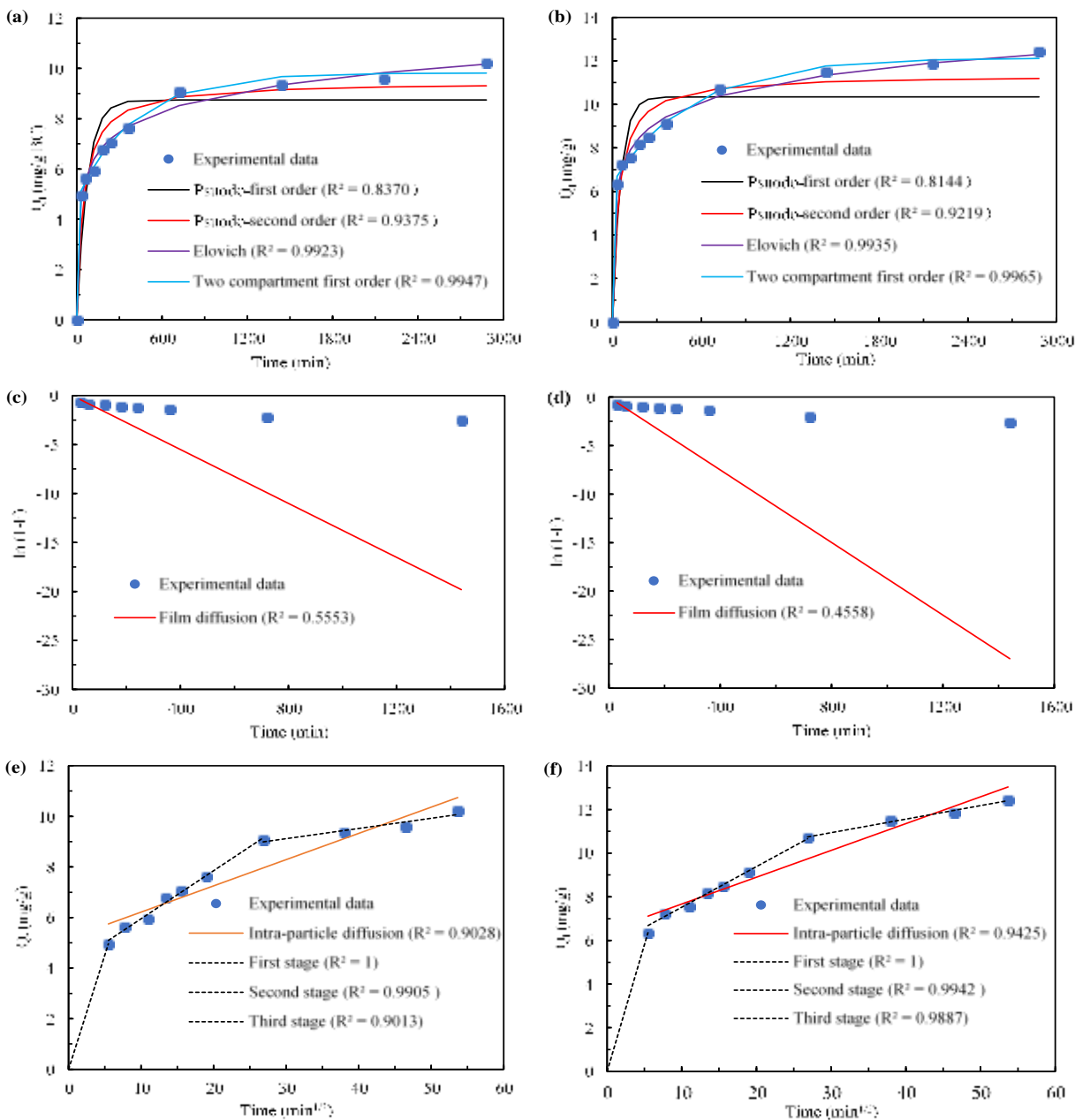


**Figure S5.8.** Adsorption kinetics of MC-LR on FA-BC by fitting the pseudo-first order, pseudo-second order, two compartment first order and Elovich ((a) and (b)), film diffusion model ((c) and (d)), and intra-particle diffusion model ((e) and (f)) under two different initial concentrations of 500 µg/L((a), (c) and (e)) and 1000 µg/L((b), (d) and (f)).

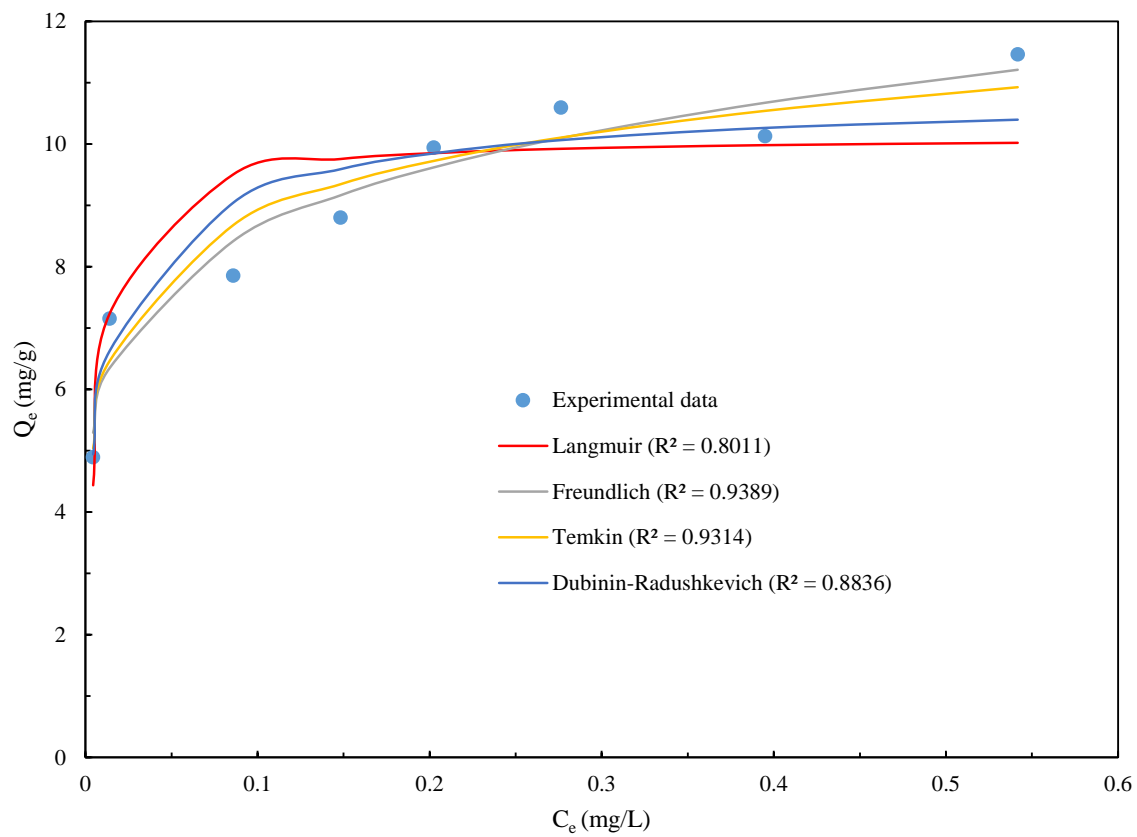


**Figure S5.9.** Adsorption isotherm of MC-LR on FA-BC.



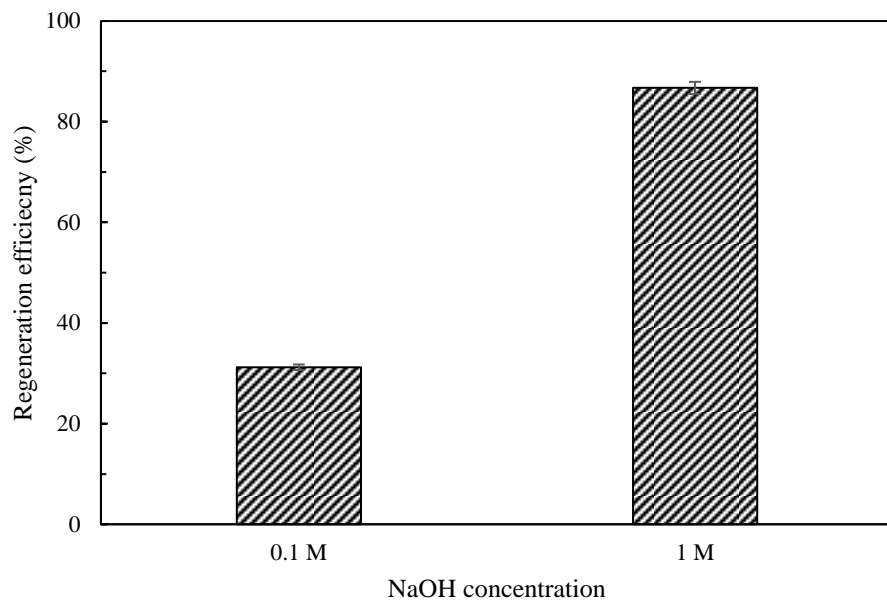


**Figure S5.10.** Regeneration of MC-LR spent FA-BC by NaOH desorption.

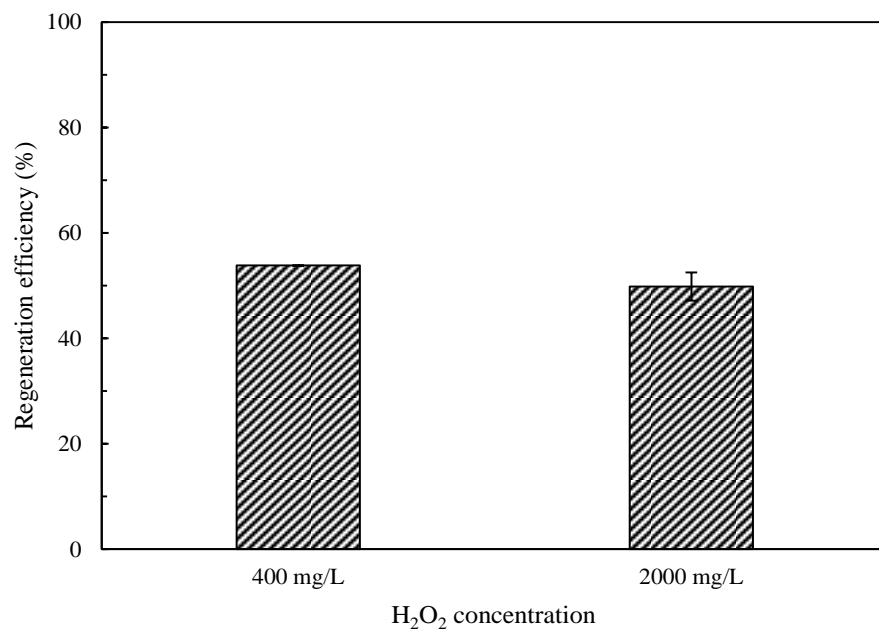


**Figure S5.11.** Regeneration of MC-LR spent FA-BC by Fenton oxidation.

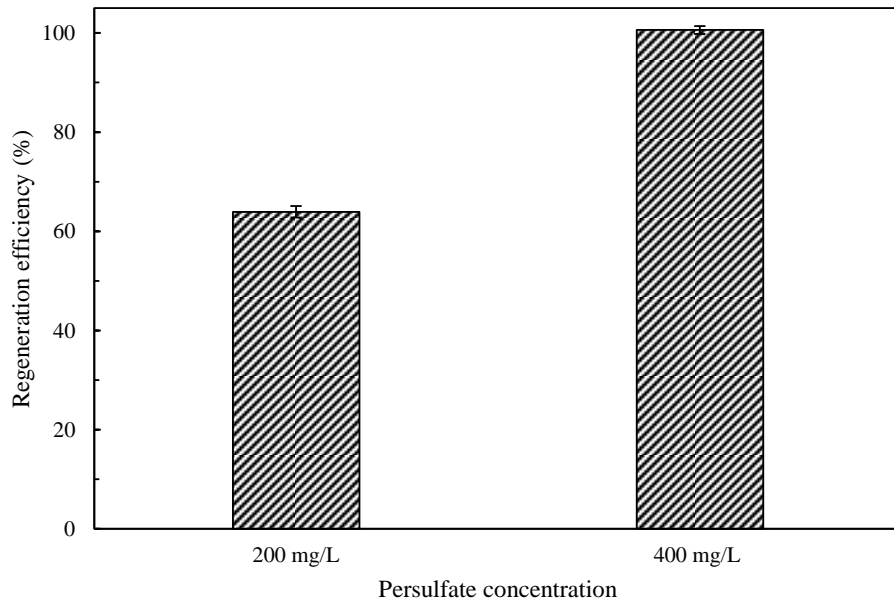


**Figure S5.12.** Regeneration of MC-LR spent FA-BC by persulfate oxidation.

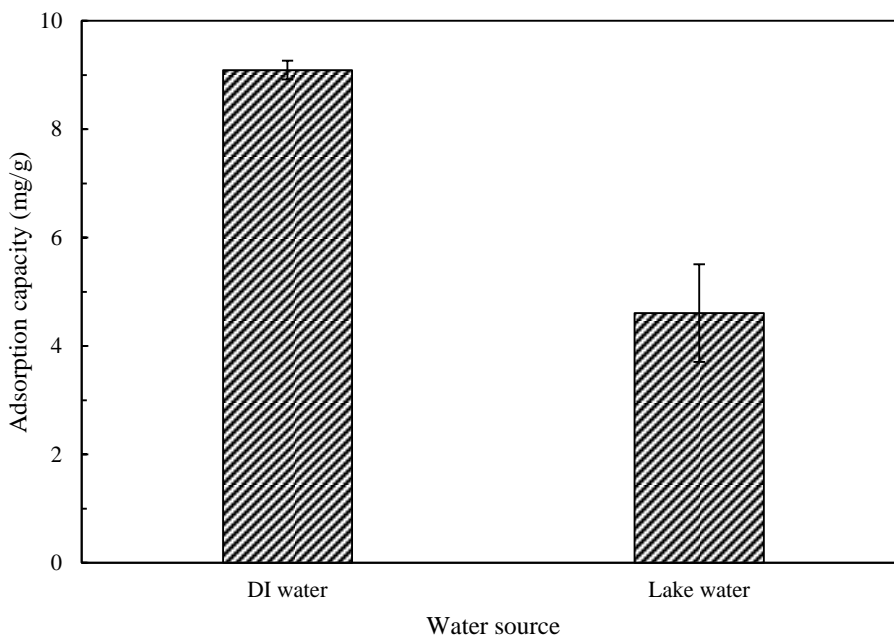


**Figure S5.13.** MC-LR adsorption capacity in DI water and lake water.

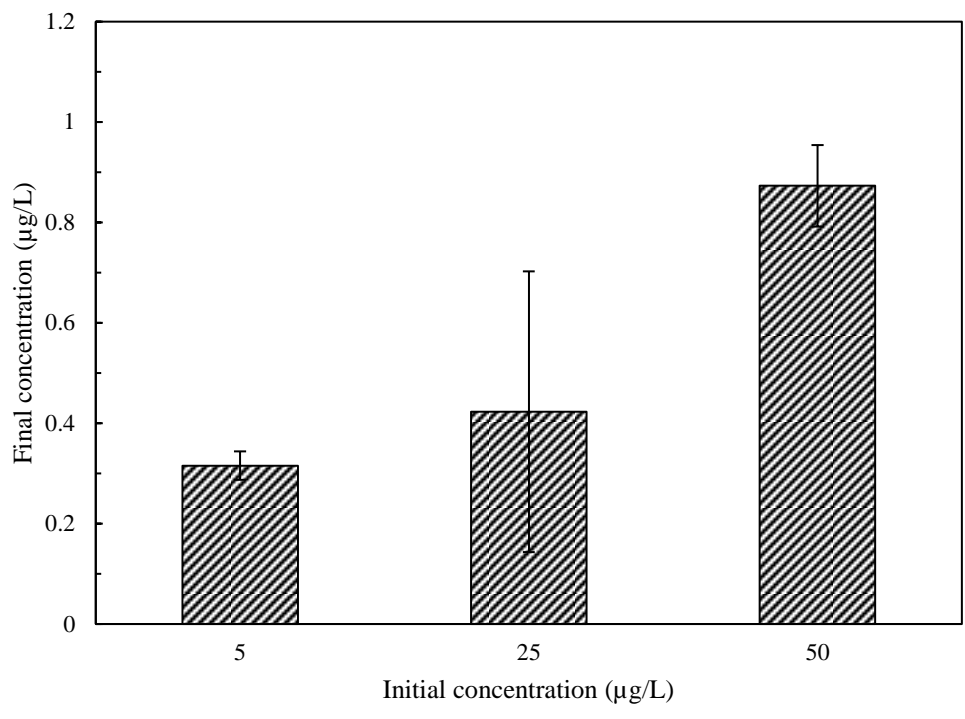


**Figure S5.14.** MC-LR adsorption in lake water with various initial concentrations.

## APPENDIX E

### SUPPORTING INFORMATION FOR CHAPTER VI

**Table S6.1** Summary of regeneration of contaminants spent adsorbents by persulfate oxidation.

Adsorbents	Contaminants	Activation methods for persulfate	Regeneration results	References
Metal-organic frameworks: MIL101(Cr)	Sulfadimethoxine (SDM)	Thermal; UV	Thermal activation of persulfate showed better performance for SDM removal (95.3%) than UV activation of persulfate (87.3%).	(Peng et al., 2019)
Commercial activated carbon (Calgon Carbon Corp., F400)	Trichloroethylene	Fe <sup>2+</sup>	About 60% of regeneration efficiency was achieved after regeneration by Fe <sup>2+</sup> /persulfate.	(Liang et al., 2009)
Commercial activated carbon (Calgon Carbon Corp., F400)	Phenol	Electrochemical/Fe <sup>2+</sup>	The highest regeneration efficiency was 58.2% with the conditions of 1000 mg/L Fe <sup>2+</sup> , 2000 mg/L persulfate, and voltage of 22.5V.	(Huang et al., 2017)
Commercial activated carbon (made from coconut)	Sulfanilic acid	Microwave	The regeneration efficiency was about 89% after seven regeneration cycles.	(Wei et al., 2012)
Commercial activated carbon (made from coconut, reactivated by KOH)	Perfluorooctane sulfonate (PFOS); Chlorinated polyfluorinated ether sulfonate (F53B)	Thermal	The regeneration efficiencies for PFOS and F53B were about 74.4% and 74.1% after six regeneration cycles.	(Du et al., 2016)
Commercial activated carbon (Calgon Carbon Corp.)	Natural organic matter	UV	87.4% of adsorption capacity was restored with the conditions of 60 g/L persulfate and 1.75*10 <sup>4</sup> mJ/cm <sup>2</sup> UV exposure.	(An et al., 2015)
Metal-organic frameworks: MIL101(Cr)	Sulfamethoxazole	Ultrasound	The readsorption abilities were almost same after regeneration by 0.1-7.5 g/L persulfate.	(Huang et al., 2018)
Commercial activated carbon (Calgon Carbon Corp., URV)	Methy tert-butyl ether (MTBE)	Thermal; alkaline; H <sub>2</sub> O <sub>2</sub> -persulfate binary mixtures	Thermal-activation of persulfate resulted in greater MTBE removal than either alkaline-activation or H <sub>2</sub> O <sub>2</sub> -persulfate binary mixtures. However, MTBE removal efficiency was less than 50%.	(Huling et al., 2011)

**Table S6.2** Iron concentration in the solution after persulfate oxidation of MC-LR spent FA-BC at various pH values. Conditions: 0.004 g of MC-LR spent FA-BC, 40 mL of 200 mg/L PS, and 20 °C.

pH	Iron concentration (mg/L)
4	1.25
6	0.87
8	0.82
10	0.02

**Table S6.3** Persulfate reaction rate constant (First order reaction rate) at various pH values during the persulfate oxidation of MC-LR spent FA-BC. Conditions: 0.004 g of MC-LR spent FA-BC, 40 mL of 200 mg/L PS, and 20 °C.

pH	S <sub>2</sub> O <sub>8</sub> <sup>2-</sup> reaction rate (h <sup>-1</sup> )
4	0.0709
6	0.0634
8	0.0638
10	0.0311

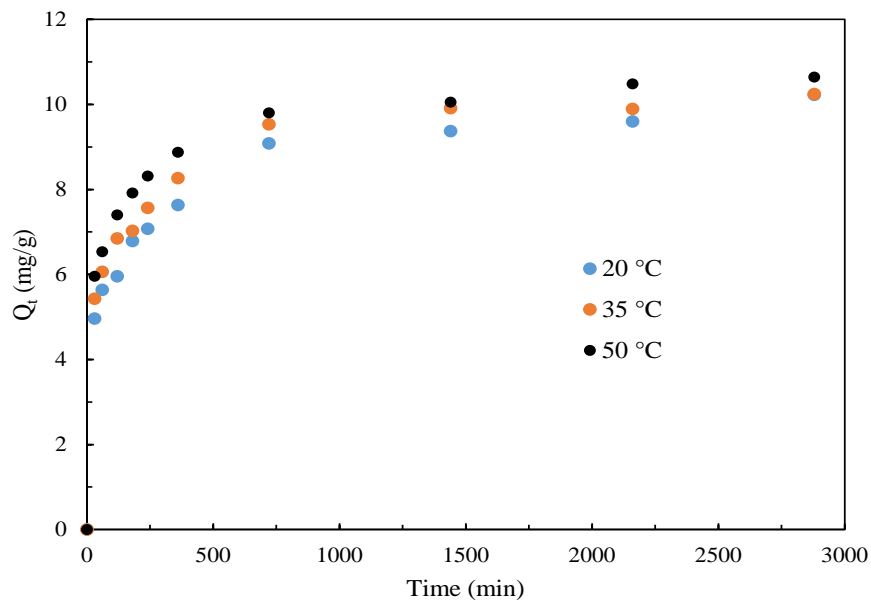


**Figure S6.1.** Adsorption of MC-LR onto FA-BC at various temperature (20-50 °C). Experimental conditions: 100 mL of 0.5 mg/L MC-LR, 0.004 g of FA-BC, and initial pH of 6.

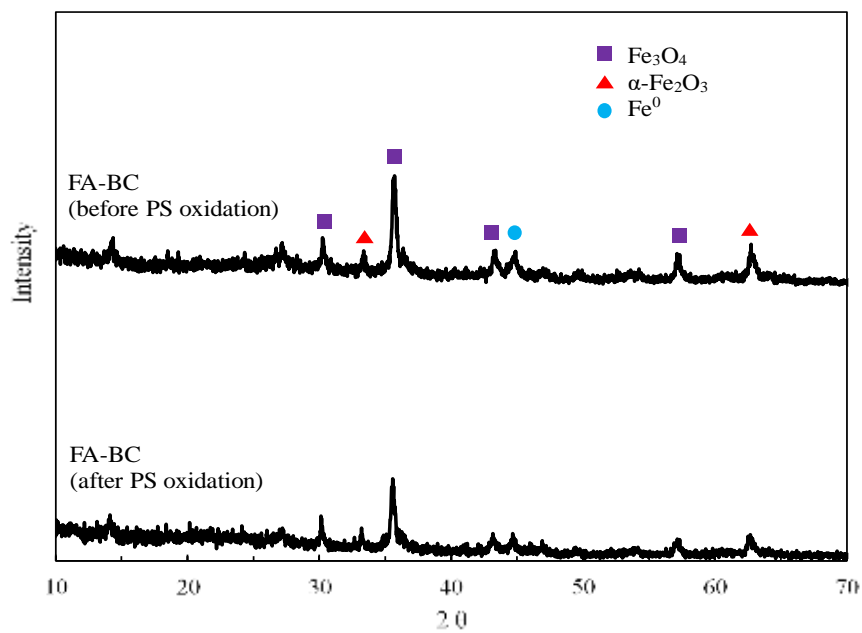


**Figure S6.2.** XRD patterns of FA-BC before and after PS oxidation.

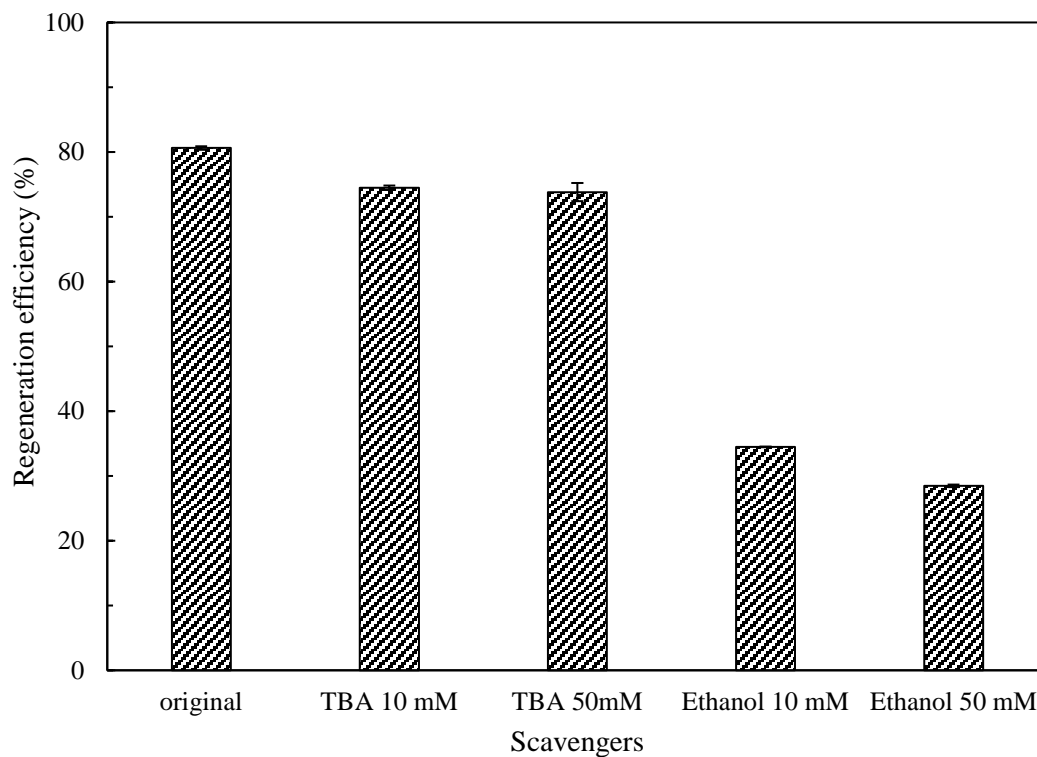


**Figure S6.3.** Regeneration of MC-LR spent FA-BC by PS oxidation in the presence/absence of TBA and ethanol. Conditions: 0.004 g of MC-LR spent FA-BC, 40 mL of 200 mg/L PS, pH 6, and 20 °C.

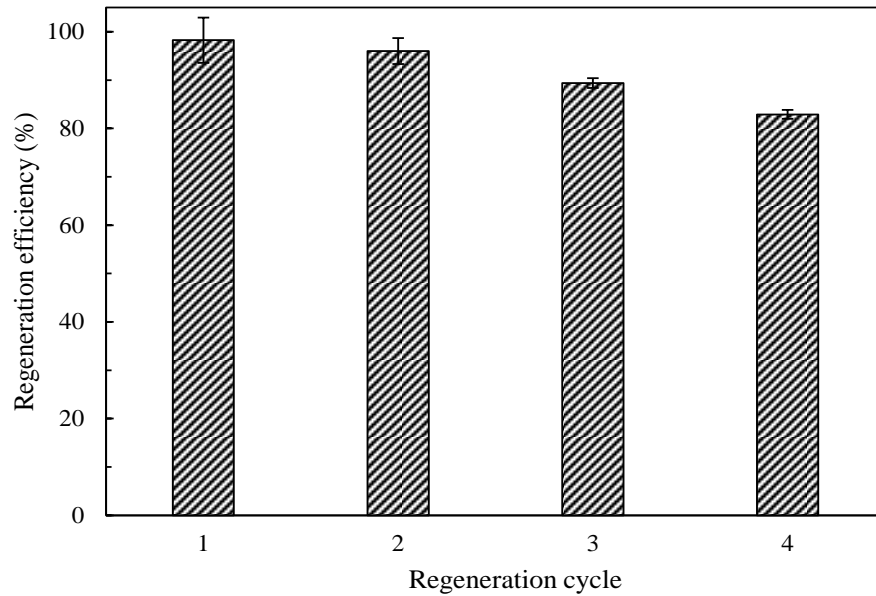


**Figure S6.4.** Reusability of FA-BC for MC-LR adsorption in lake water using PS oxidation regeneration. Adsorption conditions: 100 mL of lake water spiked with 0.25 mg/L MC-LR, 0.002 g of FA-BC, pH 8.25, 20 °C and 2 d. Regeneration conditions: 0.002 g of MC-LR spent FA-BC, 40 mL of 200 mg/L PS, pH 6, and 50 °C.

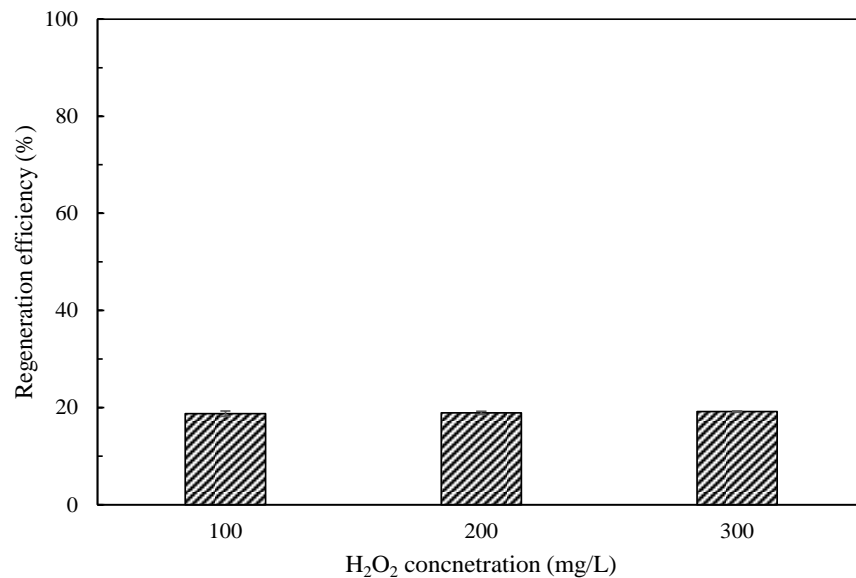


**Figure S6.5.** Fenton-driven regeneration of sulfamethoxazole spent FA-BC. Regeneration conditions: 0.01 g of sulfamethoxazole spent FA-BC, 100 mL of H<sub>2</sub>O<sub>2</sub> solution, pH 3, and 2 d.



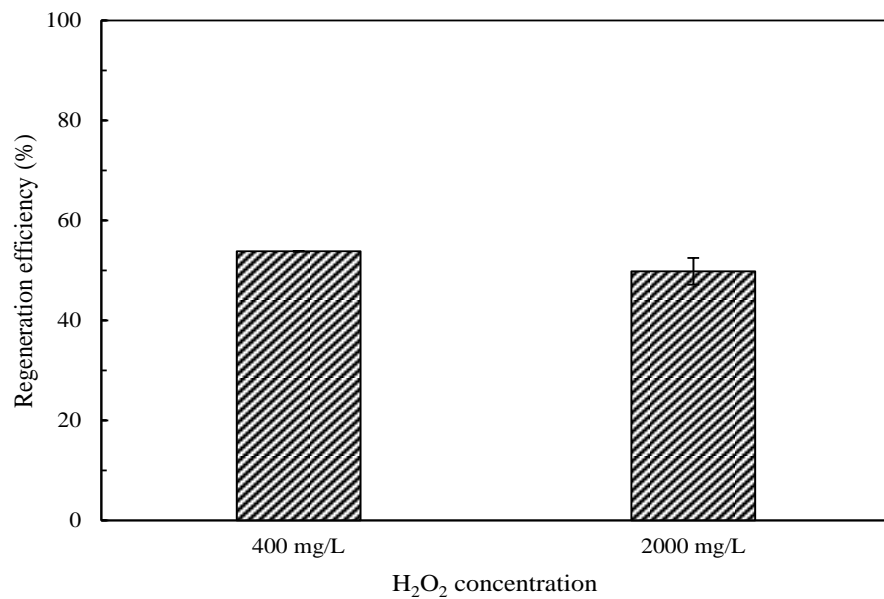


**Figure S6.6.** Fenton-driven regeneration of MC-LR spent FA-BC. Regeneration conditions: 0.004 g of MC-LR spent FA-BC, 40 mL of H<sub>2</sub>O<sub>2</sub> solution, pH 3, and 2 d.

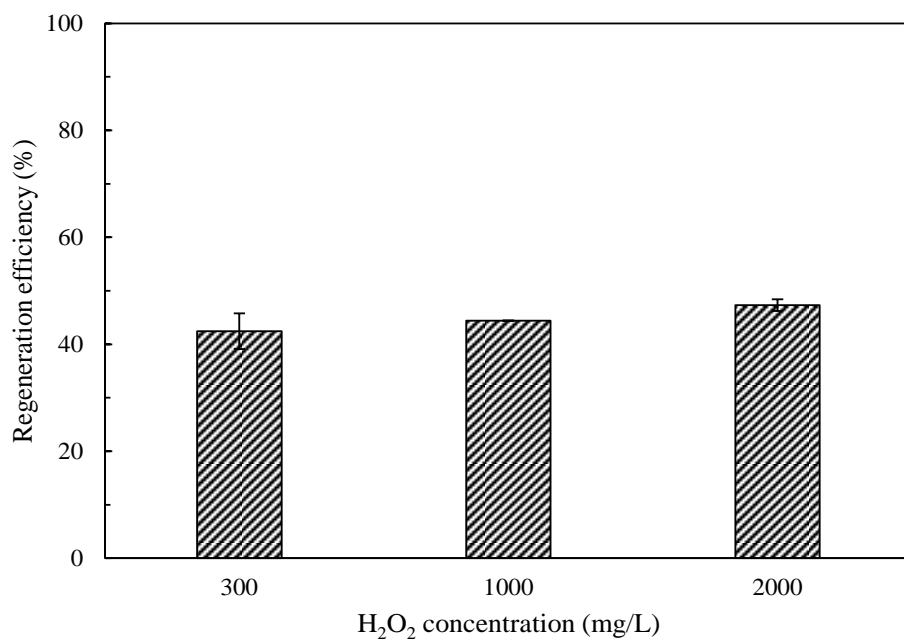


**Figure S6.7.** Fenton-driven regeneration of tetracycline spent FA-BC. Regeneration conditions: 0.02 g of tetracycline spent FA-BC, 100 mL of H<sub>2</sub>O<sub>2</sub> solution, pH 3, and 2 d.

## APPENDIX F

### SUPPORTING INFORMATION FOR CHAPTER VII

**Table S7.1** The physicochemical characteristics of AF and AF-BC.

	Elemental analysis (wt. %)				O/C	H/C	Proximate analysis (%, dry basis)		
	C	H	O	N			Fixed Carbon	Volatile Carbon	Ash
AF	43.9	5.8	38.5	2.4	0.7	1.6	5.5	85.1	9.4
AFBC	68.8	4.8	14.4	4.9	0.2	0.8	34.5	58.4	7.1
	Mineral composition (wt. %)						BET surface area		
	N	P	K	Ca	Mg	Fe	(m <sup>2</sup> /g)		
AF	2.4	0.2	2.2	1.2	0.3	<0.1	0.6		
AFBC	4.9	0.2	0.1	1.4	0.3	0.1	3.5		

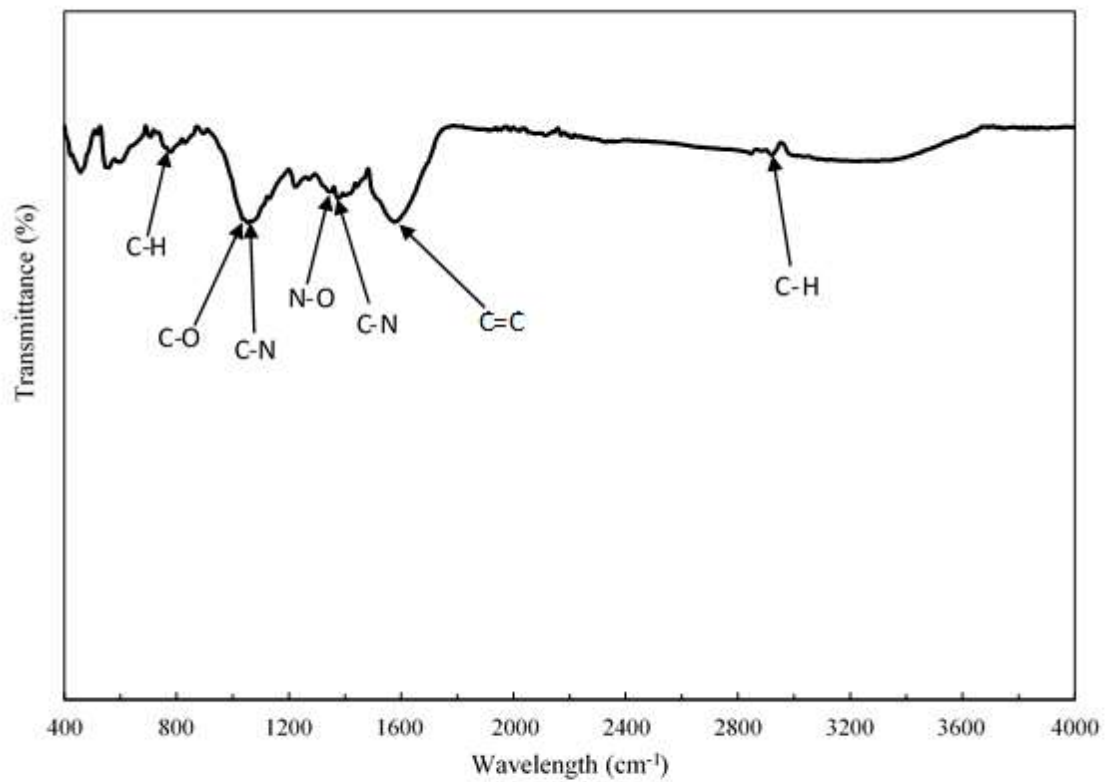


**Figure S7.1.** FT-IR spectrum of AF-BC.

**APPENDIX G**  
**SUPPORTING INFORMATION FOR CHAPTER VIII**



**Figure S8.1.** PFI mill.

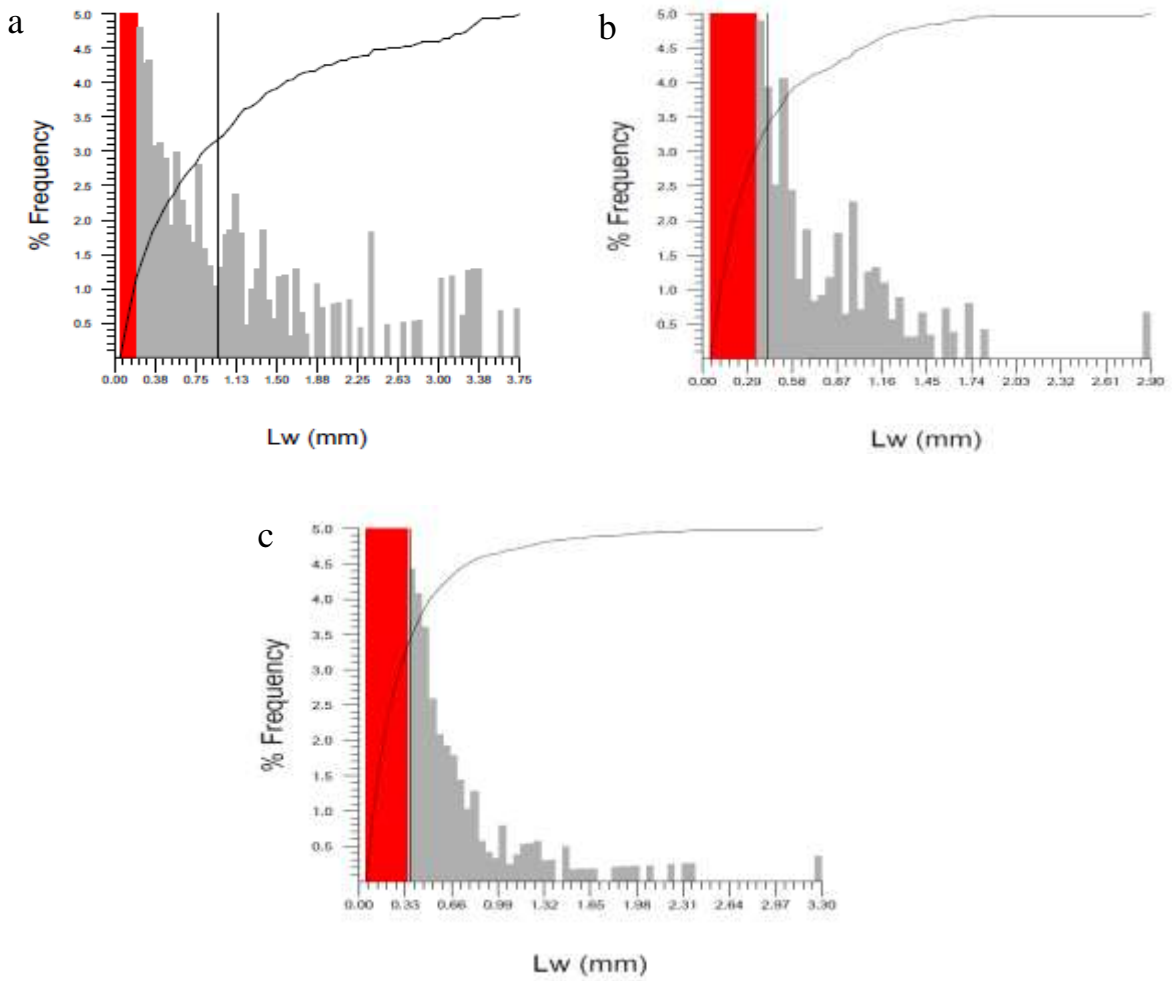


**Figure S8.2.** Length weighted manure length distribution of unrefined manure (a), and refined manure with 6K revolutions (b) and 60K revolutions (c).